

particle morphology could be observed by transmission electron microscopy (TEM) as shown in Figure 2. The particles had a spherical shape and core-shell morphology where PMMA core was presented in the light region and PEI shell was the dark periphery.

FTIR spectroscopy was employed to identify the chemical structure of PMMA/PEI particles. Figure 3 shows the main characteristic peak of PMMA at  $1731\text{ cm}^{-1}$ , which was attributed to a C=O stretching. In addition, the characteristic peaks of PEI at  $3440\text{ cm}^{-1}$  corresponding to N-H stretching was observed. Also, the signals at  $1635\text{ cm}^{-1}$  and  $1557\text{ cm}^{-1}$  corresponded to  $1^\circ$  and  $2^\circ$  amines, respectively. This information could imply that both PEI and PMMA were included in the core-shell nanoparticles.

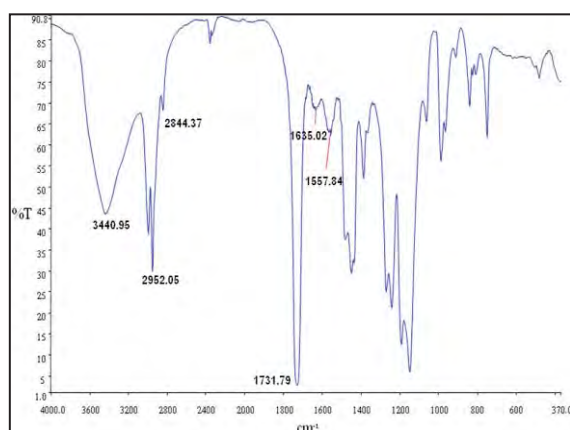


Figure 3. FT-IR spectrum of PMMA/PEI core-shell nanoparticles.

### 3.3 Effect of pH on adsorption of Cu(II)

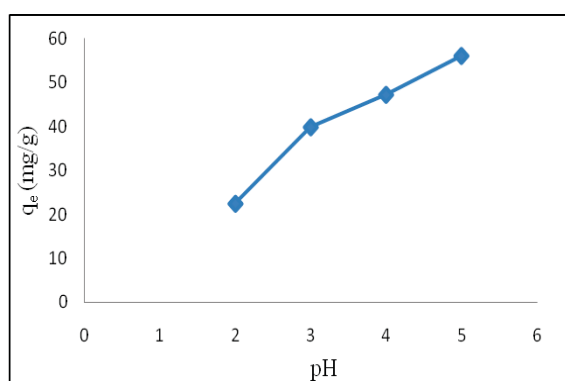


Figure 4. Effect of pH on adsorption of Cu(II).

Adsorption capacity was found to be influenced by the pH value because PEI has charges on its surface, depending on pH value. At low pH, amine groups of PEI were protonated, resulting in a decrease of binding ability to the Cu(II) due to the Cu(II) ions had a similar charge, causing the repulsion force between protonated amine groups and Cu(II) ions. Increasing pH of

solution, PEI had more negative charge on surface, so the adsorption ability increased.

### 3.4 Adsorption isotherms

Figure 5 shows the Cu(II) adsorption isotherm of PMMA/PEI core-shell nanoparticles. At first, the equilibrium adsorption capacity was rapidly increased from  $24.45\text{ mg/g}$  to  $50.94\text{ mg/g}$ , and then the adsorption capacity reached to saturation that was the maximum adsorption capacity ( $q_m$ ) at  $50.94\text{ mg/g}$ .

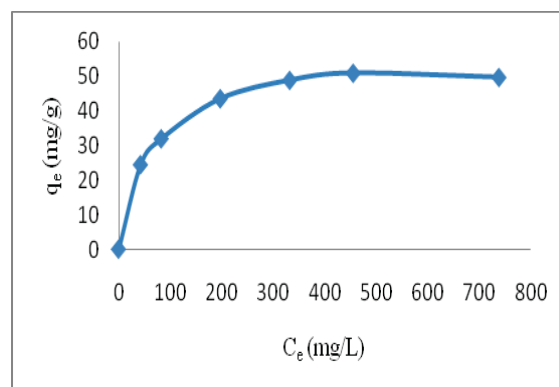


Figure 5. Cu(II) adsorption isotherm of PMMA/PEI core-shell nanoparticles.

The adsorption isotherm of Cu(II) on PMMA/PEI core-shell nanoparticles was found to be in accord with Langmuir adsorption isotherm as shown in Figure 6. The Langmuir model assumes that the adsorption occurs as monolayer and all adsorption sites are equal on the surface [11] as represented by Eq. 4.

$$\frac{C_e}{q_e} = \frac{1}{q_m K_L} + \frac{C_e}{q_m} \quad (4)$$

where,  $C_e$  is the equilibrium concentrations of Cu(II) in solutions (mg/L),  $q_e$  is the equilibrium adsorption capacity (mg/g),  $q_m$  is the maximum adsorption capacity (mg/g) and  $K_L$  is the affinity constant (L/mg).

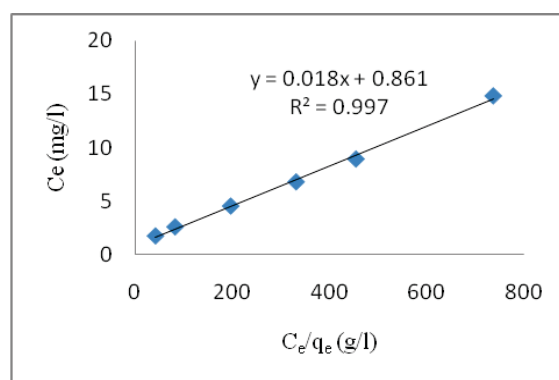


Figure 6. Langmuir isotherm for adsorption of Cu(II) on PMMA/PEI core-shell nanoparticles.

From Figure 6, the values of  $q_m$  and  $K_L$  that were associated to the maximum adsorption capacity and adsorption energy, respectively, can be calculated. The calculated  $q_m$  was 55.55 mg/g that closely the experimental  $q_m$  (50.94 mg/g) and calculated  $K_L$  was 0.02 L/g.

Another adsorption model was Freundlich model that assumes the adsorption occurs on heterogeneous surfaces as well as multilayer sorption and is expressed by the following equation: [12, 13].

$$q_e = K_F C_e^{1/n} \quad (5)$$

$$\log q_e = \log K_F + \frac{1}{n} \log C_e \quad (6)$$

where  $K_F$  is the Freundlich constants and  $n$  is the adsorption intensity.

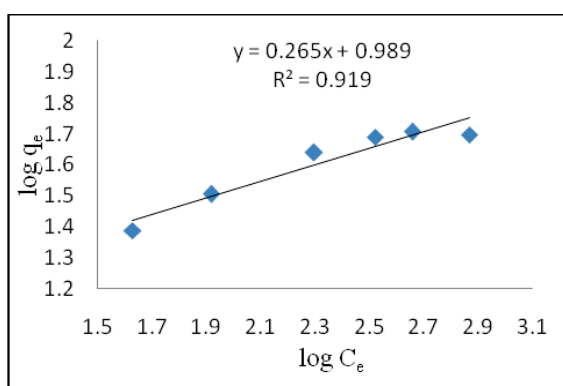


Figure 7. Freundlich isotherm for adsorption of Cu(II) on PMMA/PEI core-shell nanoparticles.

The linear plot of  $\log q_e$  versus  $\log C_e$  was able to determine the value of  $K_F$  and  $n$ . The calculated  $K_F$  was 9.75 and  $n$  was 3.77. Considering the correlation coefficients ( $R^2$ ) of Figures 6 and 7 (0.997 and 0.919), it was found that the adsorption of Cu(II) ions by PMMA/PEI core-shell nanoparticles was well corresponded to the Langmuir model.

#### 4. Conclusion

The PMMA/PEI core-shell nanoparticles were synthesized *via* an emulsifier-free emulsion polymerization. The particle size and zeta-potential exhibited around 254.6 nm and 39.7 mV at pH 6.5, respectively. The effect of adsorption time of the complex between PEI and Cu(II) was studied by UV-Visible spectrometry showed the PEI was a good material for removal of Cu(II) ions. The adsorption capacity was influenced by the pH value. The adsorption of Cu(II) on the core-shell nanoparticles was found to correspond to Langmuir isotherm with the maximum adsorption capacity ( $q_m$ ) on the particles of 55.55 mg/g, which was nearly the experimental value and  $K_L$  was 0.02 L/g. So, the PMMA/PEI core-

shell nanoparticles would be the effective and fast adsorbents for removal of Cu(II) ions.

#### Acknowledgements

This work is funded by TGIST, NANOTEC, NSTDA, and NRCT.

#### References

- [1] Chen J, et al. A facile approach for cupric ion detection in aqueous media using polyethyleneimine/PMMA core-shell fluorescent nanoparticles. *Nanotechnology*. 2009;20(36):365502.
- [2] Qi J, Li X, Li Y, Zhu J, Qiang L. Selective removal of Cu(II) from contaminated water using molecularly imprinted polymer. *Frontiers of Chemical Engineering in China*. 2008;2(1):109-14.
- [3] David M. Ayres APD, Paul M. Gietka. *Removing Heavy Metals from Wastewater*, University of Maryland. 1994.
- [4] Stella Lacour J-CB, Bernard Serpaud, Pierre Chantron, Richard Arcos. Removal of heavy metals in industrial wastewaters by ion-exchanger grafted textiles. *Analytica Chimica Acta*. 2001;428:121 - 32.
- [5] Wu A, Jia J, Luan S. Amphiphilic PMMA/PEI core-shell nanoparticles as polymeric adsorbents to remove heavy metal pollutants. *Colloids and Surfaces A: Physicochemical and Engineering Aspects*. 2011;384(1-3):180-5.
- [6] Copello GJ, Diaz LE, Campo Dall'Orto V. Adsorption of Cd(II) and Pb(II) onto a one step-synthesized polyampholyte: Kinetics and equilibrium studies. *Journal of Hazardous Materials*. 2012;217-218(0):374-81.
- [7] Deng S, Ting Y-P. Characterization of PEI-modified biomass and biosorption of Cu(II), Pb(II) and Ni(II). *Water Research*. 2005;39(10):2167-77.
- [8] Bayramoğlu G, Yakup Arica M. Adsorption of Cr(VI) onto PEI immobilized acrylate-based magnetic beads: Isotherms, kinetics and thermodynamics study. *Chemical Engineering Journal*. 2008;139(1):20-8.
- [9] Fields R. The rapid determination of amino groups with TNBS. In: C. H. W. Hirs SNT, editor. *Methods in Enzymology*: Academic Press; 1972. p. 464-8.
- [10] Li P, Zhu J, Sunintaboon P, Harris FW. New Route to Amphiphilic Core-Shell Polymer Nanospheres: Graft Copolymerization of Methyl Methacrylate from Water-Soluble Polymer Chains Containing Amino Groups. *Langmuir*. 2002 2002/10/01;18(22):8641-6.
- [11] Ren Y, Zhang M, Zhao D. Synthesis and properties of magnetic Cu(II) ion imprinted composite adsorbent for selective removal of copper. *Desalination*. 2008;228(1-3):135-49.
- [12] Pang Y, Zeng G, Tang L, Zhang Y, Liu Y, Lei X, et al. PEI-grafted magnetic porous powder for highly effective adsorption of heavy metal ions. *Desalination*. 2011;281:278-84.
- [13] Ho Y, Porter J, McKay G. Equilibrium Isotherm Studies for the Sorption of Divalent Metal Ions onto Peat: Copper, Nickel and Lead Single Component Systems. *Water, Air, & Soil Pollution*. 2002;141(1):1-33.

# SYNTHESIS OF CALCIUM SILICATE FROM RICE HUSK AND EGG SHELL BY HYDROTHERMAL METHOD

Warinda Marujiwat<sup>1</sup>, Ratchadaporn Puntharod<sup>1,2\*</sup>

<sup>1</sup> Department of Chemistry, Faculty of Science, Maejo University, Chiang Mai, 50290 Thailand

<sup>2</sup> Nanoscience and Nanotechnology Laboratory, Maejo University, Chiang Mai 50290, Thailand

\* Author for correspondence; E-Mail: ratchada@mj.ac.th, Tel. +66 53 873530, Fax. +66 53 873548

**Abstract:** Calcium silicate ( $\text{CaSiO}_3$ ) can be used in several applications such as ceramics, construction, and medical. In this work, the cheap agricultural materials such as rice husk and egg shell were the starting materials to synthesize calcium silicate by hydrothermal method. The silica from rice husk was extracted by 1 M sodium hydroxide then filtered the solution and adjusted pH of solution to 8 by adding 1 M hydrochloric acid. The silica gel was formed and the gel was dried in the oven. Calcium oxide was prepared from egg shell by calcination in a muffle furnace at 800 °C for 3 hr. Silica in 1 M sodium hydroxide and calcium oxide in 1 M hydrochloric acid with mole ratio of 1:1 were mixed in Teflon tube and heated at 100 and 150 °C for 24 hr. The white solid products were calcined at 800 °C for 2 hr. The scanning electron microscope image of calcium silicate at 150 °C with calcinations shows a good dispersion and uniform particles with an average particle size less than 1  $\mu\text{m}$ . The Fourier transform infrared spectra could confirm the formation of Ca-O-Si identified at 927  $\text{cm}^{-1}$ . The calcination could influence on the shape and calcium to silicon ratio of calcium silicate.

## 1. Introduction

Rice husk and egg shell are biomass which are valuable source of raw materials used in many applications. Rice husk has been used as organic and inorganic adsorbent [1] and energy generator resources [2]. It contains silica around 15-20 % [3]. Egg shell was adsorbent for water and wastewater treatment [4] and a ceramic raw material for wall tile industry [5]. It has calcium carbonate as major component with 94 % [6]. A propose of this work is for synthesis of calcium silicate from agricultural waste as rice husk and egg shell.

Calcium silicate or wollastonite ( $\text{CaSiO}_3$ ) is prepared by silica ( $\text{SiO}_2$ ) and calcium oxide ( $\text{CaO}$ ). The reaction between silica and calcium oxide as reaction:



Calcium silicate can be used in several applications such as electrical insulator [7], substituted material for asbestos [8], artificial bond substitute [9], and root canal sealer [10]. The well known methods to synthesize calcium silicate are solid-state reaction [11], hydrothermal method [12, 13], and sol-gel [14]. In this work, the hydrothermal method was used to synthesis of calcium silicate from rice husk and egg shell. The specific objective of this work was to investigate the effect of calcination on the crystalline

shape of calcium silicate and the ratio of calcium to silicon.

## 2. Materials and Methods

### 2.1 Preparation of silica and calcium oxide

**Silica:** The preparation of silica was modified from Kalapathy's method [15]. The 50.00 g rice husk was dissolved by 500 mL of 1 M sodium hydroxide then heated and stirred for 1 hour. The solution was filtered through Whatman filter paper No. 1 by the vacuum filtration. Further, the pH of solution was adjusted to 7-9 by 1 M hydrochloric acid. The white silica gel was then obtained. The gel was allowed to stand at room temperature for 12 hr. Then, the gel was filtered and washed with hot water. In the final step, the gel was dried at 80 °C until the silica powder was obtained.

**Calcium oxide:** The egg shell was washed by tap water and dried in air. The shell was crushed and calcined in the muffle furnace at 800 °C for 3 hr.

### 2.2 Preparation of calcium silicate

A 0.88 g of calcium oxide and 20 mL of hot water was mixed with 3 mL of conc. hydrochloric acid and added with 0.60 g of silica in 30 mL of 1 M sodium hydroxide. The mixed solutions were transferred to Teflon tube and heated at 100 and 150 °C for 24 hr. The solid product was calcined in a muffle furnace at 800 °C for 2 hr.

### 2.3 Characterization of calcium silicate

Calcium silicate was characterized by Fourier transform infrared spectroscopy (FTIR), scanning electron microscopy (SEM), and electron dispersive X-ray (EDX) spectroscopy.

**FTIR:** The infrared spectra were measured on Perkin Elmer with KBr preparation. The spectra were collected over the range of wavenumber 4,000-400  $\text{cm}^{-1}$  with 32 scanning and resolution at 4.

**SEM:** The morphology and aggregate of particles were examined by JEOL.

**EDX:** The calcium and silicon content of the samples were estimated by using energy dispersive X-ray (EDX) spectroscopy.

## 3. Results and Discussio

The solid products with calcination at 800 °C were whiter particle than without calcination since some organic compounds in rice husk ash and egg shell were

removed [16, 17]. The scanning electron microscopy (SEM) image of silica from rice husk and calcium oxide from egg shell were illustrated in Figure 1(a) and 1(b), respectively. Figure 2 was SEM morphology of calcium silicate at 100 and 150 °C showed smaller size and fair dispersion with calcium silicate via hydrothermal temperature at 150 °C. Calcium silicate with calcination in at 100 °C show the agglomerated particles consisted of small particles, where a good dispersion and uniform particles with an average particle size less than 1  $\mu\text{m}$  was obtained at calcined temperature of 150 °C (Figure 3).

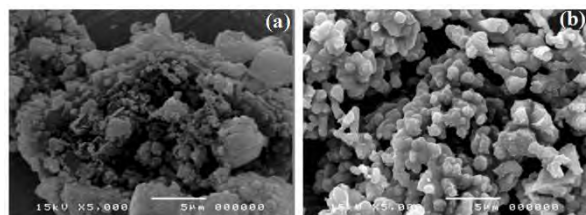


Figure 1. SEM morphology of (a) silica from rice husk (b) calcium oxide from egg shell

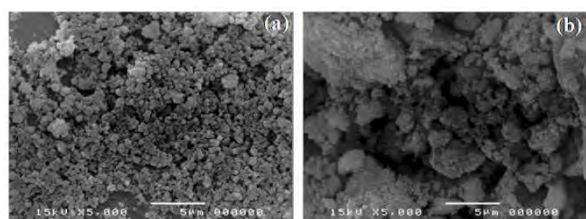


Figure 2. SEM morphology of calcium silicate heated at (a) 100 and (b) 150 °C.

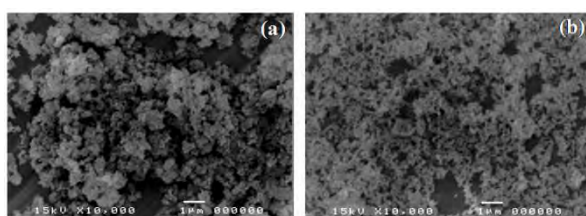


Figure 3. SEM morphology of calcium silicate heated at (a) 100 and (b) 150 °C with calcination at 800 °C for 2 hr.

Figure 4 shows the FTIR spectra of silica from rice husk and calcium oxide from egg shell. Figure 4(a) presents the broad band at  $3458\text{ cm}^{-1}$  of silanol ( $\text{OH}^-$ ) groups and adsorbed water. The bands in range of 1100 to  $820\text{ cm}^{-1}$  are the characteristic of the vibrational mode of the gel network [15]. Figure 4(b) illustrates a sharp peak at  $3644\text{ cm}^{-1}$  assigned to  $\text{OH}^-$  stretching band from water molecule. The bands at 1472, 1419, 1060, and  $875\text{ cm}^{-1}$  were the stretching band of carbonate group which still existed in calcium oxide [18].

In FTIR analyses of synthesis calcium silicate, the bands observed at  $3445$  and  $3452\text{ cm}^{-1}$  in Figure 5(a) and 5(b) were the absorbed water molecule,

respectively. The band at  $972\text{ cm}^{-1}$  was assigned to  $\text{Si-O-Ca}$  bond [19]. Further, this band was reported and assigned to  $\text{Si}(\text{OSi})_3\text{O-Ca}$  of dicalcium silicate hydrate [20]. In Figure 5(c) and 5(d) displayed the calcium silicate after calcination. The band at  $972\text{ cm}^{-1}$  was shifted to  $927\text{ cm}^{-1}$  which was assigned to  $\text{Ca-O-Si}$  of  $\beta$ -dicalcium silicate [20]. As a result of powder X-ray diffraction,  $\alpha$ -dicalcium silicate hydrate was formed in the temperature range 130 to  $220\text{ }^\circ\text{C}$  by hydrothermally method [21]. This evidence confirmed the products of silica and calcium oxide, synthesized by hydrothermal method at 100 and  $150\text{ }^\circ\text{C}$  without calcinations, were dicalcium silicate hydrate. The temperature above  $230\text{ }^\circ\text{C}$ ,  $\alpha$ -dicalcium silicate hydrate was unstable [22]. It suggested that  $\beta$ -dicalcium silicate was formed and hydrate was decomposed after calcination. The FTIR spectra in Figure 5 illustrated that dicalcium silicate hydrate and  $\beta$ -dicalcium silicate was obtained when calcination was applied after hydrothermal process and without calcination step, respectively.

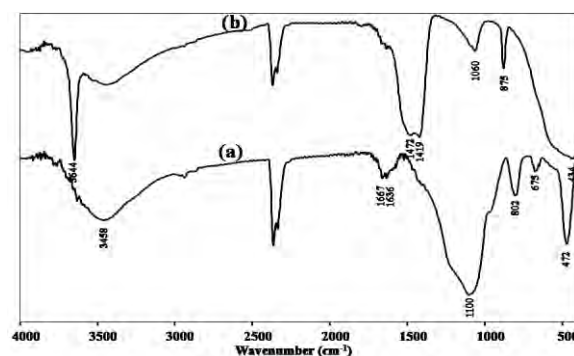


Figure 4. FTIR spectra of (a) silica from rice husk (b) calcium oxide from egg shell

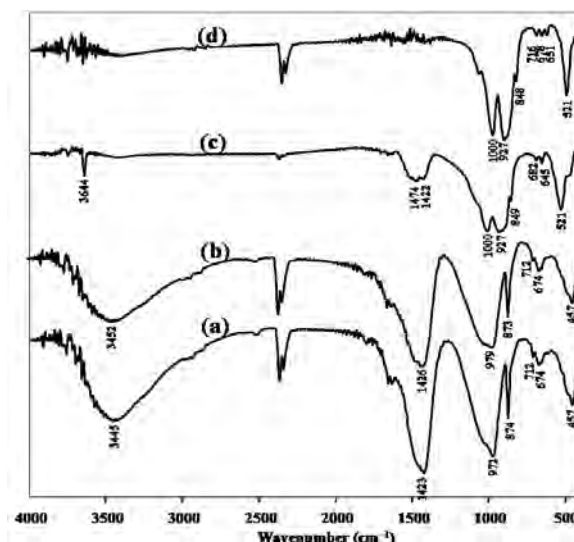


Figure 5. FTIR spectra of calcium silicate heated at (a) 100, (b)  $150\text{ }^\circ\text{C}$  and calcium silicate heated at (c) 100, (d)  $150\text{ }^\circ\text{C}$  with calcination at  $800\text{ }^\circ\text{C}$  for 2 hr.



Figure 6 and 7 shows EDX elemental spectra of calcium silicate with and without calcination, respectively. EDX spectra could confirm the major elements of products of silica from rice husk and calcium oxide from egg shell by hydrothermal method were calcium and silicon. The content of calcium and silicon in the samples were estimated, the mole ratio is closed to 2:1 which dicalcium silicate corresponded with FTIR result.

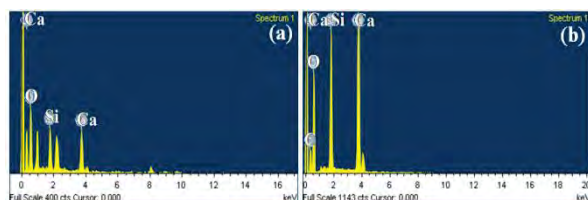


Figure 6. EDX spectra of calcium silicate heated at (a) 100 and (b) 150 °C.

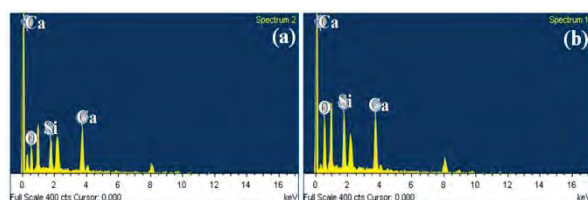


Figure 7. EDX spectra of calcium silicate heated at (a) 100 and (b) 150 °C with calcination at 800 °C for 2 hr.

From SEM, FTIR and EDX results were proved that calcination has affected on the shape and the size of calcium silicate by provided good dispersion and uniform particle. The calcination has also affected on the hydrate of calcium silicate. The organic impurities were decomposed at high temperature especially above 500 °C. The mole ratio of calcium and silicon is not different between with and without calcination. The mole ratio of calcium and silicon of calcium silicate were close to 2:1 as unexpected result.

#### 4. Conclusions

Calcium silicate was synthesized by silica from rice husk and calcium oxide from egg shell by hydrothermal method. Surprisingly, at the heating temperature at 150 °C with calcination could provide good dispersion and uniform particle. The calcination could influence the shape and calcium to silicon ratio of calcium silicate.

#### Acknowledgements

This research was supported by Nano Nanoscience and Nanotechnology Laboratory, Faculty of Science, Maejo University and Science Achievement Scholarship of Thailand.

#### References

- [1] M. Ahmaruzzaman and V.K. Gupta, *Ind. Eng. Chem. Res.* **50** (2011) 13589–13613.
- [2] T. Kapur, T.C. Kandpal and H.P. Garg, *Biomass & Bioenergy*, **10** (1996) 393–403.
- [3] L. Sun, *Ind. Eng. Chem. Res.* **40** (2001) 5861–5877.
- [4] J. Carvalho, J. Araujo and F. Castro, *Waste Biomass Valor.* **2** (2011) 157–167.
- [5] M.N. Freire and J.N.F. Holanda, *Cerâmica*, **52** (2006) 240–244.
- [6] E.M. Rivera, M. Araiza, W. Brostow, V.M. Castaño, J.R. Díza-Estrada, R. Hernández and J.R. Rodríguez, *Mat. Lett.* **41** (1999) 128–134.
- [7] N.S. Negmatov and Zh. Z. Abdullaev, *Glass Ceram.* **58** (2001) 396–397.
- [8] N.I. Demidenko and G.B. Tel'nova, *Glass Ceram.* **61** (2004) 183–186.
- [9] H. Teramoto, A. Kawai, S. Sugihara, A. Yoshida, and H. Inoue, *Acta Med. Okayama*, **59** (2005) 201–207.
- [10] T.E. Bryan, K. Khechen, M.G. Brackett, R.L.W. Messer, A. El-Awady, C.M. Primus, J.L. Gutmann and F.R. Tay, *JOE*, **36** (2010) 1163–1169.
- [11] K. Lin, J. Chang, Y. Zeng, and W. Qian, *Mat. Lett.* **58** (2004) 2109–2113.
- [12] K. Lin, J. Chang and J. Li, *Mat. Lett.* **60** (2006) 3007–3010.
- [13] K. Lin, J. Chang, G. Chen, M. Ruan and C. Ning, *J. Cryst. Growth*, **300** (2007) 267–271.
- [14] H. Wang, Q. Zhang, H. Yang and H. Sun, *Ceram. Int.* **34** (2008) 1405–1408.
- [15] U. Kalapathy, A. Proctor and J. Shultz, *Bioresour. Technol.* **73** (2000) 257–262.
- [16] S. Vichupund, M. Kitiwan, D. Atong and P. Thavorniti, *J. Eur. Ceram. Soc.* **31** (2011) 2435–2440.
- [17] P.J. Ramadhansyah, A.W. Mahyun, M.Z.M. Salwa, B.H. Abu Bakar, M.A. Megat Johari and M.H. Wan Ibrahim, *Procedia Eng.* **50** (2012) 101–109.
- [18] B. Engin, H. Demirtaş and M. Eken, *Radiat. Phys. Chem.* **75** (2006) 268–277.
- [19] A. Meiszterics and K. Sinkó, *Colloids Surf. A* **319** (2008) 143–148.
- [20] A. Meiszterics, L. Rosta, H. Peterlik, J. Rohonczy, S. Kubuki, P. Henits and K. Sinkó, *J. Phys. Chem. A* **114** (2010) 10403–10411.
- [21] T. Yano, K. Urabe, H. Ikawa, T. Teraushi, N. Ishizawa and S. Udagawa, *Acta Cryst. C* **49** (1993) 1555–1559.
- [22] K. Yanagisawa, X. Hu, A. Onda and K. Kajiyoshi, *Cement Concrete Res.* **36** (2006) 810–816.

# SAPONIFIED NATURAL RUBBER COMPOSITE FROM MACCA CHARCOAL

Sutaporn Yakkul<sup>1</sup>, Jitladda Sakdapipanich<sup>1,2\*</sup>

<sup>1</sup>Department of Chemistry, Faculty of Science, Mahidol University, Bangkok 10400, Thailand

<sup>2</sup>Polymer project, Institute of Molecular Biosciences, Mahidol University, Salaya Campus, Nakhonpathom 73170, Thailand

\* Author for correspondence; E-mail: [jitladda.sak@mahidol.ac.th](mailto:jitladda.sak@mahidol.ac.th) Tel. +66 28893116, Fax. +66 28893116

**Abstract:** Natural rubber (NR) latex from *Hevea brasiliensis* consists of rubber particles and non-rubber components such as proteins, lipids, carbohydrates, fatty acids, and inorganic compound. The problems of NR for human are allergy and contamination of accelerators of a carcinogenic substance such as nitrosamine. Type I allergy is immediate hypersensitivity caused by protein. Type IV allergy can compare as well as contamination of nitrosamine are caused by accelerator in sulphur cure. In this work, saponified NR (SPNR) cured by peroxide offers the solution for solving those problems. SPNR was prepared by diluting high ammonia latex in the presence sodium dodecylsulphate (SDS) and sodium hydroxide (NaOH) at 70°C for 3 hours. SPNR was coagulated by formic acid, followed by washing with water. Then, it was dried in an oven. Finally, SPNR was compounded with macca charcoal at 0, 0.5, 1.0, 1.5, 2.0, 3.0, and 5.0 phr and was subjected to vulcanization by peroxide system at 160°C for 24 minutes. The vulcanizates were measured for their hardness and tensile properties such as 100, 200, 300, and 500% modulus, and tensile strength at break. Moreover, the effect of macca charcoal content on thermal retention estimation, thermal intensity, and depth of FIR diffusion on pork was also investigated in this work. The results show that hardness and tensile properties increased with increasing an addition of macca charcoal in SPNR. In addition, the increasing of macca charcoal content enhance thermal retention estimation and thermal intensity, but has no substantial effect on depth of FIR diffusion on pork.

**Keywords:** Macca charcoal; Natural rubber; Far infrared rays; Carbonization process

## 1. Introduction

NR latex from *Hevea brasiliensis* fundamentally consists of cis-1,4-polyisoprene and non-rubber components such as proteins, lipids, carbohydrates, fatty acids, and inorganic compounds. It is used in variety of products such as tires, hoses, rubber gloves and so on. The problem of NR is type I allergy, which is immediate hypersensitivity for human caused by proteins. Recently, saponification of NR in the presence of surfactant has been reported that it could produce purified NR with undetectable of allergic protein.[1-2] Moreover, type IV allergy and contamination of nitrosamine as carcinogenic substances are normally caused by accelerator in sulphur cure. So, saponified NR cured by peroxide offers the solution for solving those problems.[3]

Macadamia nut shell, the waste from production of macadamia nut in Doitung development project, is modified to charcoal via carbonization process. This charcoal names "Macca charcoal". Macca charcoal can release far infrared rays (FIR) in the range of 6-14 microns.[4] FIR has ability of penetration, refraction, radiation, and reflection. Body of human can absorb FIR because of its deep penetrating ability. Light energy can be changed to thermal energy when FIR penetrates from skin to the subcutaneous tissues.[5-6] Thermal properties of macca charcoal and reduced allergic of SPNR was interested to prepare macca charcoal- filled SPNR composites for applying to area of pain.

In this study, SPNR was compounded with macca charcoal at 0, 0.5, 1.0, 1.5, 2.0, 3.0, and 5.0 phr and was subsequently vulcanized by peroxide system. SPNR composites were determined for their hardness, tensile properties. The effect of macca charcoal content on thermal retention estimation, thermal intensity, and depth of FIR diffusion on pork was also investigated.

## 2. Materials and Methods

### 2.1 Chemicals and reagents

High ammonium latex (HANR) was supplied by Thai rubber latex Co.,Ltd. Sodium dodecylsulphate (SDS), Sodium hydroxide (NaOH), and Formic acid (HCOOH) were purchased from RCI Lab Scan, Butylated hydroxytoluene (BHT) was purchased from Fluka. Dicumyl peroxide (DCP) was purchased from Nippon Yusi Corporation. Macca charcoal was supplied by Macca charcoal laboratory research of Mahidol university.

### 2.2 Preparation of SPNR

SPNR was prepared by diluting HANR with distilled water in the presence 0.5% SDS and 0.3% NaOH at 70°C for 3 hours. SPNR was coagulated by 2.0% formic acid, followed by soaking and washing in water. Then, it was soaked in BHT solution as an antioxidant and dried in an oven.

### 2.3 Preparation of SPNR composites

SPNR was mixed with 1.0 phr DCP, 0.5 phr BHT and 0, 0.5, 1.0, 1.5, 2.0, 3.0, and 5.0 phr macca charcoals in internal mixer at 40°C. SPNR composites were vulcanized using compression machine at 160°C for 24 minutes

## 2.4 Measurements

Hardness of SPNR composites was measured by Shore A Hardness Tester (Wallace-cogenix) as measured 10 times. Tensile properties of SPNR composites were determined according to ASTM D 412-98 using tensile tester (Instron 5566), cross head speed 500 mm/minute and load cell 1kN as measured 5 times. The effect of macca charcoal content on SPNR composites was reported as thermal retention estimation, thermal intensity, and depth of FIR diffusion on pork. The temperature, where halogen light at 500 W located at distance 100 cm from SPNR composites was considered to be Thermal retention estimation monitored by IR thermometer. Thermal intensity is emissivity of FIR in SPNR composites at 7-13 microns detected by Thorlabs instrument. Radiation of FIR using dual channel thermometer was the temperature in skin of pork at 37°C for 30 minutes.

## 3. Results and Discussion

The hardness value of macca charcoal-filled SPNR composites is given in Figure 1. The hardness of SPNR composites increased as macca charcoal content increased.

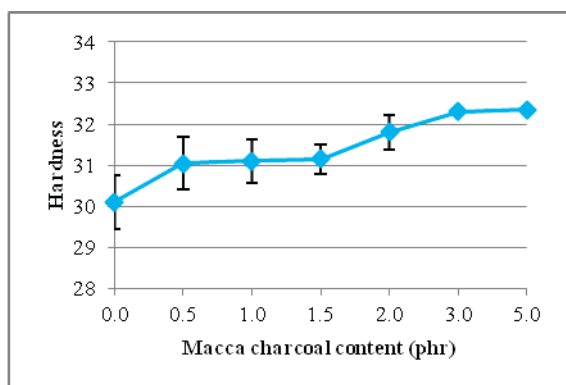


Figure 1. Hardness of macca charcoal-filled SPNR composites at various quantities of macca charcoal.

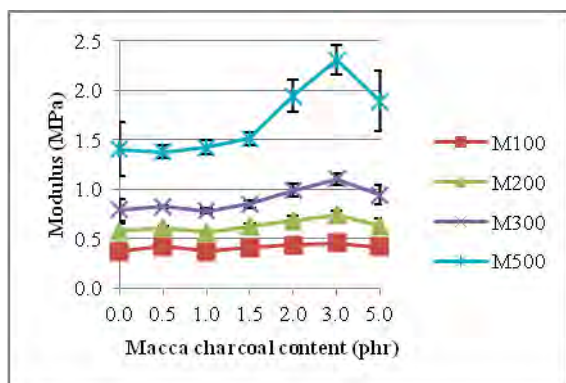


Figure 2. Modulus of macca charcoal-filled SPNR composites at various quantities of macca charcoal.

Figure 2 presents 100%, 200%, 300%, and 500% modulus of macca charcoal-filled SPNR composites. The results show that 100%, 200%, 300%, and 500% modulus increased with increasing macca charcoal

content. However, tensile strength of macca charcoal-filled SPNR composites is not significant when macca charcoal content increase as shown in Figure 3.

Figure 4 shows thermal intensity of macca charcoal-filled SPNR composites at 7-13  $\mu\text{m}$  which is the range of FIR radiation of macca charcoal. The results show that thermal intensity increased when the amount of macca charcoal was increased. This is because macca charcoal can generate FIR at 6-14  $\mu\text{m}$  and FIR can transfer to heat energy.[7-8]

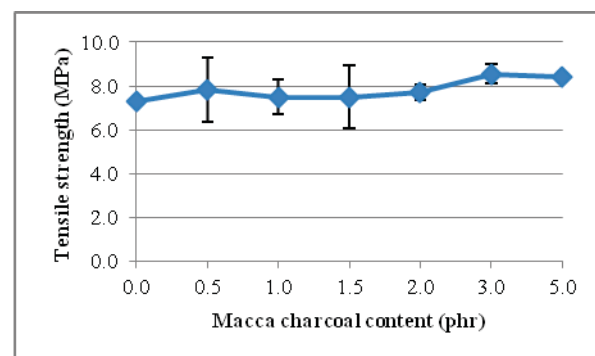


Figure 3. Tensile strength of macca charcoal-filled SPNR composites at various quantities of macca charcoal.

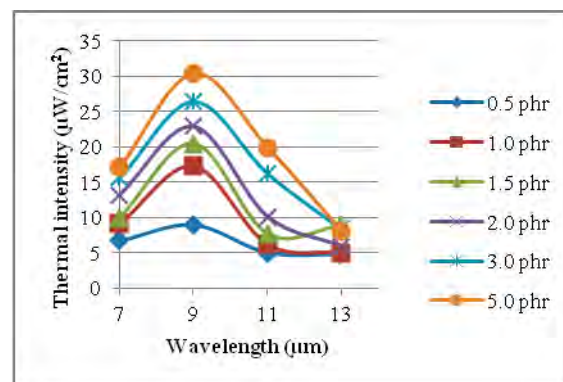


Figure 4. Thermal intensity of macca charcoal-filled SPNR composites at various quantities of macca charcoal.

Relative temperature retention ( $\Delta T_r$ ) and relative temperature ascension ( $\Delta T_a$ ) values indicated thermal retention estimation of macca charcoal-filled SPNR composites. The surface temperatures of non-filled SPNR and macca charcoal-filled SPNR composites before radiation were recorded as  $T_{0c}$  and  $T_{0m}$ , respectively. Then non-filled SPNR and macca charcoal-filled SPNR composites were irradiated by a 500Watt of halogen light for 10 minutes, and the light was turned off subsequently. The surface temperature values of both non-filled SPNR and macca charcoal-filled SPNR composites after 10 minutes radiation were recorded as  $T_{1c}$  and  $T_{1m}$ , and afterward  $T_{2c}$  and  $T_{2m}$  data were recorded as the surface temperatures of the point 30 second later than when the light was turned off. Consequently, the difference between  $T_{1c}$

and  $T_{0c}$  represents the temperature ascension of non-filled SPNR composites and the difference between  $T_{2c}$  and  $T_{0c}$  represents the temperature retention of non-filled SPNR composites; the difference between  $T_{1m}$  and  $T_{0m}$  represents the temperature ascension of macca charcoal-filled SPNR composites and the difference between  $T_{2m}$  and  $T_{0m}$  represents the temperature retention of macca charcoal-filled SPNR composites.  $\Delta T_r$  and  $\Delta T_a$  were defined as the difference between the temperature retention and ascension of non-filled and macca charcoal-filled SPNR composites, which were calculated by equation 1 and 2.[9]

$$\Delta T_r = (T_{2m} - T_{0m}) - (T_{2c} - T_{0c}) \quad \dots (1)$$

$$\Delta T_a = (T_{1m} - T_{0m}) - (T_{1c} - T_{0c}) \quad \dots (2)$$

$\Delta T_r$  and  $\Delta T_a$  values of macca charcoal-filled SPNR composites were enhanced when macca charcoal content increased. The surface temperature of Macca charcoal-filled SPNR composites raised after radiation by halogen lamp and  $\Delta T_a$  values are higher than 3°C for all sets of specimens, which may be related to the effect of high thermal conductivity as well as low specific heat additives.

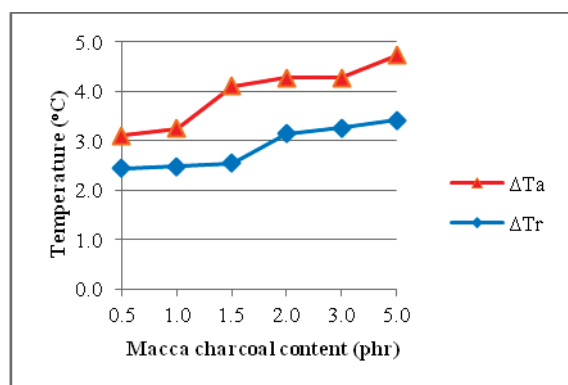


Figure 5. The comparison of thermal retention performance (relative temperature ascension ( $\Delta T_a$ ) and relative temperature retention ( $\Delta T_r$ )) of macca charcoal-filled SPNR composites at various quantities of macca charcoal.

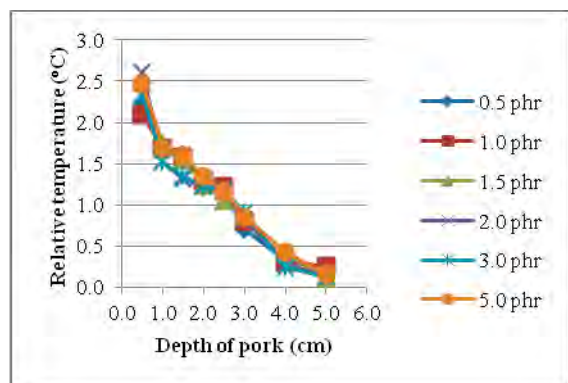


Figure 6. Relative temperature of macca charcoal-filled SPNR composites at various depth of pork as the function of macca charcoal content.

Depth of FIR diffusion was measured by monitoring the raising of temperature at various depths of pork for 30 minutes. This result demonstrates that the temperature increased with decreasing the depth of pork (Figure 6). However, macca charcoal content has no effect on heat power and depth of FIR rays diffusion because FIR has ability to penetrate 4-5 cm of skin layer.[10,11]

#### 4. Conclusions

From the results observed in this work, it can be concluded that macca charcoal content in SPNR composites affects to hardness and tensile properties. Macca charcoal can generate FIR, subsequently changed to heat energy. Thermal intensity and thermal retention estimation increased with increasing macca charcoal content, whereas depth of FIR diffusion is not affected by macca charcoal content. Thus, macca charcoal-filled SPNR composite is interesting material for applying to area of pain in human.

#### References:

- [1] J. Yunyongwattanakorn, Y. Tanaka, J. Sakdapipanich, and V. Wongsatuthikul, *Rubber Chem Tech.* **81** (2008) 121-137.
- [2] S. Amnuaypornsi, J. Sakdapipanich, and Y. Tanaka, *J Appl Polymer Sci.* **118** (2010) 3524-3531.
- [3] R. S. Holzman, R. H. Brown, C. A. Hirshman, S. B. Kinsella, C. Petrovich, R. Hamid, G. I. Randel, S. A. Vassallo, and J. D. Katz, *American Society of Anesthesiologists*, (2005)
- [4] P. Tangvijitsakul, *Master's Thesis (Polymer Science and Technology)*, Mahidol University, (2010)
- [5] R. Norrie, *Wellness and health Innovation project*, (2009)
- [6] R. Beever, *Can J Diabetes.* **34** (2010) 113-118.
- [7] C.A. Lin, T.C.An, Y.H. Hsu, *Polym Plast Technol Eng;* **46** (2007) 1073.
- [8] C.W. Lou, J.H. Lin, *Fibers Polym;* **55** (2011) 433.
- [9] T. C. An C. A. Lin, C. H. Chiu, C. H. Liu, and P. T. Hu, *Polym. Plast. Technol.* **47** (2008) 895-901
- [10] S. Nurman, *Miracle Patches: Revealing the Healing Powers of Detox Patched, Negative ion, and Far Infrared Rays.*
- [11] M. Hertel, G. Hoffmann, M.N. Wentz, M.E. Martignoni, M.W. Buchler, Friess H., *Brit J Surg;* **93**(2006) 952-960.



# FABRICATION OF 3-HYDROXYBENZOATE 6-HYDROXYLASE-IMMOBILIZED ULTRAFINE FIBERS BY ELECTROSPINNING TECHNIQUE

Tiyaporn Srisook<sup>1</sup>, Pimchai Chaiyen<sup>2</sup>, Jeerus Sucharitakul<sup>3</sup>, Thammasit Vongsetskul<sup>1\*</sup>

<sup>1</sup> Department of Chemistry, Faculty of Science, Mahidol University, Rama VI Road, Ratchathewi, Bangkok, 10400

<sup>2</sup> Department of Biochemistry, Faculty of Science, Mahidol University, Rama VI Road, Ratchathewi, Bangkok, 10400

<sup>3</sup> Department of Biochemistry, Faculty of Dentistry, Chulalongkorn University, Henri Dunant Road, Patumwan, Bangkok, 10330

\* Author for correspondence; E-Mail: thammasit.von@mahidol.ac.th, Tel. +66 2201-5110, Fax. +66 2354-7151

**Abstract:** Electrospun polycaprolactone (PCL) (MW ~  $7 - 9 \times 10^4$  g/mol) ultrafine fibers with diameters from 100 to 2225 nm were successfully fabricated. The PCL concentrations were 13, 14, and 15 %w/w in 1:3 formic acid:acetic acid mixed solvent. Scanning Electron Microscope (SEM) images revealed that the optimum condition for fabricating fibers was 13% w/w and 16 kV. Then, 3-hydroxybenzoate 6-hydroxylase (3HB6H), an enzyme involved in microbial aromatic degradation, was immobilized onto PCL ultrafine fibers. 3HB6H immobilized PCL ultrafine fibers were characterized by attenuated total reflectance-Fourier transform infrared spectroscopy (ATR-FTIR) and by UV-Vis spectrophotometer at 340 nm for assessing the biocatalytic activities of the prepared fibers. Both ATR-FTIR and biocatalytic activity test results confirmed the presence of amide functional groups and 3HB6H on the fiber surface, respectively. However, the mechanism of enzyme immobilization and the improvement of enzyme immobilization are required to be investigated further.

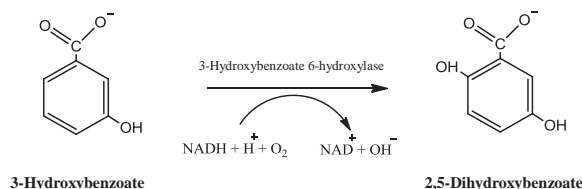
## 1. Introduction

Aromatic compounds such as benzene are among major chemicals causing environmental pollution because they are degraded very slowly, and the degraded products are toxic. Therefore, there are several studies on the approaches to degrade aromatic compounds contaminating the environment [1]. In recent years, the degradation pathways of aromatic compounds have been reported. One of the studied pathway of aromatic degradation is Gentsiate pathway [2].

In this pathway, the use of enzyme to eliminate the aromatic contamination in environment is interesting because of two reasons. First, enzymes are well-known green catalysts that possess a high degree of specificity. The specificity involves discrimination between substrates (substrate specificity), similar part of molecules (regiospecificity), and optical isomers (stereospecificity) [3]. Second, the specificity of enzymes has a high efficiency for application in food processing, biosensors, and bioremediation.

One of the enzymes used to degrade the aromatic substances is 3-Hydroxybenzoate 6-hydroxylase (3HB6H) from *Rhodococcus jostii* RHA1 which has been recently reported by Sucharitakul et al [1]. It is a nicotinamide adenine di-nucleotide (NADH) specific flavoprotein mono-oxygenase involved in microbial aromatic degradation (Gentsiate pathway). 3HB6H is the enzyme that catalyzes the parahydroxylation of 3-hydroxybenzoate (3-HB) at C6 to form 2,5-dihydroxybenzoate (2,5-DHB) as a product (Scheme 1), the bioremediation process of aromatic degradation. The enzyme is a homodimer and contains one FAD per subunit of 47 kDa [1].

### Scheme 1. Catalytic Reaction of 3HB6H



Unfortunately, in general, the application of enzymes is limited because they are unstable and hard to be reused as they are homogeneous catalysts. Therefore, an enzyme immobilization is one of the efficient ways to solve these problems.

However, when an enzyme is immobilized on the surface of solid support, the activity of enzyme normally decreased. Thus, to solve this problem, the amount of enzyme molecules attached on the surface of support has to be high in number.

Ultrafine fibers are materials with extremely high surface area to volume ratios. Furthermore, when compared to the other types of nanomaterials such as mesoporous silica, ultrafine fibers are prominent alternatives because their porosity and pore size can be modified to benefit enzyme activity [3].

An electrospinning technique is chosen to fabricate ultrafine fibers because it is the only technique that is convenient to control the fiber dimension and is capable

of producing ultrafine fibers in a continuous way [4]. Also, the electrospinning setup is simple because there are three major components only: a high-voltage power supply, a container where a polymer liquid (i.e., a solution or melt) is placed with a small opening to be used as a nozzle and a conductive collection device. Under the influence of a high electric field, a partially spherical droplet of the polymer liquid at the capillary tip is deformed into a conical one. The increase in the electric field causes an ejection of a charged stream of the polymer liquid, which deposits in a random fashion on the collection device in the form of a nonwoven fabric [4]. Polycaprolactone (PCL) was chosen to fabricate ultra-fine fiber for immobilizing the enzyme because of its slow biodegradability, biocompatibility, and water insoluble.

In this research, the electrospun PCL ultrafine fibers were fabricated. The effect of the electrical voltages, and the concentration of PCL solutions on the prepared fibers were studied inclusively.

## 2. Materials and Methods

### 2.1 Materials

PCL with MW of 80 kD, NADH, and Tris buffer were purchased from Sigma-Aldrich (USA) and used as received. Formic acid (96%) and acetic acid (99%) (RCI Labscan, Thailand) were used as mixed solvents (25% v/v formic acid: 75% v/v acetic acid) for preparing the electrospinning solution. 3HB6H was synthesized from *Rhodococcus jostii* RHA1. 3HB was purchased from Merck (USA) and used as received.

### 2.2 Preparation of PCL electrospinning solution

PCL pellets were dissolved in 1:3 (formic acid: acetic acid) mixed solvent and stirred for 2 hours to obtain the homogeneous PCL solutions with the concentrations of 13, 14 and 15 wt% [5].

### 2.3 Fabrication and characterization of PCL ultrafine fibers

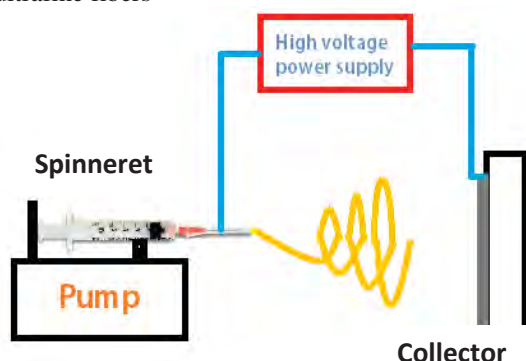


**Figure 1** Schematic drawing of the electrospinning apparatus used in this research

An electrospinning setup utilized in this work is shown in Figure 1. In this process, each of the spinning solutions was loaded into a glass syringe. A Gamma High Voltage Research ORMOND BEACH power supply (DES50PN-20w/QAM) was used to charge the spinning solution by connecting the emitting electrode of positive polarity to the nozzle and the grounding electrode to an aluminum sheet wrapped around a rigid plastic backing, used as a collection device. The PCL concentrations were 13, 14 and 15 wt%. The applied positive electrical potentials were in between 14 and 19 kV. Fiber collection distance (TCD) and time were 12.5 cm and 5 min, respectively. The flow rate was 1 ml/hr. The diameter of inner needle was 0.9 mm. Morphology of PCL ultrafine fibers was observed by scanning electron microscope (SEM, S-2500, Hitachi, Japan). The fibers were dried on an aluminium foil in a dust-free environment before being stuck on the sample holder with a double-coated carbon conductive tape and sputter-coated (E-102, Hitachi, Japan) under vacuum. An average diameter of the electrospun fiber mats was measured directly from SEM (at 15 kV) using a Photoshop 5.0 ( $n \geq 50$ ).

### 2.4 Immobilization 3HB6H onto PCL ultrafine fibers

#### 2.4.1 Preparation and characterization of 3HB6H-immobilized PCL fibers

PCL ultrafine fibers film was electrospun at the optimum condition (PCL 13%wt, 16kV) for 3 h. Then, PCL film was cut into 0.5x0.5 cm and sloughed from alumina foil. Next, a PCL mat was immersed into 1 ml 150  $\mu$ M of 3HB6H for 2 and 12 days at 0<sup>o</sup> C. When the reaction is completed, the mat was washed with tris buffer 3 times. The obtained 3HB6H-immobilized PCL fibers were studied by attenuated total reflectance-Fourier transform infrared spectroscopy (ATR-FTIR, Equinox 55, Bruker, Germany) and SEM (S-2500, Hitachi, Japan).

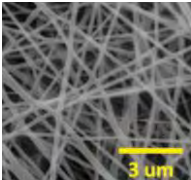
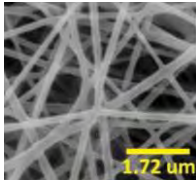
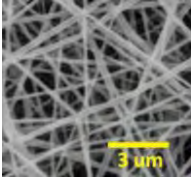
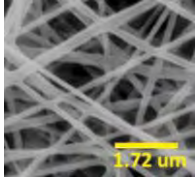
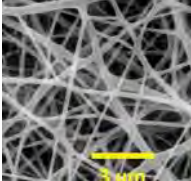
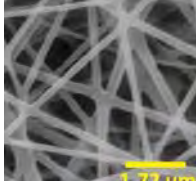
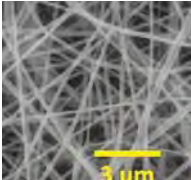
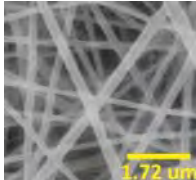
#### 2.4.2 Measurement of enzyme activity

A mat of enzyme-immobilized PCL fibers was immersed into 5 ml mixtures of 200  $\mu$ M of NADH, 1mM of 3HB, and 100 mM of tris buffer. The NADH degradation was investigated by measuring an absorbance at 340 nm every 5 min.

## 3. Results and Discussion

Table 1 shows SEM images of the electrospun PCL fibers obtained from 13% wt PCL solution and various applied electrical voltages.

**Table 1** SEM images of the electrospun fibers of 13% wt PCL solution at 12.5 cm

Conditions	4000x	7000x
14 kV		
15 kV		
16 kV		
17 kV		

SEM micrographs suggest that all the chosen processing conditions give the smooth and uniform ultrafine fibers. To obtain deeper information, fiber diameters were measured. The results are shown in Table 2.

**Table 2:** Diameter of PCL ultrafine fibers fabricated from several conditions

Condition	13% w/w of PCL				14% w/w of PCL 16 kV	15% w/w of PCL 16 kV
	14kV	15kV	16kV	17kV		
Average	218	186	188	203	353	439
Max.	386	461	345	426	771	1425
Min.	119	102	101	111	157	195
SD	72	64	50	69	125	214

The fiber diameters shown in Table 2 indicate that the diameter of ultrafine fibers decrease with increasing in the applied voltages except those processed from 17 kV because the polymer jet obtained from 17 kV had a travelling time from spinneret to fiber collector too low to be stretched. Therefore, the diameter of fibers obtained from 17 kV was larger than that done from 16 kV. It can be concluded that the best condition for fabricating PCL

ultrafine fibers was 16 kV and 13 % w/w PCL solutions. Then, the fibers obtained from the best conditions were then immersed in 3HB6H buffer solutions to immobilize enzyme onto fibers. Figure 2 shows ATR-FTIR spectra of PCL and PCL-3HB6H.

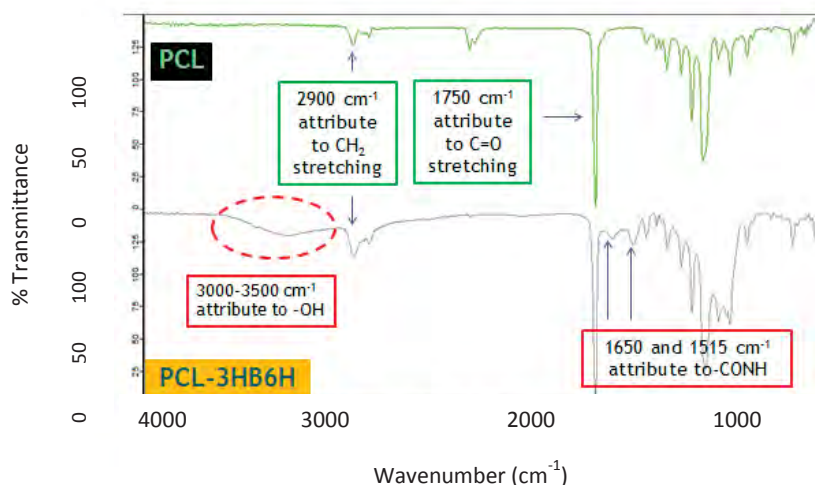
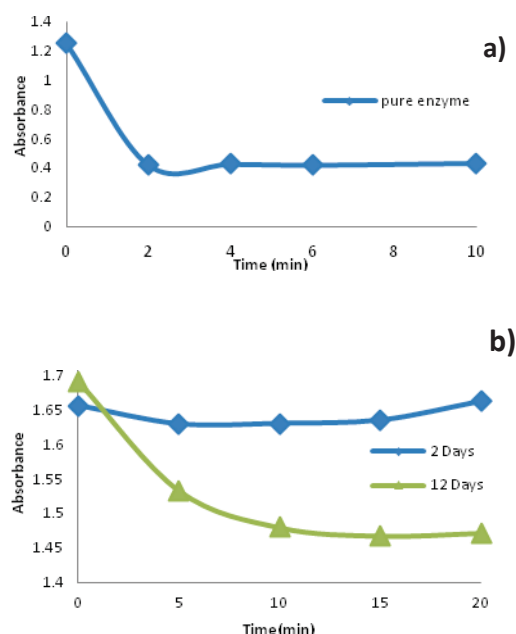


**Figure 2:** ATR-FTIR spectra of a) PCL and b) PCL-3HB6H

Figure 2a) shows the peak at 2900  $\text{cm}^{-1}$  attribute to  $\text{CH}_2$  stretching, at 1750  $\text{cm}^{-1}$  attribute to  $\text{C}=\text{O}$  stretching, and at 1200  $\text{cm}^{-1}$  attribute to  $\text{C}-\text{O}$  stretching. On the other hand, Figure 2b) shows the peak at different positions. It shows the broad peak at 3000-3500  $\text{cm}^{-1}$  attribute to  $-\text{OH}$  stretching and at both 1650 and 1515  $\text{cm}^{-1}$  attribute to amide functional group. Therefore, ATR-FTIR spectra confirmed the success of enzyme immobilization onto PCL ultrafine fiber. Graph 1 shows the activity of 3HB6H and 3HB6H-immobilized PCL fibers.



**Graph 1:** the absorbance of NADH as a function of time (min) with the presence of 3HB6H (a) and 3HB6H-immobilized PCL fibers (b) at 2, and 12 days

Graph 1 displays the activity of 3HB6H and 3HB6H-immobilized PCL ultrafine fibers. The results suggest that the immersion time of fiber has influenced the activity of 3HB6H-immobilized fibers. The more the time of fiber immersion, the higher the activity of enzyme-immobilized fibers. Graph 1 indicates that there was no 3HB6H molecules immobilized onto PCL ultrafine fibers. However, when the fibers were immersed in enzyme buffer solution for 12 days, the 3HB6H molecules were bound onto the fiber surface because the NADH degradation could be observed.

Therefore, it can be concluded that the stability of 3HB6H was improved when it is immobilized onto PCL ultrafine fibers. The longer the immersing time of fiber, the higher the number of 3HB6H molecules present on the fiber surface.

## 5. Conclusion

In this work, the optimum condition for preparing PCL ultrafine fibers was 13% wt of PCL solution and 16 kV. The thinnest diameter of PCL uniform ultrafine fiber was  $188 \pm 50$  nm. The enzyme activity testing revealed that the more the time of fiber immersion in enzyme solution, the more the enzyme activity of PCL fibers. The most appropriate time for immersing fibers in enzyme buffer solution was 12 days.

## Acknowledgments

This work was performed under the support of Department of Biochemistry, Faculty of Science, Mahidol University.

## References

- [1] J. Sucharitakul, T. Wongnate, S. Montersino, J. H. Willem, and P. Chaiyen, *Biochemistry* **51** (2012) 4309-4321.
- [2] C.N. Jones and R.A. Cooper. *Microbiology* **154** (1990) 489-495.
- [3] G.W. Zhen, S.W. Ling, M.L. Zhen, J.H. Xiao, and K.X. Zhi, *J. Mol. Catal. B: Enzym.* **56** (2009) 189-195.
- [4] N. Bhardwaj and S.C. Kuundu, *Biotechnol. Adv.* **28** (2010) 325-347.
- [5] V.D.S. Lien, D.S. Bert, I.K. Ozlem, and K.D.C. Kalaogluaren, *Eur Polym J.* **47** (2011) 1256-1263.



# FABRICATION OF POWDER-FREE NATURAL RUBBER GLOVES COATED BY ELECTROSPUN QUATERNIZED CHITOSAN-LOADED ULTRAFINE FIBERS

Preeyaporn Wongsomboon, Panya Sunintaboon, Pramuan Tangboriboonrat, Thammasit Vongsetskul\*

Department of Chemistry, Faculty of Science, Mahidol University, Rama VI Road, Ratchathewi, Bangkok, 10400

\*E-mail: [thammasit.von@mahidol.ac.th](mailto:thammasit.von@mahidol.ac.th) Tel. +66 2201-5110, Fax. +66 2354-7151

**Abstract:** The quaternized chitosan (QCh)-loaded poly (vinyl alcohol) (PVAI) (MW  $\sim 8.9 - 9.8 \times 10^4$  g/mol) ultrafine fibers with diameters from 300 to 450 nm were successfully fabricated by electrospinning technique. The total concentration of mixed aqueous solutions of QCh, an antibacterial agent, and PVAI was 14% w/v with a fiber collection distance set at 12 cm. The morphology of electrospun QCh/PVAI fibers on powder-free natural rubber gloves was characterized by scanning electron microscope (SEM), which revealed that the average fiber diameter decreased with decreasing the applied voltage (from 12 to 20 kV).

## 1. Introduction

Natural rubber (NR), composed of *cis*-1,4 polyisoprene mainly, is one of the most used materials for fabricating thin products such as gloves. Although NR film possesses excellent inherent elastic property, its tack and high surface friction are serious drawbacks, and, hence, limit its use in certain applications. Normally, this problem could be solved by using talcum powder or cornstarch for reducing the friction between the rubber film surfaces. However, these additives could result in contamination of surgical wounds. Therefore, the powder-free gloves are of great interest.

Coating ultrafine fibers on the glove surface is one of the solutions and was chosen for this work. Coating ultrafine fibers is not only solving the sticking problem of glove, but it is also possible to introduce the antibacterial characteristics to the glove.

Poly(vinyl alcohol) (PVAI) possess several desirable characteristics making it perfect for coating on glove such as high flexibility and non-toxicity [1].

Quaternized chitosan (QCh) is a derivative of chitosan (CS), a natural polysaccharide consisting of  $\beta$ -(1 $\rightarrow$ 4)-D-glucosamine and  $\beta$ -(1 $\rightarrow$ 4)-N-acetyl D-glucosamine units. It is normally synthesized by alkylation of CS. Even though some literatures suggest that both CS and QCh show the antibacterial properties [2], CS could only be dissolved in acid solution and not be dissolved in water. Then, the chemical modification of CS to improve its aqueous solubility is required. Among all the types of QCh, *N,N,N*-Trimethylated chitosan (TMC), a water-soluble compound, is one of the easiest QCh to be synthesized. It is generally prepared by reacting CS with methyl iodide ( $\text{CH}_3\text{I}$ ) [3].

Ultrafine fiber or fibrous structure can be fabricated by electrospinning process, exploiting electric field to draw a polymer strand for producing fibers. In principle, when the electric force overcomes the surface tension of polymer solution, the polymer strand is stretched and travels to the collector, and the solvent evaporation simultaneously occurs [4].

The preparation of QCh/polymer composite fibers has been previously reported in 2007 [5]. In this work, *N*-butyl-*N,N*-dimethyl CS iodide/Polyvinylpyrrolidone (PVP) fibers were prepared. However, PVP is hygroscopic and unstable to be exposed on highly humid conditions. Therefore, the crosslinking of PVP fibers, which used expensive chemicals, was required.

Therefore, this study aims to produce antibacterial natural rubber gloves by coating electrospun TMC/PVAI ultrafine fibers on natural rubber gloves which could be stable to water and highly humid environment. The effects of applied voltage on the average diameters and morphology of the prepared fibers have also been studied.

## 2. Materials and Methods

### 2.1 Materials

PVAI (>99% hydrolyzed) with MW of  $9.35 \times 10^4$  g/mol, *N*-Methyl-2-pyrrolidone (NMP), sodium iodide (NaI), and iodomethane ( $\text{CH}_3\text{I}$ ) were purchased from Sigma-Aldrich (United States), and used as received. CS with MW of 150 kDa was purchased from Seafresh Chitosan Lab., Thailand, and used to synthesize TMC. TMC was synthesized by the methylation of CS [3]. The chemical structure of TMC is shown in Figure 1.

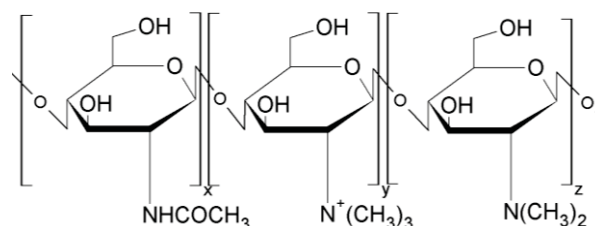


Figure 1. Chemical structure of TMC

The synthetic procedure was briefly described as follows. 1 g of CS and 2.4 g of NaI were added to 40 ml of NMP and 6 ml of 15% w/v aqueous NaOH solution mixture. Then, the solution was heated to 60°C and stirred for 20 min. Next, 6 ml of CH<sub>3</sub>I was added, and the reaction mixture was refluxed for 60 min. After that, 3 ml of 15% NaOH solution and 3 ml of CH<sub>3</sub>I were added, and the solution was stirred for 60 min. The reaction was worked up by dropping the solution in a 200 ml mixture of diethyl ether and ethanol (50/50). The obtained precipitate was washed with diethyl ether. The products were dissolved in 50 ml 10% w/v NaCl aqueous solution and put on a shaker for 18 hr. The products were dialyzed at room temperature against deionized water for 3 days by changing buffer twice daily, filtered through 0.8 mm of filter and freeze dried. The obtain product was characterized by nuclear magnetic resonance spectroscopy (NMR). NMR spectrum revealed that the degree of quaternization of CS was 60%.

## 2.2 Preparation of electrospinning mixture

PVAI and TMC were dissolved in deionized water (DI, 2A grade) to obtain 12% w/v PVAI and 2% w/v TMC mixtures. .

## 2.3 Fabrication of PVAI/TMC 60 mats of ultrafine fibers

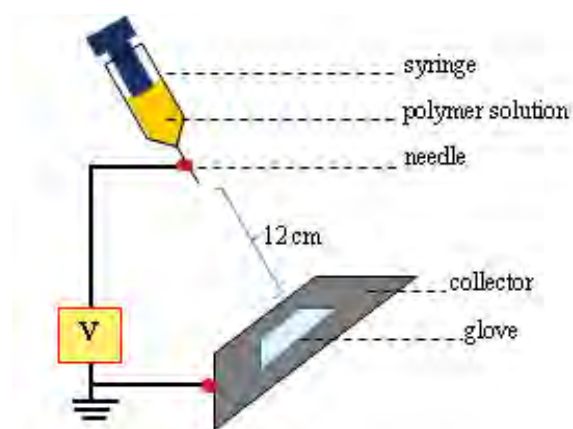


Figure 2. Electrospinning setup used in this work

The experimental set up is shown in Figure 2. Each of the spinning solution was loaded into a plastic syringe using a blunt 20-G stainless-steel needle (ID = 0.90 mm) as a nozzle. A Gamma High Voltage Research ORMOND BEACH power supply (D-ES50PN-6 20w/QAM, FL, USA) was used to charge the spinning solution by connecting the emitting electrode of positive polarity to the nozzle. The distance between the tip of the nozzle and the collection device was 12 cm. The applied electrical voltages (12, 14, 16, 18, and 20 kV) were varied in order to investigate its effect on the morphological appearance of the obtained composite fibers. The feed rate of the solutions was controlled at ~ 0.5 ml h<sup>-1</sup>. Electrospinning was carried out in room conditions.

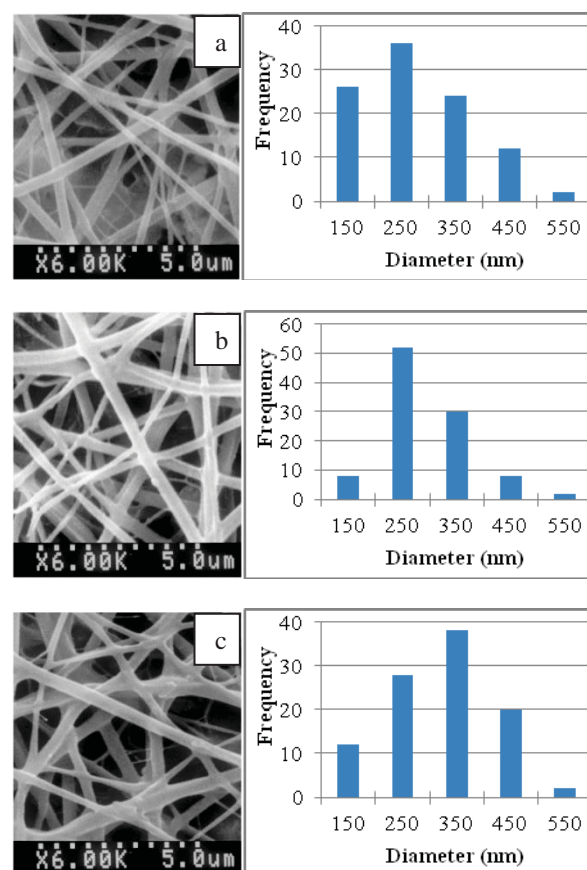
The collection time was fixed at 30 min. The piece of natural rubber glove was attaced to the collector, and was aligned at 30 degrees to the ground.

## 2.4 Morphological study of nanofibers

The morphology of the electrospun fibers was investigated under a scanning electron microscope (SEM; S-2500, Hitachi, Japan). Dried glove samples were sized to obtain 8 mm<sup>2</sup> specimens and fixed to SEM stubs in a dust-free environment before being stuck on the sample holder with a double-coated carbon conductive tape and sputter-coated (E-102, Hitachi, Japan) under vacuum condition. An average diameter of the electrospun fiber mats was measured directly from the SEM (at 15 kV) using an Image-J digital image analysis (n ≥ 50).

## 3. Results and Discussion

SEM images of the natural rubber glove coated by ultrafine fibers are shown in Figure 3(a) 12 kV (b) 14 kV (c) 16 kV (d) 18 kV and (e) 20 kV. The results showed that diameters of the electrospun fibers ranged from 150 to 550 nm, depending on the applied voltage.



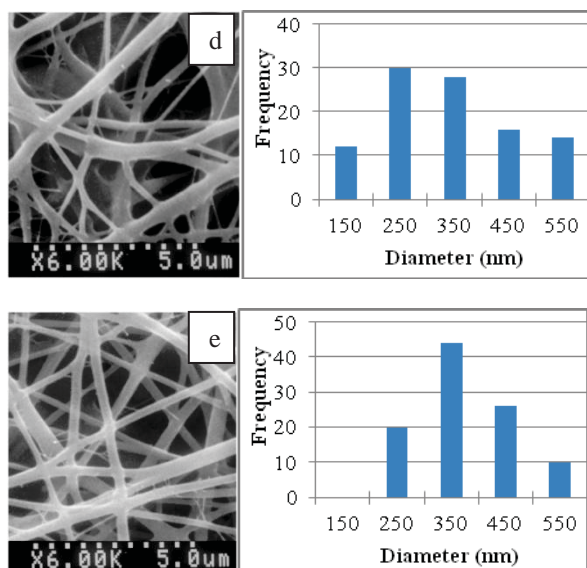


**Figure 3** SEM image (left) and diameter distribution (right) of ultrafine fibers coated on natural rubber glove at the applied voltage of (a) 12 kV (b) 14 kV (c) 16 kV (d) 18 kV and (e) 20 kV

It is clear that the applied voltage of the spinning solutions had a significant effect on the average diameter and size distribution of the fibers. To illustrate the relationship between the applied voltage and the average fiber diameter, this relation is shown in Figure 4.

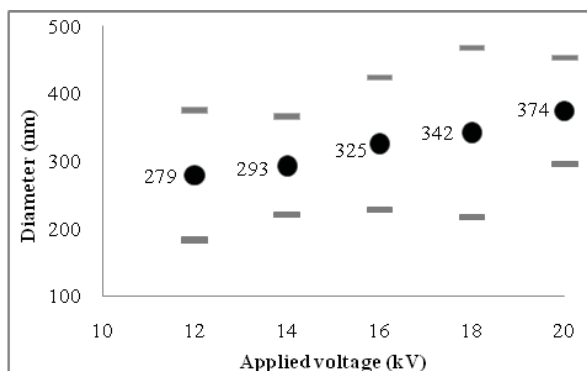


**Figure 4.** The applied voltage versus the fiber diameter

The results shown in Figure 4 suggest that, with increasing the applied voltages, the fiber diameter increased. It was because when the strength of electric field increased, the force that pulled the polymer strand was greater and the travelling time of the charged polymer jet from the spinneret to the fiber collector became less. Therefore, the polymer fiber could not be stretched fully [6].

#### 4. Conclusions

Ultrafine fibers prepared from 12% PVAI and 2% TMC with diameter of 150-550 nm were successfully coated on natural rubber glove by the electrospinning techniques. SEM images revealed that the fiber

diameter increased with increasing the applied voltage. The optimal applied voltage for preparing the fiber was 12 kV.

#### Acknowledgements

This research was financially supported by The Thailand Research Fund (TRF)/the Commission on Higher Education (MRG54) and Mahidol University. P.T. is TRF Senior researcher.

#### References

- [1] C.C. DeMerlis and D.R. Schoneker, *Food Chem. Toxicol.* **41** (2003) 319–326.
- [2] M. Thanou, B.I. Florea, M. Geldof, H.E. Junginger, and G.Borchard, *Biomaterials* **23** (2002) 153–159.
- [3] R. J. Verheul, M. Amidi, S. Wal, E. Riet, W. Jiskoot, and W. E. Hennink, *Biomaterials* **29** (2008) 3642–3649.
- [4] G.C. Rutledge and S.V. Fridrikh, *Adv. Drug Deliv. Rev.* **59** (2007) 1384–1391.
- [5] M. Ignatova, N. Manolova, and I. Rashkov, *Eur. Polym. J.* **43** (2007) 1112–1122.
- [6] S. Ramakrishna, K. Fujihara, W. Teo, T. Lim and Z. Ma, *An Introduction to Electrospinning and Nanofibers*, World Scientific Publishing, Singapore, Singapore (2005).

# FABRICATION OF GINGER EXTRACT-LOADED CELLULOSE ACETATE ULTRAFINE FIBERS BY ELECTROSPINNING TECHNIQUE

Thanaporn Chantarodsakun, Patoomratana Tuchinda, Thammasit Vongsetskul\*

Department of Chemistry, Faculty of Science, Mahidol University, Rama VI Road, Ratchathewi, Bangkok, 10400 Thailand

\* Author for correspondence; E-Mail: thammasit.von@mahidol.ac.th, Tel. +66 2201-5110, Fax. +66 2354-7151

**Abstract:** Electrospun cellulose acetate (CA; MW  $\sim 3 \times 10^4$  g/mol) fiber (375 – 1006 nm) containing ginger (*Zingiber officinale* Roscoe) extract, widely known for its wound healing, antioxidant and anti-inflammatory properties was successfully prepared from 12% w/v CA with 6% w/v ginger extract solution in acetone. The effect of Tween 80 addition (5% w/v), a nonionic and biocompatible surfactant, on the fiber diameter and morphology was also studied. The effect of Tween 80 addition and the applied voltages on the morphology and diameter of fibers was examined by scanning electron microscope (SEM). SEM images revealed that the optimal applied voltage for fabricating the thinnest uniform fibers (375 $\pm$ 107 nm) were + 7.5 kV, and the spinning mixtures with 5% w/v Tween 80 were more suitable to be spun than those without Tween 80.

## 1. Introduction

Electrospinning is a simple and convenient technique to fabricate ultrafine fibers, in which their interesting characteristics are high surface area to mass or volume ratio and ease to be functionalized. In this technique, either polymer solution or polymer melt is placed in a container connected with the spinneret in which the diameter is in millimeter range. When an electrostatic force is applied to the spinneret, the polymer solution or melt is ejected from the capillary and deposited as a nonwoven fiber mat on a fiber collector. In general, three types of parameters influence the morphology and diameter of the electrospun fibers, which are solution parameters such as viscosity, processing parameters such as applied voltages, and ambient parameters such as humidity.

Among various applications of electrospun fiber [1], the use of ultrafine fibers as a drug-controlled release system is one of them. There are some reports on the electrospun drug-loaded ultrafine fibers. For example, Suwantong et al. have prepared the electrospun curcumin-loaded CA ultrafine fibers to be used as topical or transdermal delivery of curcumin [2]. Various properties (i.e. morphological, mechanical, swelling and weight loss, and cytotoxicity) of the ultrafine fibers as well as their release characteristic were investigated. Comparisons were made against the corresponding solvent-cast films. Both the chemical integrity and the antioxidant activity of the as-loaded curcumin in the curcumin-loaded CA ultrafine fibers were also investigated.

CA, a derivative of naturally occurred cellulose, can be easily processed into films, membranes, and fibers from either melts or solutions. Electrospinning of 5 and 8 (w/w) % CA in acetone has been shown to generate short fibers with diameters around 1  $\mu$ m with a “beads on the string”

morphology. The morphology resulted from the low viscosity of acetone. Because the low boiling point of acetone also caused fast evaporation and gelation of the polymer solution. Furthermore, electrospinning of a 12% w/v CA solution in acetone in this study produced much finer fibers [3].

Ginger (*Zingiber officinale* Roscoe, Zingiberaceae) is widely used around the world in food as a spice. Its principal uses include treatment of motion sickness and disorders of the gastrointestinal tract. It has also been used as an anti-inflammatory agent for musculoskeletal diseases, including rheumatism, in Ayurvedic and Chinese medicine for more than 2500 years. Evidence from previous studies suggests that ginger reduce osteoarthritis pain [4]. The main pharmacological actions of compounds isolated from ginger are immuno-modulatory, anti-tumorigenic, anti-inflammatory, anti-apoptotic, anti-hyperglycemic, anti-lipidemic and anti-emetic actions. It is considered a safe herbal medicine with only few and insignificant adverse/side effect. [5,6,7,8]

Even though the ultrafine CA fibers have been used as a drug delivery system, there is no report on the preparation of ginger extract-loaded ultrafine fibers prepared by the electrospinning technique. Therefore, the aim of this study is to produce mats of electrospun ginger extract-loaded CA ultrafine fibers for treating osteoarthritis pain via transdermal drug administration. The effects of ginger concentrations, CA concentrations, Tween 80 concentrations, and applied electrical voltages on the prepared fibers were studied inclusively.

## 2. Materials and Methods

### 2.1 Materials and chemicals

CA (Mw = 30 kDa; acetyl content = 39.8 wt%) was purchased from Sigma-Aldrich (USA). The ginger extract was obtained by supercritical fluid CO<sub>2</sub> extraction of ginger roots (P. Tuchinda Laboratory, Department of Chemistry, Faculty of Science, Mahidol University, Thailand). Acetone was received from RCI Labscan (Asia) (Thailand) and used as received. Polysorbate 80 (Tween 80) was purchased from Rankem (India).

### 2.2 Preparation and characterization of spinning mixture materials and chemicals

A appropriate amount of CA powder and ginger extract was dissolved in acetone to obtain the spinning



mixtures with the final CA and ginger extract concentrations of 8, 12, 16 %w/v and 2, 4, 6, 8 %w/v, respectively. The concentrations of Tween 80 were 5, 10, and 15 %w/v. These mixtures were stirred to make them homogeneous. The conductivity of the spinning mixture was determined by a conductivity meter (Orion 105, Orion Research, USA).

### 2.3 Fabrication of ultrafine fibers

The electrospinning set up used in this work is shown in Fig 1. Each of the spinning solution was contained in a glass syringe with a plane tip of stainless-steel needle with an inner diameter of 0.9 mm. The feed rate of the spinning solution was 7  $\mu$ L/min controlled by a syringe pump (NE-300, New Era Pump Systems, USA). A Gamma High-Voltage Research ORMOND BEACH power supply (D-ES50PN-20w/QAM, FL, USA) was used to charge the spinning solution by connecting the emitting electrode of positive polarity to the nozzle.

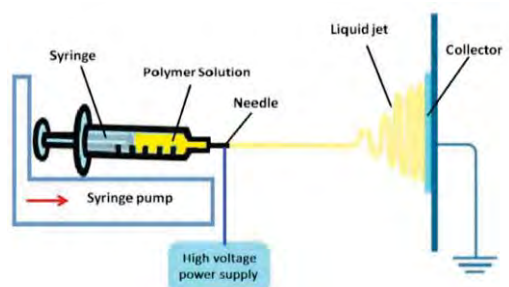


Figure 1. Schematic drawing of electrospinning set up used in this work.

The applied electrical voltages (7.5, 10.0, 12.5, 15.0, and 17.5 kV) were varied in order to investigate their effect on the morphological appearance of the electrospun fibers. The electrospun fibers were collected on aluminum foil. The electrospinning process was conducted at room temperature (25 °C). The collection time was 15 min, and the fiber collection distance was 10 cm.

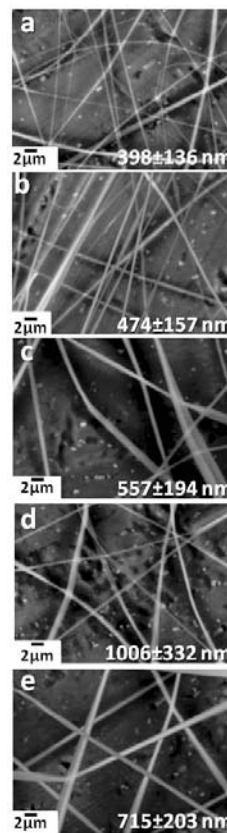
### 2.4 Morphological study of electrospun fibers

The morphology of the electrospun composite fibers was investigated under scanning electron microscope (SEM; TM-1000, Hitachi, Japan). The fibers were dried on an aluminium foil in a dust-free environment before being stuck on the sample holder with a double-coated carbon conductive tape. An average diameter of the electrospun fiber mats was measured directly from SEM (at 15 kV) using a Photoshop 5.0 ( $n \geq 30$ ). Only smooth and uniform part of the fibers was measured.

## 3. Results and Discussion

Usually, three typical morphologies which are bead structure, bead-on-string structure and fiber structure can be obtained by adjusting electrospinning conditions. In this study, the concentrations of CA solution and ginger extract, applied voltages, and Tween 80 addition were evaluated as follows.

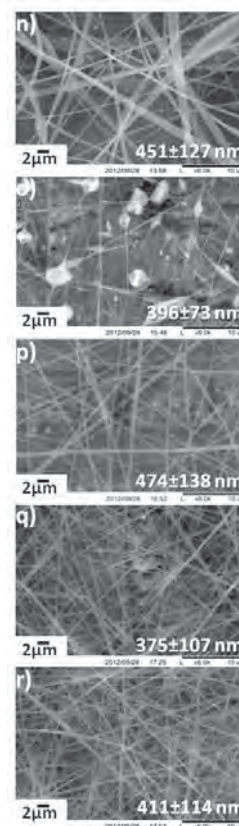
Figure 2. SEM images of electrospun ginger extract-loaded CA fibers fabricated from 2% (w/v) ginger extract with 12% (w/v) CA solution at various applied electrical voltages (a) 7.5 kV (b) 10.0 kV (c) 12.5 kV (d) 15.0 kV (e) 17.5 kV.



### 3.1 Effect of applied voltages:

Figure 2 shows SEM images of electrospun fibers at various applied voltages ranging from 7.5 to 17.5 kV. Figure 2 suggest that, with increasing the applied voltages, the fiber diameter increased because, with the high electrical voltages, the time of the polymer strand for travelling from the nozzle to the fiber collector was so short that the Coulombic repulsion could not stretch the charged jet fully. Therefore, smooth and uniform fibers were well formed when the applied voltage was 7.5 kV. However, the fiber diameter decreased again when the applied voltage was 17.5 kV. Unfortunately, the amount of electrospun fibers decreased largely as shown in Figure 2e).

Figure 3. SEM images of electrospun fiber mats obtained from the various concentrations of ginger extract with the 12% w/v CA solution at (n) 0 % w/v (o) 2 % w/v (p) 4 % w/v (q) 6 % w/v (r) 8 % w/v at applied electrical voltage was 7.5 kV.



### 3.2 Effect of ginger extract concentrations

The morphology of electrospun fibers is showed in Fig. 3. When the concentration of ginger extract was 2% w/v, the morphology of the obtained fibers changed from uniform fibers to beaded fibers. However, when the ginger extract concentrations were 4%, 6%, and 8% w/v, the morphology of the

electrospun fibers was smooth and uniform. SEM images in Fig 3 indicate that, with the ginger extract concentration of 6% w/v, the thinnest uniform electrospun fibers were obtained. The diameter of fibers fabricated from this condition was  $375 \pm 107$  nm.

### 3.3 Effect of CA concentrations

Fig 4 shows SEM images of electrospun CA fibers when the concentrations of CA were 8, 12, 14, and 16% w/v. The physicochemical properties of the spinning mixtures shown in Table 1 suggest that, with increasing in the CA concentration, the conductivity decreased. SEM micrographs of 8% w/v CA solution display the formation of short and beaded fibers. When the concentration of the solution increased to 12% w/v, uniform electrospun fibers were obtained. It was found that the diameter of electrospun fibers increased with increasing the concentration and decreasing the conductivity of CA solution.

Table 1: The conductivity and diameter of electrospun fiber mats in various concentrations of CA and Tween 80

Spinning solution CA (% w/v)	Conductivity Tween80 (%w/v)			
	0	5	10	15
0	$16.3 \pm 2.1$	-	-	-
8	$6.2 \pm 0.1$	-	-	-
12	$4.8 \pm 0.1$	$14.4 \pm 0.7$	$22.3 \pm 1.1$	$24.4 \pm 1.6$
16	$4.4 \pm 0.3$	-	-	-

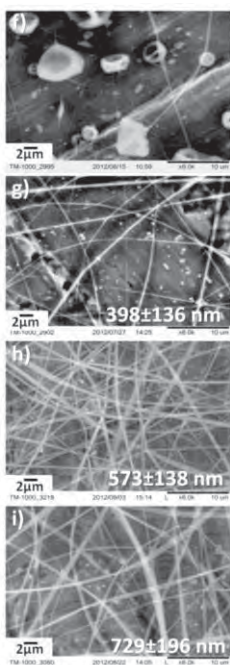


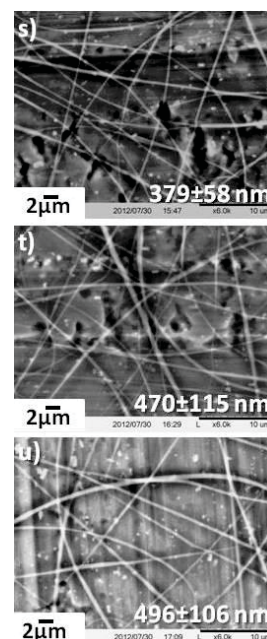
Figure 4. The SEM images of electrospun fibers obtained from 2% w/v ginger extract-loaded with the concentration of CA at (f) 8% w/v, (g) 12% w/v, (h) 14% w/v, and (i) 16% w/v at applied electrical voltage was 7.5 kV.

### 3.4 Effect of Tween 80 addition

Fig 5 shows SEM images of electrospun fibers with Tween 80 addition. When Tween 80 was added into the spinning solutions, the morphology of the fibers changed from bead-on-string fiber to smooth and uniform fiber with narrower fiber diameter distribution. It was because the addition of Tween 80 resulted in the reduction of surface tension of the spinning mixtures, which normally prevents the formation of electrospun fibers. The increase of conductivity resulted in increasing the electrostatic force acting on the charged jet, causing the jet to travel to the collector at a much greater speed. Therefore, the onset for the bending instability occurred closer to the collector. The addition of Tween 80 also

increased the charge density in the ejected jet which caused a strong elongation force of the jet. Therefore, the degree of fiber uniformity and the fiber diameter increased with increasing in the addition of Tween 80.

Figure 5. SEM images and diameter of electrospun fiber mats when the concentrations of CA was 12% w/v, of ginger extract was 2% w/v, and of Tween 80 were (s) 5% w/v, (t) 10% w/v, (u) 15% w/v at applied electrical voltage was 7.5 kV.



## 4. Conclusions

Ginger extract-loaded CA ultrafine fibers with diameter of 375 and 1,006 nm were successfully prepared by electrospinning technique. The conditions providing the thinnest uniform fibers ( $375 \pm 107$  nm) were 6% w/v ginger extract, 12% w/v CA, +7.5 kV, and no Tween 80. These ginger extract-loaded CA ultrafine fibers would be potentially used in biomedical applications such as wound healing patch in the future.

## References

- [1] T. Vongsetskul, P. Kongjumnean, P. Sunintaboon, R. Rangkupan, and P. Tangboriboonrat, *Polym. Bull.* **69**(9) (2012) 1115-1123.
- [2] O. Suwantong, P. Opanasopit, U. Ruktanonchai, and P. Supaphol, *Polymer* **48** (2007) 7546-7557.
- [3] H. Liu, and Y. L. Hsieh, *J. Polym. Sci. Pol. Phys.* **40** (2002) 2119-2129.
- [4] A. Haghighi, N. Tavalaei, and M. B. Owlia, *India. J. Rheum.* **1**(1) (2006) 3-7.
- [5] H. W. Kim, A. Murakami, M. Abe, Y. Ozawa, Y. Morimitsu, M. V. Williams, and H. Ohgashi, *Antioxid. Redox. Signal.* **7** (2005) 1621-1629.
- [6] M. Afzal, D. Al-Hadidi, M. Menon, J. Pesek, and M. S. Dhama, *Drug Metab. Drug Interact.* **18** (2001) 159-190.
- [7] M. S. Weidner and K. Sigwart, *J. Ethnopharmacol.* **73** (2000) 513-520.
- [8] R. Grzanna, L. Lindmark, and C. G. Frondoza, *J. Med. Food* **8** (2005) 125-132.

# SYNTHESIS AND CHARACTERIZATION OF THE NOVEL 1,3-ALTERNATE CALIX[4]ARENES TETRABENZOIC ACID AS ORGANIC LINKERS IN METAL-ORGANIC FRAMEWORKS

Suppachai Krajangsri and Buncha Pulpoka\*

Department of Chemistry, Faculty of Science, Chulalongkorn University,  
Bangkok 10330, Thailand

\* Author for correspondence; E-Mail: buncha.p@chula.ac.th, Tel. +66 2218 7643, Fax. +66 2218 7598

**Abstract:** Metal-organic frameworks (MOFs) are a class of porous materials constructed by metal ions or metal clusters and organic linkers. Because of the high pore volume and specific surface area of MOFs, many researches have been published for various applications in gas separation and storage, sensors, heterogeneous catalysis and drug delivery. Organic linkers play an important role in dictating structures and properties of the resulted frameworks. Herein, we synthesized the novel organic linkers, 1,3-alternate tetrabenzoic acid calix[4]arenes (3A and 3B) and applied for calix[4]arene-based MOFs synthesis with the aim that carboxylate groups of synthesized linkers at different substituted position may affect the morphologies and properties of the frameworks. These organic linkers were synthesized by functionalization of calix[4]arene with methyl-4-(bromomethyl) benzoate (2A) and methyl-3-(bromomethyl)benzoate (2B), following with hydrolysis of methyl ester derivatives (2A and 2B) with potassium hydroxide (KOH) that provided the desired organic linkers. All compounds were characterized by spectroscopic techniques. Surprisingly, we succeed in crystallization of 2B and 3A. Crystal structures demonstrated that the carboxylate groups pointed out in different directions, which may affect the morphologies and structures of the obtained MOFs as mentioned above. The syntheses of metal organic frameworks of 3A and 3B with  $\text{Zn}^{2+}$  ion were successfully carried out by solvothermal methods, providing needle-like and cubic shape crystals of MOFs, respectively. In the case of 3A and 3B with  $\text{Cd}^{2+}$  ion, only 3B afforded polyhedral shape crystals. We are currently exploring their properties for using as gas storage and heterogeneous catalysts.

## 1. Introduction

Metal-organic frameworks (MOFs)<sup>[1]</sup> are a class of crystalline materials which self-assembled by the bonding of metal ions with multifunctional organic ligands. Because of the high pore volume and surface area of MOFs, many researches have reported for application in the absorption of light gases such as hydrogen, nitrogen and methane<sup>[2]</sup> etc. Moreover, MOFs have many other potential applications, for example, gas separation<sup>[3]</sup>, catalysis<sup>[4]</sup>, drug delivery<sup>[5]</sup>, luminescence<sup>[6]</sup> etc. There are many factors that should be considered in the formation of MOFs, not only metal ions and organic linkers but also temperature, pH values, solvent, synthetic methods etc.<sup>[7]</sup> which play an important role in directing the topologies and properties of frameworks leading to their applications.<sup>[8]</sup> Many studies have been reported the

new MOFs using commercially available or synthesized organic linkers in the laboratory with the appropriate metal ions under optimum conditions to provide a beautiful architecture frameworks and also useful applications. In this research, we designed and synthesized the new organic linkers using calix[4]arene as building block. Calix[4]arene is one of the most popular building blocks in supramolecular chemistry due to cavity-shaped cyclic molecule and have a lot of  $\pi$ -electron which may provide a specific properties of new MOFs. There are two designed organic linkers (3A and 3B) that were functionalized as 1,3-alternate form. They are structural isomers and have the carboxylate group as the chelating group possessing the strong bonds with the metal ions. In the work, synthesis of MOFs composing of d10 transition metal ions is reported.

## 2. Experiment

### 2.1 Materials

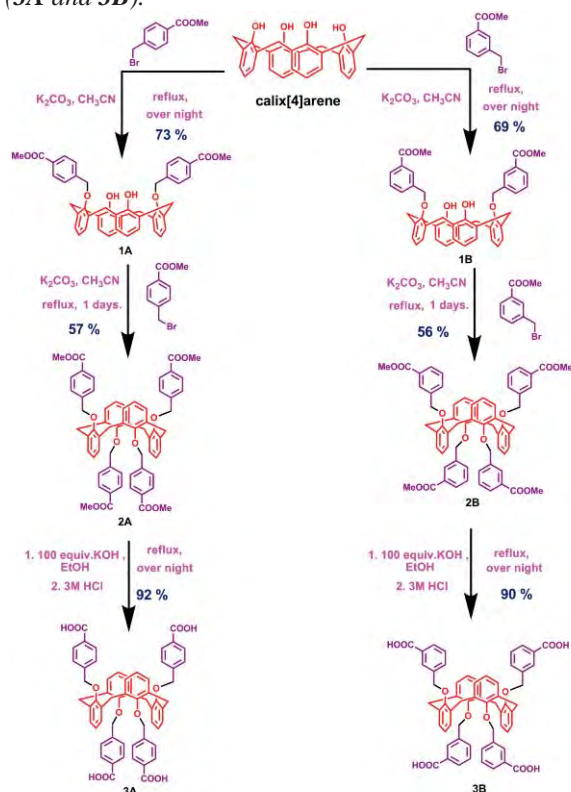
All reagents were analytical grade and purchased from Sigma-Aldrich, Merck, Acros organics and used as received without further purification.

### 2.2 Instrumentation

$^1\text{H}$  NMR spectra were obtained in  $\text{CDCl}_3$  at 400 MHz (Varian, USA).  $^{13}\text{C}$  NMR spectra were obtained in  $\text{CDCl}_3$  or DMSO at 100 MHz (Bruker, UK). Chemical shifts ( $\delta$ ) were reported in parts per million (ppm). Coupling constant ( $J$ ) are reported in Hertz (Hz). Mass spectra were obtained using matrix-assisted laser desorption ionization mass spectrometry (MALDI-MS) by using  $\alpha$ -hydroxycyano cinnamic acid (CCA) as a matrix. XRD pattern was obtained by X-Ray Diffractometer, Rigaku DMAX 2200 Ultima+/Cu lamp. IR spectrum was obtained by Fourier Transform Infrared Spectroscopy, Nicolet Impact 412. Nitrogen adsorption analysis was obtained by Surface area analyzer, BELSORP- mini instrument. The morphology of MOFs were obtained by Scanning Electron Microscope, Philips XL30CP. And The thermal stability of MOFs obtained by Thermogravimetric Analysis, TG-DTA Perkin-Elmer Pyris diamond.



### 2.3 Synthesis and characterization of organic linkers: (3A and 3B).



Scheme 1. Synthetic pathway of 1,3-alternate calix[4]arene tetrabenzoic acid (3A and 3B)

#### 2.3.1 Synthesis of 1,3-dimethyl-*p*-benzoate calix[4]arene (1A)

Into a 100 mL two-necked round-bottom flask, a mixture of calix[4]arene (0.531 g, 1.25 mmol) and potassium carbonate (K<sub>2</sub>CO<sub>3</sub>) (0.691 g, 6.25 mmol) in dried acetonitrile (30 mL) was refluxed under nitrogen atmosphere for 1 hr. A solution of methyl-4-(bromomethyl)benzoate (0.573 g, 2.5 mmol) in dried acetonitrile (10 mL) was then added and the reaction mixture was refluxed overnight. Potassium carbonate was filtered and the filtrate was dried under reduced pressure. The crude product was dissolved in dichloromethane (30 mL) and then washed with aqueous 3M HCl (10 mL), water and brine, respectively. The organic layer was dried over anhydrous Na<sub>2</sub>SO<sub>4</sub> and concentrated to one third of volume by rotary evaporator. The product was precipitated by methanol. The white solid was filtered and washed with methanol to obtain the desired product (1A) (0.664 g, 73%). <sup>1</sup>H NMR (400 MHz, CDCl<sub>3</sub>) δ: 7.98 (4H, d, *J* = 8.0 Hz), 7.81 (4H, d, *J* = 6.4 Hz), 7.06 (4H, d, *J* = 7.6 Hz), 6.91 (4H, d, *J* = 7.2 Hz), 6.78 (2H, t, *J* = 7.6 Hz), 6.66 (2H, t, *J* = 7.6 Hz), 5.13 (4H, s), 5.28 (4H, d, *J* = 13.2 Hz), 3.92 (6H, s), 3.36 (4H, d, *J* = 13.2 Hz); <sup>13</sup>C NMR (100 MHz, CDCl<sub>3</sub>) δ: 166.8, 153.2, 151.7, 141.8, 133.0, 130.1, 129.8, 129.2, 128.6, 127.8, 126.9, 125.7, 119.2, 77.6, 52.1, 31.4; IR (Nujol): ν<sub>max</sub> 3373, 2924, 1722, 1463, 1279, 1197, 1108, 1018, 756.

#### 2.3.2 Synthesis of 1,3-dimethyl-*m*-benzoate calix[4]arene (1B)

1,3-dimethyl-*p*-benzoate calix[4]arene (1B) was obtained by a similar procedure that used for preparation of 1A but methyl-3-(bromomethyl)benzoate (0.573 g, 2.5 mmol) was used as starting material instead of methyl-4-(bromomethyl)benzoate. The white solid of 1B was yielded (0.625 g, 69%). <sup>1</sup>H NMR (400 MHz, CDCl<sub>3</sub>) δ: 8.16 (2H, s), 8.02 (4H, t, *J* = 7.2 Hz), 7.73 (2H, s), 7.32 (2H, t, *J* = 7.6 Hz), 7.04 (4H, d, *J* = 7.6 Hz), 6.88 (4H, d, *J* = 7.6 Hz), 6.76 (2H, t, *J* = 7.4 Hz), 6.66 (2H, t, *J* = 7.4 Hz), 5.11 (8H, s), 4.50 (4H, d, *J* = 12.8 Hz), 3.87 (12H, s), 3.33 (4H, d, *J* = 13.2 Hz); <sup>13</sup>C NMR (100 MHz, CDCl<sub>3</sub>) δ: 166.8, 153.3, 151.7, 137.2, 133.1, 132.2, 130.4, 129.3, 129.2, 129.1, 128.6, 128.5, 127.9, 125.6, 119.1, 77.8, 52.2, 31.4; IR (Nujol): ν<sub>max</sub> 3394, 2949, 1721, 1590, 1465, 1287, 1202, 1087, 747.

#### 2.3.3 Synthesis of 1,3-alternate calix[4]arene tetra-*p*-benzoate (2A):

Into a 100 mL two-necked round-bottom flask, a mixture of 1,3-calix[4]arene-dimethyl-*p*-benzoate (1A) (0.433 g, 0.60 mmol) and potassium carbonate (K<sub>2</sub>CO<sub>3</sub>) (1.382 g, 10.0 mmol) in dried acetonitrile (30 mL) was refluxed under nitrogen atmosphere for 1 hr. A dried acetonitrile (10 mL) solution of methyl-4-(bromomethyl)benzoate (0.302 g, 1.32 mmol) was then added, the reaction mixture was refluxed for 2 days. After solid was filtered off, the solvent was removed under vacuo. The residue was dissolved with dichloromethane (30 mL) and then washed with 3M HCl (10 mL), water and brine, respectively. The organic layer was dried over anhydrous Na<sub>2</sub>SO<sub>4</sub>, filtered and removed the solvent under reduced pressure to one third. The desired product (2A) was precipitated by methanol. The white solid of 2A was obtained (0.352 g, 57%). <sup>1</sup>H NMR (400 MHz, CDCl<sub>3</sub>) δ: 8.15 (8H, d, *J* = 7.6 Hz), 7.20 (8H, d, *J* = 7.6 Hz), 6.66 (8H, d, *J* = 7.6 Hz), 6.45 (4H, t, *J* = 7.4 Hz), 4.92 (4H, s), 4.05 (12H, s), 3.63 (4H, s); <sup>13</sup>C NMR (100 MHz, CDCl<sub>3</sub>) δ: 167.2, 155.5, 143.0, 133.9, 131.1, 129.2, 129.1, 126.5, 122.7, 71.2, 52.2, 37.4; IR (Nujol): ν<sub>max</sub> 2949, 1718, 1613, 1452, 1287, 1196, 1107, 1020, 754.

#### 2.3.4 Synthesis of 1,3-alternate calix[4]arene tetra-*m*-benzoate (2B):

1,3-alternate calix[4]arene tetramethyl-*m*-benzoate (2B) was obtained by a similar procedure that used for preparation of 2A but using 1B (0.702 g, 1.0 mmol) and methyl-3-(bromomethyl)benzoate (0.504 g, 2.2 mmol) as starting material instead of 1A and methyl-4-(bromomethyl)benzoate. The white solid was filtered and washed with methanol to obtain the desired product (2B) (0.580 g, 56%). <sup>1</sup>H NMR (400 MHz, CDCl<sub>3</sub>) δ: 8.05 (4H, d, *J* = 7.6 Hz), 7.95 (4H, s), 7.50 (4H, d, *J* = 8.0 Hz), 7.33 (4H, d, *J* = 7.2 Hz), 6.68 (8H, d, *J* = 7.2 Hz), 6.46 (4H, t, *J* = 7.6 Hz), 4.86 (8H, s), 3.97 (12H, s), 3.57 (8H, s); <sup>13</sup>C NMR (100 MHz, CDCl<sub>3</sub>) δ: 167.2, 155.7, 138.4, 133.8, 132.2, 131.1, 129.9, 128.4,



128.2, 127.7, 122.4, 71.9, 52.1, 37.1; IR (Nujol):  $\nu_{\max}$  2949, 1721, 1588, 1454, 1367, 1286, 1200, 1092, 747.

#### 2.3.5 Synthesis of 1,3-alternate calix[4]arene tetra-*p*-benzoic acid (**3A**):

Tetramethyl-*p*-benzoate calix[4]arene (**2A**) (1.018 g, 1 mmol) was dissolved in ethanol (30 mL) in a 100 mL two-necked round-bottom flask and gently heated until tetrabenzoate-calix[4]arene (**2A**) was completely soluble. The solution of potassium hydroxide (5.60 g, 100 mmol) in water (10 mL) was then added. The reaction mixture was refluxed until completion (TLC analysis). The reaction mixture was concentrated by rotary evaporator and then acidified by aqueous 3M HCl (30 mL). The precipitate was filtered and washed with water to afford the desired product **3A** (0.870 g, 90%).  $^1\text{H}$  NMR (400 MHz, DMSO- $d_6$ )  $\delta$ : 12.93 (4H, s), 8.00 (8H, d,  $J = 7.6$  Hz), 7.23 (8H, d,  $J = 7.6$  Hz), 6.59 (8H, d,  $J = 7.6$  Hz), 6.28 (4H, d,  $J = 7.0$  Hz), 4.86 (4H, s); 3.59 (4H, s);  $^{13}\text{C}$  NMR (100 MHz, DMSO- $d_6$ )  $\delta$ : 167.3, 155.6, 143.1, 133.7, 130.4, 129.5, 128.6, 126.9, 121.7, 71.0, 36.5; FT-IR (KBr pellet)  $\nu/\text{cm}^{-1}$ : 3466, 2915, 1682, 1453, 1418, 1279, 1195, 1092, 1034, 757.

#### 2.3.6 Synthesis of 1,3-alternate calix[4]arene tetra-*m*-benzoic acid (**3B**):

1,3-alternate calix[4]arene tetra-*m*-benzoic acid (**3B**) was obtained by a similar procedure that used for preparation of **3A** using **2B** (0.309 g, 0.30 mmol) as starting material instead of **2A**. White precipitate of **3B** was obtained (0.265 g, 90% yield).  $^1\text{H}$  NMR (400 MHz, DMSO- $d_6$ )  $\delta$ : 12.88 (4H, s), 7.89 (4H, d,  $J = 9.2$  Hz), 7.42 (4H, d,  $J = 7.4$  Hz), 7.22 (4H, d,  $J = 7.6$  Hz), 6.60 (8H, d,  $J = 7.6$  Hz), 6.26 (4H, t,  $J = 7.2$  Hz), 4.74 (8H, s), 3.52 (8H, s);  $^{13}\text{C}$  NMR (100 MHz, DMSO- $d_6$ )  $\delta$ : 167.4, 155.5, 138.4, 133.6, 132.2, 130.4, 130.2, 127.9, 127.8, 121.6, 71.4, 36.4; FT-IR (KBr pellet)  $\nu/\text{cm}^{-1}$ : 3432, 2917, 1691, 1588, 1456, 1409, 1303, 1250, 1200, 1090, 748.

### 2.4 Synthesis of metal organic frameworks

The syntheses of metal organic frameworks were carried out by using solvothermal method. This method normally uses polar organic solvent to dissolve organic linker and metal salts which is heated up to desired temperature. There are many types of containers and heating sources such as conventional heating, autoclave with temperature program and isothermal vial in oven.

#### 2.4.1 By conventional heating

A round-bottomed flask containing **3A** (0.489 g, 0.5 mmol) and  $\text{Zn}(\text{NO}_3)_2 \cdot 6\text{H}_2\text{O}$  (0.301 g, 1.0 mmol) were charged with freshly distilled DMF (20 mL). The reaction mixture was heated to 110 °C for 24 hr. The solid was filtered and washed with DMF to obtained the desired MOFs (**3A-Zn**) (0.458 g).

#### 2.4.2 By auto clave

A mixture of **3B** (0.241 g, 0.25 mmol) and  $\text{Zn}(\text{NO}_3)_2 \cdot 6\text{H}_2\text{O}$  (0.074 g, 0.25 mmol) was placed in a

100 mL of Teflon-lined stainless steel with anhydrous DMF:DEF(1:1, 30 mL). The mixture was heated to 150 °C in 6 h and kept to this temperature for 48 h. After cooling to room temperature for 24 h, cubic colorless crystals of MOF(**3B-Zn**) were obtain.

#### 2.4.3 By isothermal in vial

MOF(**3B-Cd**) was obtained from this method, a mixture of **3B** (20.2 mg, 0.02 mmol) and  $\text{Cd}(\text{NO}_3)_2 \cdot 4\text{H}_2\text{O}$  (6.5 mg, 0.02 mmol) was dissolved in mixture solvent of DMF:DEF (1:1, 2 mL) in a 10 mL vial then kept in the oven at 90 °C for 24 h.

### 3. Results and Discussion

#### 3.1 Synthesis and characterization of organic linkers: **3A** and **3B**.

The synthesis of 1,3-alternate calix[4]arene tetrabenzoic acid (**3A** and **3B**) were shown in the scheme 1. The first step, calix[4]arene reacted with methyl-4-(bromomethyl) benzoate or methyl-3-(bromomethyl) benzoate in dry  $\text{CH}_3\text{CN}$  and used  $\text{K}_2\text{CO}_3$  as base to provide 1,3-calix[4]arene-dimethyl-*p*-benzoate (**1A**) and 1,3-calix[4]arene-di methyl-*m*-benzoate (**1B**), respectively. In second step, the reaction of 1,3-calix[4]arene dimethyl-*p*-benzoate (**1A**) with methyl-4-(bromomethyl) benzoate and 1,3-calix[4]arene-dibenzoate (**1B**) with methyl-3-(bromomethyl) benzoate providing the 1,3-alternate calix[4]arene tetramethyl-*p*-benzoate (**2A**) and 1,3-alternate calix[4]arene tetramethyl-*m*-benzoate (**2B**), respectively. The products in each step were easily precipitated in  $\text{CH}_2\text{Cl}_2/\text{MeOH}$  system to obtain white precipitate. In the final step, 1,3-alternate calix[4]arene tetramethyl-*p*-benzoate (**2A**) and 1,3-alternate calix[4]arene tetramethyl-*p*-benzoate (**2B**) were hydrolyzed using KOH 100 equiv. and then acidified by 3M HCl to provide 1,3-alternate calix[4]arene tetra-*p*-benzoic acid (**3A**) and 1,3-alternate calix[4]arene tetra methyl-*m*-benzoic acid (**3B**) in high yield. The obtained products were characterized by spectroscopic techniques and were in accordance with their structures.

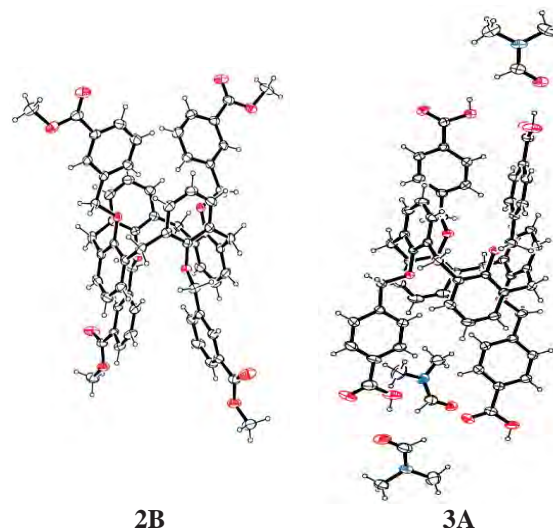


Figure 1. ORTEP draws of **2B** and **3A**. Displacement ellipsoids are scaled to the 25% probability level.

The crystal structures of **2B** and **3A** were shown in Figure 1. The carboxylate groups pointed out in different directions that may affect to the distinct morphologies of prepared MOFs.

### 3.2 Synthesis and characterization of 1,3-alternate calix[4]arene based MOFs

The obtained MOFs were characterized by IR spectroscopy. The compared infrared spectra of 1,3-alternate calix[4]arene tetra-*p*-benzoic acid **3A** and MOFs (**3A-Zn**) was shown in figure 2. The carbonyl (C=O) and C-O stretchings of MOFs (**3A-Zn**) shifted to lower wavenumber comparing with **3A** due to complexation of carboxylic group with  $\text{Zn}^{2+}$  ion. In the case of MOFs (**3B-Zn**) and MOFs (**3B-Cd**), the same phenomena was observed.

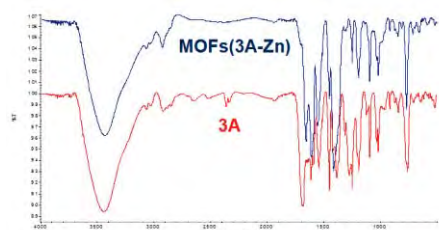


Figure 2. Compared IR spectra of **3A** and MOFs (**3A-Zn**).

The morphology of MOFs (**3A-Zn**), MOFs (**3B-Zn**), MOFs (**3B-Cd**) were investigated by SEM images and microscope images as shown in figure 3 with different topologies as rectangular bar shape, cubic shape and polyhedral shape, respectively. A particle size of MOFs (**3A-Zn**) was around 20  $\mu\text{m}$  x 200  $\mu\text{m}$ , while those of both MOFs (**3B-Zn**) and MOFs (**3B-Cd**) were around 200  $\mu\text{m}$ .

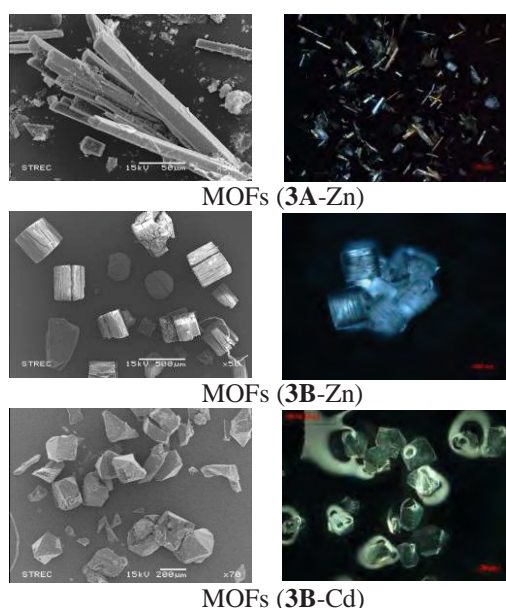


Figure 3. SEM images(left) and microscope images (right) of MOFs (**3A-Zn**), MOFs (**3B-Zn**), MOFs (**3B-Cd**).

This result may be due to the use of different metal ions, organic linkers and different synthesis conditions. It is so important to optimize the reaction condition to obtain the crystalline MOFs with desired properties.

The thermal stability of synthesized MOFs was studied by TGA. The thermogram of MOFs (**3A-Zn**) was displayed in figure 4 which suggested that MOFs (**3A-Zn**) was thermally stable up to 300  $^{\circ}\text{C}$ .

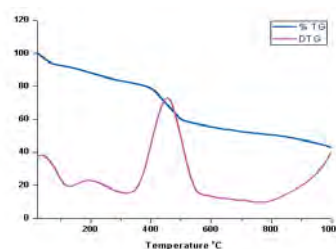


Figure 4. Thermogram of MOFs (**3A-Zn**)

We also investigated the porosity of the MOFs (**3A-Zn**) by using the nitrogen adsorption-desorption method after the sample was pretreated at 250  $^{\circ}\text{C}$  for 3 hr. According to nitrogen absorption isotherm, it showed that MOFs (**3A-Zn**) has low surface area (5.0829  $\text{m}^2/\text{g}$ ) and small pore volume (1.1678  $\text{cm}^3/\text{g}$ ).

## 4. Conclusions

The organic linkers, 1,3-alternate calix[4]arene tetrabenzoic acid (**3A** and **3B**), were successfully synthesized and used to synthesized calix[4]arene-based MOFs. The obtained MOFs provided different morphologies which implied that the structure of organic linkers play an important role in their morphologies besides the effects of metal ions and reaction conditions. We are currently exploring their properties for using as gas storage and heterogeneous catalysts.

## Acknowledgements

We would like to thank the Supramolecular Chemistry Research Unit and Graduate School of Chulalongkorn University for partially financial support for this research.

## References

- [1] H.-C. Zhou, J. R. Long and O. M. Yaghi, *Chem. Rev.* **112** (2012) 673–674.
- [2] A. W. Thornton, K. M. Nairn, J. M. Hill, A. J. Hill and M. R. Hill, *J. Am. Chem. Soc.* **131** (2009) 10662–10669.
- [3] J. R. Li, R. J. Kuppler and H. C. Zhou, *Chem. Soc. Rev.* **38** (2009) 1477–1504.
- [4] D. Farrusseng, S. Aguado and C. Pinel, *Angew. Chem., Int. Ed.* **48** (2009) 7502–7513.
- [5] J. D. Rocca, D. Liu and W. Lin, *Accounts Chem Res.* **44** (2011) 957–968.
- [6] M. D. Allendorf, C. A. Bauer, R. K. Bhakta and R. J. T. Houka, *Chem. Soc. Rev.* **38** (2009) 1330–1352.
- [7] H.-S. Liu, Y.-Q. Lan and S.-L. Li, *Cryst Growth Des.* **10** (2010) 5221–5226.
- [8] Y. Fu, J. Su, S. Yang, G. Li, F. Liao, M. Xiong and J. Lin, *Inorg Chim Acta.* **363** (2010) 645–652.

# AMINO ACID FUNCTIONALIZED SILICA NANOPARTICLE AS AN EFFECTIVE ADSORBENT FOR MERCURY REMOVAL

Ploypailin Numprasanthai<sup>1,2</sup>, Panya Sunintaboon<sup>1</sup>, Rattaporn Thonggoom<sup>1,2\*</sup>

<sup>1</sup>Department of Chemistry, Faculty of Science, Mahidol University, Phayathai, Bangkok, 10400 Thailand

<sup>2</sup>Center for Surface Science and Engineering, Faculty of Science, Mahidol University, Salaya, Nakhon Pathom, 73170 Thailand

\* Author for correspondence; E-Mail: Rattaporn.tho@mahidol.ac.th, Tel. 02-4419817, Fax. 02-4419817 ext. 1173

**Abstract:** In order to develop an effective adsorbent for mercury ( $\text{Hg}^{2+}$ ) removal, a biological-inorganic hybrid adsorbent ( $\text{SiO}_2\text{-NH-Cys}$ ) was prepared by functionalization of silica nanoparticle ( $\text{SiO}_2\text{-NH}_2$ ) with cysteine using aminopropyltriethoxysilane as a coupling agent. The obtained adsorbent was characterized by Fourier transform infrared spectroscopy (FT-IR), thermogravimetric analysis (TGA), elemental analysis (CHN analyzer), and a particle size analyzer. The results reveal that the surface of  $\text{SiO}_2\text{-NH}_2$  nanoparticle was chemically modified by cysteine. Flame atomic adsorption spectrometer (Flame AAS) technique was used to determine the  $\text{Hg}^{2+}$  adsorption. The  $\text{SiO}_2\text{-NH-Cys}$  was shown to be effective for the removal of  $\text{Hg}^{2+}$  ion with the adsorption efficiency of 60%. This hybrid material has a potential as an effective and selective adsorbent for the  $\text{Hg}^{2+}$  removal application.

## 1. Introduction

Pollution is harmful contaminant toward the environment, which affects plants and living organisms. There are many forms of pollution in nature such as air, soil, and water-pollution. However, water pollution is a major global problem that requires an evaluation and treatment as water is the most important component of the ecosystem. Various organic and inorganic pollutants, especially heavy metals, are mostly toxic even at very low concentration. Mercury, in particular, is considered the most toxic metal. It is the leading worldwide cause of deaths and diseases. When metals enter human body, they form complexes with proteins that can inactivate important enzyme systems or affect protein structures. Therefore, biological molecules lose their ability to function properly. Toxic heavy metals accumulated in fatty tissue of living organisms could affect the nervous, digestive, and, reproductive systems, leading to cancer [1].

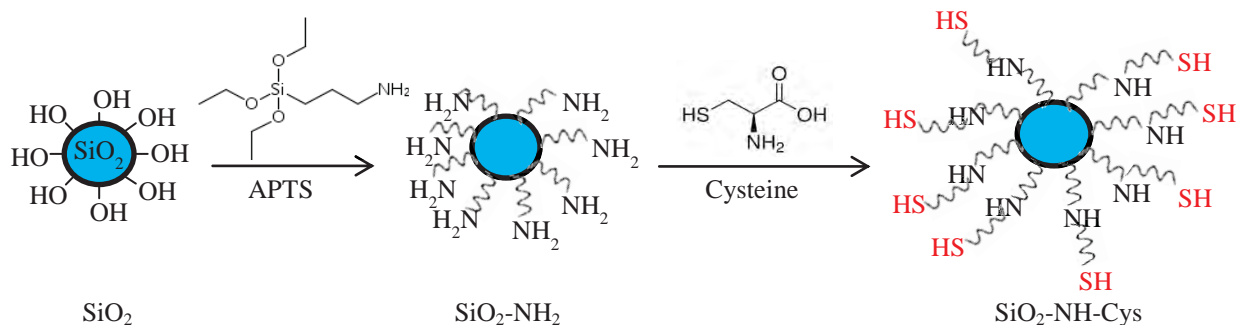
The sources of mercury pollution are mining activities, manufacture of batteries, printing industry, chemical manufactures, petroleum refining industry, and paper industry [2]. The toxic mercury must be removed from wastewaters before discharging directly into natural water. The commonly used procedures for removing heavy metal from wastewaters are chemical precipitation, lime coagulation, ion exchange, reverse osmosis and solvent extraction. These processes are complicated and expensive [3]. Among them, the

adsorption technique is one of the most techniques because of its simplicity and relatively low operational cost. Various adsorptive compounds currently used in the industry are activated carbon, zeolite and clay. However, these materials exhibit low selectivity for heavy metals [4]. Silica, an inorganic material that possesses high thermal and mechanical stabilities is chosen to be an adsorbent support material in this study. However, silica still remains a non-selective material for heavy metal removal. Therefore, to improve its selectivity toward heavy metals, -chemical functionalization onto silica surface is necessary [5].

In previous work, Feng et al. chemically modified silicas by heteroatomic functional groups ( $-\text{NH}_2$ ,  $-\text{SH}$ ,  $-\text{S}$ ) to increase the ability to interact strongly with metallic cations. The thiol-functionalized silicas showed exceptional selectivity for  $\text{Hg}^{2+}$  adsorption, especially when using propylthiol derivatives; namely, (3-Mercaptopropyl)trimethoxysilane (MPTMS) [6]. In addition, several chelating agents containing N, O or S donor atoms have been successfully modified onto silica surface. And, it was found that the chemisorption of chelating between functional groups and metal ion has occurred. As a result, efficiency, sensitivity and selectivity of these silica adsorbents were increased [7]. This could be explained by the Hard-Soft-Acid-Base (HSAB) theory, which states that stability of complexes comes from the fact that hard acids prefer to bind with hard bases, while soft acids prefer to bind with soft bases. Heavy metal cations which can be classified as a soft acid such as  $\text{Hg}^{2+}$ ,  $\text{Cd}^{2+}$ , and  $\text{Pb}^{2+}$ , are acceptor atoms that prefer to coordinated with soft bases that are donor atoms such as S, P, N, and halide ions. Therefore, based on HSAB theory many effective ligands have been synthesized and developed for the removal of heavy metals and other applications of heavy metals.

In order to improve the efficiency and selectivity of adsorptive silica nanoparticles ( $\text{SiO}_2$  NPs), cysteine, an amino acid, is chosen to functionalize onto the surface of silica NPs because it is a biological molecule that can be biosynthesized in human body, and has been widely used in series of environmental and biomedical applications. In addition, the thiol side chain in cysteine has a high affinity for heavy metals, especially mercury. Therefore, the functionalization of  $\text{SiO}_2$  nanoparticle surface with this amino acid is an alternative approach to develop a new selective adsor-





Scheme 1. Preparation process of the cysteine-functionalized silica NPs.

bent for heavy metal removal.

The purpose of this study is to develop an effective adsorbent for  $\text{Hg}^{2+}$  removal by functionalization of  $\text{SiO}_2$  nanoparticles with cysteine. Finally, the efficiency of the  $\text{Hg}^{2+}$  removal of these obtained biological-inorganic hybrid silica NPs will be investigated.

## 2. Materials and Methods

### 2.1 Chemicals and reagents

Tetraethoxysilane (TEOS, 98%, Sigma-aldrich), Ammonium hydroxide ( $\text{NH}_4\text{OH}$ , Labscan), Ethanol (EtOH, Labscan), Aminopropyltriethoxysilane (APTS, Sigma-aldrich), Cysteine (Cys, Sigma-aldrich), Dimethylformamide (DMF, Labscan), Mercury(II)nitrate ( $(\text{Hg}(\text{NO}_3)_2)$ , Sigma-aldrich), Hydrochloric acid ( $\text{HCl}$ , 37%, Labscan). All reagents and organic solvents were of analytical grade and used without further purification.

### 2.2 Synthesis of silica nanoparticles ( $\text{SiO}_2$ NPs)

The source of silicon was TEOS.  $\text{SiO}_2$  NPs were prepared by adding TEOS (0.018 mol) into a solution containing of EtOH (0.80 mol) and  $\text{NH}_4\text{OH}$  (0.085 mol). The reaction was stirred at room temperature (RT) for 24 h. The molar composition of the mixture of TEOS:EtOH: $\text{NH}_4\text{OH}$  was 1.0:4.4:4.7. Finally, the silica nanoparticle was purified by centrifugation, washed with ethanol, and then dried at  $80^\circ\text{C}$  overnight.

### 2.3 Preparation of silica nanoparticles with coupling agent ( $\text{SiO}_2\text{-NH}_2$ )

The silica colloidal dispersion from previous step was further functionalized by quickly adding APTS (0.0035 mol) into the mixture and kept at RT for 24 h. The obtained solid particle ( $\text{SiO}_2\text{-NH}_2$ ) was purified by centrifugation, washed with ethanol, and then dried at  $80^\circ\text{C}$  overnight.

### 2.4 Preparation of cysteine-functionalized silica nanoparticle ( $\text{SiO}_2\text{-NH-Cys}$ )

The method for functionalization of  $\text{SiO}_2$  NPs is demonstrated in Scheme 1. Cysteine (0.1 mol) in DMF was added dropwise into a flask containing a dispersion of  $\text{SiO}_2\text{-NH}_2$  (0.1 mol) in DMF. The mixture was stirred for 24 h. Then, the obtained silica nanoparticles with cysteine groups at their surface ( $\text{SiO}_2\text{-NH-Cys}$ ) was washed with DMF and dried at  $80^\circ\text{C}$  overnight.

### 2.5 Adsorption of $\text{Hg}^{2+}$ ions on the functionalized $\text{SiO}_2$ NPs

In order to study the  $\text{Hg}^{2+}$  adsorption capacities of  $\text{SiO}_2$  NPs before and after functionalization. The adsorbent (0.05 g) was added to 50 ml  $80\text{ }\mu\text{g/L}$  (80 ppb) of  $\text{Hg}^{2+}$  solution. In addition, the effect of adsorption time on the adsorption of  $\text{Hg}^{2+}$  ions was investigated by sampling the solution at the interval of 5, 10, 30, 50, 60 and 120 minutes, respectively, then the solution was filtered to collect the final solution. Both of the initial and final solutions were determined by Flame Atomic Absorption Spectrometer (Flame AAS).

### 2.6 Characterization

The chemical structure of adsorbent material was determined using Nicolet 6700 FT-IR Spectrometer/Thermo Scientific. DLS measurements and zeta potential of the silica NPs were measured by a Malvern Zetasizer which. The quantitative evaluation of organic groups on silica NPs was performed by carbon, hydrogen, nitrogen analysis using an elemental analyzer (CHN analyzer). The thermal property of silica NPs were investigated by a thermogravimetric analysis (TGA). The  $\text{Hg}^{2+}$  adsorption capacity of the silica NPs before and after cysteine functionalization were determined by Flame Atomic Absorption Spectrometer (Flame AAS).

## 3. Results and discussion

### 3.1 Chemical composition

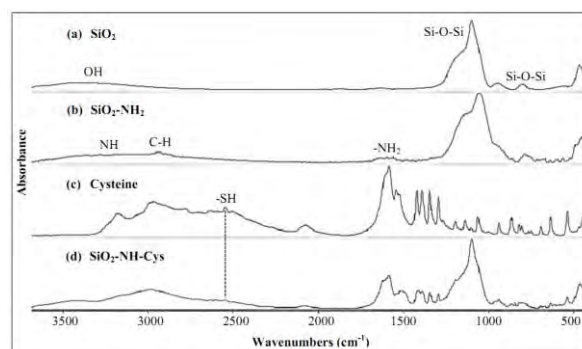


Figure 1. FT-IR spectra of silica nanoparticles ( $\text{SiO}_2$  NPs) before and after modification.



FTIR spectra of the silica nanoparticles ( $\text{SiO}_2$  NPs) before and after modification are illustrated in Figure 1. According to the FT-IR spectra of the  $\text{SiO}_2$  NPs (a), the characteristic peaks of  $\text{SiO}_2$  were observed at  $3450\text{ cm}^{-1}$  corresponding to stretching vibration of silanol groups ( $\text{Si-OH}$ ) on the silica surface, and the absorption bands at  $1100\text{ cm}^{-1}$ , and  $800\text{ cm}^{-1}$  that correspond to asymmetric and symmetric stretching vibrations of  $\text{Si-O-Si}$  bands, respectively. After functionalization with aminopropyl groups (b), the weak band in the region of  $2907\text{-}2986\text{ cm}^{-1}$  referred to asymmetric and symmetric stretching of  $\text{CH}_2$  groups was observed. In addition, the region of  $3300\text{-}3500\text{ cm}^{-1}$  and  $1586\text{ cm}^{-1}$  showed signals of the N-H stretching and bending vibration, respectively [8]. In Figure 1(c), a main peak of cysteine showed a characteristic peak of S-H stretching vibration at  $2554\text{ cm}^{-1}$  [2]. The peaks at  $3000\text{ cm}^{-1}$  and  $2966\text{ cm}^{-1}$  were assigned to asymmetric and symmetric stretching vibrations of N-H bands, respectively. The carboxylate stretching of the cysteine molecule was observed at  $1588\text{ cm}^{-1}$ , and the peak of  $\text{CH}_2$  group was found at  $1425\text{ cm}^{-1}$  [9,10]. After cysteine functionalization onto  $\text{SiO}_2\text{-NH}_2$  surface (d), the peaks at  $1103\text{ cm}^{-1}$  and  $800\text{ cm}^{-1}$  were observed and assigned to asymmetric and symmetric stretching vibrations of  $\text{Si-O-Si}$ . In addition, a band at  $1586\text{ cm}^{-1}$  is corresponding to the overlapping of carboxylate stretching and amide bond stretching. The peak of S-H stretching vibration of cysteine was observed at  $2554\text{ cm}^{-1}$ . These result indicated that cysteine was successfully chemically functionalized onto the silica surfaces.

### 3.2 Particle size measurement

The average particle size and the surface charge of silica NPs determined by particle size analyzer and zeta potential measurements were shown in Table 1.

Table 1: Characteristics of silica nanoparticles

Sample	Zeta Potential	Mean diameter (nm)	PDI*
$\text{SiO}_2$	-44.7	155.5	0.04
$\text{SiO}_2\text{-NH}_2$	0.48	Aggregated	-
$\text{SiO}_2\text{-NH-Cys}$	26.1	486.4	0.63

\* PDI : Polydispersity index (PDI) is a measure of distribution of particle

The functionalization of surface was determined by a change of surface charge of silica nanoparticles which was represented by zeta potential measurement. The  $\text{SiO}_2$  NPs were well dispersed in solutions and showed a negative zeta potential at about  $-44.7\text{ mV}$  corresponding to  $\text{OH}^-$  group of  $\text{SiO}_2$ . After aminopropyl groups functionalized onto  $\text{SiO}_2$  NPs surface, a zeta potential were increase to  $0.48\text{ mV}$ . In addition, the result showed that the presence of organic functional groups, namely, APTS and cysteine could increase the size of the silica nanoparticles. Moreover,

all PDI values were shown to be less than 1 indicating monodispersed or uniformed particles.

### 3.3 Elemental Analysis

CHN analyzer was used to analyze the presence of amino silane chains and cysteine groups that are modified onto the silica nanoparticles surface. The C, H, N contents of these samples were summarized in Table 2.

Table 2: The elemental analysis of the functionalized silica nanoparticles

Sample	C (mmol/g)	H (mmol/g)	N (mmol/g)	C/N (mmol/g)
$\text{SiO}_2$	0	13.90	0	0
$\text{SiO}_2\text{-NH-Cys}$	12.88	32.30	4.11	3.13

According to obtained data in Table 2, the content of carbon and nitrogen increased after functionalization with cysteine ( $\text{SiO}_2\text{-NH-Cys}$ ). This indicated that silane coupling agent and cysteine were successfully modified onto the silica surface. In addition, since the C/N ratio of the cysteine functionalized silica was  $3.13 : 1$ , it was confirmed that the cysteine were chemically reacted with silane coupling modified silica surfaces [4].

### 3.4 TGA analysis

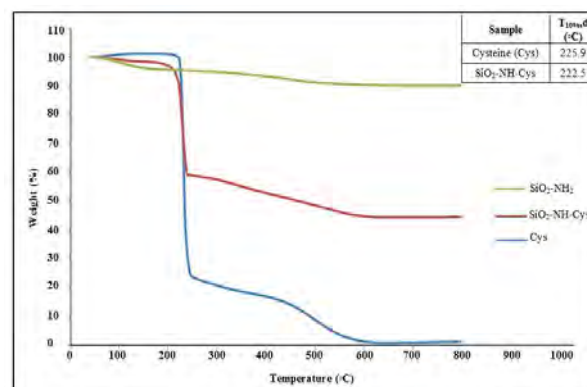
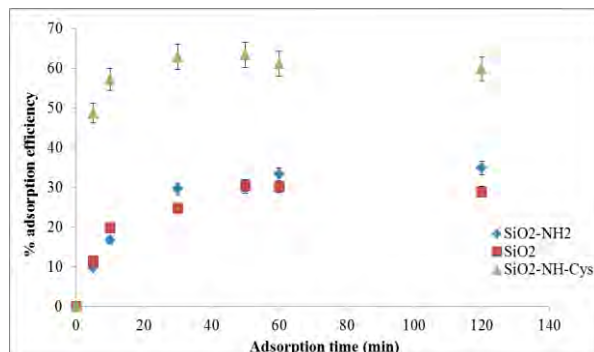


Figure 2. Representative TGA curves of  $\text{SiO}_2$  with functional groups.

According to the TGA curve in Figure 2, thermal stability of the APTS modified silica ( $\text{SiO}_2\text{-NH}_2$ ) showed two stages of mass loss. First, loss at  $100^\circ\text{C}$  corresponded to the desorbed water, trapped residual ethanol, and partial decomposition of unreacted APTS. The second stage of mass loss in the range between  $200\text{-}500^\circ\text{C}$  related to the decomposition of silane-modified group on the silica surface, while the inorganic  $\text{SiO}_2$  still remained above  $600^\circ\text{C}$  [11]. In addition, the temperatures ranging from  $220\text{-}600^\circ\text{C}$  could be described to the decomposition of the cysteine whose melting point was about  $240^\circ\text{C}$ .

Therefore, it was confirmed that cysteine was attached on the silica NPs surface.

### 3.5 Adsorption time of $\text{Hg}^{2+}$ ions from aqueous solution



**Figure 3.** Effect of adsorption time on the adsorption efficiency of the  $\text{Hg}^{2+}$  ions.

Figure 3 showed the  $\text{Hg}^{2+}$  adsorption of silica NPs before and after functionalization. It appeared that the adsorption kinetics of  $\text{SiO}_2\text{-NH-Cys}$  was faster than  $\text{SiO}_2\text{-NH}_2$  and  $\text{SiO}_2$ . This could be due to the influence of thiol group in cysteine. In addition, the adsorption kinetics of all adsorbents occurred within the first 5 minutes, and the adsorption equilibrium was reached after 60 minutes [12].

## 4. Conclusions

The coupling-functionalized silica nanoparticles ( $\text{SiO}_2\text{-NH}_2$ ) were successfully synthesized from silica precursors using sol-gel method. Then  $\text{SiO}_2\text{-NH-Cys}$  can be successfully prepared by chemical functionalization of cysteine onto the surface of  $\text{SiO}_2$  NPs. The  $\text{SiO}_2\text{-NH-Cys}$  NPs was shown to be an effective adsorbent for the removal of  $\text{Hg}^{2+}$  ions.

## Acknowledgement

This work was supported by the center for surface science and engineering (SSE) from Department of Chemistry, Mahidol University.

## References

- [1] J.O. Duruibe, M.O.C. Ogwuegbu and J.N. Ekwurugwu, *Int. J. Phys. Sci.* **2** (2007) 112-118.
- [2] J. Aguado, J.M. Arsuaga and A. Arencibia, *Ind. Eng. Chem. Res.* **44** (2005) 3665-3671.
- [3] A. Shahbazi, H. Younesi and A. Badiei, *Chem. Eng. J.* **168** (2011) 505-518.
- [4] L. Zhang, C. Yu, W. Zhao, Z. Hua, H. Chen, L. Li and J. Shi, *J. Non-Cryst.Solids.* **353** (2007) 4055-4061.
- [5] M. Muresanu, A. Reiss, I. Stefanescu, E. David, V. Parvulescu, G. Renard and V. Hulea, *Chemosphere.* **73** (2008) 1499-1504.
- [6] T.W. Clarkson, *Environ. Health Perspect.* **75** (1987) 59-64.

- [7] T.M. Abdel-Fattah, S.M.S. Haggag and M.E. Mahmoud, *Chem. Eng. J.* **175** (2011) 117-123.
- [8] M. Najafi, Y. Yousefi and A.A. Rafati, *Sep. Purif. Technol.* **85** (2012) 193-205.
- [9] P.R. Reddy, M. Radhiha and P. Manjula, *J. Chem. Sci.* **117** (2005) 239-246.
- [10] A. Barth, *Prog Biophys Mol Bio.* **74** (2000) 141-173.
- [11] I.A. Rahman, M.Jafarzedeh and C.S. Sipaut, *Ceram. Int.* **35** (2009) 1883-1888.
- [12] M. Puanngam and F. Unob, *J. Hazard. Mater.* **154** (2008) 578-587.

# THE EFFECT OF CHOLESTEROL CONTENTS IN CHOLESTEROL-GRAFTED GELATIN MICELLES ON CURCUMIN LOADING

Nungruthai Jaichawa, Sorada Kanokpanont\*

Department of Chemical Engineering, Faculty of Engineering, Chulalongkorn University, Bangkok, 10330 Thailand

\* Author for correspondence; E-Mail: sorada.k@chula.ac.th, Tel. +66 22186867, Fax. +66 22186877

**Abstract:** The aim of this study was to produce cholesterol-grafted gelatin micelles, to be used as a hydrophobic drug carrier. Gelatin is a biocompatible hydrophilic protein with controllable degradation. However, it has limit interactions with hydrophobic drugs. Gelatin (Type A, pI = 9) was grafted with cholesterol using DSC (N'-Disuccinimidyl carbonate) as a conjugating agent. Cholesterol contents were varied from 10 - 50% (by mole of free amine groups in gelatin). The success of conjugating was evaluated using 2, 4, 6-trinitrobenzenesulfonic acid (TNBS) method and FTIR techniques. Reductions of free amine groups in gelatin after conjugated with 10, 25, and 50% (CG10, CG25, and CG50, respectively) were 6.41, 11.69 and 76.10%, respectively. The CG50 micelles were loaded with various concentrations of curcumin at 0.25, 0.50 and 0.75 mg/ml. Drug loading was in the range of 0.05 – 1.46%wt. Average size and zeta potential of the micelles were at  $112.39 \pm 1.18$  nm and  $-2.96 \pm 0.13$  mV, respectively.

## 1. Introduction

Curcumin is a polyphenolic compound isolated from rhizome of the herb *Curcuma longa*. Studies have indicated that curcumin possesses a wide range of pharmacological affect including anti-oxidant, anti-inflammatory and anti-tumor activities [1]. The anti-tumor of curcumin is due to its anti-angiogenesis effect via the inhibition of vascular endothelial growth factor (VEGF) and cyclooxygenase-2 (COX-2) [2]. However, the main problem of utilizing curcumin is low bioavailability, low stability and poor water solubility. Its complexation with serum components in human body could lead to complications such as embolism [3]. To overcome these problems, development of curcumin delivery systems has been attempted [4 - 10].

To increase curcumin stability, solubility and bioavailability, attempts have been made though encapsulation in nanoparticle, polymeric, hydrogel, microsphere and nanosphere etc. Mukerjee et.al formulated curcumin encapsulated PLGA nanosphere using solid-in-oil-in-water (s/o/w) and solvent evaporation technique. The smooth, spherical PLGA nanosphere had the diameter around 45 nm with drug

entrapment of  $90.88 \pm 0.14\%$ . *In vitro*, these curcumin-loaded nanosphere could be uptaken robustly in the prostate cancer cells [5]. Das et.al reported nanoformulation of curcumin using alginate, chitosan, and pluronic acid (ALG-CS) in nanoparticles. The ALG-CS nanoparticles had an average size of  $100 \pm 20$  nm and curcumin encapsulation efficiency of 12 %wt. The *in vitro* cytotoxicity assay showed that at a concentration of 500  $\mu\text{g/ml}$ , the nanoparticles were non-toxic to human cervical cancer cell line (HeLa) [6]. Song et.al reported the curcumin-loaded PLGA-PEG-PLGA micelles with the average size of 26.29 nm, zeta potential of -0.71 mV, and curcumin loading of  $6.40 \pm 0.02\%$ wt. Biodistribution of the micelles in mice showed the decreases drug uptaking in liver and spleen and the enhanced drug distribution in lung and in brain [7].

In our previous works, we developed a sustained release system for curcumin using hydrogel patch made from cholesterol-grafted gelatin (Figure 1). The hydrogel patches with curcumin loading of 4%wt were able to sustain the releases of curcumin for at least 2 weeks in BALB/c-nude mice. The drug releases were according to the patch's biodegradation [8]. The system has been adjusted to be more convenient to apply through injection by fabricating into micelles. The micelles with 12.90%wt curcumin loading reduced growth of human hepatocellular carcinoma cell line (HepG2) in rats [9]. To continue the studies, we investigated the effect of cholesterol contents in the grafted gelatin on size, zeta-potential, drug loading, and loading efficiency. These factors are vital to applications of the delivery system. This curcumin delivery system would be advantaged to cancer treatments. The application could extend to other hydrophobic active agents for pharmaceutical and cosmetic purposes.

## 2. Materials and Methods

### 2.1 Materials

Type A gelatin (G) with an isoelectric point of 9.0 ( $M_w = 100,000$ ), was kindly supplied by Nitta Gelatin Inc., Osaka, Japan. Cholesterol (C) ( $M_w = 386.65$ ) was purchased from Wako Co., Japan. Curcumin (Cur) ( $M_w = 368.97$ ) was purchased from Cayman, USA. Dimethyl sulfoxide (DMSO) was purchased from

Fluka, USA. N, N'-Disuccinimidyl carbonate was obtained from Sigma-Aldrich Inc., USA.

## 2.2 Preparation of Cholesterol-grafted gelatin (CG)

Gelatin was grafted with cholesterol according to the method by Rujisomnana et al. [8]. Gelatin and conjugating agent were dissolved in DMSO solution and cholesterol (10, 25, and 50% mole by mole of amine groups in gelatin) were dissolved separately in pyridine. The solution was mixed and was stirred at 60 °C overnight for conjugating reaction. The mixture was dialyzed against deionized water using dialysis tube (MWCO=12,000-14,000, Viskase, Japan) for 3 days at room temperature. Then the solution was centrifuged at 9,000 rpm, 15 °C for 15 minutes. The supernatant was freeze-dried and was stored at 4 °C for further uses.

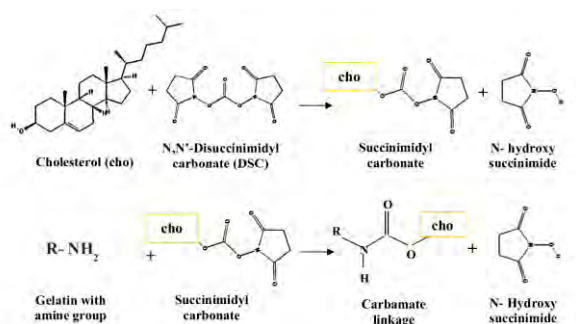


Figure 1. Chemical reaction in a gelatin modification process [adapted from 10]

## 2.3 Characterization of cholesterol-grafted gelatin

*Reducing of free amine groups in cholesterol grafted gelatin:* Reduction of reactive free amine groups in gelatin's structure was used to evaluate the success of conjugation using 2, 4, 6-trinitrobenzenesulfonic acid (TNBS) method. Numbers of free amine groups were estimated using a colorimetric reaction [11]. Briefly, The CG was digested in NaHCO<sub>3</sub> (4% w/v) solution and the TNBS solution (0.5% w/v) was added. The mixture was incubated at 40 °C for 2 hrs. Then concentrated hydrochloric acid was added, and the solution mixture at 60 °C for 1.5 hrs. An optical density of yellow color complex of the reaction product was measured spectrophotometrically at 415 nm in comparison to β-alanine standard graph.

*FTIR analysis:* The dried CG films were investigated using Fourier Transform Infrared spectrometer (FT-IR, Spectrum GX, Perkin Elmer, UK) with an attenuated total reflection (ATR) mode. Spectra of the CG samples were recorded at room temperature in the 600-4000 cm<sup>-1</sup> range.

## 2.4 Preparation of curcumin cholesterol grafted gelatin micelles (CurCG)

CurCG micelles were prepared by dialysis method. CG and curcumin were dissolved separately in DMSO at 37 °C. The micelles curcumin ratios were varied from 1:40 to 1:120. Then they were mixed and were dialyzed (Viskase, Japan, MWCO = 12,000-14,000)

against in DI water for 3 days. After dialysis, the solution was centrifuged at 9,000 rpm, at 4 °C, for 20 minutes to separate precipitants. The obtained micelles in the supernatant were freeze-dried and were kept dried in a dark container at room temperature before uses. Average size and zeta potential of the CG and CurCG micelles was determined using light scattering technique (Zetasizer 650, Malvern, UK).

## 2.5 Drug loading and loading efficiency

HPLC system (Varian, Pro Star, USA) was used to evaluate curcumin in CurCG micelles using C18 column with 10% (w/v) acetic acid and acetonitrile (60:40 by volume) as a mobile phase. The flow rate was at 1.0 mL/min. Curcumin was detected at the wavelength of 420 nm. The drug loading and loading efficiency were estimated using the following equations.

$$\text{Drug loading (\%)} = \frac{\text{Weight of detected Cur}}{\text{Weight of CurCG micelles}} \times 100 \quad (1)$$

$$\text{Loading Efficiency (\%)} = \frac{\text{Drug loading in (1)}}{\text{Theoretical loading}} \times 100 \quad (2)$$

## 2.6 Statistical Analysis

All experiments were repeated three times. All measurements were done in triplicate. Data are expressed as mean ± standard deviations. Statistical analysis was performed using ANOVA. Statistically differences were considered significant at  $p < 0.05$ .

# 3. Results and Discussion

## 3.1 Characterization of cholesterol-grafted gelatin (CG) and curcumin loaded in cholesterol-grafted gelatin micelles (CurCG)

The success of gelatin grafting with cholesterol was evaluated from the reduction of free amine groups in gelatin (Table 1). The results showed the reduction of free amine groups of CG50 was higher than those of the CG10 and CG25. Reduction of free amine groups in gelatin increased when the cholesterol contents increased. Figure 1 showed that an amine group in gelatin and a carboxyl group in cholesterol would be consumed for one grafting site. However, freeze drying process used in the preparation step could also induce amine groups consumption of gelatin structure due to condensation (water loss) reaction [12]. Figure 2 presents IR spectra of gelatin, which featured bands at 1600-1700 (Amide I, C=O Stretching), 1510-1580 (Amide II, N-H bending), 1396 (Amide III, C-N stretching), 1025-1200 (C-N stretching) cm<sup>-1</sup>. IR spectra of cholesterol featured the bands at 2800-2950 (C-H stretching), 1056 (C-O stretching) cm<sup>-1</sup> [13-15]. The general transformation was the reaction of the carboxyl group of cholesterol with gelatin, leading to formation of characteristic carbamate linkage (Figure 1). The characteristic adsorption of carbamate linkage formed due to carboxyl condensation were found band in the 1025-1200 cm<sup>-1</sup> in CG, but not found in gelatin



(G0). This indicated the successful grafting of cholesterol.

Table 1: Reduction of free amine group in grafted gelatin

Samples	Ratio (C:G) (by mole of free amine groups in gelatin)	Amine groups (by mole)	Reduction of free amine group (%)wt.
G0	-	20.30±0.05	0 <sup>a</sup>
CG10	10:1	19.00±0.15	6.41 <sup>b</sup>
CG25	25:1	17.90±0.72	11.69 <sup>b</sup>
CG50	50:1	4.85±0.01	76.10 <sup>c</sup>

\* a - c represents significant differences among all samples at p < 0.05

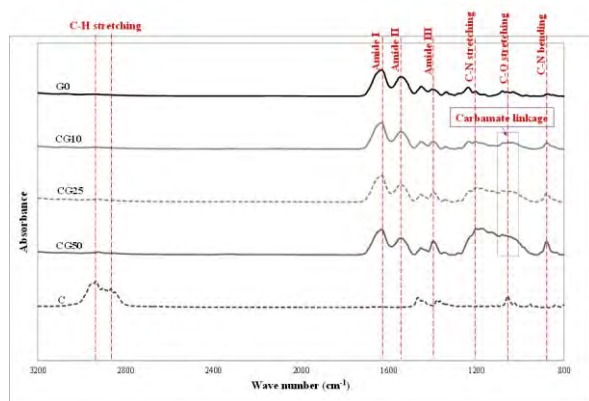


Figure 2 FTIR spectra of the cholesterol grafted gelatin (CG10, CG25 and CG50), gelatin (G0) and cholesterol (C)

Average size and zeta potential of CG micelles and CurCG micelles are showed in Table 2. The CurCG micelles had average size from 108 - 147 nm which was larger than CG micelles (103 – 125 nm). Average size of CG micelles increased when the cholesterol contents increased. Zeta potential of CG and CurCG micelles in water pH 5.6 were at -2.96±0.13 mV and -4.25±0.15 mV, respectively. This showed that curcumin-loaded micelles had higher stability than those of the CG micelles since their zeta potential were higher compared to other reported. For example Song et.al reported the curcumin-loaded PLGA-PEG-PLGA micelles with zeta potential of -0.71 mV [7] and Tanigo T et.al prepared of L-lactic acid oligomers (LAOs) grafted gelatin micelles which zeta potential of -5.42 mV [4]. CG50 had the highest reduction of free amine groups and largest size so encapsulation of curcumin by CG50 could be greater than those of the CG10 and CG25. They were selected for further experiments.

Table 2: Average sizes and zeta potential of CG and CurCG micelles in water

Samples	Average size (nm)		Zeta potential (mV)	
	CG	CurC G	CG	CurC G
CG10	103.23 ±1.37 <sup>a</sup>	108.00 ±0.40 <sup>a,c</sup>	-3.64 ±0.34 <sup>a,c</sup>	-4.35 ±0.58 <sup>c</sup>
CG25	108.03 ±0.57 <sup>a,c</sup>	112.4± 4.37 <sup>c</sup>	-2.86 ±0.09 <sup>b</sup>	-4.10 ±0.35 <sup>c</sup>
CG50	125.93 ±1.61 <sup>b</sup>	147.00 ±4.70 <sup>d</sup>	-2.91 ±0.74 <sup>a,b</sup>	-4.21 ±0.35 <sup>c</sup>

\* a - d represents significant differences among all samples at p < 0.05

### 3.2 Drug loading and loading efficiency

Table 3 showed drug loading and loading efficiency of curcumin loaded in CG50 micelles. The result showed CG50 which had ratio of CG micelles: curcumin at 1:120 had drug loading and loading efficiency at 1.46%wt and 1.77%wt, respectively. This result showed the decreased of drug loading and loading efficiency when the curcumin concentration increased. Drug entrapments of the micelles were low. This is generally one of the disadvantages of the nano-sized micelles.

Table 3: Drug loading and loading efficiency of CurCG50 micelles were varied Curcumin loaded.

Ratio of CG micelles : curcumin (by mole)	Drug loading (%wt.)	Loading efficiency (%wt.)
1:120	1.46±0.14 <sup>a</sup>	1.77±0.17 <sup>a</sup>
1:60	1.12±0.09 <sup>b</sup>	0.68±0.05 <sup>b</sup>
1:40	0.05±0.00 <sup>c</sup>	0.02±0.00 <sup>c</sup>

\* a - c represents significant differences among all samples at p < 0.05

## 4. Conclusions

We successfully grafted gelatin with cholesterol using cholesterol at from 10 - 50% (by mole of free amine groups in gelatin). The reduction of free amine groups increased with cholesterol contents. The cholesterol grafted gelatin micelles (CG50) entrapped curcumin were successfully prepared using simple dialysis method. The micelles had an average size of 112.39±1.18 nm with the curcumin loading efficiency of 1.77%wt. We are studying micelles at higher cholesterol contents (75-125% by mole). The effect of curcumin micelles in inhibition of tumor growth *in vitro* is currently under investigation.

## Acknowledgements

This work was supported partly by grants from National Nanotechnology Center (NANOTEC), National Science and Technology Development

Agency (NSTDA) Thailand and Chulalongkorn University Centenary Academic, (The Biomedical Engineering Development project).

## References

- [1] L. Song, Y. Shen, J. Hou, L. Lei, S. Guo and C. Qian, *Colloids Surf., A.* **390** (2011) 25-32.
- [2] P. Yoysungnoen, P. Wirachwong, P. Bhattarakosol, and S. Patumraj. *Clinical Hemorheology and Microcirculation.* **33** (2005) 127-136.
- [3] Y. J. Wang, M. H. Pan, A. L. Cheng, Y. S. Ho, L. I. Lin, C. Y. Hsieh and J. K. Lin. *J. Pharm. Biomed. Anal.* **15** (1997) 1867-1876.
- [4] T. Tanigo, R. Takaoka and Y. Tabata. *J. Controlled Release.* **143** (2010) 201-206.
- [5] A. Mukerjee and J. K. Vishwanatha. *Anticancer research.* **29** (2009) 3867-3876.
- [6] R. K. Das., N. Kasaju., and U. Bora. *Nanomedicine: Nanotechnology, Biology, and Medicine.* **6** (2010) 153-160.
- [7] Z. Song, R. Feng, M. Sun, C. guo, Y. Gao, L. Li and G. Zhai. *J. Colloid Interface Sci.* **354** (2011) 116-123.
- [8] J. Rujisomnana. *Modification of gelatin structure with cholesterol for curcumin delivery.* Master's Thesis, Chulalongkorn University, (2007).
- [9] M. Wareechuensook., Y. Tabata. and S. Kanokpanont. *Advanced Materials Research,* **93-94** (2010) 595-598.
- [10] G. T. Hermanson. *Bioconjugation, Academic Press ISBN.* 0-12-342336-8, (1996) 156.
- [11] R. J. Hall, N. Trinder and D. I. Givens. *Analyst.* **98** (1973) 673-686.
- [12] S. D. Allison, T. W. Randolph, M. C. Manning, K. Middleton, A. Davis and J. F. Carpenter. *Arch. Biochem. Biophys.* **358** (1998) 171-181.
- [13] Y. Dan-bo, Z. Jia-bi, H. Zhang-jian, R. Hai-xia and Z. Zeng-juan. *Colloids Surf., B.* **63** (2008) 192-199.
- [14] V. L. Furer. *J. Appl. Spectrosc.* **53** (1990) 860-863.
- [15] L-H Lin, K-M Chen, H-J Liu, H-C Chu, T-C Kuo, M-C Hwang and C-F Wang. *Colloids Surf., A.* **408** (2012) 97-103.

# PREPARATION AND PROPERTIES OF PLA/PCL COMPOSITE FOR BONE TISSUE ENGINEERING APPLICATION

Pai Timasart<sup>1,2</sup>, Nattawut Chaityut<sup>1,2\*</sup>

<sup>1</sup> Department of Materials Science and Engineering, Faculty of Engineering and Industrial Technology, Silpakorn University, Nakhon Pathom 73000, Thailand

<sup>2</sup> Center of Excellence on Petrochemical and Materials Technology, Chulalongkorn University, Bangkok 10330, Thailand

\* Author for correspondence; Email: nchaityut@hotmail.com, Tel. 034-219-363

**Abstract:** Poly(lactic acid) (PLA) and polycaprolactone (PCL) are well known as biopolymers for tissue engineering applications. In this study, polymer blends of PLA and PCL were prepared by solution method in various blending ratios of 95:5, 90:10 and 85:15. All blends were incorporated with NaCl at various contents of 75, 85, and 95%wt during solution blending process. Then polymer blends were compression molded to produce cylindrical specimens. After that the specimens underwent the salt leaching process to dissolve NaCl in order to provide a high porous scaffold. Factors affecting on morphology and mechanical and thermal properties of scaffold, which are size and volume of NaCl as well as blending ratio of PLA/PCL were studied. Compressive mechanical properties exhibit decreasing in modulus and strength with increasing NaCl contents, whereas size of NaCl does not affect on the properties. Furthermore, increasing PCL contents in blend shows rising in compressive modulus and strength of scaffold. Thermogravimetric analysis (TGA) and differential scanning calorimeters (DSC) data indicate that the factors show no significant effect on thermal properties. Scanning electron microscope (SEM) reveals that the greater amount of NaCl added the more porosity increased. Moreover, small pores and pore interconnection obviously increase with increasing PCL contents in the blend. In addition, all scaffolds exhibit very regular porous structure with homogeneously distributed and interconnected pores, which however depends on physical structure of NaCl particles.

## 1. Introduction

Bone tissue engineering is an interdisciplinary field that combines the knowledge and technology of materials that can be temporary substitute of damaged natural bone. An ideal scaffold should have following characteristics: (1) an extensive network of interconnecting pores; (2) channels through which oxygen and nutrients are provided to cells deeps inside scaffold, and the waste products can be easily carried away; (3) biocompatibility with a high affinity for cells to attach and proliferate; (4) right shape, however complex as desired by surgeon; and (5) appropriated mechanical strength and biodegradation profile [1]. Biodegradation polymers are widely used in the fabrication of scaffold because they posses suitable biocompatibility, biodegradation rate, mechanical properties and easy to process in variety of shapes and sizes.

PLA is a linear aliphatic thermoplastic polyester, produced from renewable resource and readily

biodegradable. It is produced by polymerization of lactides or lactic acid monomers that are from the fermentation of sugar feedstock [2]. PLA is versatile material with many applications including medical field because it possesses excellent mechanical properties but its brittleness and high price when compare with petroleum-based thermoplastics.

PCL is another non-toxic aliphatic polyester for biological tissues and suitable for many uses. Owing to its good compatibility and easy-processing capability, PCL has interesting compatibility with various polymers, making possible the preparation of blends. Unfortunately, PCL has hydrophobicity and slow degradation rate that might limit to be used as scaffold [3, 4].

Various methods have been used for the preparation of scaffold. In this study, we use method based on the leaching of soluble particulates, which was sodium chloride (NaCl). PLA/PCL blends with different PCL contents were prepared by solution method and all blends were incorporated with different NaCl contents during solution blending process. Then polymer blends were compression molded to produce cylindrical specimens. After that the specimens underwent the salt leaching process to dissolve NaCl away. Effect of PCL and NaCl contents on mechanical properties, thermal properties and porosity were investigated.

## 2. Materials and Method

### 2.1 Materials

Poly(lactic acid) (PLA; commercial grade 2002D; Mw  $\approx$  212,000 Da) was obtained from NatureWorks LLC. Polycaprolactone (PCL; Capa<sup>TM</sup> 6800; Mw  $\approx$  80,000 Da) was obtained from Perstorp Co.,Ltd. Sodium chloride (NaCl; Analytical grade; Sodium chloride 99%) was obtained from RCI Labscan Co.,Ltd. Dichloromethane and ethanol were purchased from Science Diagnostic Materials Co.,Ltd.

### 2.2 Preparation of polymer-salt composite

Each PLA and PCL pellets were dissolved in dichloromethane to obtain 10% w/v solution at room temperature. Then PCL solution was poured into PLA solution to get blend ratios of 95:5, 90:10 and 85:15. After the blend solution mixed well, salt particles (75 and 85% by weight) were added to the polymer solution. The salt particles were previously sieved to

get size ranges of 355-150, 250-150 and 150-106  $\mu\text{m}$ . Salt-incorporated polymer blend solutions were then precipitated into excess of ethanol. The solid polymer-salt composite could be separated from the non-solvent.

### 2.3 Preparation of porous structures

After drying, the precipitate was compression molded into cylinder-shape (8 mm in thickness, 17 mm in diameter) in a hot press (Compression molding machine; LP-5-50; Lab Tech; UK) operated at a 3.5 MPa, 175  $^{\circ}\text{C}$  and then rapidly cooled at room temperature.

The compression molded polymer-salt composite were gently stirred in distilled water for a while to leach out all the salt. The water was changed 2-3 times a day. The resulting porous polymer scaffold were dried for a period of 24 hr. and stored before use.

### 2.4 Scanning electron microscope

Characteristic of pore was examined by scanning electron microscope (SEM; JEOL; MX200; Japan) at an accelerating 15 kV. Samples were broken in liquid nitrogen and sputter coated with gold prior to observation.

### 2.5 Thermal analysis

Thermal analysis was measured by thermogravimetric analyzer (TGA; TGA7HT; Perkin Elmer; USA) and differential scanning calorimeter (DSC; Model Pyris 1; Perkin Elmer; USA). All measurements were performed under nitrogen atmosphere. In this study, the thermal degradation behavior of the samples was recorded in the range from room temperature to 400  $^{\circ}\text{C}$  at a rate 20  $^{\circ}\text{C}/\text{min}$ . DSC measurement was carried out by heating from room temperature to 200  $^{\circ}\text{C}$  at rate of 10  $^{\circ}\text{C}/\text{min}$ . The crystallinity was calculated by Eq. (1).

$$X_c [\%] = \frac{100 \times (\Delta H_m + \Delta H_c)}{93 \times X_{\text{PLA}}} \quad (1)$$

Where  $\Delta H_m$  and  $\Delta H_c$  are the enthalpy of melting crystallization of PLA, respectively, Enthalpy of fusion of PLA is 93 J/g.  $X_{\text{PLA}}$  is the weight fraction of PLA [4].

### 2.6 Determination of porosity

The density and porosity of the porous scaffolds were determined by measuring the dimensions and the mass of the scaffolds was calculated as follows:

$$d = \frac{m}{V} \quad (2)$$

Where  $m$  is the mass and  $V$  is the volume of the porous scaffold.

The porosity of the porous scaffold,  $p_o$ , was calculated by Eq. (3).

Where  $d_p$  is the density of non-porous polymer, compression molded in the same manner.

### 2.7 Mechanical property

The compressive mechanical property was measured by universal testing machine (LR50 K; LLOYD Instruments; UK). Ten samples of each composition were tested. The compression tests were carried out at a loading rate of 2.5 mm/min until a maximum reduction in sample's height of 75%. The Young's modulus was calculated as the slope of the initial linear region of the stress-strain curve.

## 3. Results and Discussion

### 3.1 Scanning electron microscopy

Fig. 1 and Fig. 2 present the SEM micrographs of scaffold cross-sections. The scaffolds have homogeneously distributed and interconnected pores. The shape and size of pores depend on the characteristic of NaCl particles. The porosity strongly depends on NaCl content.

Ideal scaffold should have pore size at least 100  $\mu\text{m}$  for successful diffusion of essential nutrients and oxygen for cell survivability and pore size in the range of 200-350  $\mu\text{m}$  are optimum for bone tissue ingrowth [10].

From SEM micrographs, it is obvious that scaffolds with composed of NaCl in particle size of 250-150  $\mu\text{m}$  gave optimum pore size. The porous wall of PLA/PCL blends appears rougher than that of neat PLA because PCL was immiscible with PLA, which could be advantage because scaffolds should rule both micro and macro porosities [10].

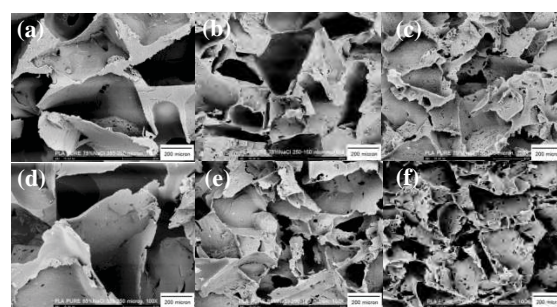


Fig 1. SEM micrographs of:

- (a) Neat PLA with 75% wt. of 355-250  $\mu\text{m}$  NaCl
- (b) Neat PLA with 75% wt. of 250-150  $\mu\text{m}$  NaCl
- (c) Neat PLA with 75% wt. of 150-106  $\mu\text{m}$  NaCl
- (d) Neat PLA with 85% wt. of 355-250  $\mu\text{m}$  NaCl
- (e) Neat PLA with 85% wt. of 250-150  $\mu\text{m}$  NaCl
- (f) Neat PLA with 85% wt. of 150-106  $\mu\text{m}$  NaCl at 100X magnification



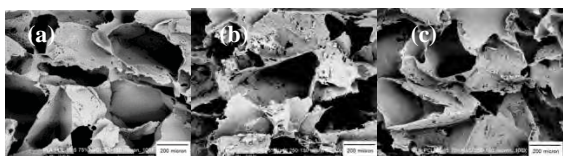


Fig 2. SEM micrographs of:  
 (a) 95:5 PLA:PCL blend with  
 with 75% wt. of 250-150  $\mu\text{m}$  NaCl  
 (b) 90:10 PLA:PCL blend with  
 with 75% wt. of 250-150  $\mu\text{m}$  NaCl  
 (c) 85:15 PLA:PCL blend with  
 with 75% wt. of 250-150  $\mu\text{m}$  NaCl  
 at 100X magnification

### 3.2 Thermal analysis

Table 1: TGA results of neat PCL, neat PLA, PLA/PCL blends and PLA/PCL blends with NaCl.

Samples		Onset Temp.	T <sub>d</sub> (°C)
Neat PCL	0% NaCl	396.36	426.10
Neat PLA	0% NaCl	349.63	373.54
	75% NaCl(1)	325.24	347.17
	75% NaCl(2)	320.11	343.04
	75% NaCl(3)	324.27	346.58
	85% NaCl(1)	319.20	340.60
	85% NaCl(2)	316.89	339.28
PLA:PCL 95:5	85% NaCl(3)	314.89	334.01
	0% NaCl	345.85	364.46
	75% NaCl(1)	319.38	340.64
	75% NaCl(2)	321.52	343.19
	75% NaCl(3)	319.06	341.73
	85% NaCl(1)	320.42	341.46
PLA:PCL 90:10	85% NaCl(2)	306.28	333.17
	85% NaCl(3)	312.26	339.77
	0% NaCl	343.53	362.46
	75% NaCl(1)	310.67	340.64
	75% NaCl(2)	312.47	343.19
	75% NaCl(3)	312.33	341.73
PLA:PCL 85:15	85% NaCl(1)	304.61	341.46
	85% NaCl(2)	300.32	333.17
	85% NaCl(3)	304.10	339.77
	0% NaCl	344.76	364.86
	75% NaCl(1)	311.80	335.29
	75% NaCl(2)	318.20	337.64
PLA:PCL 85:15	75% NaCl(3)	317.40	340.35
	85% NaCl(1)	317.45	342.04
	85% NaCl(2)	319.17	340.04
	85% NaCl(3)	299.13	325.27

\* (1), (2) and (3) are NaCl with particle size of

355-250  $\mu\text{m}$ , 250-150  $\mu\text{m}$  and 150-106  $\mu\text{m}$ , respectively.

The thermal stability and degradation temperature of neat PLA exhibits lower than neat PCL, whereas the thermal stability and degradation temperature of blends are similar to neat PLA. It is evident that PCL content does not effect on thermal stability. Porous PLA/PCL blends have lower density than non-porous one that makes better heat distribution. Therefore, incorporation of NaCl, that produce pore in blends, affects lower thermal stability but size and volume of NaCl not effect on this property.

Table 2: Density of neat PCL, neat PLA, PLA/PCL blends and PLA/PCL blends with NaCl.

Samples		Density
Neat PLA	0% NaCl	1.0721
	75% NaCl(1)	0.4246
	75% NaCl(2)	0.3893
	75% NaCl(3)	0.4254
	85% NaCl(1)	0.2361
	85% NaCl(2)	0.2589
PLA:PCL 95:5	85% NaCl(3)	0.2606
	0% NaCl	0.9937
	75% NaCl(1)	0.4066
	75% NaCl(2)	0.4062
	75% NaCl(3)	0.3879
	85% NaCl(1)	0.2378
PLA:PCL 90:10	85% NaCl(2)	0.2296
	85% NaCl(3)	0.2258
	0% NaCl	0.9800
	75% NaCl(1)	0.3615
	75% NaCl(2)	0.3472
	75% NaCl(3)	0.3615
PLA:PCL 85:15	85% NaCl(1)	0.2207
	85% NaCl(2)	0.2041
	85% NaCl(3)	0.1849
	0% NaCl	1.0005
	75% NaCl(1)	0.3467
	75% NaCl(2)	0.3449
PLA:PCL 85:15	75% NaCl(3)	0.3260
	85% NaCl(1)	0.2093
	85% NaCl(2)	0.2129
	85% NaCl(3)	0.1834

The glass transition temperature of PLA and PCL are 55-60 and -60 °C , the melting temperature 60-62 and 150-160 °C , respectively [11,12].The DSC

analysis showed that glass transition temperature ( $T_g$ ) and melting temperature ( $T_m$ ) of PLA/PCL blends are similar to neat PLA suggested that NaCl content, NaCl particle size and PCL content are no significant effect on thermal properties. The crystallinity of PLA in PLA/PCL blends is higher than neat PLA indicating that crystallization of PLA activated by PCL blending. Furthermore, size and volume of NaCl is no significant effect on this property. Crystallinity of PCL are not interested because melting temperature of PCL include in the same region with glass transition temperature of PLA that effect to accuracy of calculated crystallinity.

Table 3: DSC results neat PLA, PLA/PCL blends and PLA/PCL blends with NaCl.

Samples		$T_g$ ( $^{\circ}\text{C}$ )	$T_m$ ( $^{\circ}\text{C}$ )	$X_{c,PLA}$ (%)
Neat PLA	0% NaCl	63.35	152.96	31.42
	75% NaCl(1)	69.94	153.06	28.71
	75% NaCl(2)	68.18	155.26	48.28
	75% NaCl(3)	68.51	153.59	29.40
	85% NaCl(1)	68.96	152.12	37.47
	85% NaCl(2)	75.36	154.10	40.90
	85% NaCl(3)	69.63	153.31	30.72
PLA:PCL 95:5	0% NaCl	66.07	157.88	62.27
	75% NaCl(1)	70.30	153.78	50.65
	75% NaCl(2)	69.45	155.25	46.75
	75% NaCl(3)	75.43	154.12	49.93
	85% NaCl(1)	75.86	153.12	47.83
	85% NaCl(2)	67.58	153.13	49.12
	85% NaCl(3)	68.08	153.78	48.97
PLA:PCL 90:10	0% NaCl	65.28	155.87	31.38
	75% NaCl(1)	69.30	154.30	55.76
	75% NaCl(2)	68.57	154.26	47.01
	75% NaCl(3)	68.83	155.13	54.46
	85% NaCl(1)	68.09	154.43	53.02
	85% NaCl(2)	66.59	154.59	53.67
	85% NaCl(3)	66.07	153.96	58.73
PLA:PCL 85:15	0% NaCl	67.06	152.08	63.64
	75% NaCl(1)	68.78	154.95	55.79
	75% NaCl(2)	69.05	155.12	61.55
	75% NaCl(3)	68.94	153.63	64.60
	85% NaCl(1)	69.18	155.24	71.44
	85% NaCl(2)	68.28	154.62	58.99
	85% NaCl(3)	65.22	154.63	55.76

### 3.3 Mechanical property

All stress-strain curves represent characteristics of porous polymer foam: a linear elastic region appeared at small strain, followed by a plateau region at larger

strain and a solidify region where the stress increased sharply at very large strain [4]. The compressive modulus of polymeric scaffold decreases with increasing porosity (increasing NaCl content). The results agree well with the theory, which is in heterogeneous porous structure, pore could affect the compression modulus [5]. As in this study the dependence of the compressive modulus on the pore size is negligible. Moreover, the results show that PLA/PCL blends give higher compressive modulus than neat PLA. Due to PLA have brittle behavior which opposite to ductile behavior of PCL, suggesting that the existence of PCL tends to enhance ability of absorb and distribute load.

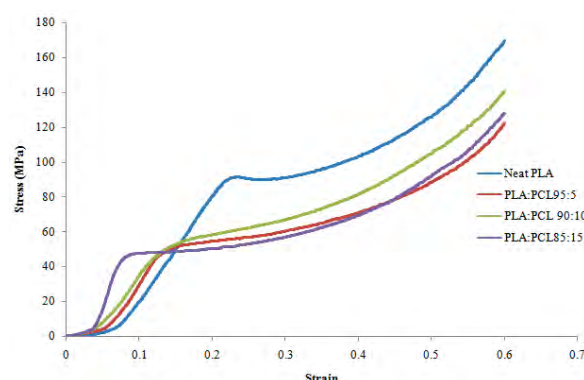


Fig 3. Stress-strain curve of neat PLA and PLA/PCL blends

## 4. Conclusions

The porous PLA/PCL composite scaffolds and pure PLA scaffold were prepared by coagulation, compression molding and salt leaching method. SEM images reveal that scaffolds have high porosities and interconnected pore networks. Porosity and pore size can be controlled by variation of salt content and salt particle, respectively. DSC and TGA tests show that PCL content, NaCl content and particle size of NaCl, are not significant effect on thermal properties. The compressive modulus decreases with increasing in porosity but it is independent of pore size. Moreover, the compressive modulus is found to be increased by blending with PCL. The results suggest that PLA/PCL composite scaffolds might be promising materials for bone engineering applications.

## Acknowledgements

The authors would like to thank Department of Materials Science and Engineering, Silpakorn University and Center of Excellence on Petrochemical and Materials Technology, Chulalongkorn University for financial support.

## References

- [1] C. Liu, Z. Xia and J.T. Czernuszka, *DESIGN AND DEVELOPMENT OF THREE-DIMENSIONAL SCAFFOLDS FOR TISSUE ENGINEERING*. Vol 85(A7), Trans IChemE, Part A, Chemical Engineering Research and Design, 2007, pp. 1051-1064.
- [2] Lunt J., *Polym Degrad Stab*, Vol 59, 1998, pp. 145-52.
- [3] F. Rezgui, M. Swistek, J.M. Hiver, C. G'Sell, T. Sadoun, *Deformation and damage upon stretching of degradable polymers (PLA and PCL)*, *Polymer* 46 (2005), pp.7370-7385.
- [4] Fan Wu, Changsheng Liu, Brian O'Neill, Jie Wei, Yung Ngothai, *Fabrication and properties of porous scaffold of magnesium phosphate/polycaprolactone biocomposite for bone tissue engineering*, *Applied Surface Science* 258 (2012), pp. 7589-7595
- [5] Qingpu Hou, Dirk W., Grijpma, Jan Feijen, *Porous polymeric structures for tissue engineering prepared by a coagulation, compression moulding and salt leaching technique*, *Biomaterials* 24 (2003), pp. 1937-1947
- [6] Chien-Chung Chen, Ju-Yu Chueh, How Tseng, Haw-Ming Haung, Sheng-Yang Lee, *Preparation and characterization of biodegradable PLA polymeric blends*, *Biomaterials* 24 (2003), pp. 1167-1173
- [7] Ferenc Tuba, László Oláh, Péter Nagy, *Characterization of reactively compatibilized poly(D,L-lactide)/poly( $\epsilon$ -caprolactone) biodegradable blends by essential work of fracture method*, *Engineering Fracture Mechanics* 78 (2011), pp.3123-3133
- [8] V. Vilay, M. Mariatti, Zulkifli Ahmah, K. Pasomsouk, Mitsugu Todo, *Improvement of microstructures and properties of biodegradable PLLA and PCL blends compatibilized with triblock copolymer*, *Materials Science and Engineering A* 527 (2010), pp. 6930-6937
- [9] M. Todo, S.-D. Park, T. Takayama, K. Arakawa, *Fracture micromechanisms of bioabsorbable PLLA/PCL polymer blends*, *Engineering Fracture Mechanics* 74 (2007), pp. 1872-1883
- [10] Susmita Bose, Mangal Roy, Amit Banyopadhyay, *Recent advances in bone tissue engineering scaffolds*, Vol 30, *Trends in Biotechnology*, 2012, pp. 546-5
- [11]<http://www.buckell.com/engineering/PLA%202002d.pdf> (Retrieved September 2, 2012).
- [12]<http://photos.imageevent.com/bolt/plastics/Processing%20CAPA%20Thermoplastics%20Pp.pdf> (Retrieved September 2, 2012).

# SYNTHESIS OF MCM-48 MAGNETIC NANOPARTICLE COMPOSITES FOR REMOVAL OF MERCURY(II) IONS

Sumitra Khonsa-nga<sup>1\*</sup>, Numpon Insin<sup>2</sup>, Fuangfa Unob<sup>2\*</sup>

<sup>1</sup>Program of Petrochemistry and Polymer Science, Faculty of Science, Chulalongkorn University, Bangkok, 10330, Thailand

<sup>2</sup>Department of Chemistry, Faculty of Science, Chulalongkorn University, Bangkok, 10330, Thailand

\*E-mail: flu\_aor\_ride@hotmail.com (S.Khonsa-nga), fuangfa.u@chula.ac.th (F.Unob)

**Abstract:** The purpose of this work is to develop new MCM-48 based sorbents which have magnetic properties and abilities for Hg(II) ion adsorption by using  $\gamma$ -Fe<sub>2</sub>O<sub>3</sub> nanoparticles for the effective separation of sorbents from aqueous media. The synthesized MCM-48 showed as large surface area as 920 m<sup>2</sup>/g. Monodisperse  $\gamma$ -Fe<sub>2</sub>O<sub>3</sub> nanoparticles were synthesized using iron-oleate complex as starting materials.  $\gamma$ -Fe<sub>2</sub>O<sub>3</sub> nanoparticles showed high magnetic response with particles size of 5-12 nm as monitored by TEM. Composites of MCM-48 and  $\gamma$ -Fe<sub>2</sub>O<sub>3</sub> nanoparticles were prepared by mixing MCM-48 with  $\gamma$ -Fe<sub>2</sub>O<sub>3</sub> nanoparticles of various amount ranging from 40-70 %w/w in hexane. SEM images revealed the particles size of  $\gamma$ -Fe<sub>2</sub>O<sub>3</sub> nanoparticles and MCM-48 composites ( $\gamma$ -Fe<sub>2</sub>O<sub>3</sub>@MCM-48) to be 244±40 nm in diameter.  $\gamma$ -Fe<sub>2</sub>O<sub>3</sub>@MCM-48 prepared by using 40, 50, 60 and 70 %w/w  $\gamma$ -Fe<sub>2</sub>O<sub>3</sub> nanoparticles showed surface area of 846, 777, 806 and 803 m<sup>2</sup>/g, respectively, which are slightly different from each other. All of  $\gamma$ -Fe<sub>2</sub>O<sub>3</sub>@MCM-48 were further functionalized with 3-(mercaptopropyl)-trimethoxysilane(3-MP). All of 3-MP- $\gamma$ -Fe<sub>2</sub>O<sub>3</sub>@MCM-48 prepared by using 40-70 %w/w  $\gamma$ -Fe<sub>2</sub>O<sub>3</sub> nanoparticles successfully adsorbed Hg(II) ions. At pH 5, Hg(II) ions were removed with high removal efficiency (> 99%) from 10 mg/L Hg(II) solution. The results suggest that  $\gamma$ -Fe<sub>2</sub>O<sub>3</sub>@MCM-48 can be used as an adsorbent for efficient removal of mercury ions from aqueous solutions.

## 1. Introduction

Nowadays, heavy metals are widely used in petrochemical industry as catalysts and reagents in production process, causing contaminations and accumulations of heavy metals in an environment [1]. Some heavy metals, especially mercury, can accumulate in human body and have adverse effects on human health both acute and chronic poisoning after being exposed [2]. The toxicity of mercury includes damaging of brain and other associated functions and potentially causing of death [3]. Therefore, several methods for removing of mercury ions from wastewater such as adsorption [4], chemical precipitation [5], ion-exchange [6,7], and coprecipitation [8] have been studied. Adsorption is one of the most popular techniques for this purpose because of its simplicity and low operating cost [9]. Some functionalized mesoporous silica including SBA-15 and MCM-41 [10] are used as sorbents for mercury ions adsorption due to their large surface area. However, one of major drawbacks of using these

materials is when they are used in water treatment application they encountered some difficulties in separation from water due to their small particle sizes. For this reason, development of new sorbents by addition of magnetic properties to MCM-48 in order to easily separate these solids from water by applying an external magnetic field is studied.

MCM-48 is an attractive candidate as sorbents since its cubic structure provides 3-dimensional channels and exceptionally high surface area [11,12].  $\gamma$ -Fe<sub>2</sub>O<sub>3</sub> nanoparticles are superparamagnetic materials with great physical and chemical stabilities and low toxicity thus,  $\gamma$ -Fe<sub>2</sub>O<sub>3</sub> nanoparticles are chosen in this study for the synthesis of MCM-48 and magnetic nanoparticle composites ( $\gamma$ -Fe<sub>2</sub>O<sub>3</sub>@MCM-48).

In this work, new MCM-48 sorbents with magnetic properties and ability for Hg(II) ion adsorption are prepared and surface modification of the composites with 3-(mercaptopropyl)-trimethoxysilane for Hg(II) ions adsorption was also performed.

## 2. Materials and method

### 2.1 Chemicals and apparatus

**Chemicals:** Hexadecyltrimethyl ammonium bromide (CTAB) was obtained from Fluka. Tetraethoxysilane (TEOS) was purchased from ACROS ORGANICS. 1-Octadecene, oleic acid, NaOH, ethanol and mercury(II) standard solution were purchased from Merck. 3-(Mercaptopropyl)-trimethoxysilane (MP) and hexane was distributed from Sigma-Aldrich and CarLo Eaba, respectively. Iron (III) chloride (FeCl<sub>3</sub>) was purchased from Fisher Scientific.

**Apparatus:** X-ray diffraction (XRD) patterns of the prepared materials were recorded on a Rigaku DMAX 2200/Ultima<sup>+</sup> diffractometer. The determination of BET surface area and pore diameters by N<sub>2</sub> sorption was performed on a surface area analyzer (BEL Japan BELSORP-Mini). Transmission electron microscopy (TEM) images and scanning electron microscopy (SEM) images of the composites were obtained using JEM-2100 microscope and JOEL (JSM-5410LV) microscope, respectively. Mercury ion concentration was monitored by cold vapor atomic absorption spectrometer (FIAS-100 Perkin Elmer).



## 2.2 Preparation of MP-Fe<sub>2</sub>O<sub>3</sub>@MCM-48 composites

The procedure for MP-Fe<sub>2</sub>O<sub>3</sub>@MCM-48 preparation includes three steps: the synthesis of MCM-48 and  $\gamma$ -Fe<sub>2</sub>O<sub>3</sub> magnetic nanoparticles, the synthesis of  $\gamma$ -Fe<sub>2</sub>O<sub>3</sub>@MCM-48 composites and the modification of MP onto the composite (MP-Fe<sub>2</sub>O<sub>3</sub>@MCM-48). In the first step, MCM-48 and  $\gamma$ -Fe<sub>2</sub>O<sub>3</sub> magnetic nanoparticles were prepared. MCM-48 was prepared using a stepped template sol-gel method described by Gies et al. [13] with some modifications. In this method, NaOH was dissolved in a bottle and then CTAB solution was added under continuous stirring for 15 min. Tetraethoxysilane (TEOS) was added drop-wise and the mixture was stirred and heated at 40-50°C. The composition of the gel mixture was 1(TEOS):0.70(CTAB):0.5(NaOH):64H<sub>2</sub>O. The gel mixture was crystallized at 90 °C in an oven for 4 days. The obtained crystalline product was washed with de-ionized water, dried overnight and then washed again with a solution of water, ethanol, HCl in mol ratio of 90:5:10. The solid was dried at room temperature. After purification, white powder was obtained. Before used in the next step, the powder was calcined at 540°C for 5 hours to remove the template.

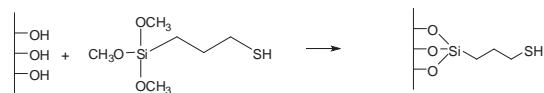
$\gamma$ -Fe<sub>2</sub>O<sub>3</sub> nanoparticles were synthesized using a two-stepped procedure modified from the report by Park et al. [14]. In this process, iron-oleate complex was used as starting materials, and oleic acid was used as surfactant. For the preparation of iron-oleate complex, 24 mmol Na-oleate and 8 mmol iron(III) chloride were first dissolved in a mixed solvent of 16 ml ethanol, 12 ml distilled water and 28 ml hexane. The solution was refluxed at 70°C for 4 hours. After refluxing, the mixture was divided into two layers. Iron-oleate solution in the upper layer was washed with 6 ml distilled water for three times in a separation funnel. Hexane in this phase was removed by evaporation, and subsequently iron-oleate complex as a waxy solid was obtained. Then, 8 mmol of the as-synthesized iron-oleate complex and 4 mmol of oleic acid were added to 20 g of 1-octadecene. The mixture was heated to 320°C with a rate of 3.3°C/min and maintained at 320°C for 30 min. After heating, the solution became a brownish-black turbid solution containing nanocrystals. The mixture was cooled to room temperature and the nanocrystals were then separated out of the mixture by centrifugation.

For the second step, The  $\gamma$ -Fe<sub>2</sub>O<sub>3</sub>@MCM-48 composites were synthesized. In this step, the as-synthesized MCM-48 (1 g) was mixed with  $\gamma$ -Fe<sub>2</sub>O<sub>3</sub> nanoparticles of various amount within the range of ranging 0.4 to 0.7 g dispersed in hexane (40-70% of MCM-48 weight). The mixture was stirred at room temperature for 4 hours and then hexane was evaporated. The obtained brown solid was washed with hexane and 6M HNO<sub>3</sub> and dried overnight.

Finally,  $\gamma$ -Fe<sub>2</sub>O<sub>3</sub>@MCM-48 surface was modified with MP.  $\gamma$ -Fe<sub>2</sub>O<sub>3</sub>@MCM-48 was immersed in dried toluene and MP was added with ratio of 20 mmol of MP : 1 g of  $\gamma$ -Fe<sub>2</sub>O<sub>3</sub>@MCM-48. The suspension was refluxed under nitrogen atmosphere for 5 hours and the solid was separated from solvent using a permanent

magnet. Then the solid was washed with ethanol and was dried at 120°C overnight to yield mercapto-functionalized  $\gamma$ -Fe<sub>2</sub>O<sub>3</sub>@MCM-48 (MP-Fe<sub>2</sub>O<sub>3</sub>@MCM-48).

Reaction of mercaptopropyltrimethoxysilane with silanol group on the surface of  $\gamma$ -Fe<sub>2</sub>O<sub>3</sub>@MCM-48 is shown in Scheme 1.



Scheme 1. Reaction of MP with  $\gamma$ -Fe<sub>2</sub>O<sub>3</sub>@MCM-48

## 2.3 Procedure for Hg (II) adsorption

A portion of 10 mg MP-Fe<sub>2</sub>O<sub>3</sub>@MCM-48 and 50 ml 0.01M NaNO<sub>3</sub> solution containing mercury ions 5 and 10 mg/L were stirred at pH 5 for 1 hour. NaNO<sub>3</sub> solution was used to control the ionic strength of the solution. After adsorption, MP-  $\gamma$ -Fe<sub>2</sub>O<sub>3</sub>@MCM-48 was separated from solution using a permanent magnet while the concentrations of mercury ions in the remaining solution were analyzed by a cold vapor atomic absorption spectrometer.

The adsorption efficiency (R, %) and the amount of Hg adsorbed on adsorbent (Q, mg/g) were calculated according to the Eq. (1) and (2):

$$R = \frac{C_0 - C}{C_0} \times 100 \quad (1)$$

$$Q = \frac{(C_0 - C)V}{W} \quad (2)$$

where  $C_0$  is the initial concentration,  $C$  is the final concentration of Hg(II) ions in mg/L,  $V$  is the solution volume in L and  $W$  is the weight in g of the  $\gamma$ -Fe<sub>2</sub>O<sub>3</sub>@MCM-48.

## 3. Results and Discussion

### 3.1 Characterization

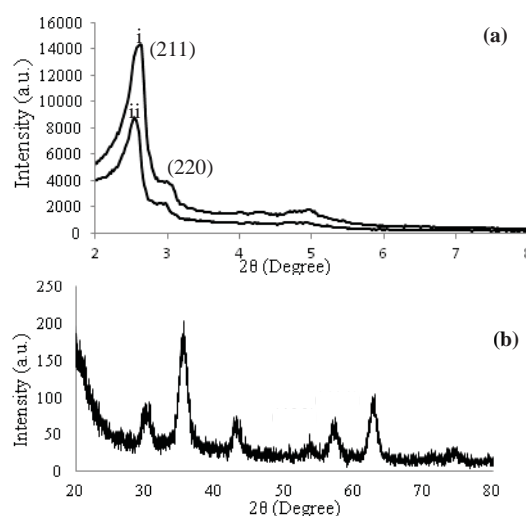


Figure 1. XRD patterns of (a) MCM-48(i) and 40% $\gamma$ -Fe<sub>2</sub>O<sub>3</sub>@MCM-48 composites (ii), and (b)  $\gamma$ -Fe<sub>2</sub>O<sub>3</sub> nanoparticles.

At low diffraction angle, XRD patterns of MCM-48 that was synthesized by a stepped template sol-gel method is shown Figure 1.(a). The MCM-48 XRD pattern (i) displays intensive diffraction peaks 211 and 220 in the  $2\theta$  range of 2-8 degree, which were assigned to three-dimensional mesoporous structure with a cubic space group [15]. Furthermore, peaks between  $2\theta$  of 4-8 degree can be indexed and correspond to the MCM-48 structure [16].

The XRD pattern of  $\gamma\text{-Fe}_2\text{O}_3\text{@MCM-48}$  composites (ii) also displays the characteristic low-angle reflection of the MCM-48 structure indicating that cubic structure of MCM-48 was preserved with some less define peaks. In high-angle region ( $2\theta$  ranging from 20 to 70 degree, Figure 1.(b)), the diffraction patterns in which six low intensity diffraction peaks 220, 311, 400, 422, 511 and 440 which are indexed to the  $\gamma\text{-Fe}_2\text{O}_3$  were observed [17]. As a result, XRD patterns indicated the co-existence of  $\gamma\text{-Fe}_2\text{O}_3$  phase in the MCM-48 structure.

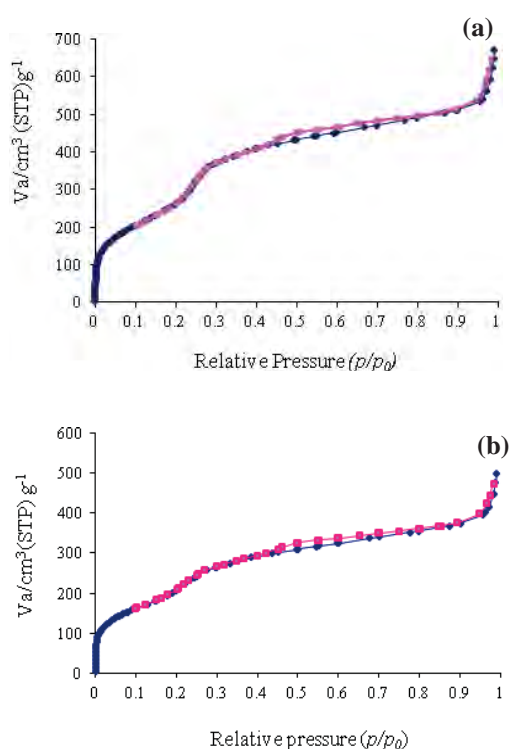


Figure 2. Nitrogen sorption isotherms of (a) as-synthesized MCM-48 and (b) 40% $\gamma\text{-Fe}_2\text{O}_3\text{@MCM-48}$  composites.

Isotherms of nitrogen sorption by MCM-48 and  $\gamma\text{-Fe}_2\text{O}_3\text{@MCM-48}$  are shown in Figure 2. These results were used to calculate the specific surface area by Brunauer Emmett Teller method, BET ( $S_{\text{BET}}$ ) and average pore diameter. Defined step occurs between  $P/P_0 = 0.1$  and 0.3, indicating the filling into mesoporous structure. The nitrogen sorption isotherms of (a) MCM-48 and (b)  $\gamma\text{-Fe}_2\text{O}_3\text{@MCM-48}$  composites were type IV according to the IUPAC nomenclature [18], confirming that the MCM-48 and the composites were mesoporous materials.

BET surface area and pore size of MCM-48 was  $920.08 \text{ m}^2/\text{g}$  and  $3.6 \text{ nm}$ , respectively, as shown in Table 1. After preparing  $\gamma\text{-Fe}_2\text{O}_3\text{@MCM-48}$  composites using 40-70% w/w of  $\gamma\text{-Fe}_2\text{O}_3$ , the BET surface area of the sorbents decreased most likely due to the presence of  $\gamma\text{-Fe}_2\text{O}_3$  on the surface which partially blocked the adsorption of nitrogen molecules into the channels of MCM-48.

Table 1: Surface area and pore diameter of the materials

Materials	BET surface area ( $\text{m}^2/\text{g}$ )	Pore diameter (nm)
MCM-48	920	3.7
40 % $\gamma\text{-Fe}_2\text{O}_3\text{@MCM-48}$	846	4.4
50 % $\gamma\text{-Fe}_2\text{O}_3\text{@MCM-48}$	777	4.1
60 % $\gamma\text{-Fe}_2\text{O}_3\text{@MCM-48}$	806	4.0
70 % $\gamma\text{-Fe}_2\text{O}_3\text{@MCM-48}$	803	3.9

These results indicate that  $\gamma\text{-Fe}_2\text{O}_3$  nanoparticles were deposited and incorporated into the sorbents and the pore systems of MCM-48 framework are still accessible.

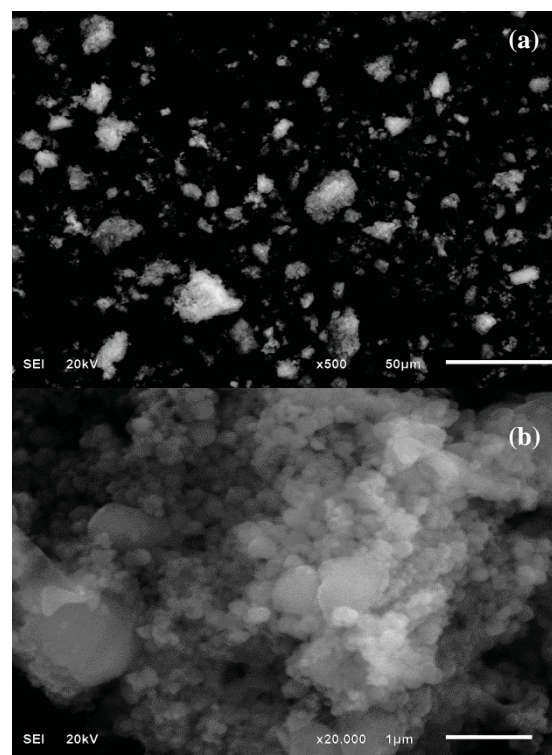


Figure 3. SEM images of 40% $\gamma\text{-Fe}_2\text{O}_3\text{@MCM-48}$  composites with (a) low and (b) high magnifications.

The SEM images of  $\gamma\text{-Fe}_2\text{O}_3\text{@MCM-48}$  Figure 3 revealed the spherical particles and particles size of  $\gamma\text{-Fe}_2\text{O}_3\text{@MCM-48}$  of  $244 \pm 40 \text{ nm}$  in diameter and showed some aggregations of the dried particles of the composites.

The TEM images of  $\gamma\text{-Fe}_2\text{O}_3\text{@MCM-48}$  composites are shown in Figure 4. The TEM images suggested that  $\gamma\text{-Fe}_2\text{O}_3$  nanoparticles can be deposited onto MCM-48 and displayed  $\gamma\text{-Fe}_2\text{O}_3$  particles size of 5-12 nm on outer surface.

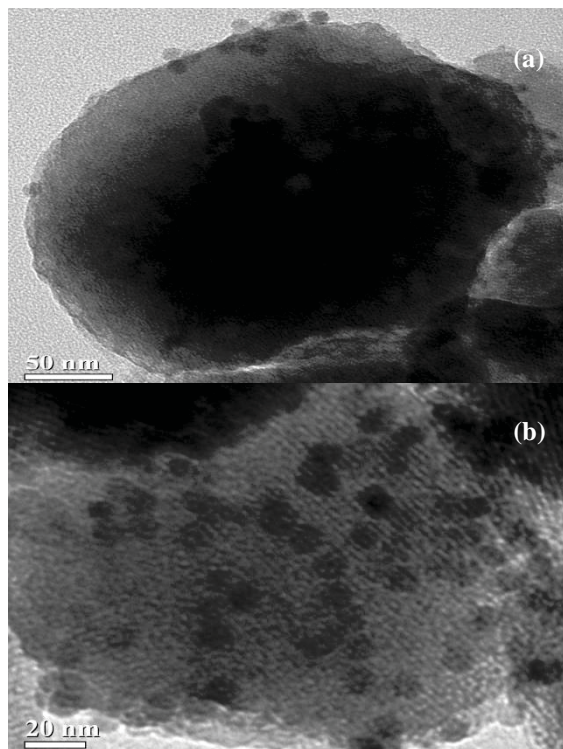


Figure 4. TEM images of 40%  $\gamma\text{-Fe}_2\text{O}_3\text{@MCM-48}$  composites with (a) low and (b) high magnifications.

### 3.2 Adsorption of Hg by MP- $\text{Fe}_2\text{O}_3\text{@MCM-48}$

MP- $\text{Fe}_2\text{O}_3\text{@MCM-48}$  could adsorb Hg ions from 10 mg/L Hg (II) solution with high adsorption efficiency (> 99%) as shown in Table 2. It is due to the strong affinity of S atom containing in MP towards Hg ions.

Table 2: Adsorption efficiency of MP- $\text{Fe}_2\text{O}_3\text{@MCM-48}$  composites prepared using different amount of  $\gamma\text{-Fe}_2\text{O}_3$

Material	R, %	Q, mg/g
40 % $\gamma\text{-Fe}_2\text{O}_3\text{@MCM-48}$	99.96	48.48
50 % $\gamma\text{-Fe}_2\text{O}_3\text{@MCM-48}$	99.95	48.48
60 % $\gamma\text{-Fe}_2\text{O}_3\text{@MCM-48}$	99.90	48.48
70 % $\gamma\text{-Fe}_2\text{O}_3\text{@MCM-48}$	99.88	48.47

In Table 2,  $R$  is the adsorption efficiency and  $Q$  is the amount of Hg adsorbed on adsorbent MP- $\text{Fe}_2\text{O}_3\text{@MCM-48}$  in mg/g.

The results from experiments suggest that MP- $\text{Fe}_2\text{O}_3\text{@MCM-48}$  composites can be used as effective sorbents for mercury ion removal from aqueous solution. According to the adsorption, MP- $\text{Fe}_2\text{O}_3\text{@MCM-48}$  prepared using 40 % w/w of  $\gamma\text{-Fe}_2\text{O}_3$  was chosen because it show high adsorption efficiency

with least quantities of  $\gamma\text{-Fe}_2\text{O}_3$  while magnetic separation is still achievable. Adsorption parameters, adsorption isotherm and reusability of  $\gamma\text{-Fe}_2\text{O}_3\text{@MCM-48}$  are further studied.

## 4. Conclusion

New magnetic  $\gamma\text{-Fe}_2\text{O}_3\text{@MCM-48}$  composites with high surface area and high magnetic response were successfully prepared. After functionalization, the sorbents MP- $\text{Fe}_2\text{O}_3\text{@MCM-48}$  can be used as a highly effective sorbents for removal of mercury with ability for magnetic separation.

## Acknowledgement

This study was financially supported by Environmental Analysis Research Unit (EARU), Department of Chemistry and the Program of Petrochemistry and Polymer Science, Faculty of Science, Chulalongkorn University.

## References

- [1] A.T. Reis, S.M. Rodrigues, C. Araújo, J.P. Coelho, E. Pereira and A.C. Duarte, *Sci. Total Environ.* **407** (2009) 2689-2700.
- [2] R.A. Bernhoft, *J. Environ. Publ. Health.* **2012** (2012) 1-10.
- [3] T.M. Clarkson and L. Magos, *Crit. Rev. Toxicol.* **36** (2006) 609-622.
- [4] C. Namasivayam and K. Periasamy, *Water Res.* **27** (1993) 1663-1668.
- [5] M.M. Matlock, B.S. Howerton and D.A. Atwood, *Water Res.* **36** (2002) 4757-4764.
- [6] A. Oehmen, R. Viegas, S. Velizarov, M.A.M. Reis and J.G. Crespo, *Desalination.* **199** (2006) 405-407.
- [7] A.A. Khan and Inamuddin, *Sensors Actuat. B.* **120** (2006) 10-18.
- [8] K. Larison and J. Wiencek, *Ind. Eng. Chem. Res.* **31** (1992) 2714.
- [9] X. Chen, K.F. Lam and K.L. Yeung, *Chem. Eng. J.* **172** (2011) 728-734.
- [10] D.P. Quintanilla, I.d.Hierro, M. Fajardo and I. Sierra, *Micropor. Mesopor. Mater.* **89** (2006) 58-68.
- [11] S.G. Wang and J.L. Li, *Chinese Chem. Lett.* **17** (2006) 221-224.
- [12] K. Schumacher, M. Grün and K.K. Unger, *Micropor. Mesopor. Mater.* **27** (1999) 201-206.
- [13] H. Gies, S. Grabowski, M. Bandyopadhyay, W. Grünert, O.P. Tkachenko, K.V. Klementiev and A. Birkner, *Micropor. Mesopor. Mater.* **60** (2003) 31-42.
- [14] J. Park, K. An, Y. Hwang, J.G. Park, H.J. Noh, J.Y. Kim, J.H. Park, N.M. Hwang and T. Hyeon, *Nature Mater.* **3** (2004) 891-895.
- [15] O. Olkhoviyk, V. Antochshuk and M. Jaroniec, *Colloid. Surf. A: Physicochem. Eng. Aspects.* **236** (2004) 69-72.
- [16] A.A. Romero, M.D. Alba, W. Zhou and J. Klinowski, *J. Phys. Chem. B.* **101** (1997) 5294-5300.
- [17] S. Brunauer, L.S. Deming, W.S. Deming and E. Teller, *J. Am. Chem. Soc.* **62** (1940) 1723.
- [18] V.R. Elias, M.I. Olivia, E.G. Vascetto, S.E. Urreta, G.A. Eimer and S.P. Silvetti, *J. Magn. Magn. Mater.* **322** (2010) 3438-3442.



# SYNTHESIS AND SURFACE FUNCTIONALIZATION OF COLLOIDAL GOLD FOR *E. coli* DETECTION BASED ON LATERAL FLOW ASSAY

Sasithon Rodtamai, Raweewan Thiramanas, Gamolwan Tumcharern and Duangporn Polpanich\*

National Nanotechnology Center, National Science and Technology Development Agency,  
Thailand Science Park, Pathum Thani, Thailand 12120

\*E-mail: [duangporn@nanotec.or.th](mailto:duangporn@nanotec.or.th)

**Abstract:** Colloidal gold or gold nanoparticles (AuNPs)-based lateral flow assay is one of the most important point-of-care products in diagnostic industry. It is well known that, to obtain the high efficiency test based on the principle of sandwich immunoassay by the specific binding of antigen and antibody, conjugation of antibody onto the AuNPs and the stability of AuNPs conjugate should be consistently studied. In this work, we aimed to synthesize the AuNPs by sodium citrate reduction and stabilized the particles by various stabilizers including mercaptoundecanoic acid, poly (acrylic acid) and sodium citrate. The prepared AuNPs were systematically characterized in terms of their maximum absorption wavelength, particle size and morphology by UV-vis spectrophotometer, nanosizer and transmission electron microscope (TEM). After that, the prepared AuNPs were functionalized with polyclonal anti-*E. coli* antibody via physical and chemical interactions using various types and pHs of the buffer. The amount of antibody presented onto the AuNP surface was determined by UV-vis spectrophotometer. Considering the physical appearance of the AuNPs after functionalized with the antibody, the sodium citrate stabilized AuNPs was found to be suitable particle for the antibody immobilization via physical adsorption when using borate buffer (pH 8.5). In addition, the citrate stabilized AuNPs were incubated with various concentrations of the anti-*E. coli* antibody at a given pH and subsequently determined the particle stability by adding of high concentration NaCl.

## 1. Introduction

Not only nutrients containing in foods, but their qualities also impact on the health of consumers. The major important quality of food products is the cleanliness throughout their processing, packaging, transporting and maintaining on shelf waiting for the buyers. Contamination of *Escherichia coli* (*E. coli*), normal flora living predominantly in human gut, is referred to the undesirable hygiene of the food products. Most strains of *E. coli* are harmless; however, some strains can cause severe infections which can be categorized into three types: intestinal diseases (gastroenteritis), urinary tract infections (UTI), and neonatal meningitis [1]. Conventional methods for detection of food-borne pathogens including culture technique and biochemical tests are greatly restricted by time-consuming and tedious process. However, clinical laboratories and food industries need user friendly operation, less time-consuming, and portable devices.

Lateral flow assay (LFA) is one of the rapid, easy-to-use, and low cost techniques for food pathogen detection [2]. The assay requires the specific

interaction between antibody onto colloidal nanoparticle conjugate and the antigen presented in the sample. The result would be judged by the visual color band on the paper strip which comes from the used particle such as colloidal gold nanoparticles (AuNPs), colored latex particles, carbon nanoparticles and magnetic beads. Due to its simple to synthesize and conjugate to antibodies, the AuNPs are commonly used in the strip tests [3]. In the present work, procedures for AuNPs preparation and immobilization of antibody, which considered as the critical steps for development of LFA, were studied. To prepare the reliable and consistent LFA for *E. coli* detection, the stability of the gold-antibody conjugate was, therefore, investigated.

## 2. Materials and Methods

**2.1. Preparation and characterization of citrate stabilized AuNPs:** AuNPs were prepared by sodium citrate reduction according to the previous report [4]. First, hydrogen tetrachloroaurate (III) ( $\text{HAuCl}_4$ ) solution (1% (w/v), 1 mL) (Sigma, USA) was mixed with deionized (DI) water (100 mL) and boiled while stirring for 15 min. Afterwards, sodium citrate (1% (w/v), 2.5 mL) was added into solution under continuous heating and then stirring for 15 min until the color of solution changed to red-wine. The obtained AuNPs was left to cool at room temperature under stirring and stored at 4°C prior to use. The citrate stabilized AuNPs (AuNPs-citrate) were characterized by using UV-vis spectrophotometer (Perkin-Elmer, Lambda 650), transmission electron microscopy (TEM) (JEOL, JEM-2010), and Nano sizer (Malvern Instruments, Nano ZS).

**2.2. Functionalization of AuNPs-citrate by 11-mercaptoundecanoic acid (MUA) or poly (acrylic acid) (PAA):** MUA stabilized AuNPs (AuNPs-MUA) were prepared according to Hupp et al. with some modifications [5]. Briefly, the AuNPs-citrate (1 mL) was mixed with an aqueous solution of MUA (0.01 M, 1 mL) in ethanol. After stirring the mixture for 12 h at room temperature, the AuNPs-MUA was obtained. While, PAA stabilized AuNPs (AuNPs-PAA) prepared by thiol binding of PAA-SH to AuNPs-citrate were kindly provided by Associate Professor Voravee P. Hoven (Chulalongkorn University, Thailand)

**2.3. Preparation of antibody-AuNPs conjugate:** The pH of AuNPs was adjusted to pH 7-8 by using  $\text{K}_2\text{CO}_3$  (0.2 M) [6]. In physical adsorption process, the

initial concentration of polyclonal anti-*E. coli* antibody (Thermo Scientific, USA) used in the experiment was varied from 0.4 to 1.0 mg/mL (in borate buffer (pH 8.5), phosphate buffer saline (pH 7.4) or phosphate buffer (pH 7.0)). Stock solution of the antibody was added to the AuNPs (200  $\mu$ L, OD<sub>520</sub> = 1) and the suspension was incubated at room temperature for 2 h. To reduce nonspecific interaction, BSA solution (100  $\mu$ L, 3% (w/v) in borate buffer (pH 8.5) or deionized water) was then added and incubated at room temperature for 1 h. After centrifugation (10,000 rpm, 20 min) and washing, the antibody-AuNPs conjugate was resuspended in BSA solution (3% (w/v) in borate buffer (pH 8.5) or deionized water). The OD of the AuNPs conjugate was investigated by UV-vis spectroscopy and the absorbed amount of antibody ( $\Gamma_{ads}$ ) was evaluated [7].

In the case of covalent immobilization, the carboxyl groups of the AuNPs-PAA were activated by (*N*-ethyl-*N'*-(3-(dimethylamino)propyl)carbodiimide hydrochloride) (EDC) (1 mM) (Sigma-Aldrich, Protein sequence grade) in phosphate buffer saline (PBS) (10 mM, pH 7.4). After adding of antibody solution, the mixture was incubated at room temperature for 2 h. The residual antibody was removed by centrifugation (10,000 rpm, 20 min).

**2.4. Stability test of AuNPs conjugate:** The stability of the AuNPs conjugate at various initial antibody concentrations was examined by addition of NaCl solution (10  $\mu$ L, 10% w/v) and, subsequently, shaking before observation of color change after 2 h [8]. After incubating for 30 min, the OD of the AuNPs conjugate was investigated by UV-vis spectroscopy. The lowest amount of polyclonal anti-*E.coli* antibody that can be stabilized the AuNPs conjugate was defined as the optimal antibody concentration.

### 3. Results and Discussion

For AuNPs preparation, the sodium citrate was used to reduce HAuCl<sub>4</sub> to neutral gold atoms. After the reaction was completed, the color of AuNPs-citrate suspension was changed from yellow to red-wine. UV-vis spectrum of the AuNPs-citrate was recorded as presented in Fig. 1(a). It can be seen that the maximum absorbance of the as-prepared AuNPs-citrate was appeared at the wavelength of 520 nm, which similar to another report [4]. TEM micrograph, Fig. 2, demonstrated that the as-prepared AuNPs-citrate was spherical in shape and their average particle size of the AuNPs-citrate was 17 nm. While, the maximum absorbance and average particle size of the AuNPs-PAA were found to be 520 nm and 20 nm, respectively (data not shown).

In the case of the AuNPs-MUA, the flocculation of these particles which possibly induced by hydrogen bonding interaction between surface carboxyl groups of each AuNPs-MUA was observed after adding of MUA to the AuNPs-citrate (Fig. 3(b)) [9]. As the

particle size increased, the wavelength of surface plasmon resonance related to an absorption spectrum shifted to longer, and thus the color of the suspension was tuned from red-wine to violet. Thus, the AuNPs-MUA did not further used in antibody immobilization process.

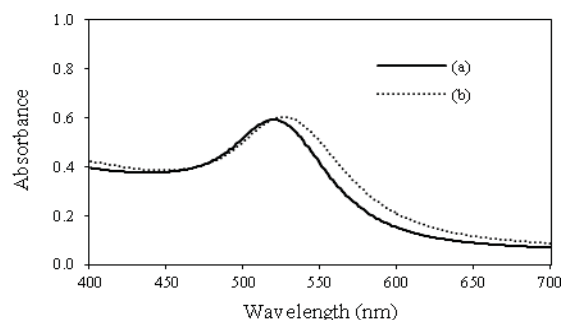


Fig. 1. UV-vis spectra of (a) AuNPs-citrate and (b) AuNPs-citrate conjugate.

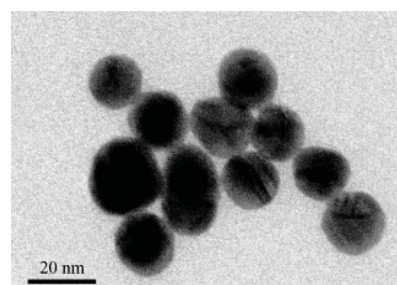


Fig. 2. TEM micrograph of the AuNPs-citrate.

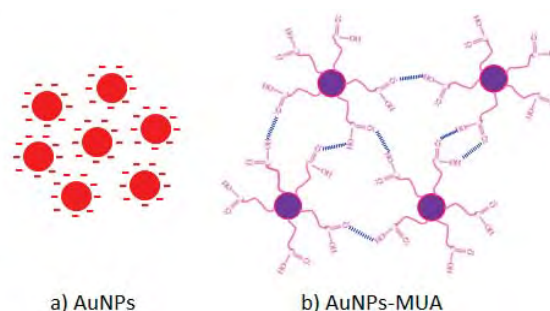


Fig. 3. Surface characteristic of (a) AuNPs-citrate and (b) AuNPs-MUA.

In antibody immobilization process, the initial antibody concentration added in the reaction was adjusted (0.4 to 1.0 mg/mL) and the  $\Gamma_{ads}$  values of the AuNPs-citrate conjugate are shown in Fig. 4.

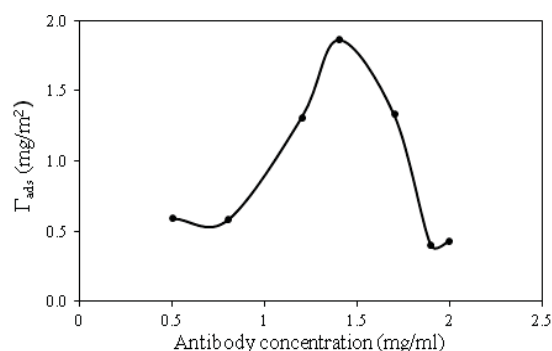


Fig. 4.  $\Gamma_{\text{ads}}$  of anti-*E. coli* antibody absorbed onto AuNPs-citrate by using various initial antibody concentrations.

It can be seen that the  $\Gamma_{\text{ads}}$  linearly increased with increasing the initial antibody concentration and approached the maximum value of  $1.86 \text{ mg/m}^2$  at antibody concentration of  $1.4 \text{ mg/ml}$  before decreasing. The AuNPs-citrate conjugate was stable and dispersed well in the buffer medium and its maximum absorbance was slightly shifted from  $520 \text{ nm}$  (before antibody adsorption) to  $525 \text{ nm}$  as shown in the UV-vis spectrum in Fig. 1(b).

However, the aggregation of the AuNPs-PAA after antibody immobilization by both physical adsorption and covalent coupling was obviously observed which inhibited the use of this conjugate in LFA.

The stability of the AuNPs-citrate conjugate at various initial antibody concentrations was investigated by addition of a certain amount of high concentration of NaCl solution. The lowest amount of antibody which can provide the stable AuNPs-citrate conjugate was assigned to be the optimal concentration. Fig. 5 shows the UV-Vis spectra of the AuNPs-citrate conjugate before and after addition of NaCl solution and its color change at a corresponding concentration is also presented in Fig. 6.

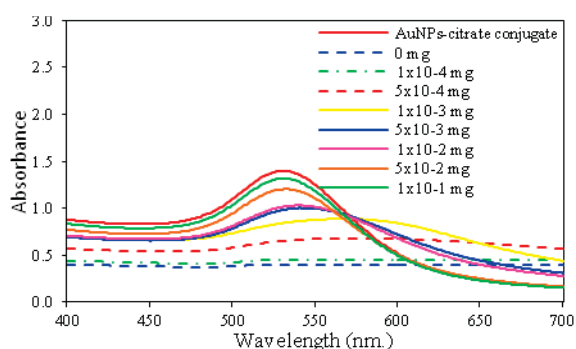


Fig. 5. UV-vis spectra of the AuNPs-citrate conjugate with different initial antibody concentrations after addition of a certain amount of NaCl for 30 min.

It was observed in Fig. 5 that after adding of NaCl solution, the maximum adsorption wavelength of the AuNPs-citrate conjugate was not changed ( $525 \text{ nm}$ ) compared to that before NaCl addition when using the initial antibody concentration of  $5 \times 10^{-2}$  and  $1 \times 10^{-1} \text{ mg}$ .

However, when decreasing amount of antibody ( $1 \times 10^{-2}$  to  $0 \text{ mg}$ ), the maximum absorbance of the AuNPs-citrate conjugate had a small red-shifted ( $540 \text{ nm}$ ). This indicated that this antibody concentration range ( $1 \times 10^{-2}$  to  $0 \text{ mg}$ ) was not enough to retain the stability of the conjugated particle leading to the particle aggregation. The color of the unstable AuNPs-citrate conjugate was tuned from red-wine to gray as shown in Fig. 6. From these results, it was suggested that the optimal antibody concentration was  $5 \times 10^{-2} \text{ mg}$  which was selected for further experiment.

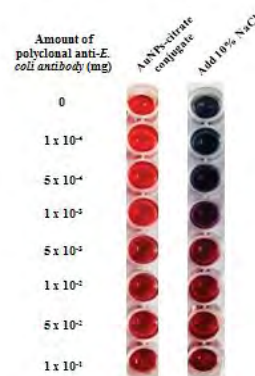


Fig. 6. Color change of the AuNPs-citrate conjugate with different initial antibody concentrations after addition of a certain amount of NaCl for 30 min.

Zeta potential ( $\zeta$ ) measurement of the AuNPs-citrate conjugate (initial antibody concentration  $5 \times 10^{-2} \text{ mg}$ ) was performed at pH 3.0 to 9.0 and the data are shown in Fig. 7.

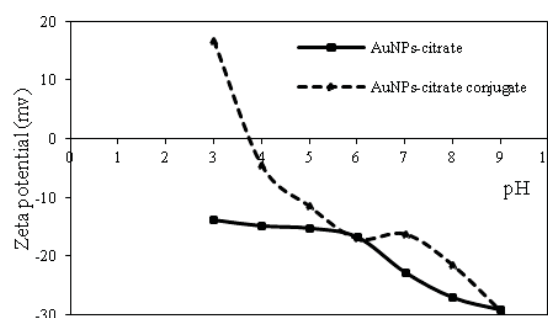


Fig. 7. Zeta potential values of the AuNPs-citrate conjugate compared to the AuNPs-citrate at various pHs.

From Fig. 7, it was found that the  $\zeta$  value of the AuNPs-citrate conjugate was positive at pH 3.0 and then turned to be negative when increasing pH. Whereas the  $\zeta$  values of bare AuNPs-citrate were negative in all pHs. At pH 6.0 and 7.0, the  $\zeta$  value of the AuNPs conjugate was approximately  $-20 \text{ mV}$  and more negative values were given at pH 8.0 and 9.0 which indicated that the stable conjugate was obtained. In addition, the isoelectric point (pI) of the conjugated particle was presented at pH 3.8. Its pI tended to move

to that of the polyclonal anti-*E. coli* antibody. A similar effect has been reported when BSA was adsorbed onto the silica colloidal particles [10]. These results confirmed the binding of the antibody onto the surface of AuNPs-citrate. Physical adsorption of the anti-*E. coli* antibody onto the AuNPs-citrate using other buffers including phosphate buffer saline and phosphate buffer was also carried out, however, the instability conjugated particles were observed. This might be due to the destabilization of the AuNPs by  $\text{Na}^+$  contained in those buffers.

#### 4. Conclusions

Stable gold nanoparticles (AuNPs) were successfully synthesized by sodium citrate reduction. Average particle size of the AuNPs-citrate determined by TEM was 17 nm. Polyclonal anti-*E. coli* antibody can be immobilized onto the AuNPs-citrate surface via physical adsorption and the amount of immobilized antibody onto the surface can be regulated by controlling of the initial antibody concentration. The optimum antibody concentration was to stabilize the AuNPs-citrate conjugate was  $5 \times 10^{-2}$  mg. Results from zeta potential measurement indicated that the prepared AuNPs-conjugate was stable at  $\text{pH} \geq 6.0$  which was suitable for lateral flow assay applications.

#### Acknowledgements

Research grant given by National Nanotechnology Center (NANOTEC) is gratefully acknowledged.

#### References

- [1] J. P. Nataro and J. B. Kaper, *Clin. Microbiol. Rev.* **11** (1998) 142-201.
- [2] R. Tanaka, T. Yuhi, N. Nagatani, T. Endo, K. Kerman, Y. Takamura, and E. Tamiya, *Anal. Bioanal. Chem.* **385** (2006) 1414-1420.
- [3] B. Cvak, D. Pum, A. Molinellia, and R. Krskac, *Analyst* **137** (2012) 1882-1887.
- [4] W. Dungchai, W. Siangproh, W. Chaicumpa, P. Tongtawe, and O. Chailapakul, *Talanta* **77** (2008) 727-732.
- [5] Y. Kim, R. C. Johnson, and J. T. Hupp *Nano Lett.* **1** (2001) 165-167.
- [6] X. Zhao, X. He, W. Li, Y. Liu, L. Yang and J. Wang, *Afr. J. Microbiol. Res.* **4** (2010) 663-670.
- [7] J. Revilla, A. Elaissari, P. Carriere and C. Pichot, *J. Colloid Interf. Sci.* **180** (1996) 405-412.
- [8] Y.S. Lia, Y. Zhou, S.Y. Lub, D.J. Guoc, H.L. Renb, X.M. Mengd, B.H. Zhib, C. Linb, Z. Wang, X.B. Lia, and Z.S. Liub, *Food Control* **24** (2012) 72-77.
- [9] C. S. Weisbecker, M. V. Merritt, and G. M. Whitesides, *Langmuir* **12** (1996) 3763-3772.
- [10] K. Rezwan, A.R. Studart, J. Vörös, and L.J. Gauckler, *J. Phys. Chem. B.* **109** (2005) 14469-14474.



# EFFECTS OF INORGANIC NANOPARTICLES ON PHOTOSTABILISATION OF WOOD CLEAR COATINGS

Akaporn Limtrakul<sup>1\*</sup>, Aungkapon Chaiyod<sup>1</sup>, Winyu Chitsamphandhvej<sup>1</sup>, Boonnak Sukhumme<sup>1\*</sup>

<sup>1</sup> Department of Chemistry / Faculty of Science, King Mongkut's University of Technology Thonburi, Bangkok, Thailand

\* Author for correspondence; E-Mail: boonnak.suk@kmutt.ac.th, Tel. +66 24 709557, Fax. +66 24 708843

**Abstract:** The purpose of this study was to investigate the photostabilisation of wood clear coating containing inorganic nanoparticles in comparison to an organic UV absorber commonly used to stabilize the wood product's colour. The nano-sized metal oxides e.g.  $\text{Al}_2\text{O}_3$ ,  $\text{SiO}_2$ ,  $\text{TiO}_2$  and  $\text{ZnO}$  in the ratio of 0.1, 0.2, 0.3 and 0.4 %wt, and the organic UV absorber, using a concentration as that advised by the manufacturer, were dispersed in an acrylic resin. Dispersions were carried out with a high speed mixer at 800 rpm and 2,000 rpm for the organic absorbers and the inorganic nanoparticles, respectively. The wood clear coatings were also aged with an accelerated weathering by QUV test. Results showed that incorporation of all nanoparticles revealed lower absorbance in the range of UV-B as compared to that incorporated with the organic UV absorber, while those incorporated with  $\text{TiO}_2$  and  $\text{ZnO}$  exhibited higher absorbance in the UV-A range. For IR reflectance, coatings modified with all nanoparticles showed higher reflectance as compared to that modified with the organic UV absorber. After the fourth QUV cycle, the gloss of coatings was accepted for both the organic UV absorber and the nanoparticles except that incorporated with  $\text{TiO}_2$ . However, only the coatings containing  $\text{TiO}_2$  and  $\text{ZnO}$  revealed no cracking after the 4<sup>th</sup> cycle of QUV.

## 1. Introduction

Wooden furniture always is favoured for their beauty, durability and workability. Woods have become scarcer and more expensive because of a rapid forest decline all over the world [1-2], especially teak wood. To protect the wood furniture's colour simultaneously with the nice appearance, wood coating is used to apply on its surface. Exterior wood coating is normally subjected to water and ultraviolet light, an invisible part of both natural sunlight and interior fluorescent light. They are responsible to yellowing, loss of gloss and loss of the originally attractive colour, tearing of the coating, cracking, and bleaching to grey [3-5]. To prolong the furniture lifetime, clear wood coating incorporated with UV absorbers is needed. In general, organic compounds are more vulnerable to UV light as compared with inorganic compounds [6-7]. When a molecule of absorber material absorbs a light photon, it converts photon energy to be heat, consequently, the absorber molecule vibrates [8]. For long exposure to the Sun, the attacked UV absorbers will eventually broken down by the ultraviolet light, subsequently the woods underneath will lose their colour and properties. However, to keep looking classy and long lasting, wooden furniture should be reapplied the coating at least every few years [9].

This paper presents a comparative study of some nano-sized inorganic oxides and organic UV absorber used in wood coating applications. The aim of this study is to keep a good photostabilisation performance and improve a long lifetime in use of wood clear coating. The correlation between coating performance and the influence of UV absorbers on film properties was also examined.

## 2. Materials and Methods

### 2.1 Materials

Organic UV absorber was a blend of two commercial products, one in liquid form and another one in solid form. This organic UV absorber was used as a reference with a concentration recommended by the manufacturer to maximize wood protection and also to maintain transparency of coatings. Inorganic compounds were nanoparticles with different chemical compositions e.g.  $\text{Al}_2\text{O}_3$ ,  $\text{SiO}_2$ ,  $\text{TiO}_2$  and  $\text{ZnO}$  in powder form. Other chemicals used to produce an acrylic based resin such as driers, anti-skimming agent, anti-fungal agents, binders and solvent were used as received.

### 2.2 Clear coatings

A various concentration ratios of the inorganic nanoparticles at 0.1, 0.2, 0.3 and 0.4 %wt were selected to examine the effect of concentration of the inorganic metal oxide on photostabilisation of wood clear coating. The nanoparticles selected were directly added into the chemicals used to prepare the acrylic resin at the early stages of a formulation shown in Table 1, and dispersed with a high speed mixer at 2,000 rpm for 30 minutes to avoid destabilizing polymer emulsions. After cooling down to room temperature, the coating prepared was kept in a 300 g bottle waiting for characterization. The reference coating incorporated with the UV organic absorbers was prepared as the same procedure as that mentioned above with a high speed mixer at 800 rpm for 30 minutes. The coatings obtained were adjusted their viscosity by adding solvent and checked their fundamental properties e.g. density, % non-volatile solid (% NV), gloss, to fit in a standard coating limitation. All coating incorporated with various types and concentration of nano-sized inorganic absorbers had passed the coating standard limitations. For coating analysis, clear coatings were applied by a bar applicator on glass slides with a dimension of 3.0 cm x

7.0 cm and 100  $\mu\text{m}$  thickness of wet films. The coated slides were left to dry at ambient temperature for 7 days. All coatings were analysed by UV-visible Perkin-Elmer spectrophotometer LAMDA 35/FIAS 300 in a wavelength range from 280 to 800 nm and by fiber optic spectroscopy technique in the reflectance mode.

Table 1: Formulation of wood clear coating.

Chemical	% Weight
Drier	2.0
Anti-skimming	0.15
Bioside	1.05
Absorber	vary
Binder	74.2
Solvent	21.4

#### Remarks

- Solvent content might be changed due to adjustment of viscosity of coatings to pass the fundamental standard.
- For organic UV absorber, the ratio of incorporation was 1.2 wt%.

### 2.3 Accelerated aging

Coated specimens were subjected to accelerated aging in a QUV Accelerated Weathering (Model QUV/SE) according to ASTM 154-00a. To simulate natural exposure and reduce testing time, a bulb radiating UVB with a 313-nm wavelength and irradiance of  $0.63 \text{ W}\cdot\text{m}^{-2}$  were used. Direct exposition under a dry condition at  $60^\circ\text{C}$  for 8 h and a condensed water vapor condition at  $50^\circ\text{C}$  for another 4 h were used in aging process. For one cycle of testing, these two processes were alternated to complete a week. The mirrors with a dimension of 7.5 cm x 15.0 cm were conducted with the wet coatings of 100  $\mu\text{m}$  thick and the coated specimens were left to completely dry for a week before aging treatment. Each specimen was subjected to four cycles of aging treatment. The parameters analysed for the accelerated aging test were as follows.

**Gloss:** The gloss of the different coatings before and after the aging treatment was measured with a glossmeter (BYK-Gardner Micro-TRI-gloss) according to the ASTM D523 method (ASTM 1994). The gloss was measured with a  $60^\circ$  geometry in according with the standard. Average value of three readings was recorded.

**Micro-crack:** The appearance of cracking was evaluated by a Dino-Lite versatile digital microscope equipped with a Dino Eye for an accurate display on a computer screen. Three readings were recorded for each specimen.

## 3. Results and Discussion

### 3.1 Efficiency of UV absorbers

The UV-visible absorbance spectra of coatings incorporated with various UV absorbers were shown in Figures 1-4. All absorbers exhibited a high and broad absorbance band in the UV zone, especially in the UV-B range,  $\lambda = 280$  to 315 nm, but they showed a

gradual decrease at higher energy wavelength,  $\lambda > 315$  nm. Besides, they revealed no significant absorption in the visible zone,  $\lambda = 400$  to 700 nm. The UV absorption of organic absorber was greater than those of inorganic absorbers, especially in the range of the UV-A zone. Increasing inorganic content, the absorption was a marginal increase and reached a maximum point. Further increasing in inorganic absorber loading, the absorption exhibited a minimal decline. This might be caused an aggregation was formed at high concentration, consequently reduced the ability of the particles to absorb the UV light [10-12]. However, among inorganic absorbers,  $\text{TiO}_2$  revealed the closest one to the organic absorber acted as the reference.

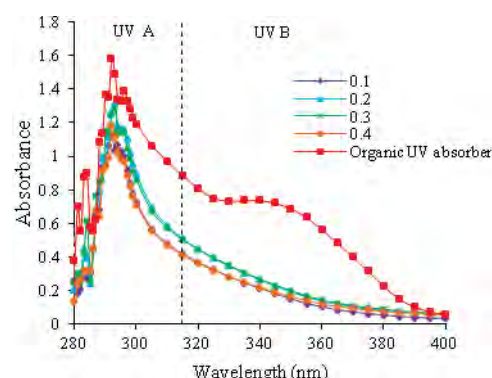


Figure 1. Absorbance spectra of  $\text{Al}_2\text{O}_3$  as compared with that of organic absorber.

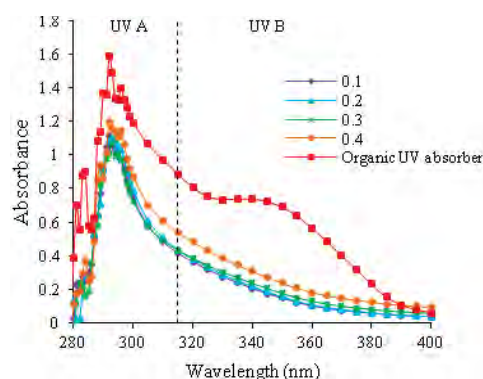


Figure 2. Absorbance spectra of  $\text{SiO}_2$  as compared with that of organic absorber.

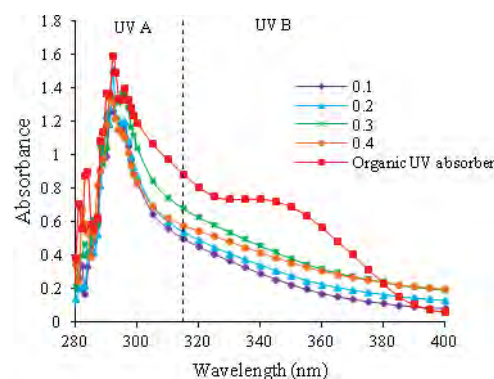


Figure 3. Absorbance spectra of  $\text{TiO}_2$  as compared with that of organic absorber.

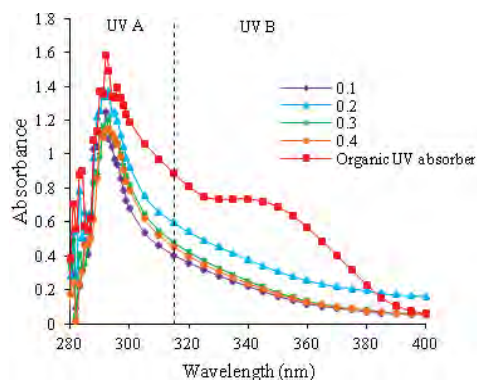


Figure 4. Absorbance spectra of ZnO as compared with that of organic absorber.

Reflectance spectra, received by using a fiber optic spectroscopy with a reflectance mode, of ZnO were shown in Figure 5. Compared to the reference organic absorber, the IR reflection of ZnO was higher. Besides, higher ZnO content caused higher reflectance and reached the highest spectra at 0.2 wt% loading. Adding further higher absorber content gave lower reflectance than that with 0.2 wt% loading. It was believed that, the particles may aggregate at high concentration as mention above. Other inorganic absorbers also performed as a similar behaviour to those of ZnO (did not show here). However, ZnO and SiO<sub>2</sub> at 0.2 wt% content revealed the highest reflectance.

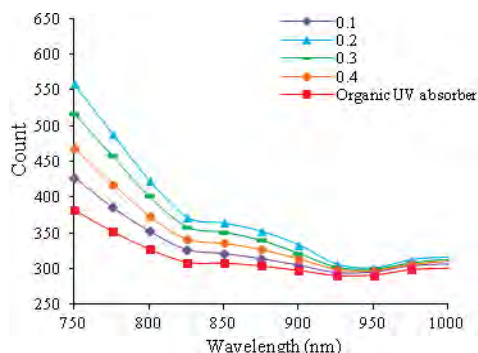


Figure 5. Reflectance spectra of ZnO as compared with that of organic absorber.

### 3.2 Accelerated aging

**Gloss:** Optical property of a clear coating was monitored from gloss changes. Incorporation of UV absorbers into clear coating can cause a change in gloss. The effect of UV radiation on gloss was shown in Figures 6-7. Incorporation of inorganic absorbers revealed lower gloss as compared with that incorporated with organic absorber. Increasing inorganic absorber content exhibited a gradually reduction of gloss, while for TiO<sub>2</sub>, it caused a significant decrease. After passing the aging process, all coatings both incorporated with organic and inorganic absorbers revealed a small reduction as the number of aging cycle increased. However, all clear coating had passed the gloss standard point, at an average value of 70. Whereas, those incorporated with

TiO<sub>2</sub> revealed failure of gloss from the standard point even they just subjected to only the first aging cycle. Higher exposure cycles, the coating mixed with TiO<sub>2</sub> showed a clearly deteriorated damage of gloss. This should be depended on the dimension of TiO<sub>2</sub> particles and its dispersion efficiency in the polymer medium [13]. However, more studies are needed to conclude this finding.

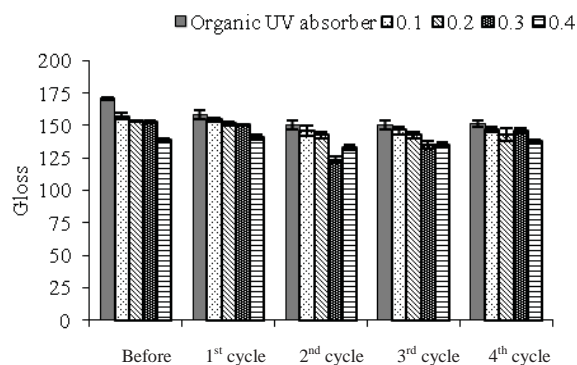


Figure 6. Gloss performance of ZnO at various wt% as compared with that of organic absorber after passing aging process.

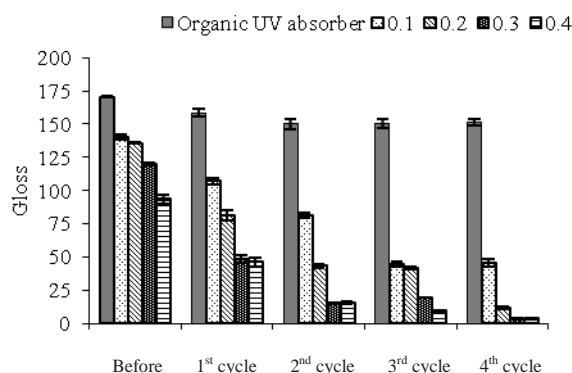


Figure 7. Gloss performance of TiO<sub>2</sub> at various wt% as compared with that of organic absorber after passing aging process.

**Micro crack:** Under a microscope of a high magnification, the first appearance of cracking was observed from both coatings incorporated with organic and inorganic absorbers e.g. Al<sub>2</sub>O<sub>3</sub> and SiO<sub>2</sub>, at the end of the third aging cycle. For longer exposure, the coatings revealed seriously deteriorated, showing some tearing and peeling out of coatings, as seen in Figure 8. Surprisingly, no cracking was found from the coatings mixed with ZnO for all range of the concentration and the ones incorporated with TiO<sub>2</sub> at a concentration range of 0.3-0.4 wt% even passed four aging process cycles. Generally, incorporation of UV absorbers in the coating used to prevent the polymer matrix of coating from being attacked by UV radiation. Thus, the UV absorbers are expected to absorb or reflect the UV radiation, subsequently, give high photostability of coating [14-16]. Therefore, the results showing high resistance to weathering exposure of ZnO and TiO<sub>2</sub> should be attributed to their abilities



of high UV absorption of  $\text{TiO}_2$  and high IR reflectance of  $\text{ZnO}$ , subsequently the radiation in the aging process could not attack to the polymer matrix. Moreover, higher the concentrations revealed higher protection of polymer matrix. However, to have more understanding to explain this finding more characterization should be performed, including analysis with scanning electron microscopy and Fourier Transform Infrared (FT-IR) spectroscopy techniques. Besides, glass temperature,  $T_g$ , of the clear coatings should be recommended to examine.

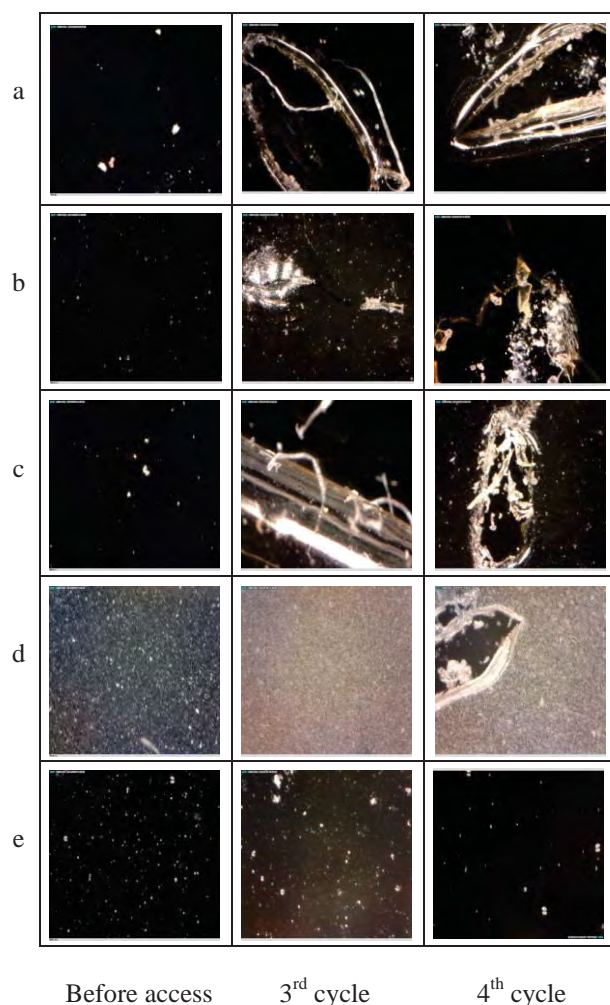


Figure 8. Cracking performance of UV absorbers a) organic UV absorber b)  $\text{Al}_2\text{O}_3$  c)  $\text{SiO}_2$  d)  $\text{TiO}_2$  and e)  $\text{ZnO}$  versus aging process cycle in a QUV apparatus. The loading of inorganic absorbers is 0.2 wt%.

#### 4. Conclusions

In this work, the photostabilization of wood clear coating incorporated with inorganic UV absorbers was studied in comparison with that incorporated with organic UV absorber. The organic UV absorber showed high ability in UV absorption in the whole range of UVA and UVB. The inorganic absorbers showed less efficiency in UV absorption than the organic absorber. The protective effect of inorganic

absorbers revealed to reach a maximum with concentration. High concentration showed a reduction in UV absorption. IR reflection ability of the inorganic absorbers exhibited higher than that of the organic absorber, especially  $\text{ZnO}$  and  $\text{TiO}_2$ . However, they also exhibited a peak effect with concentration. This might be caused at high concentration the particles tended to agglomerate and reduced their properties. After passing a QUV test, the gloss of all absorbers were accepted, except  $\text{TiO}_2$  which showed flat, out of specification. Higher aging cycle showed more serious deterioration. Surprisingly, the incorporation of  $\text{ZnO}$  for all concentration range and  $\text{TiO}_2$  at the concentration range of 0.3-0.4 wt% performed no cracking even passing the fourth aging cycle test. This finding will be necessary to do more study to get completely understanding.

#### Acknowledgements

The authors would like to thank TOA Paint (Thailand) Co., Ltd. for supplying all ingredients, operation support and some characterization instruments.

#### References

- [1] S.Y. Woo, *African Journal of Biotechnology* **8** (2009) 7409-7410.
- [2] F. Bussotti and M. Ferretti, *Environmental Pollution* **101** (1998) 49-65.
- [3] D. N. Izekor and J.A. Fuwape, *J. Apply. Sai. Environ. Manage.* **15** (2011) 217-222.
- [4] P.D. Evans, N.I. Owen, S. Schmid and R.D. Webster, *Polym. Degrad. Stabil.* **76** (2002) 291-303.
- [5] P. Hayoz, W. Peter and D. Rogez, *Progress in Organic Coatings* **48** (2003) 1-27.
- [6] F. Aloui, A. Ahajji, Y. Irmouli, B. George, B. Charrier, and A. Merlin, *Applied Surface Science* **253** (2007) 3737-3745.
- [7] N. Auclair, B. Riedl, V. Blanchard, P. Blanchet, *Forest Prod. J.* **61** (2011) 20-26.
- [8] P. L. Chou, H. T. Chang, T. F. Yeh, and S. T. Chang, *Bioresour. Technol.* **99** (2008) 1073-1079.
- [9] P.D. Evans, A.J. Michell and K. Schmalzl, *Wood Sci. Technol.* **26** (1992) 151-163.
- [10] V. Blanchard and P. Blanchet, *BioResources* **6** (2011) 1219-1229.
- [11] H. Schmidt, M. Naumann, T.S. Muller and M. Akarsu, *Thin Solid Films* **502** (2006) 132-137.
- [12] D. Koziej, F. Fischer, N. Kranzlin, W.R. Caseri and M. Niederberger, *ACS Appl. Mater. Interface* **1** (2009) 1097-1104.
- [13] D. Scaroni, M. Lazzari and O. Chiantore, *Polymer Degradation and Stability* **97** (2012) 2136-2142.
- [14] B. George, E. Suttie, A. Merlin and X. Deglise, *Polym. Degrad. Stabil.* **88** (2005) 268-274.
- [15] H. Zweifel, *Stabilization of Polymeric Materials, State of the Art, Scope and Limitation*, Springer, Berlin, Germany (1997).
- [16] J. Pospisil and S. Nespurek, *Progr. Polym. Sci.* **25** (2000) 1261-1335.



# CETYLPIRIDINIUM CHLORIDE MICELLE AS A NEW ELECTROLYTE SYSTEM FOR DYE-SENSITIZED SOLAR CELLS

Sakon Thanacharoenchumrut<sup>1,3</sup>, Pasit Pakawatpanurut<sup>2,3\*</sup>

<sup>1</sup> Materials Science and Engineering Program, Faculty of Science,  
Mahidol University, Ratchatewi, Bangkok 10400, Thailand

<sup>2</sup> Department of Chemistry, and Center of Excellence for Innovation in Chemistry, Faculty of Science,  
Mahidol University, Ratchathewi, Bangkok 10400, Thailand

<sup>3</sup> Center for Alternative Energy, Faculty of Science, Mahidol University,  
Salaya, Putthamonthon, Nakon Pathom 73170, Thailand

\*E-mail: pasit.pk@gmail.com, Tel. +66 22015133, Fax. +66 23 547151

**Abstract:** Dye-sensitized solar cell (DSSC) is one of the promising photovoltaic technologies that have potential for practical use. DSSC consists of many components such as dye, semiconductor, electrolyte, working and counter electrodes. One of the most important parts of DSSC is the electrolyte, which can be categorized into three groups: liquid electrolyte, quasi-solid electrolyte, and solid-state electrolyte. Liquid electrolyte exhibits best performance of all types and is the point of focus in this work. In this research, micelles from cationic surfactant cetylpyridinium chloride (CPC) were used with  $I^-/I_3^-$  redox couple as an electrolyte system to promote the electron transfer in DSSC. The results showed that the presence of CPC micelles in the electrolytes enhanced the efficiency ( $\eta$ ) of DSSCs compared with those using the conventional liquid electrolytes. The measured value of  $\eta$  of DSSC with CPC micelles was 5.09%, when the electrolyte consisted of 8.9 mM CPC, 0.5 M LiI, 0.05 M  $I_2$ , 0.1 M 1-methyl-3-propylimidazolium iodide (MPII), and 0.5 M 4-tert-butylpyridine (TBP) in acetonitrile.

## 1. Introduction

Dye-sensitized solar cell (DSSC) is the promising photovoltaic device for practical use. The important part of DSSC is the electrolyte, and liquid electrolyte exhibits best performance of all types to date [1]. Therefore, the improvement of liquid electrolyte is focused in this work.

Surfactant is the molecule that is widely used in various fields such as physical chemistry, pharmaceutical, cosmetics, and food science. These molecules contain hydrophilic and hydrophobic regions which form micelle structure when in water or polar solvent. Micellization of the surfactants can be characterized by critical micelle concentration (CMC). Cationic surfactant cetylpyridinium chloride (CPC) micelle is used in the study of kinetic reaction [2]. This study shows that the rate of electron transfer is increased in the presence of CPC micelle due to the positive potential field of micelle.

In this research, micelles from CPC were used with  $I^-/I_3^-$  redox couple as an electrolyte to promote the electron transfer in DSSC.

## 2. Materials and Methods

### 2.1 Materials

The cationic surfactant cetylpyridinium chloride (CPC), lithium iodide (LiI), iodine ( $I_2$ ), 1-methyl-3-propylimidazolium iodide (MPII), 4-tert-butylpyridine (TBP), and acetonitrile were purchased from Sigma-aldrich and used as received.

Conducting glass plates fluorine-doped tin oxide (FTO) glass with sheet resistance of about  $\sim 8 \Omega/\text{square}$  was purchased from Solaronix.

$TiO_2$  paste, Pt paste, and cis-dithiocyanate- $N,N'$ -bis-(4-carboxylate-4-tetrabutylammoniumcarboxylate-2,2-bipyridine)ruthenium(II) (N719) were purchased from Dyesol, Australia

### 2.2 Conductivity measurement

The determination of critical micelle concentration (CMC) of CPC can be accessed by measuring the conductivity using a conductometer ORION model 145+ with conductivity probe model 011510 and cell constant  $1.0 \text{ cm}^{-1}$  at 298.15K for different concentrations of CPC solutions. The conductivity cell was calibrated with standard NaCl solution,  $1413 \mu\text{S}/\text{cm}$ .

### 2.3 Assembly of DSSCs

$TiO_2$  photoelectrode and Pt counter electrode were prepared by coating  $TiO_2$  paste and Pt paste, respectively, on an FTO glass by screen printing method and later annealing at  $450^\circ\text{C}$  for 1.30 h in air atmosphere. After that, the photoelectrode was immersed in 0.3 mM N719 dye solution for 24 h. The obtained photoelectrode had active area  $0.25\text{cm}^2$  ( $0.5\text{cm} \times 0.5\text{cm}$ ). Cells were prepared by placing surlyn between the photoelectrode and the counter electrode, with two holes drilled on the counter electrode for subsequent filling of the electrolyte. Then, these cells were placed in oven at  $120^\circ\text{C}$  for 30 min to melt surlyn. Two liquid electrolytes, with and without CPC as in Table 1, were injected into the cells and then sealed by an aluminium tape.

Table 1: Two liquid electrolytes used

Electrolyte	8.9mM CPC	0.5M LiI	0.05 M I <sub>2</sub>	0.1M MP11	0.5M TBP
Reference	-	√	√	√	√
8.9mM CPC	√	√	√	√	√

## 2.4 Photocurrent and photovoltage of DSSCs

The current–voltage (I–V) characteristics of DSSCs with two liquid electrolytes were measured using the Keithley 2420 current source under light illumination of 100 mW cm<sup>-2</sup>, AM 1.5.

## 3. Results and Discussion

### 3.1 Determination of CMC of CPC

The determination of CMC of CPC was assessed by the conductivity method. A plot between specific conductivity ( $\kappa$ ) of CPC as a function of CPC concentration ([CPC]) at 298.15°C is shown in Figure 1. The CMC of CPC can be found from the point of an abrupt change in the slope of the plot. However, in the case of weak change in the slope, equation (1) can be applied to find the CMC

$$\frac{d\kappa}{dc} = \frac{1}{2} \left( \frac{\kappa_{i+1} - \kappa_i}{c_{i+1} - c_i} + \frac{\kappa_i - \kappa_{i-1}}{c_i - c_{i-1}} \right) \quad (1)$$

where  $\kappa$  denotes the specific conductivity and  $c$  is the surfactant concentration [3]. This first derivative is derived again with the same formula to obtain the second derivative ( $\kappa''$ ), and it is fitted by a Gaussian function using equation (2) in ORIGIN program to obtain the CMC of surfactant.

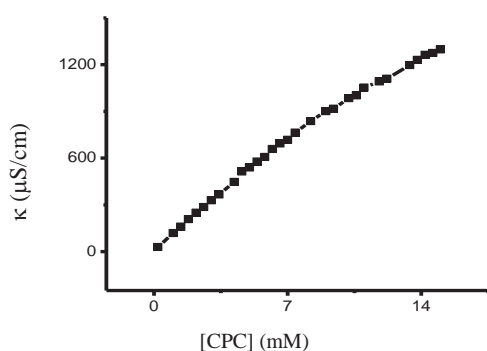


Figure 1. The plot of  $\kappa$  and [CPC] in acetonitrile

$$\kappa'' = \kappa_0'' + \frac{A}{w\sqrt{\frac{\pi}{2}}} e^{\frac{-2(c-c_0)}{w^2}} \quad (2)$$

where  $\kappa_0''$ ,  $A$ , and  $w$  are the offset, area, and width of the curve, respectively, and  $c_0$  is the CMC of

surfactant. This formula gives the bell shape plot as shown in Figure 2. The CMC of CPC was estimated by the Gaussian fitting curve to be 8.91 mM.

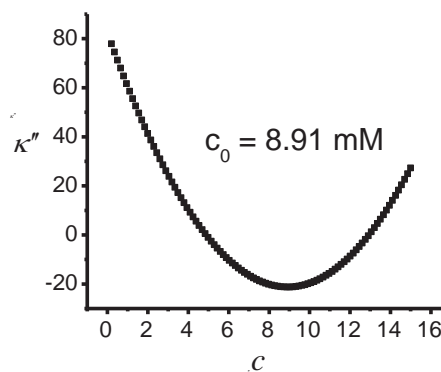


Figure 2. Gaussian fitting curve of  $\kappa''$

### 3.2 Photovoltaic characterizations of DSSCs

The photovoltaic characterizations of the DSSCs were performed using the current–voltage (I–V) measurements under 100 mW cm<sup>-2</sup>, AM 1.5 illumination, which can be described by the following equations:

$$FF = \frac{J_{\max} V_{\max}}{J_{sc} V_{oc}} \quad (3)$$

$$\eta = \frac{J_{sc} V_{oc}}{P_{in}} FF \times 100\% \quad (4)$$

where  $FF$  is fill factor – the ratio of the actual power output ( $J_{\max} \times V_{\max}$ ) to the theoretical power output ( $J_{sc} \times V_{oc}$ ),  $J_{\max}$  (mA/cm<sup>2</sup>) the maximum current density,  $V_{\max}$  (V) the maximum voltage,  $J_{sc}$  (mA/cm<sup>2</sup>) the short-circuit current density,  $V_{oc}$  (V) the open-circuit voltage,  $P_{in}$  (mW/cm<sup>2</sup>) the incident light power, and  $\eta$  the efficiency of DSSCs.

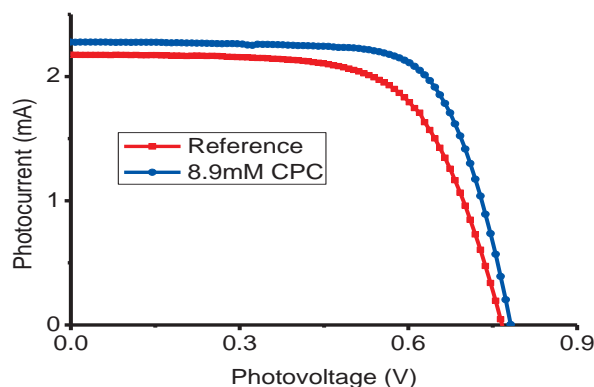


Figure 3. The I–V curve of DSSCs with reference (red line) and 8.9 mM CPC electrolytes (blue line).

The photovoltaic characteristics of DSSCs with two liquid electrolytes, with and without CPC micelle, are showed in Figure 3 and summarized in Table2.

From Table 2, in the presence of CPC micelle in the electrolyte, the efficiency was increased, possibly due to the role of CPC micelle in facilitating the electron transfer process in the electrolyte. This hypothesis is consistent with an observed increase in  $J_{sc}$ . As a result, the cell efficiency was improved to 5.09%.

Table 2: Photovoltaic characteristics of DSSCs with reference and 8.9mM CPC electrolytes

Electrolyte	$\eta(\%)$	$FF$	$V_{oc}$	$J_{sc}$
Reference	4.37	0.658	0.76	8.70
8.9mM CPC	5.09	0.715	0.78	9.11

#### 4. Conclusions

This research aims to study the influence of the CPC micelles in the liquid electrolyte on the solar conversion efficiency of DSSCs. The Gaussian fitting model was applied to assess the CMC of CPC in acetonitrile, which revealed the CMC value of 8.91mM. This CMC value was then used to prepare the liquid electrolyte. DSSCs prepared using CPC micelles, indeed, showed an improved efficiency. Our first tests showed that the CPC micelles in the electrolyte helped increase the DSSC efficiency by about 16%, from 4.37% to 5.09%.

#### Acknowledgements

This research was supported by the research funds from the Department of Chemistry and the Center of Excellence for Innovation in Chemistry, Faculty of Science, Mahidol University, the National Science and Technology Development Agency, and Mahidol University.

#### References

- [1] J. Wu, Z Lan, S. Hao, P. Li, J. Lin, M. Huang, L. Fang, and Y. Huang, *Pure Appl. Chem.* 80 (2008) 2241-2258.
- [2] L.K. Patterson and M. Grätzel, *J. Phys. Chem.* 79 (1975) 956-960.
- [3] A.M. Khan, and S.S. Shah, *J. Chem. Soc. Pak.* 30 (2008) 186-191.

# THERMAL BEHAVIOUR AND LONG-TERM STABILITY OF BISTRIFLAMIDE IONIC LIQUIDS

Parncheewa Udomsap\* and Somsak Supasitmongkol

Bioenergy Laboratory, National Metal and Materials Technology Center, Pathumthani, Thailand

\* Author for correspondence; E-Mail: parncheu@mtec.or.th, Tel. +66 2 5646500, Fax. +66 2 5646401

**Abstract:** Ionic liquids (ILs), including cations and anions, were usually used as potential absorbents in gas separation process. Due to their favourable properties such as low vapour pressures under normal operation conditions and excellent thermal and chemical stability at low temperatures. However, these properties depend on the chemical structure of both the anionic and the cationic ILs. The thermal stability of ionic liquids is one of the important properties which define the stable temperature limit of ionic liquids for their practical applications. Therefore, a comparative study of thermal behaviour and long-term stability in ionic liquids were carried out. The ionic liquids used in this research can be classified into three categories: imidazolium, pyridinium and trialkyltetradecylphosphonium. These included: 1-ethyl-3-methylimidazolium ethyl sulphate [C<sub>2</sub>mim][EtSO<sub>4</sub>], 1-ethyl-3-methylimidazolium bis(trifluoromethylsulfonyl) imide [C<sub>2</sub>mim][Tf<sub>2</sub>N], 1-butyl-3-methylimidazolium bis(trifluoromethylsulfonyl)imide [C<sub>4</sub>mim][Tf<sub>2</sub>N], 1-butyl-3-methylpyridinium bis(trifluoromethylsulfonyl) imide [C<sub>4</sub>mpy][Tf<sub>2</sub>N] and Trihexyltetradecyl phosphonium bis(trifluoromethylsulfonyl)imide [P<sub>66614</sub>][Tf<sub>2</sub>N]. A thermogravimetric analysis (TGA) technique was used to evaluate the thermal decompositions of all ionic liquids. The results show that the imidazolium ionic liquids appeared better thermal stability than the pyridinium and trialkyltetradecylphosphonium when comparing the onset-decomposition temperature (T<sub>onset</sub>). The T<sub>onset</sub> of imidazolium group, pyridinium group and trialkyltetradecylphosphonium group were around 445, 400 and 395 °C, respectively. By contrast, the long-term thermal stability showed less stable behaviour for imidazolium when compared to pyridinium. Besides cation-anion interaction, this different behaviour in thermal stability may cause from detectable vapour pressure for the ionic liquids.

## 1. Introduction

Ionic liquids, composed of cations and anions, have been proposed as potential absorbents. This is due to the favourable properties of ionic liquids such as low vapour pressures under normal operational conditions, the formation of low-temperature molten salts (mp < 100 °C) and excellent thermal and chemical stability at low temperatures [1-3]. The most commonly of ionic liquids have an alkyl-substituted imidazolium and pyridinium salts as cations, and a variety of anions such as hexafluorophosphate ([PF<sub>6</sub>]), tetrafluoroborate ([BF<sub>4</sub>]), bis(trifluoromethylsulfonyl) imide ([Tf<sub>2</sub>N]) and halide anions(*e.g.*, [F], [Br] and [Cl]) for many chemical processes such as catalysis, extraction and

absorption [4]. Many properties such as melting point, viscosity, thermal stability and solubility in gas and liquid are affected by changing structure of either the anion or the cation. Such the large size of the cationic structure of ionic liquids may reduce electrostatic attraction, lowering their melting point.

Moreover, the cationic, anionic structure and alkyl substituent cause the stability of thermal decomposition of ionic liquids also. Thermal stability is essential for determining the feasibility of temperature operating range of the fluid in gas separation system. The thermal stability of ionic liquids has been extensively published in literature, based on thermogravimetric analysis (TGA), where the majority of the reported data are the onset-decomposition temperature (up to 400 °C) determined from scanning TGA experiments [2]. Studies have shown that anion ionic liquids, rather than the nature of the cation, dominate the degree of thermal stability. The thermal stability increases with anion size, and decreases with degree of nucleophilicity of anion. Halide anions dramatically reduce the thermal stability of several imidazolium salts with the onset of decomposition occurring at temperatures below 300 °C [5]. Although the decomposition temperatures of ionic liquids are easily measured and reproducible value, recent constant temperature studies [6] have reported appreciable decomposition of ionic liquids at temperatures significantly lower than the onset-decomposition temperatures determined from scanning TGA experiments. Therefore, the thermal stability range of ionic liquids is not precisely defined by the onset-decomposition temperature. Data about long-term thermal stabilities and start-decomposition temperatures of ionic liquids are rare in the published literature, which led to the study to define the stable temperature limit of ionic liquids for their practical applications.

In this research, thermal stability and long-term stability are evaluated to determine which ionic liquids are suitable in gas separation systems. Moreover, the results could be presented the effect of cation, anion and alkyl substituent to thermal stability of ionic liquid.

## 2. Materials and Methods

### 2.1 Chemicals

Five different ionic liquids used in this work can be divided into three broad groups: imidazolium,



pyridinium and trialkyltetradecylphosphonium. These included 1-ethyl-3-methylimidazolium ethyl sulphate  $[\text{C}_2\text{mim}][\text{EtSO}_4]$ , 1-ethyl-3-methylimidazolium bis(trifluoromethylsulfonyl)imide  $[\text{C}_2\text{mim}][\text{Tf}_2\text{N}]$ , 1-butyl-3-methylimidazolium bis(trifluoromethylsulfonyl)imide  $[\text{C}_4\text{mim}][\text{Tf}_2\text{N}]$ , 1-butyl-3-methylpyridinium bis(trifluoromethylsulfonyl)imide  $[\text{C}_4\text{mpy}][\text{Tf}_2\text{N}]$  and Trihexyltetradecyl phosphonium bis(trifluoromethylsulfonyl)imide  $[\text{P}_{66614}][\text{Tf}_2\text{N}]$  which were obtained from Aldrich and Fisher. Their chemical structures were presented in Table 1.

Table 1: The structure of ionic liquids studied

Ionic Liquid	Molecular Structure
$[\text{C}_2\text{mim}][\text{EtSO}_4]$	
$[\text{C}_2\text{mim}][\text{Tf}_2\text{N}]$	
$[\text{C}_4\text{mim}][\text{Tf}_2\text{N}]$	
$[\text{C}_4\text{mpy}][\text{Tf}_2\text{N}]$	
$[\text{P}_{66614}][\text{Tf}_2\text{N}]$	

## 2.2 Instrument

Thermal decomposition profiles were determined by Thermogravimetric Analysis (Perkin-Elmer Pyris TGA 7) over the temperature range of 20 to 900 °C at a heating rate of 10 °C/min under a nitrogen atmosphere.

## 2.3 Thermal decomposition of ionic liquids

A thermogravimetric analyser (Perkin-Elmer TGA 7) was used to measure the thermal decomposition of the ionic liquids. In this research, 25-28 mg ionic liquids were placed in an open platinum pan and heated over the temperature range of 20 to 650 °C at a constant heating rate (10 °C/min), while purging with 20 ml/min of dry  $\text{N}_2$  at 1 atm. Based on the course of the TGA scan, the start, onset and peak decomposition temperatures can be determined from the weight loss thermogram and the differential thermogravimetry (DTG) plot as can be seen in Figure 1. The start decomposition temperature ( $T_{\text{start}}$ ) is the beginning temperature of the sample decomposition. The onset decomposition temperature ( $T_{\text{onset}}$ ) is the intersection of the tangent of the initial baseline weight with the sharply sloping weight loss curve. The peak decomposition temperature ( $T_{\text{peak}}$ ), which is determined from the DTG plot, is the temperature at the maximum rate of weight loss with temperature.

However, this research focused on the  $T_{\text{start}}$  and  $T_{\text{onset}}$  only for evaluation the thermal stability of ionic liquids.

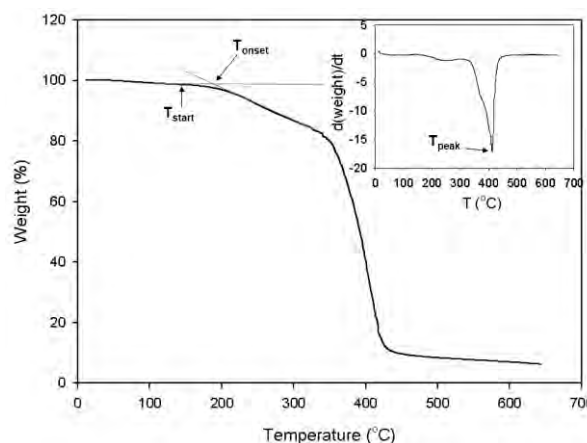


Figure 1. The weight loss thermogram and differential thermogram of  $[\text{C}_2\text{mim}][\text{EtSO}_4]$  indicating several decomposition temperature,  $T_{\text{start}}$ ,  $T_{\text{onset}}$  and  $T_{\text{peak}}$ .

## 3. Results and Discussion

### 3.1 Thermal stability

The ionic liquids, including  $[\text{C}_2\text{mim}][\text{EtSO}_4]$ ,  $[\text{C}_2\text{mim}][\text{Tf}_2\text{N}]$ ,  $[\text{C}_4\text{mim}][\text{Tf}_2\text{N}]$ ,  $[\text{C}_4\text{mpy}][\text{Tf}_2\text{N}]$  and  $[\text{P}_{66614}][\text{Tf}_2\text{N}]$ , were measured the thermal decomposition by using TGA which the results of  $T_{\text{start}}$  and  $T_{\text{onset}}$  were reported in Table 2.

Table 2: The decomposition temperatures of the ionic liquid

Ionic liquid	$T_{\text{start}}$ (°C)		$T_{\text{onset}}$ (°C)	
	$T_{\text{start}}$	$T_{\text{start}}$ (lit.)	$T_{\text{onset}}$	$T_{\text{onset}}$ (lit.)
$[\text{C}_2\text{mim}][\text{EtSO}_4]$	150.48 ± 3.17	138.6 [11]	205.35 ± 1.87	190 [11]
$[\text{C}_2\text{mim}][\text{Tf}_2\text{N}]$	329.25 ± 2.75	N/A	449.57 ± 2.15	455 [5]
$[\text{C}_4\text{mim}][\text{Tf}_2\text{N}]$	328.83 ± 2.04	330 [12]	444.98 ± 0.57	439 [2]
$[\text{C}_4\text{mpy}][\text{Tf}_2\text{N}]$	323.43 ± 4.07	317 [9]	400.24 ± 0.16	397 [9]
$[\text{P}_{66614}][\text{Tf}_2\text{N}]$	271.46 ± 1.58	N/A	395.43 ± 1.62	N/A

The thermal stability of the ionic liquids can be classified into three categories: imidazolium, pyridinium and trialkyltetradecylphosphonium. The terms of  $T_{\text{start}}$  and  $T_{\text{onset}}$  are referred to as the decomposition temperature ( $T_{\text{dec}}$ ) in this work. From the Table 2, The increasing of alkyl chain length of [mim] had little effect on the decomposition temperature based on  $[\text{Tf}_2\text{N}]$  anion. However, there was considerable difference in thermal stability with regard to the cationic structure.

With the  $[\text{Tf}_2\text{N}]$  anion, the imidazolium ionic liquids appeared to have vastly better thermal

stability than the pyridinium and trialkyltetradecylphosphonium ionic liquids. This result can be explained by the order of the molar conductivity ratio of the ionic liquids: aliphatic cations > pyridinium > imidazolium [7], which implies the degree of the dissociation of ionic liquids. This order coincides with the reverse order of the intermolecular interaction energy between cation and anion. The localised distribution of positive charge at the [C-2] proton on the imidazolium ion leads to close contact with the anion, due to high acidic character of this position. The larger pyridinium ring shows better positive-charge delocalisation, leading to weaker cation-anion ionic liquid interaction, when compared with the imidazolium ring [8]. Unlike the aromatic planar structure, the positive-charge distribution around the structure and steric hindrance of alkylphosphonium are likely to prohibit close contact with the anion, resulting in a lower interaction force of the ion-pairs and lower thermal stability.

Furthermore, the weight loss thermograms of  $[\text{C}_2\text{mim}][\text{EtSO}_4]$ ,  $[\text{C}_2\text{mim}][\text{Tf}_2\text{N}]$  and  $[\text{C}_4\text{mim}][\text{Tf}_2\text{N}]$  were compared in order to evaluate the effect of anion and number of alkyl group to the thermal stability of ionic liquid, as shown in Figure 2.

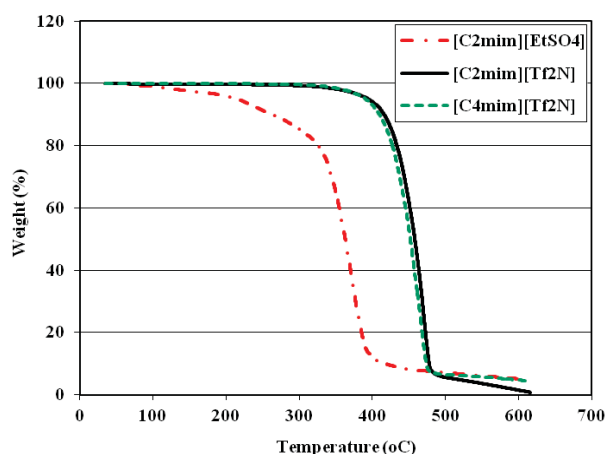


Figure 2. The weight loss thermogram of imidazolium-based ionic liquids:  $[\text{C}_2\text{mim}][\text{EtSO}_4]$ ,  $[\text{C}_2\text{mim}][\text{Tf}_2\text{N}]$  and  $[\text{C}_4\text{mim}][\text{Tf}_2\text{N}]$ .

Both thermograms of ionic liquids containing  $[\text{Tf}_2\text{N}]$  anions showed vast weight loss over 330-490 °C. The chain length of the alkyl group attached to the N atom of the imidazolium salts has little effect on the thermal stability. This result has been found in some published works with the same ionic liquids [5, 9]. In contrast with the  $[\text{Tf}_2\text{N}]$  anion, the  $[\text{EtSO}_4]$  anion showed a gradual continuous weight loss between 150 and 320 °C, followed by a bigger weight loss at 320-430°C associated with decomposition of the ionic liquid cation. The percentage of the initial weight loss reached about 18.5% corresponding to the loss of ethyl oxide via thermal degradation of the ethyl sulphate-containing ionic liquid. Accordingly,  $[\text{C}_2\text{mim}][\text{EtSO}_4]$  will decompose via 2 steps: 1) the decomposition of the ionic liquid anion (at 150-320 °C) and 2) the decomposition of the ionic liquid cation (at 320-430

°C) in agreement with data for the same type of ionic liquid in literature [10, 11]. The temperature range for decomposition of  $[\text{C}_2\text{mim}]^+$  is inside the decomposition range of the ionic liquid studied by Holbrey (300-450 °C) [10] and Fernandez (275-450 °C) [11]. The different temperature range could be explained by a number of reasons, including the temperature scan rate, the condition of equipment and the different sample weight used. The range of thermal decomposition data for the ionic liquids also implies that the different anions strongly affect the thermal stability of ionic liquids, observed for  $[\text{Tf}_2\text{N}]$  and  $[\text{EtSO}_4]$  in Figure 2.

The decomposition temperature showed a major difference between  $[\text{EtSO}_4]$  and  $[\text{Tf}_2\text{N}]$  based on imidazolium salts. The effect of ionic liquid anion on thermal stability can be explained on grounds of the coordinating ability of the anion with the cation [9]. A nucleophilic anion is an aid to either dealkylation or deprotonation of the cation in ionic liquid decomposition. The low nucleophilicity of the anion leads to hardly any proton transfer from the cation to the anion, resulting in high thermal stability of the ionic liquids. The lowest nucleophilicity shows the highest thermal stability for the  $[\text{Tf}_2\text{N}]$  anion.

### 3.2 Long-term stability

Overestimation of thermal stability from the scanning TGA data and the vapor pressure data of ionic liquids have been evaluated at below decomposition temperature [13]. Therefore, an isothermal method is proposed to determine the maximum working temperature of ionic liquids. For most of the possible applications of ionic liquids, the degradation rate is of practical importance in gas separation, especially at regeneration range between 80 and 160 °C. To screen ionic liquids for gas separation, the long-term thermal stability was determined by the isothermal method in this temperature range over 10 h in a  $\text{N}_2$  atmosphere.

Typical long-term thermal behavior of ionic liquids at constant temperature is similar to the thermogram of  $[\text{C}_2\text{mim}][\text{EtSO}_4]$  which was presented in Figure 3. The thermogram in every case consists of an initial steep portion followed by a lower linear slope. The initial steep portion is used to characterize the purity of the ionic liquids, whereas the latter slope is calculated to identify the long-term thermal stability of ionic liquids [6]. Figure 3 shows that the weight loss of  $[\text{C}_2\text{mim}][\text{EtSO}_4]$  at 160 °C stabilizes at about 18.5% after 8 hrs. This is caused by loss of ethylene oxide via thermal degradation of the ethyl sulphate containing ionic liquid, corresponding to the decomposition temperature range of the ionic liquid anion (150-320 °C) in Figure 2. There was baseline drift over the course of the isothermal scan as observed in Figure 3. This could be attributed to both water and unreacted methylimidazole loss being achieved less than 15 min at 160 °C, which is in agreement with the drying period. After the evaporation of solvent and water impurities in the initial steep step, a long-term thermal stability of the main component of the ionic liquid

should be accurately characterized in the later step. The slopes of the linear step of the ionic liquids were calculated and the mass-loss rates of the ionic liquids

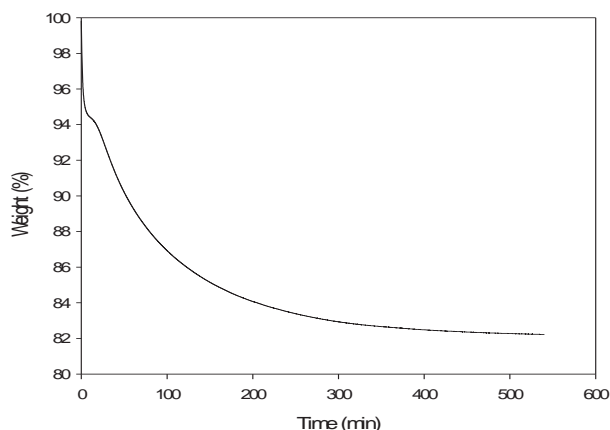


Figure 3. Isothermal thermogram of  $[C_2mim][EtSO_4]$  at 160 °C isotherm in  $N_2$  atmosphere.

Table 3: Long-term thermal stability of the ionic liquids

Ionic Liquids	T (°C)	Rate of mass loss		R <sup>2</sup>
		% wt/min ( $\times 10^{-3}$ )	% wt/hr ( $\times 10^{-2}$ )	
$[C_2mim][EtSO_4]$	80	0.99	5.99	0.9976
	120	2.24	13.44	0.9996
	160	2.39	14.32	0.9927
$[C_2mim][Tf_2N]$	80	0.35	2.09	0.9969
	120	0.39	2.38	0.9887
	160	1.19	7.13	0.9983
$[C_4mim][Tf_2N]$	80	0.13	0.76	0.9503
	120	0.21	1.27	0.9967
	160	0.48	2.88	0.9692
$[C_4mpy][Tf_2N]$	80	0.09	0.56	0.9609
	120	0.14	0.84	0.9523
	160	0.45	2.73	0.9820

Table 3 show that the higher rate of mass loss is found in the  $[C_2mim][EtSO_4]$ , when compared to all the other ionic liquids studied. The results confirmed an increased mass loss of all the ionic liquids with increasing temperature. The stability of imidazolium ionic liquid increased with increasing of alkyl chain length on the ionic liquid cation. Based on the  $[Tf_2N]$  anion, a pyridinium ionic liquid showed higher stability than imidazolium. Both the cation alkyl chain length and the cation structure can significantly affect the ionic liquids stability, whereas both were slightly different for the  $T_{start}$  values in Table 2. This implies that the scanning TGA data alone is not enough to decide ionic liquid suitability for practical applications.

#### 4. Conclusions

The results indicate limitations on the temperature range of the variety of ionic liquids used, which should

have benefits for industrial applications. The decomposition temperature in various terms of  $T_{onset}$ , and especially  $T_{start}$  for all the ionic liquids were reported. From the results, the highest thermal stability indicated that imidazolium cation and bis(trifluoromethylsulfonyl)imide anion are most stable, when compared with all the ionic liquids studied. However, the long-term thermal stability indicated less stable behaviour for imidazolium when compared to pyridinium. It is possible that the thermal stability of the ionic liquids depends on cation-anion interaction and the vapour pressure of each ionic liquid under operational conditions. Thermal stability and vapour pressure could raise concerns about the use of heat in gas separation systems, when the gas needs to be desorbed from ionic liquids as absorption media.

#### Acknowledgements

The author would like to acknowledge National Science and Technology Development Agency (NSTDA) and National Metal and Materials Technology Center (MTEC) for providing the funding for the author to carry out this project.

#### References

- [1] R. Hagiwara and Y. Ito, *J. Fluor. Chem.* **105** (2000) 221-227.
- [2] J. G. Huddleston, A.E. Visser, W. M. Reichert, H. D. Willauer, G. A. Broker and R. D. Rogers, *Green Chem.* **3** (2001) 156-164.
- [3] H. Zhao, *Chem. Eng. Commun.* **193** (2006) 1660-1677.
- [4] S. Zhang, Y. Chen, F. Li, X. Lu, W. Dai and R. Mori, *Catalysis Today*. **115** (2006b) 61-69.
- [5] H. L. Ngo, K. Lecompte, L. Hargens and A. B. McEwen, *Thermochim. Acta*. **357** (2000) 97-102.
- [6] M. Kosmulski, J. Gustafsson and J. B. Rosenholm, *Thermochim. Acta*. **412** (2004) 47-53.
- [7] H. Tokuda, K. Ishii, M. A. B. H. Susan, S. Tsuzuki, K. Hayamizu and M. Watanabe, *J. Phys. Chem. B*. **110** (2006a) 2833-2839.
- [8] Y. Hou, and R. E. Baltus, *Ind. Eng. Chem. Res.* **46** (2007) 8166-8175.
- [9] J.M. Crosthwaite, M.J. Muldoon, J.K. Dixon, J.L. Anderson and J.F. Brennecke, *J. Chem. Thermodyn.* **37** (2005), 559-568.
- [10] J.D. Holbrey, W.M. Reichert, R.P. Swatloski and G.A. Broker, *Green Chem.* **4** (2002) 407-413.
- [11] A. Fernandez, J.S. Torrecilla, J. Garcia and F. Rodriguez, *J. Chem. Eng. Data*. **52** (2007) 1979-1983.
- [12] C.P. Fredlake, J.M. Crosthwaite, D.G. Hert, S.N.V.K. Aki and J.F. Brennecke, *Chem. Eng. Data*. **49** (2004), 954-964.
- [13] O. Aschenbrenner, S. Supasitmongkol, M. Taylor and P. Styring, *Green Chem.* **11** (2009), 1217-1221.

# EFFECT OF SURFACE AREA OF NANOGRAFITE ON CAPACITANCE ENHANCEMENT OF ELECTRIC DOUBLE LAYER CAPACITOR

Santi Rattanaveeranon<sup>1</sup>, Phitsini Suvarnaphaet<sup>3</sup>, Pichet Limsuwan<sup>1,2</sup>, Piyapong Asanithi<sup>1,\*</sup>

<sup>1</sup>Applied Nanotechnology Laboratory (ANT Lab), Department of Physics, Faculty of Science, King Mongkut's University of Technology Thonburi, Bangkok 10140, Thailand

<sup>2</sup>Thailand Center of Excellence in Physics, CHE, Ministry of Education, Bangkok 10400, Thailand

<sup>3</sup> Department of Physics, Faculty of Science, Mahidol University, Bangkok 10400, Thailand

\* Author for correspondence; E-Mail: [asanithi@hotmail.com](mailto:asanithi@hotmail.com), Tel. +66 24708860, Fax. +66 2 8725254

**Abstract:** High capacitance of a capacitor is of great interest from scientific research and industrial points of view. This paper reported the preliminary data on how to increase the capacitance of electric double layer capacitor (EDLC) using nanographite film as an additional layer deposited on EDLC electrodes. Effect of surface area of nanographite on capacitance enhancement of the EDLC was discussed. Nanographites and nanographite suspension were prepared from sonication technique, i.e. sonicating graphite flakes in deionized water. Surface area of nanographites was varied by times of sonication, including 0 (without sonication), 24, 48, and 72 h. The specific surface area was measured by Brunauer-Emmett-Teller (BET) analysis using nitrogen adsorption. The analysis represented that the longer the sonication time, the higher the specific surface area of the nanographite. Physical properties of nanographites were further investigated by scanning electron microscopy (SEM), transmission electron microscopy (TEM), atomic force microscope (AFM) and Raman spectroscopy. Effect of surface area of nanographites on capacitance enhancement of the EDLC was carried out using nanographite suspensions prepared from four conditions of sonication time (0, 24, 48, and 72 h). Each nanographite suspension of the same amount and concentration was dropped and dried on EDLC electrode to form nanographite assembly or nanographite film. This nanographite film acts as an additional layer to increase the area for electron immobilization. From the current (I)-voltage (V) and capacitance (C) - frequency (f) measurements, it was found that surface area of nanographite have a significant impact on improving capacitance of the EDLC.

## 1. Introduction

Graphene is a one-atom-thick sheet of sp<sup>2</sup>-bonded carbon atoms structured in a honeycomb crystal lattice [1]. Graphene has been investigated considerably for several years due to its significant potentials for both fundamental studies and technological applications [2]. Theoretically, graphene has a large specific surface area of  $2.6 \times 10^3 \text{ m}^2 \text{ g}^{-1}$  [3], high thermal conductivity of  $3 \times 10^3 \text{ W m}^{-1} \text{ K}^{-1}$  and high Young's modulus of  $1.06 \times 10^3 \text{ GPa}$  [4]. Moreover, the hexagonal ring structure of carbon atoms provides graphene with an excellent electrical conductivity. The electrical transfer rate can

reach  $1.5 \times 10^4 \text{ cm}^2 \text{ V}^{-1} \text{ s}^{-1}$  at room temperature. In particular, it has been demonstrated that graphene shows the highest carrier mobilities exceeding  $2 \times 10^5 \text{ cm}^2 \text{ V}^{-1} \text{ s}^{-1}$  [5], which is 100 times greater than that of silicon electric double layer capacitor (EDLC) is well known many names such as supercapacitor, electrochemical capacitor or ultracapacitor. They are used for an energy storage because it has a long life, with little destruction over hundreds of thousands of charge cycles. Due to the fact that capacitor has a high number of charge-discharge cycles. (millions or more compared from 200 to 1000 times for most commercially available rechargeable batteries) [5]. EDLC has a high specific power which can exceed  $10 \text{ kW kg}^{-1}$  at an energy density of  $28.5 \text{ Wh kg}^{-1}$  [6]. Although graphene has been used widely in various applications, including EDLC, it may be struggled by the synthesis processes that are complicated and expensive [7-9].

Thus, in this paper, we reported on the possibility of using an alternative material, called nanographite that can be synthesized much easier and cheaper than graphene. Nanographite consists of several layers of graphene sheet stacked on the top of each other [4]. The planar size is on the sub-micron to micron scale. Here nanographite was synthesized by sonication treatment method. Surface area of nanographite was controlled by sonication times. Specific surface area was analyzed using Brunauer-Emmet-Teller (BET) method. Morphology of nanographite flakes was investigated by field emission scanning electron microscope (FE-SEM), atomic force microscope (AFM) and transmission electron microscope (TEM). Graphitic behavior of nanographite was evaluated using Raman spectroscopy. After physical characterization, nanographite was fabricated into the EDLC electrode. The electrical properties of the EDLC was measured measure for current (I) - voltage (V) and capacitance (C) - frequency (f) characteristics.



## 2. Materials and Methods

### 2.1 Preparation and characterization of nanographite

Graphite powder (99.99 % purity, from Lianyungang Jinli Carbon) was sieved to obtain a particle size of 20  $\mu\text{m}$ . About 5 g of sieved graphite powder was dissolved in 100 ml deionized water in a volumetric flask. Then 20  $\mu\text{l}$  of Triton X-100 (Sigma-Aldrich) was added into deionized water to enhance the dissolution of graphite in water. The graphite flakes suspended in deionized water was sonicated using ultrasonic bath at 40 kHz for four conditions: 0 (without sonication) 24, 48, and 72 h, respectively.

Field emission scanning electron microscope (FE-SEM: Hitachi S-4700 SEM) and Transmission electron microscope (TEM, JEOL 1200) were used to investigate the morphology of prepared nanographite. Raman spectroscopy (Renishaw inVia, RM 2000) with an excitation wavelength of 514 nm was used to investigate the graphitic characteristics of nanographite prepared from different times of sonication.

The Brunauer–Emmett–Teller (BET) method was employed to measure the specific surface area of each sample. Nitrogen adsorption–desorption isotherm measurements were carried out on a Micromeritics volumetric adsorption analyzer at 77 K. The total adsorbed at a relative pressure of  $0 \leq P/P_0 \leq 0.99$

### 2.2 Preparation of EDLC electrodes

Four types of the EDLC electrodes were prepared to investigate the effect of surface area of nanographite layer on the capacitance of EDLCs, including

#### 2.2.1) EDLC electrode with raw graphite (a control)

A glass slide substrate was engaged with aluminum (Al) foil. Then, gold (Au) was deposited as a film (14 nm) on the Al-foil surface using sputtering technique. Here the Au/Al electrode is obtained. For fabrication of EDLC electrode with raw graphite, assembly of raw graphite (0 h of sonication) as a film was deposited on the gold (Au) layer. Graphite film was prepared by dropping graphite suspension on the Au layer of the Au/Al substrate and kept in the oven at 35  $^{\circ}\text{C}$  for 30 min. The thickness of graphite assembly was about 2 mm. This electrode is ready for fabrication of the EDLC.

**2.2.2) EDLC electrode with nanographite prepared from 24 h of sonication:** The processes for fabrication of the Au/Al electrode are similar to those of the control sample in section 2.2.1. However, for this type of the electrode, assembly of nanographite flakes (prepared from 24 h to 72 h of sonication) as a film was deposited on the gold (Au) layer. Nanographite film was prepared by dropping nanographite suspension on the Au layer and kept in the oven at 35  $^{\circ}\text{C}$  for 30 min. The thickness of nanographite assembly was about 2 mm.

### 2.3 Fabrication and characterization of EDLCs

As shown in Fig. 1(d), a separator was made from cellulose membrane. Before used in EDLC, the membrane was soaked in KOH 30 %wt. for 30 min. Two electrodes prepared from each condition in section 2.2 were covered on both sides of the membranes as shown in Figure 1(d). The EDLC was then sealed with epoxy resin.

**2.3.1) I-V measurement:** The electrical properties of EDLCs were characterized using semiconductor parameter analyzer (Hewlett-Packard (HP type 4156B)) system with a voltage range of -0.5 to 0.5 V for measurements of current (I) - voltage (V) characteristics at 250 mV/s as shown in Figure 1(a) - (c).

**2.3.2) C-F measurement:** C-F characteristic was also measured by precision LCR meter (Hewlett-Packard (HP) type 4156B) between 100 Hz to 10 MHz. The measurements were repeated for 3 times. The capacitance of EDLC was evaluated from the discharge curves ( $dV/dt$ ) and impedance-frequency characteristics with varied frequency range from 100 Hz to 10 MHz. The capacitance was calculated from the cyclic voltammograms (CVs) according to Eq. (1) or from the charge – discharge curves according to Eq. (2)

$$C = \frac{i}{f} \quad (1)$$

where  $i$  is the average current of CV loop and  $f$  is the scan rate [8]

$$C = \frac{i}{(\Delta V/\Delta t)} \quad (2)$$

where  $i$  is the constant current for charge – discharge,  $\Delta V/\Delta t$  is the slope of the discharge curve [8]. The specific capacitance ( $C_{sp}$  in  $\text{F}\cdot\text{g}^{-1}$ ) was calculated as

$$C_{sp} = \frac{2C}{m} \quad (3)$$

where  $m$  is the mass of nanographite in each electrode. In the present study, specific capacitance calculation electrode mass was taken as 5 mg.

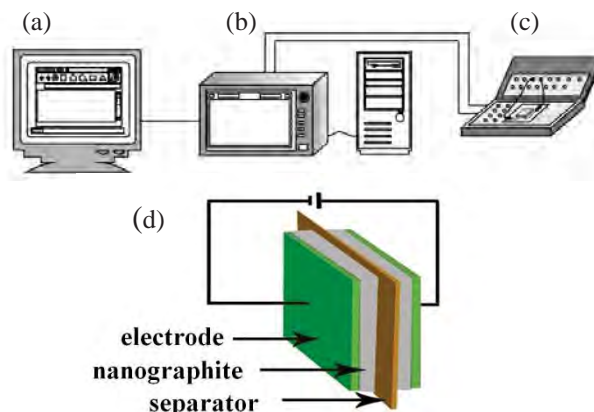


Figure 1. Schematic diagram of experimental setup (a) computer interface (b) semiconductor parameter analyzer (Agilent/HP 4156B) (c) testing box (d) a 3D-picture for an electric double layer capacitor.

### 3. Results and Discussion

#### 3.1 Nanographite

Fig. 2 shows SEM images of nanographite flakes deposited on Au/Al electrode as prepared in section 2.2. Gold was used in the electrode since it has high conductivity that could improve the charge/discharge rate of the EDLC. Au film could also increase the surface area of electrode [16].

It is clear that time of sonication affects the planar size of nanographite. It was bigger than 10  $\mu\text{m}$  for 24 h of sonication. After 72 h of sonication the planar size of nanographite was reduced to about 1  $\mu\text{m}$ . Fig. 3(a) is AFM height image of nanographite flakes prepared from 72 h of sonication. From the color bar on the right hand side of the AFM image, the brightest color refers to the thickness of about 17 nm. Thus, from this AFM data, we can estimate about 50 layers of single-sheet graphene since the interspace between single-sheet graphene is about 0.34 nm [13]. Moreover, AFM height image also represents that the thickness of nanographite is non-uniform, i.e. from the color bar the thinnest nanographite may have a thickness of about 5 nm. This information is also confirmed by TEM image in Fig. 3(b). The bright and grey colors refer to the thickness of nanographite flakes. The darker the color, the thicker the nanographite.

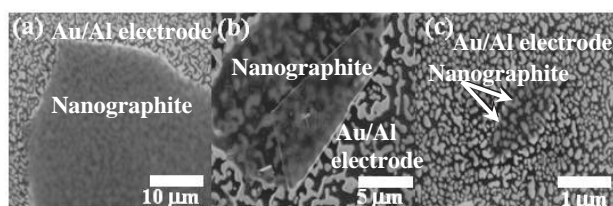


Figure 2. SEM images of nanographite flakes deposited on Au/Al electrode (a) 24 h of sonication (b) 48 h of sonication and (c) 72 h of sonication

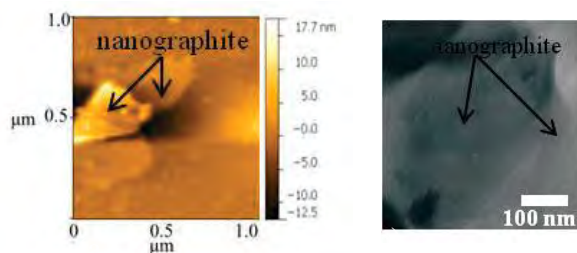


Figure 3 (a) AFM height image and (b) TEM image of nanographites prepared from 72 h of sonication

The graphitic structure of nanographite was also confirmed by Raman spectroscopy as shown in Figure 4. The technique is widely used to characterize graphitic materials, in particular to determine ordered and disordered crystal structures of graphitic materials [9]. In general, Raman spectrum of graphitic material or graphene-based materials is usually characterized by three main features, including (i) G band arising from the first order scattering of the  $E_{1g}$  phonon of  $sp^2$  C atoms (usually observed at 1575  $\text{cm}^{-1}$ ) (ii) D band

arising from disordered mode and (iii) the overtone of D line, the 2D band, at 2700  $\text{cm}^{-1}$ . [10-11]. Here, G band, D band and 2D band positions of raw graphite (0 h of sonication) are at 1582, 1350 and 2690  $\text{cm}^{-1}$ , respectively. After sonication at different time periods, G band, D band and 2D band positions of nanographite are almost the same as those of raw graphite. However, it is clearly observed that the intensity of the D-band ( $I_D$ ) in the y-axis becomes higher for longer time of sonication. This information is in agreement with SEM image in Fig. 2 that longer time of sonication can break nanographite into a smaller planar size.

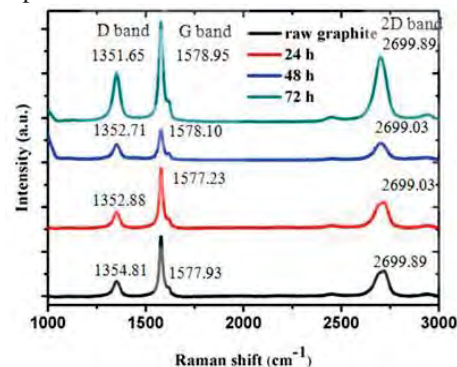


Figure 4. Raman spectra of raw graphite and nanographites prepared from different times of sonication, including 24, 48, and 72 h.

Information from BET analysis shows that surface area of nanographite can be varied using sonication treatment technique. From Table 1, it can be concluded that longer time offers higher specific surface area. Although in this experiment the surface area of nanographites prepared from different time of sonication is not different significantly, this is enough for offering a much different in capacitance of EDLC as shown in section 3.2.

Table 1. Specific surface area of raw graphite and nanographites prepared from different times of sonication, including 24, 48, and 72 h.

Type	BET specific surface area ( $\text{m}^2/\text{g}$ )
Raw graphite	7.60
Nanographite with 24 h of sonication	9.14
Nanographite with 48 h of sonication	11.92
Nanographite with 72 h of sonication	12.92

#### 3.2 Electrical properties of EDLCs

Figure 5(a) shows graph obtained from cyclic voltammetry measurements of EDLCs prepared from raw graphite (0 h of sonication) and nanographite prepared from 24, 48, and 72 h of sonication. A broad hysteresis loop (a gap between the charging and discharging curves) can be obtained from the EDLC

prepared from 72 h indicating that higher surface area of nanographite offers higher capacitance value. Figure 5(b) shows graph representing the relation between specific surface area and capacitance of EDLCs. Higher specific surface area of nanographite enhances the density of charge carrier which, consequently, increases the capacitance of the EDLC. The capacitances of EDLCs prepared from raw graphite, nanographites with 24, 48, and 72 h of sonication are  $8.78 \times 10^{-12}$ ,  $7.98 \times 10^{-10}$ ,  $7.98 \times 10^{-8}$ , and  $1.60 \times 10^{-4}$  F, respectively.

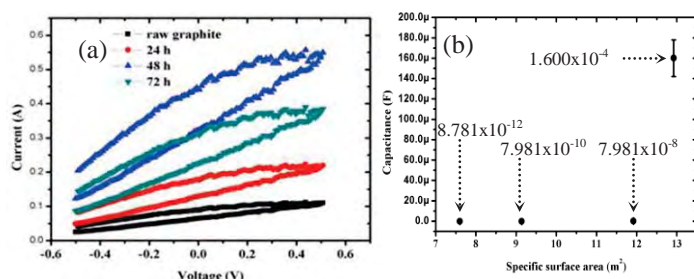


Figure 5 (a) I-V curve of raw graphite and nanographite prepared from 24, 48, and 72 h of sonication. (b) Graph representing the relation between specific surface area of EDLCs (x-axis) and their capacitances (y-axis), measured at 1 kHz.

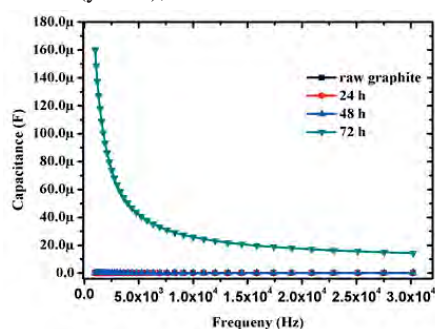


Figure 6 Variation of capacitance as a function of modulating frequency of EDLCs at a constant current density of 100 mA/g.

Figure 6. shows the decrease of capacitance as a function of modulating frequency x y of EDLC. From the graph, it can be seen clearly that surface area of nanographite plays an important role on the capacitance of the EDLC at all frequencies, especially at low frequency. Increasing modulating frequency can generate a change in dipole moment and vibration of molecule inside the EDLC. High modulating frequency makes molecules to vibrate strongly and causes the disordered in the total dipole moment [15]. Thus, at high frequency, the capacitance is decreased. For example, in the EDLC with nanographite prepared from 72 h of sonication (green line), its capacitance was about 160  $\mu$ F at low frequency and it gradually decreased to 20  $\mu$ F at high frequency.

#### 4. Conclusions

Nanographites can be synthesized easily using sonication method. Their specific surface area can be controlled by time of sonication. Longer time of

sonication offers higher surface area. The surface area of nanographite plays an important role on improving the capacitance of the EDLC. Although the capacitance of our EDLC is not reached what we expect in a Farad scale range, this preliminary data confirm that surface area of nanographite is an important factor for fabrication of EDLC in the future. Moreover, more quantitative results, such as the number of charge-discharge cycle, dielectric thickness, electrolyte, etc., will be left for future experiments.

#### Acknowledgements

This work had partially been supported by Thailand Center of Excellent in Physics (ThEP) and King Mongkut's University of Technology Thonburi under The National Research University Project. Finally, we would also like to thank Rajamangala University of Technology Rattanakosin for financial support for SR Ph.D. study.

#### References

- [1] A.K. Geim and K.S. Novoselov, *Nat. Mater.* **6** (2007) 183.
- [2] L. Qu, Y.J.B. Baek and L. Dai, *ACS Nano* **4** (2010) 1321.
- [3] I. Meric, M.Y. Han, A.F. Young, B. Ozyilmaz, P. Kim and K. L. Shepard, *Nat. Nano.* **3** (2008) 654–659.
- [4] Y.M. Lin, C. Dimitrakopoulos, K.A. Jenkins, D.B. Farmer, H.Y. Chiu, A. Grill and P. Avouris, *Science* **327** (2010) 662.
- [5] Y. Zhu, S. Murali, M. D. Stoller, K. J. Ganesh, I. W. Cai, P. J. Ferreira, A. P., R. M. Wallace, K. A. Cychosz, M. Thommes, D. Su, E. A. Stach, and R. S. Ruoff, *Science*, **332** (2011) 1537.
- [6] D. Abergel, A. Russell and V.I. Fal'ko, *App. Phys. Lett.* **91** (2007) 063125.
- [7] Y. Wang, Z. Shi, Y. Huang, Y. Ma, C. Wang, M. Chen and Y. Chen, *J. Phys. Chem. C* **113** (2009) 13103.
- [8] V. Khomenko, E. Frackowiak and F. Beguin, *Electrochimica Acta* **50** (2005) 2499–2506.
- [9] G. Wang, X. Shen, J. Yao and J. Park, *Carbon* **47** (2009) 2049–2053.
- [10] F. Tuinstra and J. L. Koenig, *J. Chem. Phys.* (1970), 1126.
- [11] A. C. Ferrari and Robertson, *J. Phys. Rev. B* **61** (2000) 14095.
- [12] S. Stankovich, A. A. Dikin, R. D. Piner, K. A. Kohlhaas, A. Kleinhammes, Y. Y. Jia, Y. Wu and S. Nguyen, R. S. Ruoff, *Carbon* **45** (2007) 1558.
- [13] V. Y. Osipov, T. Enoki, K. Takai, K. Takahara, M. Endo and T. Hayashi, *Carbon* **44** (2006) 1225–1234.
- [14] E. Barrett, L. Joyner and P. Halenda, *J. Am. Chem. Soc.* **73** (1951) 373–80.
- [16] P. Mitchell, *Solid State Physics*, Vol. 5, Wiley, New York (1996), pp. 61–78.
- [17] G. Gourdin, A. Meehan, T. Jiang, P. Smith and D. Qu, *J. Pow. Sour.* **196** (2010) 523–529.



# EFFECT OF PLASTICIZERS ON CHARACTERISTICS OF BACTERIAL CELLULOSE/ALGINATE/GELATIN COMPOSITE

Sutasinee Seetabhawang<sup>1</sup>, Muenduen Phisalaphong<sup>1\*</sup>

<sup>1</sup> Chemical Engineering Research Unit for Value Adding of Bioresources, Department of Chemical Engineering, Faculty of Engineering, Chulalongkorn University, Phayathai Road, Patumwan, Bangkok, 10330 Thailand

\*E-mail: [Muenduen.p@chula.ac.th](mailto:Muenduen.p@chula.ac.th), Tel. +66 22186875

## Abstract

Bacterial cellulose (BC) - alginate (A) - gelatin (G) composite films were fabricated by casting and curing at room temperature. The preparation of blend BC/A/G films was carried out at various proportions. The FTIR result indicated intermolecular interactions among the hydroxyl group of cellulose, the carboxyl group of alginate and the amide group of gelatin, which might disrupt the hydrogen bonding between cellulose fibers. The BC/A/G films were then plasticized with glycerol (Gly), sorbitol (S) and the mixture of glycerol and sorbitol (GS) and the effect of plasticizers on film characteristics was investigated. Glycerol was found to be a better plasticizer than sorbitol. It was shown that the BC/A/G film with the addition of glycerol to gelatin solution at the weight ratio of 2:10 has superior mechanical and chemical stability. At the optimal BC/A/G ratio of 60/20/20, the tensile strength, elongation at break and water absorption capacity of the film were 185.4 MPa, 3.1% and 333.6%, respectively. The Gly-plasticized BC/A/G films were found to be more flexible, with slightly significant difference in tensile strength compared to the one without the plasticizer.

**Keywords** Plasticizer; Glycerol; Bacterial cellulose; Alginate; Gelatin

## 1. Introduction

Biopolymer films are attractive for food packaging applications in order to enhance food quality and reduce pollution of traditional plastic films. Biopolymer films could be prepared from proteins (gelatin, casein etc.) or polysaccharides (bacterial cellulose, starch, alginate etc.) or their combination.

Bacterial cellulose (BC) is a linear polysaccharide of glucose units, which can be biosynthesized by *Acetobacter xylinum* [1]. Although BC has many feature properties such as high water holding capacity, hydrophilicity, superior water resistance and high mechanical strength, it exhibits poor rehydration ability after drying due to high crystallinity [2].

Alginate is a linear polysaccharide copolymer of (1-4)-linked  $\beta$ -D-mannuronic acid (M) and  $\alpha$ -L-guluronic acid (G) monomers, which can be isolated from algae and seaweed. It forms well-characterized hydrogel with water resistance by adding divalent cations as crosslinked agents such as  $\text{CaCl}_2$  [3].

Gelatin is a water soluble protein, which is produced by hydrolysis of animal collagen. Gelatin is unique among hydrocolloids in forming thermo-reversible

structure. However, it exhibits poor mechanical properties such as brittleness and fragility. Due to its hydrophilic nature, gelatin has poor water resistance when exposes to wet and humid conditions [4].

Gelatin could be added to provide the necessary workability to composite packaging film. Plasticizers could reduce intermolecular hydrogen bonding while increasing intermolecular spacing [5]. Therefore, it can increase film flexibility, decrease brittleness and avoid shrinking during handling and storage. The selection of plasticizer for specified system normally depends on the compatibility and permanence of the plasticizer [6]. Glycerol and sorbitol were the most used gelatin plasticizers [7]. Plasticizing effect of glycerol on alginate-based film was reported [8].

This work aims to develop composite films from the blends of BC, alginate and gelatin (BC/A/G) and investigate the effects of the blend composition and type of plasticizer on the film characteristics. The physical, chemical and mechanical properties of the films were determined for further application as packaging materials.

## 2. Materials and Methods

### 2.1 Materials

BC pellicles (size 1 cm  $\times$  1 cm  $\times$  1 cm) were supplied by the laboratory of Pramote Tammarate (the Institute of Food Research and Product Development, Kasetsart university, Bangkok). Sodium alginate was supplied by Carlo Erba, Italy. Gelatin from porcine skin type B was supplied by Fluka (isoelectric point 5.2, 180 g bloom). Glycerol (99.5% v/v) was supplied by Ajax Fine Chem Pty Ltd, Australia.

### 2.2 Preparation of BC slurry

The BC pellicles was treated with 1.0% (w/v) NaOH at room temperature (28-30°C) for 24 h to remove bacterial cells and rinsed with deionized water (DI) until the pH was 7.0. Then the purified BC pellicles were crushed and homogenized to form BC slurry by using a homogenizer at ambient temperature.



### 2.3 Preparation of Sodium alginate solution

Sodium alginate of 2% (w/v) was dissolved in distilled water with constant stirring at room temperature to form gel-like solution.

### 2.4 Preparation of Gelatin solution

Gelatin powder from porcine skin (15 g) was hydrated with distilled water at room temperature and heated up to  $50 \pm 5$  °C with constant stirring until completely dissolved to obtain the 15% (w/v) gelatin solution.

### 2.5 Preparation of BAG films

The BC slurry was mixed with the alginate and gelatin solutions at different ratios to form bacterial cellulose-alginate-gelatin blend mixtures. Glycerol and sorbitol were added as a plasticizer at a certain concentration ratio (0-3 g per 10 g gelatin solution). The mixture was thoroughly stirred at  $50 \pm 5$  °C until the homogeneous mixture was formed and subsequently it was poured into polystyrene petri plates and incubated at room temperature for 2 days to form films with an average thickness of  $50 \pm 10$  µm. After that it was cross-linked by an aqueous solution of 1% (w/v)  $\text{CaCl}_2$  for 1 hour and rinsed with distilled water to remove the excess chlorides. The cross-linked gel was air-dried at room temperature and stored in plastic bag before use.

### 2.6 Film Thickness

Film thickness was measured with a micrometer thickness gage (Mitutoyo, Japan) MYL 314 with a sensitivity of 0.01 mm. The film thickness was the average value determined from 10 measurements of each sample.

### 2.7 Fourier Transform Infrared Spectroscopy (FTIR)

FTIR spectroscopy was used to identify the chemical structure of the films. The FTIR spectra of the films were measured at wave numbers ranging from 4000 to 400  $\text{cm}^{-1}$  with a Nicolet (United States) SX-170 FTIR spectrometer.

### 2.8 Water Absorption Capacity

Water absorption capacity (WAC) was determined by immersing the pre-weighted of dried BC/A/G films in distilled water at room temperature until equilibration. After that the films were removed from the water and excess water at the surface of the films was blotted out with soft paper. The weights of the re-swollen films were measured. The procedure was repeated until no further weight change was observed. The water content was calculated using the following equation:

$$\% \text{WAC} = (W_s - W_d) / W_d \times 100 \quad (1)$$

Where  $W_s$  is the weight of re-swollen samples (g);  $W_d$  is the weight of dry samples (g). The WAC was the average value determined from 3 measurements.

### 2.9 Mechanical Strength

All the films under the study in dry and re-swollen forms were tested for tensile strength and elongation at break. The film samples were cut into strip-shaped specimens of 20 mm width and 10 cm long (70 mm between the grips). The maximum tensile strength and break strain of the film samples were determined with a Hounsfield (London, UK) H10KM universal testing machine. The test conditions followed ASTM D 882. The tensile strength and break strain were the average values determined from 5 specimens.

## 3. Results and Discussion

### 3.1 Fourier transforms infrared spectroscopy (FTIR)

The FTIR spectra of the BC/A/G films without and with plasticizer adding at a ratio of 60/10/30, 60/20/20 and 60/30/10 were determined with the wavenumber ranging from 4000 to 400  $\text{cm}^{-1}$ , as shown in Figure 1. The BC/A/G films at ratio of 60/10/30, 60/20/20 and 60/30/10 appeared peaks of main eight functional groups. The C-O-C stretching vibration of BC and alginate is observed at about 1026-1059  $\text{cm}^{-1}$ , the O-H and N-H stretching vibration at about 3400-3404  $\text{cm}^{-1}$ , the H-O-H bending vibration of absorbed water molecules consisting in the structure of BC appeared at about 1613-1650  $\text{cm}^{-1}$  [9] which it also can be assigned to the C=O stretching. The ester group stretching vibration (-COO) of alginate appeared at 1423-1424  $\text{cm}^{-1}$ . The symmetric of N-H bending vibration in amide of gelatin appeared at 1535  $\text{cm}^{-1}$ , and the C-N stretching bands appeared at about 1241-1316  $\text{cm}^{-1}$  of gelatin.

The FT-IR spectra of BC/A/G films with adding plasticizers exhibited the characteristic absorption bands with no appearance of new peaks as shown in Figure 1D, E and F. For the BC/A/G films at ratios of 60/20/20 with glycerol, sorbitol and the mixture of glycerol and sorbitol (GS) adding, multiple shifted bands were observed as follows. The C-O-C stretching peak were shifted to 1035, 1035 and 1034  $\text{cm}^{-1}$  and the O-H and the N-H stretching bands were shifted to 3401, 3400 and 3393  $\text{cm}^{-1}$ , respectively. The H-O-H bending peaks were shifted to 1650, 1635 and 1649  $\text{cm}^{-1}$  and the -COO stretching peaks were shifted to 1431, 1424 and 1431  $\text{cm}^{-1}$ , respectively. The symmetric of N-H bending peaks were shifted to 1535, no peak and 1541  $\text{cm}^{-1}$  and the C-N stretching peaks were shifted to 1243, 1250 and 1243  $\text{cm}^{-1}$ , respectively.

A comparison between types of plasticizer on BC/A/G films indicated that FTIR peaks of the films with glycerol adding tended to increase in amplitudes of the gelatin characteristic absorption band and free water peaks [10]. The C=O stretching was shifted to higher frequency at 1650  $\text{cm}^{-1}$  and appeared N-H bending vibration of at 1535  $\text{cm}^{-1}$ .

These shifts could be attributed to intermolecular interactions between the hydroxyl group of cellulose,

the carboxyl group of alginate and amide group of gelatin.

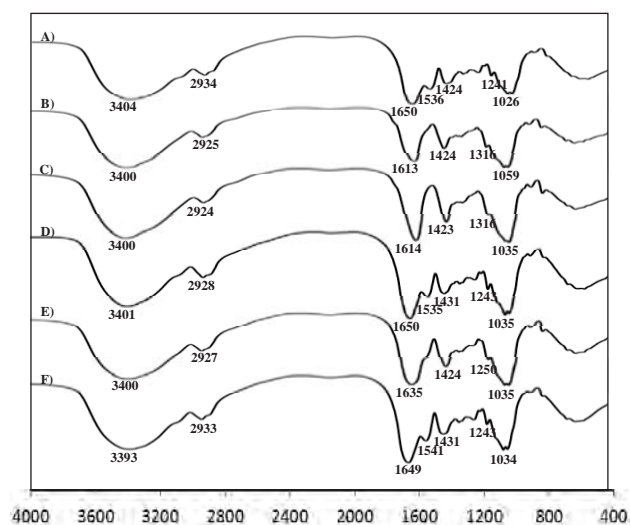


Figure 1. FT-IR of BC/A/G films at a ratio of 60/10/30 (A), 60/20/20 (B), 60/30/10 (C) and BC/A/G films at a ratio of 60/20/20 with glycerol (D), sorbitol (E) and the mixture of glycerol and sorbitol (F) addition, respectively.

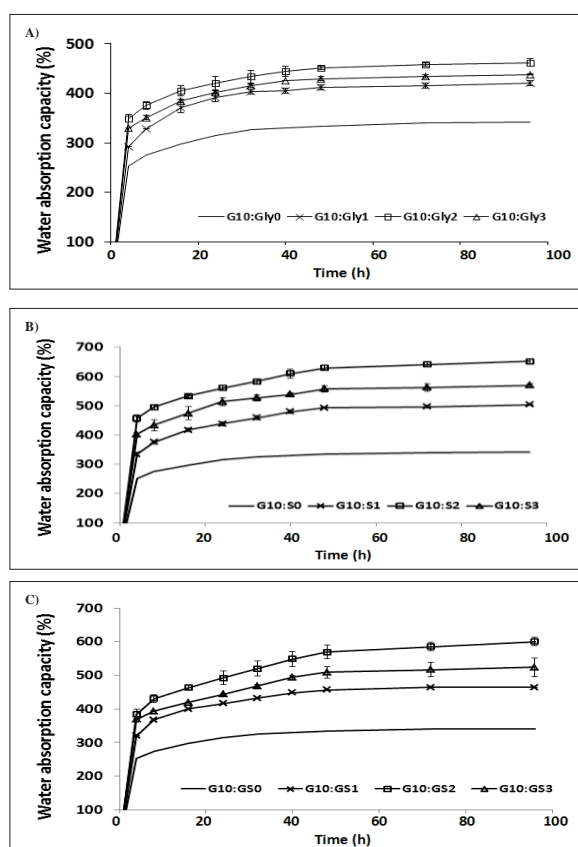


Figure 2. Water absorption capacity (%) of the composite films: BC/A/G films at a ratio of 60/20/20 with glycerol (A), sorbitol (B) and the mixture of glycerol and sorbitol (C); G:Gly, G:S and G:GS refer to a ratio of gelatin to glycerol, sorbitol and the mixture of glycerol and sorbitol (w/w), respectively.

### 3.2 Water Absorption Capacity (WAC)

The WAC of the BC/A/G films in DI water is shown in Figure 2. The result indicated that the WAC values were correlated with the gelatin content. The WAC of the BC/A/G films at a ratio of 60/10/30 was 411.9% or almost two times of that at a ratio of 60/30/10, which should be due to very hydrophilic nature and more flexible structure of gelatin. Similar observations were previously reported in modified BC by BC/gelatin composites via cross-linking [11].

The addition of plasticizer into the BC/A/G films up to certain amount as a plasticizer enhances WAC of the BC/A/G films. The results indicated that WAC increased with the increase of plasticizer content. However, excess of plasticizer at a ratio of plasticizer to gelatin solution more than 2:10 (w/w) caused the decrease of the WAC, which should be due to the migration of plasticizer from the re-swollen film surface. Similar observations were previously reported in DCMC crosslinked gelatin edible film [12]. The plasticized films at a ratio of plasticizer to gelatin at 2:10 (w/w) showed better rehydration ability and water absorption capacity.

For the effect of type of plasticizers, WAC of the BC/A/G films plasticized with sorbitol (S) had a greater WAC than that plasticized with the mixture of glycerol and sorbitol (GS) and glycerol (Gly), respectively. Because sorbitol is polyol containing multiple hydroxyl groups in the structure, it could attract with -OH of water molecules.

### 3.3 Mechanical Properties

Tensile strength and elongation at break of the BC/A/G films in dry state were shown in Figure 3A and B. The BC/A/G films exhibited significantly improved mechanical properties. Overall, the BC/A/G films at a ratio of 60/20/20 (w/w) showed superior mechanical properties; the tensile strength and elongation at break were at 181.5 and 2.8%, respectively. The results showed that there was no significant difference between the mechanical properties of the dried films with and without addition of glycerol as plasticizer. The function of plasticizer is to enhance the flexibility and plasticity to the films but it might not affect some functional properties [13].

Tensile strength and elongation at break of the films in wet state were shown in Figure 4 A and B. In wet state, the tensile strength and elongation at break of the BC/A/G film at a ratio of 60/20/20 were 9.6 MPa and 30.3%, respectively. Since both gelatin and glycerol are hydrophilic and high flexible components, significantly improved elongation at break of the BC/A/G films in re-swollen form with the addition of glycerol, sorbitol and the mixture of glycerol and sorbitol (GS) as plasticizer was observed. For the BC/A/G film at ratios of 60/10/30, 60/20/20 and 60/30/10 with glycerol adding as plasticizer, the elongation at break increased to 22.9%, 44.6% and 45.7%, respectively.

It was found that tensile strength of the re-swollen BC/A/G films was reduced with the addition of plasticizer. In the wet state, the tensile strength of the BC/A/G films plasticized with Gly was more than that plasticized with GS and S, respectively. Therefore, gelatin and glycerol helped to improve high flexibility and lowered tensile strength of the BC/A/G films in the wet state. It was previously reported that the addition of glycerol to gellan films increased extensibility, but reduced the mechanical strength [14] and the softness and flexibility of gelatin-based films could be improved by the addition of plasticizers.

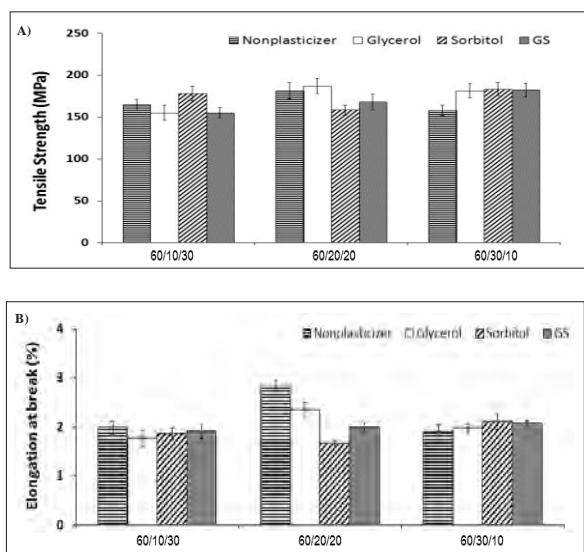


Figure 3. Mechanical properties of BC/A/G films in dry state without and with plasticizer addition: Tensile strength (A) and Elongation at break (B).

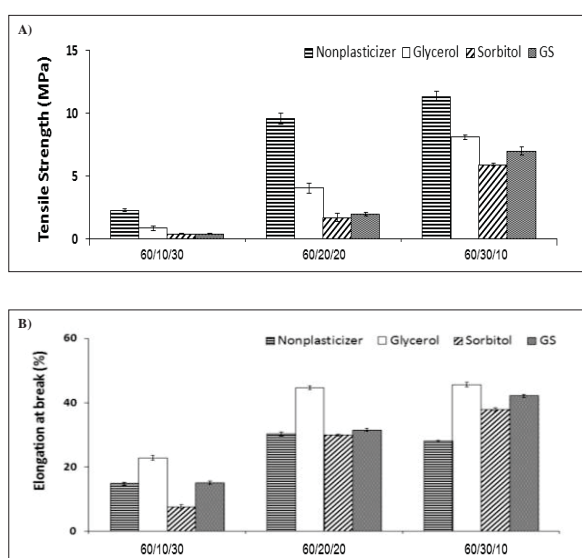


Figure 4. Mechanical properties of BC/A/G films in wet state without and with plasticizer addition: Tensile strength (A) and Elongation at break (B).

## 4. Conclusions

The BC/A/G films were successfully prepared by casting technique. Generally, the composite films shrink in dry state so that plasticizer is essential to improve the weakness of the films. The results indicated that glycerol is suitable plasticizer for BC/A/G films. The composite film with BC/A/G at a ratio of 60/20/20 has superior mechanical properties for both dry and wet states. Glycerol is a hydrophilic plasticizer so that it enhanced water absorption capacity and improved elongation at break of the re-swollen films. However, excess glycerol content could attribute to the migration of glycerol. The optimal ratio of glycerol to gelatin was at 2:10 (w/w). This biodegradable film has high potential for food packaging applications in order to reduce pollution caused by non-biodegradable plastic films.

## Acknowledgements

The authors are grateful for the financial support from Integrated Innovation Academic Center: IIAC Chulalongkorn University Centenary Academic Development (Project Code: CU56-AM01) and partially supported by the Higher Education Research Promotion and National Research University Project of Thailand, Office of the Higher Education Commission (Project Code: AM667A). M.P. also received support from TRF, contract grant number RMU 5380024.

## References

- [1] K. Mühlethaler, *Biochim. Biophys. Acta. (Amst.)* **3** (1949) 35-527.
- [2] H.C. Huang, L.C. Chen, S.B. Lin, C.P. Hsu, and H.H. Chen, *Bioresour. Technol.* **101** (2010) 6084-6091.
- [3] N. Nwe, T. Furukie and H. Tamura, *Process Biochem.* **45** (2010) 457-466.
- [4] P.J.A. Sobral, F.C. Menegalli, M.D. Hubinger and M.A. Roques, *Food Hydrocolloids*. **15** (2001) 423-432.
- [5] J.L. Audic and B. Chaufer, *Eur. Polym. J.* **41** (2005) 1934-1942.
- [6] L.H. Cheng, A.A. Karim and C.C. Seow, *J. Food Sci. E: Food Engineering and Physical Properties*. **71**(2) (2006) 62-67.
- [7] M. Thomazine, R.A. Carvalho, P.J.A. Sobral, *J. Food Sci.* **70**(3) (2005) 172-176.
- [8] M.A. Silva, A.C.K. Bierhalz and T.G. Kieckbusch, *Carbohydr. Polym.* **77**(4) (2009) 736-42.
- [9] J. Lojewska, P. Miśkowiec, T. Lojewski and L.M. Proniewicz, *Polym. Degrad. Stab.* **88** (2005) 512-520.
- [10] P. Berge and P.J.A. Sobral, *Food Hydrocolloids*. **21** (2007) 1285-1289.
- [11] S.T. Chang, L.C. Chen, S.B. Lin and H.H. Chen, *Food Hydrocolloids*. **27**(1) (2012) 137-144.
- [12] C. Mu, J. Guo, X. Li, W. Lin and D. Li, *Food Hydrocolloids*. **27**(1) (2012) 22-29.
- [13] F.M. Vanin, P.J.A. Sobral, F.C. Menegalli, R.A. Carvalho and A.M.Q.B. Habitante. *Food Hydrocolloids*. **19** (2005) 899-907.
- [14] L. Yang and A.T. Paulson, *Food Res. Int.* **33** (2000) 563-570.

# EFFECT OF FILLER PARTICLE SIZE ON MECHANICAL AND THERMAL PROPERTIES OF HIGH DENSITY POLYETHYLENE FILLED WITH BIO-FILLER FROM EGGSHELL WASTE

Wanikorn Buakaew<sup>1,2</sup>, Yupaporn Ruksakulpiwat<sup>1</sup>, Nitinat Suppakarn<sup>1</sup>, Wimonlak Sutapun<sup>1\*</sup>

<sup>1</sup>School of Polymer Engineering, Institute of Engineering, Suranaree University of Technology, Nakhon Ratchasima, 30000 Thailand

<sup>2</sup>Center of Excellence on Petrochemical, and Materials Technology, Chulalongkorn University, Bangkok, 10330 Thailand

\*Author for correspondence; E-mail: wimonlak@sut.ac.th, Tel. +66 44 224435, Fax. +66 44 224605

**Abstract:** In this work, eggshell calcium carbonate in a form of powder was used as bio-filler for HDPE. Three different average sizes of eggshell powder (ESP), 35.30, 20.35 and 13.96  $\mu\text{m}$  were used. The effect of eggshell particle size on mechanical and thermal properties of 20 wt.% ESP/HDPE composites was investigated. It was found that HDPE composites prepared with three different particle sizes of ESP had no significant differences in Young's modulus, yield strength and ultimate stress. HDPE filled with smaller particle size of ESP had higher elongation at break and impact strength than the one with larger particle size. In addition, the HDPE composite with smaller particle size of ESP had higher decomposition temperature of HDPE matrix and ESP filler. On the other hand, melting temperature crystallizing temperature and degree of crystallinity of HDPE composite were not influenced by ESP particle size.

## 1. Introduction

High density polyethylene (HDPE), a semi-crystalline polymer, is widely used as a commodity polymer with high-tonnage production due to its distinctive mechanical and physical properties. Several particulate mineral fillers as calcium carbonate, clay, talc, silica, mica and wollastonite etc., have been incorporated into HDPE [1]. The main function of the fillers is to improve certain properties such as mechanical properties weathering resistance and environmental stress cracking resistance, as well as to reduce material cost. Calcium carbonate as ground calcium carbonate (GCC) and precipitated calcium carbonate (PCC) are the most consumed reinforcing filler for HDPE, more than 60% of total filler usage [2]. By the way, raw material as sedimentary rock for calcium carbonate production takes so long time for accumulating in nature. In order to prolong this natural resource, other source for calcium carbonate should have been looking for. Eggshell calcium carbonate is one of good replacements for calcium carbonate filler due to its renewability, availability and high content in calcium carbonate (94 wt.%). Most importantly, it is regenerated from avian such as hen, duck and bird. It was reported that eggshell calcium carbonate was successfully applied as reinforcing filler for LDPE [3], PP [4] and epoxy [5]. The mechanical and flow

properties of those polymers filled with eggshell powder were comparable to those properties of the polymers filled with GCC [6]. In addition, ESP content of less than 20-30 wt.% would not significantly affect deformation and failure behavior of the filled polymers under tensile loading. Apart from filler content, filler particle size is one of important material parameters affecting physical properties of particulate filled polymers [7].

The objective of this study was to investigate the effect of ESP particle size (35.30, 20.35 and 13.96  $\mu\text{m}$ ) on mechanical and thermal properties of HDPE filled with ESP.

## 2. Materials and Methods

### 2.1 Materials

High density polyethylene, HDPE, (EL-Lene<sup>TM</sup> H5814J) with a melt flow index of 14 g/10 min and a density of 0.958 g/cm<sup>3</sup> was purchased from SCG Chemicals Co., Ltd. Three different sizes of eggshell powder were used, ESP 1, ESP 2 and ESP 3. They were prepared from Chicken eggshell waste of Bolvans Goldlind and ISA Brown (hybrid) breeds, supplied by SUT farm, Suranaree University of Technology. Their average particle size (D [4,3]), size distribution, and BET surface area are shown in Table 1.

Table 1: Volume average particle size, size distribution and BET surface area of ESP fillers.

Eggshell Powder	Particle size distribution ( $\mu\text{m}$ )				BET surface area ( $\text{m}^2/\text{g}$ )
	D [4,3]	D [0,1]	D [0,5]	D [0,9]	
ESP 1	35.30	2.33	33.69	74.41	3.71
ESP 2	20.35	3.46	18.47	39.60	3.90
ESP 3	13.96	2.64	12.37	27.56	4.23

### 2.2 HDPE composite preparation

HDPE composites were prepared with ESP 1, ESP 2 and ESP 3 at 20 wt.% eggshell powder in an internal mixer (Hakke, Rheomix 3000p). Eggshell powder was dried in an oven overnight at 70°C before mixed with



HDPE. HDPE was first melted for 5 min in the mixer and eggshell powder was then added. The mixing process was operated at 190°C under a rotor speed of 70 rpm and mixing time of 15 min. Subsequently, the HDPE composites were pelletized by a grinding machine before further molded into test specimens using an injection machine (Chuan Lih Fa, CLF 80T). The injection process was carried out at a melting temperature of 200°C, a screw speed of 208 rpm, an injection speed of 19.5 mm/sec, a holding pressure of 840 kg/cm<sup>2</sup> and a mold temperature of 30°C.

### 2.3 ESP characterization

The X-ray diffractometer (Bruker, D5005) was used to determine crystal polymorph of calcium carbonate eggshell and ground CaCO<sub>3</sub>. The measurement was carried out using CuK<sub>α</sub> radiation ( $\lambda = 0.15406$  nm) with an accelerating voltage of 40 kV and a current of 40 mA,  $2\theta$  between 5 and 70°C, a scan step of 0.02°, and a scan speed of 0.5 s/step.

Thermal decomposition temperature of eggshell powder was monitored by a thermogravimetric analyzer, TGA (Mettler Toledo, TGA/DSC1) with a heating rate of 20°C/min under a nitrogen atmosphere.

Particle morphology of eggshell powder was investigated by a scanning electron microscope (JEOL, JSM 5800LV) with an accelerating voltage of 14 kV.

### 2.4 ESP/HDPE composite characterization

Tensile properties of neat HDPE and ESP/HDPE composites were determined in uniaxial tension using a universal testing machine equipped with of 5 kN load cell, (Instron, Series 5565). The tensile test was conducted in accordance with ASTM D638 at a crosshead speed of 10 mm/min.

Unnotched Izod impact strength of neat HDPE and ESP/HDPE composites was evaluated on an impact tester (Atlas, BPI) equipped with a pendulum hammer of 5.4 J, following ASTM D256.

Thermal decomposition temperature of neat HDPE and ESP/HDPE composites was monitored by a thermogravimetric analyzer, TGA (Mettler Toledo, TGA/DSC1) with a heating rate of 20°C/min under a nitrogen atmosphere.

Melting temperature crystallizing temperature and degree of crystallinity of neat HDPE and ESP/HDPE composites were determined using a differential scanning calorimetry, DSC (Perkin Elmer, UNIX DSC-7). For DSC analysis, a sample was heated to 180°C and subsequently cooled to 25°C under a nitrogen atmosphere with a heating and cooling rate of 10°C/min. Melting and crystallizing temperatures were obtained according to ASTM D3417. Degree of crystallinity was calculated using the equation shown below.

$$X_c (\%) = [(\Delta H_f)/(\Delta H_{f*})(W_f)] \times 100 \quad (1)$$

Where,  $H_f$  is the enthalpy of fusion of the sample,  $H_{f*}$  is the enthalpy of fusion of a 100% crystalline HDPE

as 292.60 J/g [2] and  $W_f$  is the weight fraction of HDPE matrix.

Freeze fractured surface morphology of neat HDPE and ESP/HDPE composites was investigated by a scanning electron microscope (JEOL, JSM 5800LV) operated at an accelerating voltage of 14 kV. The HDPE and composites were fractured under liquid nitrogen and coated with gold for 10 min.

## 3. Results and Discussion

X-ray diffraction (XRD) patterns of ESP 1, ESP 2 and ESP 3, and ground CaCO<sub>3</sub> were comparatively illustrated in Figure 1. The pattern of ESP and ground CaCO<sub>3</sub> was well matched. The strongest peak of the calcium carbonate eggshell occurred at  $2\theta$  of 29.5°. The XRD patterns of eggshell powder are the pattern of calcite polymorph with a crystal system of rhombohedral hexagonal structure ( $a = 4.98900$ ,  $b = 4.98900$ ,  $c = 17.06200$ ,  $\alpha = 90^\circ$ ,  $\beta = 90^\circ$ ,  $\gamma = 120^\circ$ )

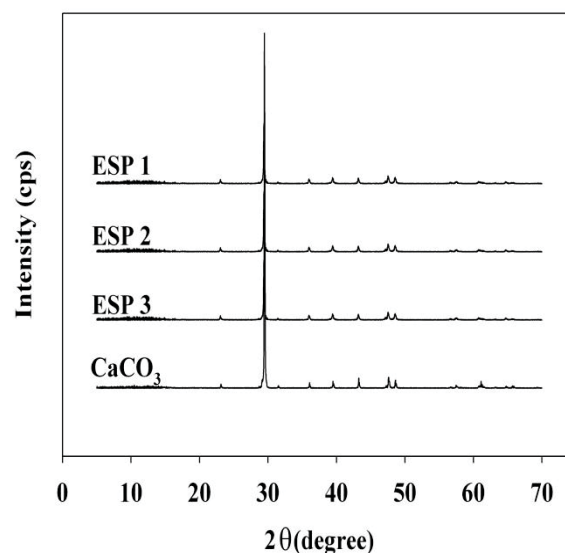


Figure 1. XRD patterns of ground CaCO<sub>3</sub>, ESP 1, ESP 2, and ESP 3.

TGA and DTGA curves as well as SEM micrographs of ESP 1, ESP 2 and ESP 3 were shown in Figure 2 (a) and 2 (b), respectively. From TGA and DTGA curves, eggshell powder shows two major thermal transitions. The first transition occurred at 230-330°C, was derived from the decomposition of organic matter of eggshell matrix and membrane. The second transition at 814°C, 809°C and 777°C were derived from thermal decomposition of eggshell CaCO<sub>3</sub> of ESP 1, ESP 2 and ESP 3, respectively [8]. The results showed that thermal stability of eggshell CaCO<sub>3</sub> decreased with smaller particle of the eggshell. The smaller particle size had larger surface area that contributes to high efficiency of heat transfer [9]. Therefore, with larger surface, ESP decomposed at lower temperature. SEM micrographs of ESP, in Figure 2 (b), show that ESP particle was in cubic and irregular shape.

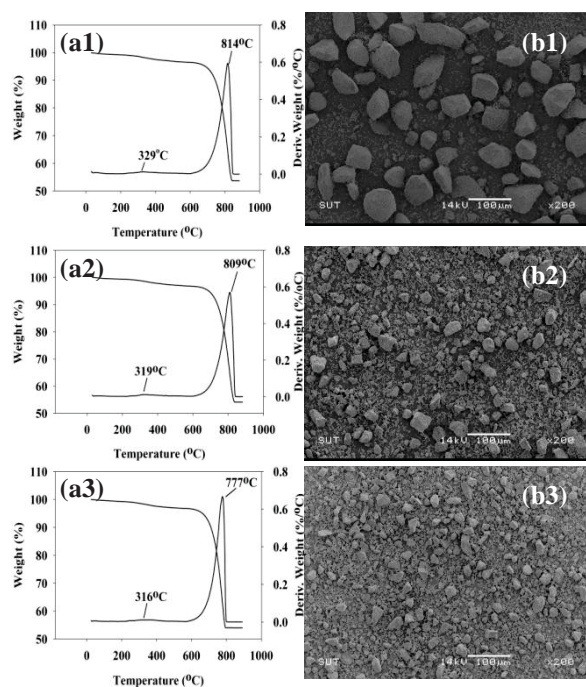


Figure 2. TGA and DTGA curves (a) and SEM micrographs (x200) (b), of ESP 1 (1), ESP 2 (2), and ESP 3 (3).

For tensile properties, ESP particle size did not affect Young's modulus, ultimate stress, and yield strength, of filled HDPE composites, as observed from Figure 3 (a) and 3 (b). However, elongation at break of ESP/HDPE composite depended on particle size of ESP. Elongation at break of the composite with smaller ESP particle size (ESP 2 and ESP 3) was higher than that of the composite with the larger size of ESP 1. This is an indication that, under tensile deformation, the HDPE composite with ESP particle size smaller than 35.30  $\mu\text{m}$  was able to absorb more applied energy prior to the composite rupture. However, under impact loading, the ability to absorb impact energy of those composites prepared with ESP 1, ESP 2, and ESP 3 was insignificantly different.

From TGA and DTGA curves shown in Figure 4, neat HDPE thermally decomposed as a single transition at 483°C whereas ESP/HDPE composites decomposed with two thermal transitions. The first transition due to decomposition of HDPE matrix was at 485°C, 490°C and 492°C for HDPE filled with ESP1, ESP2, and ESP3, respectively. The second transition derived from decomposition of eggshell calcium carbonate was around 750°C [10]. The ESP particle size did influence thermal decomposition of HDPE matrix. The decomposition temperature of HDPE matrix and ESP filler were increased with decreasing ESP particle size. This was possibly due to the increased efficiency of heat transfer of smaller particle of ESP [9].

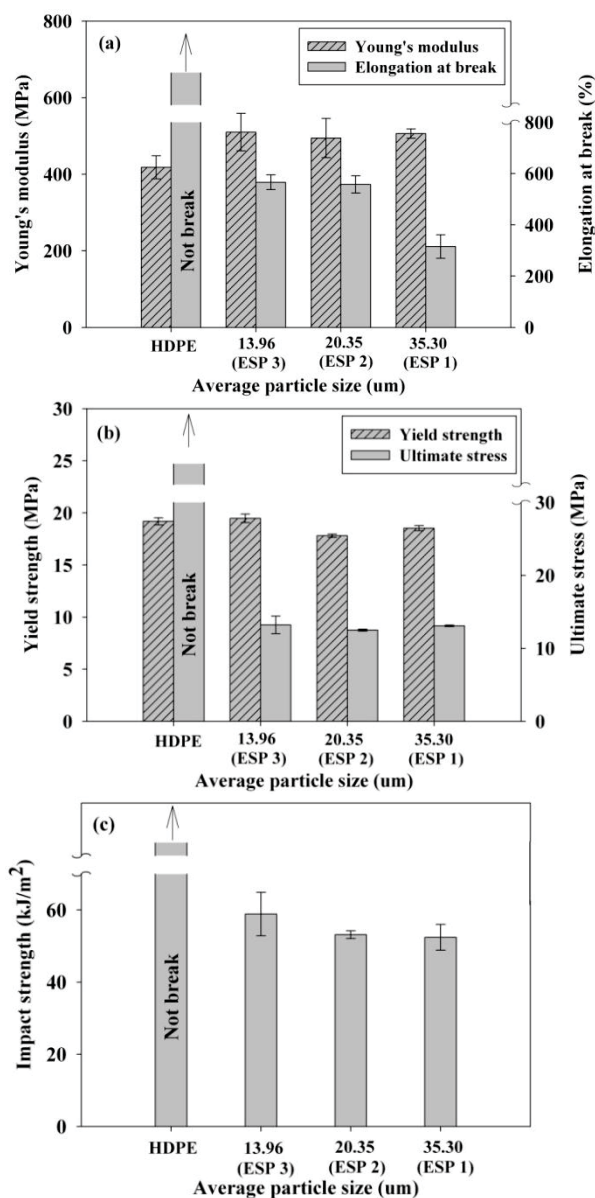


Figure 3. Plots of Young's modulus and elongation at break (a), yield strength and ultimate stress (b), and impact strength (c) of ESP/HDPE composite vs ESP particle size.

As shown in Table 3, ESP particle size did not significantly affect melting temperature, crystallizing temperature and degree of crystallinity of HDPE matrix of HDPE filled with ESP.

Fracture surface morphology of 20 wt.% ESP/HDPE composites with ESP particle sizes of 35.30 (ESP 1) and 13.96 (ESP 3)  $\mu\text{m}$  are shown in Figure 5 (a) and 5 (b). It was observed that interfacial adhesion between ESP surface and HDPE matrix was not good. Several holes were observed on the fracture surface. These holes were caused from detaching of ESP particle from HDPE matrix. The surface topology of HDPE filled with ESP 1 and ESP 3 indicated that the filled HDPE still ruptured in a ductile manner.

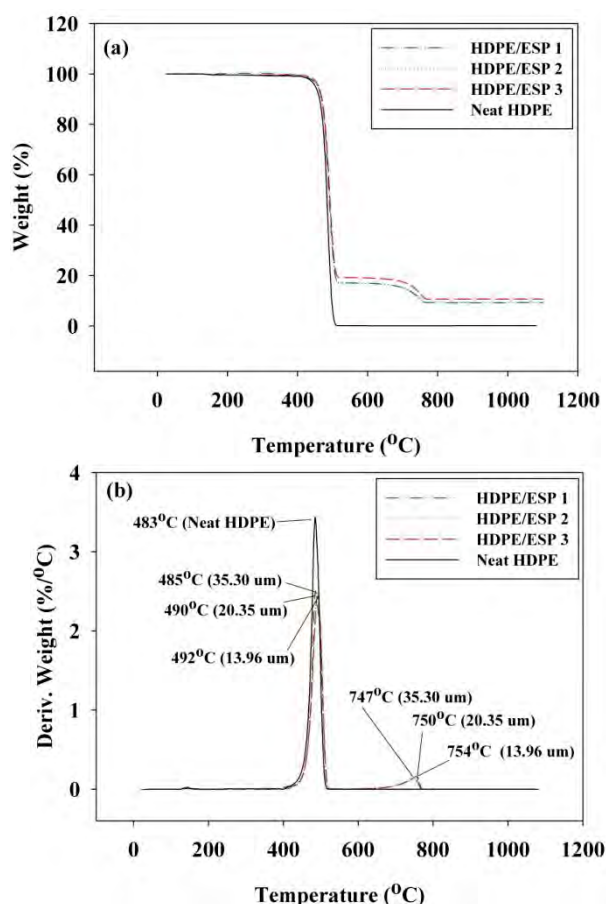


Figure 4. TGA (a) and DTGA (b) curves of neat HDPE and HDPE composites filled with ESP 1, ESP 2, and ESP 3.

Table 3: Melting temperature ( $T_m$ ), crystallizing temperature ( $T_c$ ), and degree of crystallinity ( $X_c$ ) of neat HDPE and HDPE composites filled with ESP 1, ESP 2, and ESP 3.

HDPE Composites	$T_m$ (°C)	$T_c$ (°C)	$X_c$ (%)
HDPE	128.29	115.66	70.51
ESP 1/HDPE	127.30	116.45	69.87
ESP 2/HDPE	129.06	115.30	69.58
ESP 3/HDPE	128.97	116.00	69.06

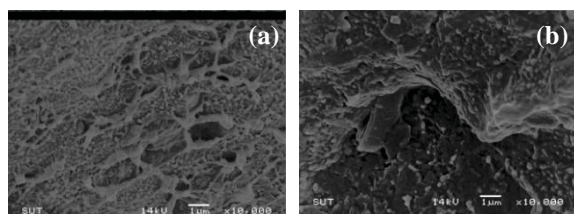


Figure 5. SEM micrographs (x10000) of freeze fractured surface of 20 wt.% ESP/HDPE composites prepared with ESP 1 (a) and ESP 3 (b).

## 4. Conclusions

In this study, it was found that under tensile deformation, HDPE composite prepared with 20 wt.% absorbed more applied energy prior to composite rupture when particle size of ESP was less than 35.30  $\mu\text{m}$ . However, ESP particle size did not much affect impact strength of the HDPE composite. Yield strength, ultimate stress and Young's modulus of the filled HDPE did not depend on ESP particle size. On the other hand, decomposition temperatures of ESP/HDPE composite were significantly influenced by ESP particle size. The decomposition temperatures of HDPE matrix and ESP filler was higher with smaller size of ESP. Melting and crystallizing temperature, and degree of crystallinity of the HDPE composite did not much differ from that of neat HDPE.

## Acknowledgements

The authors sincerely thank Suranaree University of Technology and Center of Excellence on Petrochemical, and Materials Technology, Chulalongkorn University for financial support and SUT farm for supplying chicken eggshell. The special thank is also attributed to Scientific Promotion Co., Ltd. for kindly supplying air jet sieving machine (Retsch, AS 200 jet).

## References

- [1] R.H. Elleithy, L. Ali, M. A. Ali and S. M. Al-Zahrani, *J. Appl. Polym. Sci.* 117 (2010) 2413–2421.
- [2] S. Sahebian, S. M. Zebarjad, K. J. Vahdati and S. A. Sajjadi, *J. Mater. Process. Tech.* 209(2009) 1310–1317.
- [3] S. Shuhadah and A. G. Supri, *J. Phys. Sci.* 20 (2009) 87–98.
- [4] R. Dangtungee and S. Shawaphun, *J. KMUTNB.* 18 (2008) 9–15.
- [5] G. Ji, Z. Hongqi, Q. Chenze and Z. Minfeng, *Polym. Eng. Sci.* 49 (2009) 1383–1388.
- [6] S. Fu, X. Feng, B. Lauke and Y. Mai, *Compos. B.* 39 (2008) 933–961.
- [7] M. Hancock, P. Tremayne and J. D. Rosevear, *J. Polym. Sci.* 18 (1980) 3211.
- [8] M. N. Freire and J. N. F. Holanda, *Cerâm.* 52 (2006) 240–244.
- [9] M. Mohamed, S. Yusupand and S. Maitra, *J. Eng. Sci. Tech.* 7 (2012) 1 – 10.
- [10] F.S. Murakami, P. O. Rdriguesl, C. M. T. Campos and M. A. S. Silval, *Ciênc. Tecnol. Aliment. Campinas.* 27 (2006) 658–662.



# MECHANICAL PROPERTIES OF HIGH DENSITY POLYETHYLENE AND POLY (BUTYLENE SUCCINATE) BLENDS

Ajcharaporn Aontee<sup>1</sup>, Wimonlak Sutapun<sup>1\*</sup>

<sup>1</sup>School of Polymer Engineering, Suranaree University of Technology, Nakhon Ratchasima 30000, Thailand

\* Author for correspondence; E-Mail: wimonlak@sut.ac.th, Tel. +66 44 224435, Fax. +66 44 224605

**Abstract:** In this work, the effect of PBS and HDPE blend ratio on mechanical properties of PBS/HDPE blend was investigated. PBS/HDPE blends were prepared at PBS content of 20, 30, and 40 wt.% via melt mixing process and molded using an injection machine. It was found that Young's modulus of PBS/HDPE blend gradually decreased with increasing PBS content along with considerable decrease of elongation at break. However, the yield strength did not much depend on PBS content but stress at break of PBS/HDPE blend increased with increasing PBS content. Flexural modulus of PBS/HDPE blend was lower than that of neat HDPE. On the other hand, flexural strength of the blend slightly increased with increasing PBS content. Unnotched impact strength of PBS/HDPE blend changed with PBS content. In addition, ultimate strain and impact strength of the blends were much lower than those of neat HDPE and decreased with more fraction of PBS. However, the ultimate strain and impact strength did improve when increased PBS content up to 40 wt.% due to fibrillation phase morphology of the PBS/HDPE blend. For phase morphology of PBS/HDPE blend, the blend containing 20 wt.% PBS exhibited phase morphology of dispersed in matrix. The HDPE blend with 30 wt.% PBS contained non-uniform phase morphology with spherical, elongated, and worm-like shape of PBS domain. Lastly, fibrillar phase morphology occurred when PBS content was 40 wt.%.

## 1. Introduction

With the increase in the global population, plastic materials have found wide applications in every aspect of life and industries. High Density Polyethylene (HDPE) is one of the most widely used plastics after PVC and PP [1]. Its applications including food and pharmaceutical packaging, potable water pipes, chemical containers, construction appliances and automotive parts. These widespread applications are due to its favourable mechanical and thermal properties [2, 3]. However, HDPE is a non-biodegradable plastic. The post consumer product of HDPE is end up with large quantities of plastic waste left in a landfill. In the next 5 year, approximately 10 million tons of HDPE waste will be gathered in nature causing much environmental pollution [4]. Therefore, the biodegradability of HDPE has to be enhanced in order to make it degradable in nature.

Poly (butylene succinate) (PBS) is a one type of biodegradable semi-crystalline polymers. PBS has a melting point close to that of LDPE, glass transition temperatures and tensile strength between those of PE

and PP, and stiffness between that of LDPE and HDPE [1, 5]. In addition, it can be processed with the same processing machines and technique which were applied for those thermoplastics [6]. PBS has excellent biodegradability and is degraded in compost soil, fresh water and also in sea water [7]. It has been reported by Łabużek et al. [8] that the film of polyethylene blended with 60 wt.% PBS (Bionolle<sup>TM</sup>) was degraded within 90 days by fungi which encountered in a dump. Therefore, it is expected that blending HDPE with PBS is not only able to improve biodegradability of consumer products derived from HDPE but also the preferred mechanical properties of the final product will be accessible.

However, the mechanical properties of PBS/HDPE blends strongly correlated with their phase morphology. The phase morphology of immiscible polymer blends depends on various parameters, e.g. blend ratio, mixing and processing condition, viscosity ratio and also interfacial force [9]. Material parameters as viscosity ratio and interfacial force are the significant parameters governing phase morphology of the immiscible blends. The equation for viscosity ratio is shown in Equation 1. The relationship between shear rate, a processing parameter, and interfacial force is expressed in the term of capillary number as shown below in Equation 2 [9, 10]:

$$\eta_r = \frac{\eta_d}{\eta_m} \quad (1)$$

$$Ca = \frac{\eta_m R \dot{\gamma}}{\Gamma} \quad (2)$$

Where  $\eta_d$  and  $\eta_m$  are the viscosity of dispersed phase and continuous phase, respectively,  $\dot{\gamma}$  is the shear rate,  $R$  is the droplet diameter and  $\Gamma$  is the interfacial tension.

In this study, the effect of PBS content on mechanical properties and phase morphology of PBS/HDPE blend was investigated. the blends of HDPE were prepared with PBS content of 20-40 wt.%.



## 2. Materials and Methods

### 2.1 Materials

High density polyethylene (injection grade, EL-Lene<sup>TM</sup> H5814J) was purchased from SCG Chemicals Co., Ltd. It has a melt flow index (MFI) of 14 g/10 min (2.16 kg at 190°C) and a melting temperature ( $T_m$ ) of 131°C.

Poly (butylene succinate) (GS Pla<sup>TM</sup>, AZ91TN) was obtained from Mitsubishi Chemical Co., Ltd. Its melt flow index is 4 g/10 min (2.16 kg at 190°C) and melting temperature ( $T_m$ ) is 110°C.

### 2.2 Preparation of PBS/HDPE Blends.

The pellets of neat PBS and neat HDPE were initially dried in an oven at 60°C for 12 h. before preparing polymer blend. To prepare PBS/HDPE blends, PBS and HDPE were mixed at a weight ratio of 20:80, 30:70 and 40:60 in an internal mixer (HAAKE, Rheomix3000p). The mixing process was operated at 170°C under a rotor speed of 70 rpm and mixing time of 10 min. After that, the mixtures of PBS/HDPE were cooled down to room temperature and then grinded using a grinding machine. The specimens for tensile, flexural and impact test were molded by an injection machine (Chuan Lih Fa, CLF 80T). The injection molding process was carried out with a melting temperature of 180°C, a screw speed of 130 rpm, an injection speed of 47 mm/s, a holding pressure of 617 kg/cm<sup>3</sup> and a mold temperature of 30°C.

### 2.3 Characterization of PBS/HDPE Blends.

Tensile properties including Young's modulus, yield strength, stress at break and elongation at break of PBS/HDPE blends were determined using a universal testing machine with a load cell of 5 kN (Instron, 5565), in accordance with ASTM D638. The tensile test was performed in uniaxial tension at a crosshead speed of 10 mm/min.

Flexural properties of PBS/HDPE blends were tested following ASTM D790 (procedure B) using a universal testing machine with a load cell of 5 kN (Instron, 5565) at a crosshead speed of 14 mm/min.

In addition, unnotched Izod impact strength following ASTM D 256 of the blends were evaluated, on an impact tester (Atlas, BPI), equipped with 5.4 J hammer.

The morphology of fracture surface obtained from chloroform etched specimens, using a scanning electron microscope (JEOL, JCM-5000 NeoScope) at 15kV. The specimens were coated with gold using an ion sputtering device for 9 min at a current of 10 mA.

## 3. Results and Discussion

### 3.1 Tensile properties

As observed in Figure 1, yield strength of PBS/HDPE blends was comparable to that of neat HDPE. It must be noted that neat HDPE did not break within an instrument limit. The addition of 20-40 wt.% PBS into HDPE matrix did not affect the yield strength of the blend. The stress at break of PBS/HDPE blend improved with 30 wt.% PBS, comparing to the blend with 20 wt.% PBS. However, adding PBS more than 30 wt.% did not create any more improvement of stress at break of the blends.

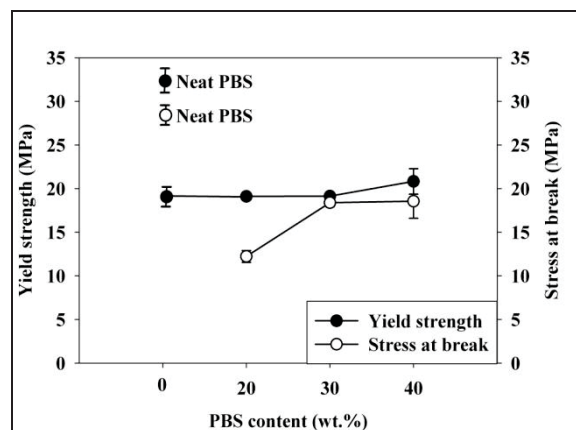


Figure 1. Plot of yield strength and stress at break of PBS/HDPE blends vs PBS content.

As presented in Figure 2, Young's modulus of neat HDPE blend was higher than that of neat PBS. Addition of PBS into HDPE matrix made a gradually decrease in Young's modulus of the blend. As mentioned previously, ultimate elongation of neat HDPE, under tensile test of a crosshead speed of 10 mm/min, was not obtained under an instrumentation limit. Addition of PBS content resulted in a decrease of elongation at break of the blends. The result corresponded well with the result obtained from unnotched impact strength of the blend. The similar result of decreasing in elongation at break of PET/HDPE blend was reported by Kim *et al.* [11] and Pietrasanta *et al.* [12]. They have found that blending HDPE with 10-40 wt.% PET (poly (ethylene terephthalate)) resulted in much decrease of elongation at break. The decreased elongation at break of the PBS/HDPE blend was a consequence of incompatibility of polar PBS and non-polar HDPE. Under tensile loading, the interfacial voids led to a propagation of premature cracks by which the plastic flow of each phase was disrupted. Therefore, PBS/HDPE blend ruptured at lower ultimate strain with higher content of PBS. However, ultimate elongation of HDPE blend did not further decrease with 40 wt.% PBS due to the fibrillar phase morphology of PBS domain, as shown in Figure 5d.

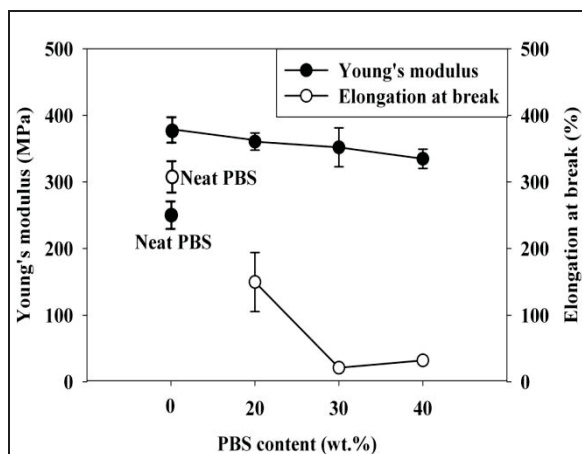


Figure 2. Plot of Young's modulus and elongation at break of PBS/HDPE blends vs PBS content.

### 3.2 Flexural properties

Flexural modulus and flexural strength of neat PBS, neat HDPE and PBS/HDPE blends at various contents of PBS were presented in Figure 3. Flexural modulus of neat HDPE was higher than that of neat PBS. PBS/HDPE blends had a flexural modulus between neat PBS and neat HDPE, and gradually decreased with increasing PBS content. On the other hand, flexural strength of neat PBS was higher than that of neat HDPE. Adding PBS into HDPE did insignificant influence flexural strength of the PBS/HDPE blends.

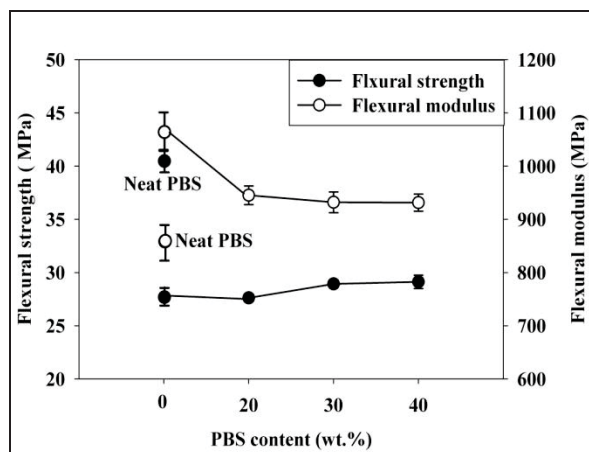


Figure 3. Plot of flexural modulus and flexural strength of PBS/HDPE blends vs PBS content.

### 3.3 Impact properties

It must be noted that unnotched impact strength of neat HDPE and neat PBS was not obtained; it was far beyond an instrumentation limit of a 135 kJ/m<sup>2</sup>. As shown in Figure 4, unnotched impact strength of PBS/HDPE blends was much lower than that of neat HDPE and neat PBS because of high interfacial tension between PBS phase and HDPE matrix. With 30 wt.% PBS, impact strength of the blend continued to drop but with 40 wt.%, the impact strength of the

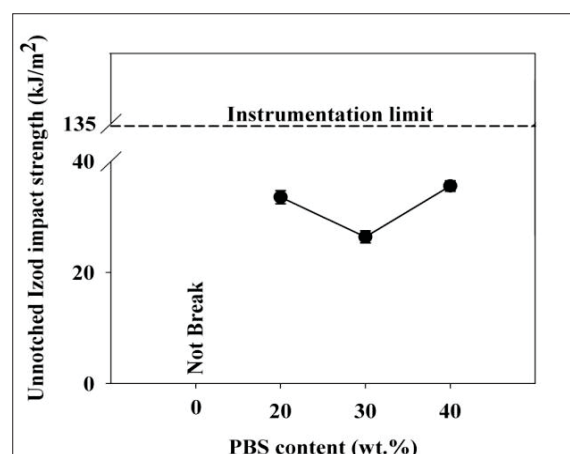


Figure 4. Plot of unnotched Izod impact strength of PBS/HDPE blends vs PBS content.

blend became higher than that of the blend with 30 wt.%. The result corresponded with elongation at break of the HDPE blends as discussed before. Fibrillar phase morphology of the 40 wt.% PBS/HDPE blend, as depicted in Figure 5d, was a key factor for improving elongation at break and impact strength.

### 3.4 Fracture Surface Morphology

SEM micrographs of neat HDPE and HDPE blends at PBS content of 20, 30, and 40 wt.% were shown in Figure 5. Fracture surface morphology of HDPE, illustrated in Figure 5a, was rough with a blocky structure which was a characteristic of ductile polymer. However, the fine mesh of deformed polymer was not observed from the SEM of magnification at x1000[13]. Addition 20 wt.% PBS into HDPE gave rise to a heterogeneous phase morphology with spherical PBS domain dispersed in HDPE matrix according to high interfacial tension between PBS and HDPE phases. In addition, smoother surface of HDPE matrix was observed in Figure 5b. This was an indication of reduction in ductility of HDPE matrix. This phase morphology was responsible for decrease of ultimate elongation and impact strength comparing to those of neat HDPE. As increase PBS content to 30 wt.%, non-uniform size and shape, including spherical, elongated and worm-like, of dispersed phase were observed in Figure 5c. Phase morphology containing elongated and worm-like shape of dispersed PBS phase resulted in slight increase of ultimate stress but not yet ultimate strain and impact strength of the blend. In addition, the fibrillation of phase domain occurred at 40 wt.% PBS, as observed in Figure 5d. These results correlated with improved ultimate elongation and impact strength of the PBS/HDPE blend.

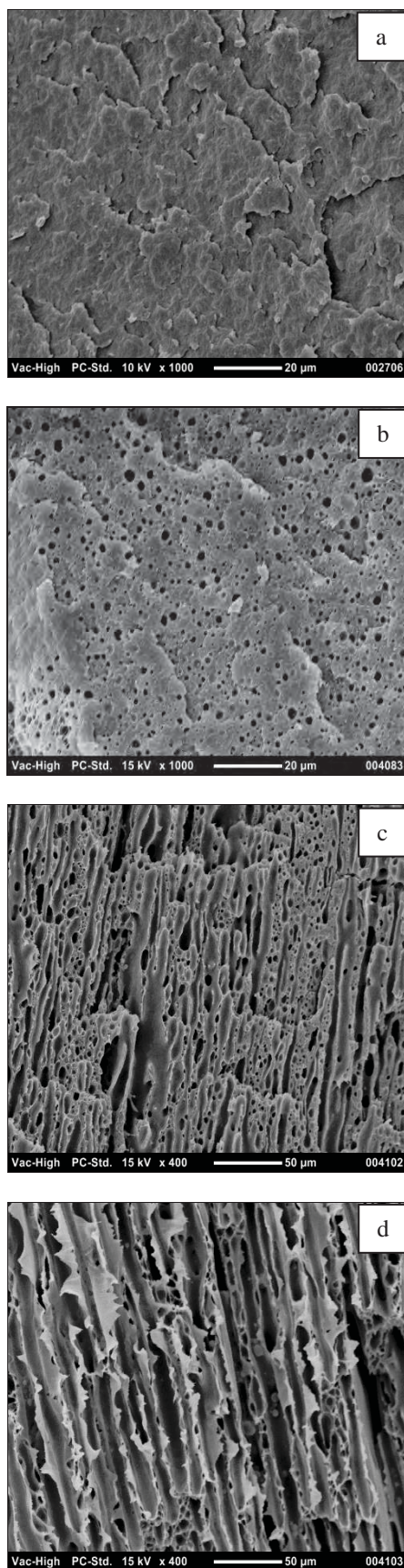


Figure 5. SEM micrographs of (a) HDPE (x1000), and PBS/HDPE of (b) 20 wt.% PBS (x1000), (c) 30 wt.% PBS (x400) and (d) 40 wt.% PBS (x400).

#### 4. Conclusions

This research work revealed that PBS/HDPE blend was an immiscible blend with a type of dispersed in matrix morphology. In addition, phase morphology of the blend related with weight fraction of PBS dispersed phase. The blend morphologies were a spherical domain in a matrix at 20 wt.% PBS, a non-uniform shape of dispersed PBS at 30 wt.%, and fibrillar phase morphology at 40 wt.% PBS.

For tensile properties, yield strength did not change with higher composition of PBS. At higher than 20 wt.% PBS, stress at break of PBS/HDPE blend slightly increased with increasing PBS content. Young's modulus gradually decreased with adding more PBS content. In addition, ultimate strain and impact strength of the blends were much lower than those of neat HDPE and decreased with more fraction of PBS. However, the ultimate strain and impact strength did improve when increased PBS content up to 40 wt.% due to fibrillation phase morphology of the PBS/HDPE blend.

Flexural modulus of PBS/HDPE blends was in between flexural modulus of neat HDPE and neat PBS. However, PBS content did not significantly affect flexural strength of the PBS/HDPE blends.

#### Acknowledgements

The authors would like to thank Suranaree University of Technology for financial support.

#### References

- [1] L. Liu, J. Yu, L. Cheng, W. Qu, *Compos. Part A-Appl.*, 40 (2009) 669-674.
- [2] A. Arkatkar, J. Arutchelvi, M. Sudhakar, S. Bhaduri, P.V. Uppara, M. Doble, *J. Environ. Eng.*, 2 (2009) 68-80.
- [3] In: High density polyethylene (HDPE), *Environmental Product Declarations of the European Plastics Manufacturers*, Brussels, Belgium, 2008.
- [4] S. Evans, in: *GlobalData 2011, European plastics industry*, 2012.
- [5] Y. Shih, T. Wang, R. Jeng, J. Wu, C. Teng, *J. Polym. Environ.*, 15 (2007) 151-158.
- [6] S.K. Lim, S.G. Jang, S.I. Lee, K.H. Lee, a.I.-J. Chin, *Macromol. Res.*, Vol. 16 (2008) 218-223.
- [7] H.Y. Tsi, W.C. Tsen, Y.C. Shu, F.S. Chuang, C.C. Chen, *Polym. Test.*, 28 (2009) 875-885.
- [8] S. Łabuzek, B. Nowak, J. Pająk, *Pol. J. Environ. Stud.*, 13 (2004) 59-68.
- [9] L. Utracki, *Polymer blends handbook*, 1 (2003) 1-122.
- [10] C. Tropea, A. Yarin, J.F. Foss, In: *Springer Handbook of Experimental Fluid Mechanics*, Berlin, 2007, pp. 714.
- [11] D.H. Kim, K.Y. Park, J.Y. Kim, K.D. Suh, *J. Appl. Polym. Sci.*, 78 (2000) 1017-1024.
- [12] J.J. Robin, Y. Pietrasanta, N. Torres, B. Boutevin, *Macromol.Chem.Phys.*, 200 (1999) 142-149.
- [13] I. Brough, R.N. Haward, G. Healey, A. Wood, *Polymer*, 45 (2004) 3115-3123.



# OPTIMIZATION OF POLYSILOXANE-COATED CARBON NANOTUBE SUPPORT FOR METAL ELECTROCATALYSTS OF METHANOL OXIDATION

Somwan Chaythawee<sup>1</sup>, Parichatr Vanalabhpatana<sup>2\*</sup>

<sup>1</sup> Program of Petrochemistry and Polymer Science, Faculty of Science, Chulalongkorn University, Bangkok 10330, Thailand

<sup>2</sup> Electrochemistry and Optical Spectroscopy Research Unit, Department of Chemistry, Faculty of Science, Chulalongkorn University, Bangkok 10330, Thailand

\* Author for correspondence; E-Mail: parichatr.v@chula.ac.th, Tel. 66 2218 7615

**Abstract:** This research focuses on optimizing polysiloxane-coated carbon nanotube (Si-CNT) supports for metal catalysts of methanol electro-oxidation. Initially, Si-CNTs were prepared by covering CNTs with polysiloxane layers polymerized from various aminosilane monomers, *e.g.*, 3-aminopropyltriethoxysilane (3-APTES), 3-aminopropyltrimethoxysilane (3-APTMS). Subsequently, metal electrocatalysts such as hexachloroplatinate ( $\text{PtCl}_6^{2-}$ ) anions, were uniformly attached to the amino groups of Si-CNTs via electrostatic interaction before being reduced to form metal nanoparticles supported on Si-CNTs (metal/Si-CNTs). Interestingly, we founded that pH conditions during metal deposition affect electrocatalytic activity of the obtained metal/Si-CNTs. Morphological and structural information of metal/Si-CNTs were characterized by X-ray diffraction (XRD) analysis and transmission electron microscopy (TEM). Furthermore, the electrocatalytic activity of metal/Si-CNT modified electrodes for methanol electro-oxidation was investigated by means of cyclic voltammetry.

## 1. Introduction

Methanol electro-oxidation reaction has received much attention from the general public and scientists [1,2] because it is the main reaction at the anode of direct methanol fuel cell (DMFC) and it can be applied to alcohol sensors utilized in daily life and industries. Nevertheless, the methanol electro-oxidation reaction rarely occurs without properly catalysts. Platinum (Pt)-based material, one group of active electrocatalysts, has been widely used to kinetically promote this electrochemical oxidation [3].

To enhance the performance of Pt-based electrocatalysts, carbon nanotubes (CNTs) were selected as supports due to their extraordinary electrical conductivity, high surface area, good chemical stability, and thermal resistance [4]. Electrocatalytic activity of the Pt catalyst also depends on the Pt particle size and the dispersion pattern over the support material. There are some problems of non-pattern dispersion and difficulty in controlling sizes of Pt nanoparticles when Pt nanoparticles are directly impregnated on CNT surfaces. Several research groups reported the modification of CNTs with functional groups to promote specific attachment with Pt nanoparticles. These types of catalysts were active for methanol oxidation at room temperatures [5,6].

In the present study, we have developed a method for achieving highly dispersed Pt nanoparticles attached to CNTs. First, the acid-treated CNTs were embedded within a polysiloxane layer, arising from polymerization of aminosilane monomers: 3-aminopropyltriethoxysilane (3-APTES) or 3-aminopropyltrimethoxysilane (3-APTMS) to yield Si-CNTs with amino group extruding outside. Then, hexachloroplatinated anions ( $\text{PtCl}_6^{2-}$ ) were deposited on Si-CNTs via electrostatic interaction between the Pt-ion precursor and the amino group of Si-CNTs before being reduced to form Pt nanoparticles supported on Si-CNTs (Pt/Si-CNTs). We anticipated that the polysiloxane coating containing specific attachment sites for Pt nanoparticles would reduce aggregation of the nanoparticles and provide pattern distribution of the nanoparticles on Si-CNT surfaces. Additionally, the effect of pH during Pt deposition on Si-CNT surfaces was studied. X-ray diffraction (XRD) analysis and transmission electron microscopy (TEM) were used to characterize the existence of polysiloxane layers and Pt nanoparticles on CNTs. Electrocatalytic properties of the Pt/Si-CNT modified electrodes for methanol oxidation were investigated by means of cyclic voltammetry.

## 2. Materials and Methods

### 2.1 Chemicals

Carbon nanotubes (CNTs, 99%) was purchased from Chiang Mai University. 3-aminopropyltriethoxysilane (3-APTES, 99%) and 3-aminopropyltrimethoxysilane (3-APTMS, 99%) were obtained from Acros Organics. Hydrogen hexachloroplatinic acid (IV) hydrate ( $\text{H}_2\text{PtCl}_6 \cdot 6\text{H}_2\text{O}$ ) was purchased from Aldrich. All solvents and other reagents were purchased from Merck and used without further purification.

### 2.2 Preparation of Polysiloxane-coated CNTs (Si-CNTs)

Firstly, CNTs were treated with concentrated acid to reduce impurities by stirring in the acid for 8 h. The preparation of polysiloxane-coated CNTs or Si-CNTs was described in detail elsewhere [7,8]. Acid-treated CNT powder was mixed with a solution of (a) 3-APTES or (b) 3-APTMS by using ultrasonic bath to form a well-dispersed suspension. In this step, the aminosilane monomer molecules were attached around



CNTs via hydrophobic interaction, allowing the amino groups extruding outside. Then, the aminosilane monomers were acid-catalytically cross-linked with Si–O–Si framework to yield Si-CNTs. After that, excess reagents were removed by dialysis. The obtained Si-CNTs were purified from the suspension by centrifuging and dried in a vacuum oven before further use.

### 2.3 Preparation of Pt Nanoparticles Deposited on Si-CNTs (Pt/Si-CNTs)

Initially, the purified Si-CNT powder was dispersed in milli-Q water and mixed with  $\text{H}_2\text{PtCl}_6$  solution. During this period, the  $\text{PtCl}_6^{2-}$  anions were attached to the amino groups of the Si-CNTs through electrostatic interaction. At this step, the effect of pH on Pt deposition onto Si-CNTs was investigated. Finally, proper reducing agent was added in the mixture to reduce Pt(IV) ions to Pt nanoparticles on Si-CNTs.

### 2.4 Characterization and Measurements

XRD (DMAX 2002, Rigaku, Japan) was used to characterize Pt/Si-CNTs whereas TEM (JEM-1220, Japan) was selected to study the Si-CNT surface morphology. Electrochemical experiments were performed with potentiostat/galvanostat ( $\mu$ -Autolab, Methrom, Switzerland) in a three-electrode cell using glassy carbon electrode modified with Pt/Si-CNTs as a working electrode, Pt wire as an auxiliary electrode, and silver/silver chloride electrode (Ag/AgCl) as a reference electrode. All electrochemical measurements were operated in 0.5 M sulfuric ( $\text{H}_2\text{SO}_4$ ) solution at the scan rate of  $50 \text{ mV}\cdot\text{s}^{-1}$ .

## 3. Results and Discussion

### 3.1 TEM Analysis of Si-CNTs

Morphological information of Si-CNTs can be explored by TEM. Figure 1 presents TEM images of CNTs and Si-CNTs. As shown in Figure 1a, the acid-treated CNTs contain thinner walls than the Si-CNTs prepared from 3-APTES (3-APTES type, Figure 1b) and 3-APTMS (3-APTMS type, Figure 1c), revealing the successful polysiloxane coating on CNTs.

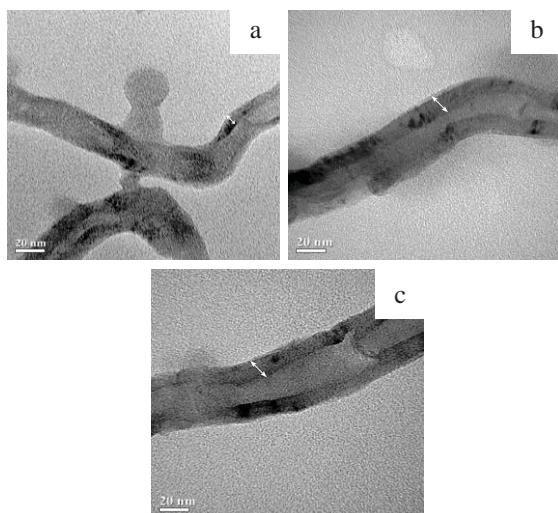


Figure 1. TEM images of (a) the acid-treated CNTs, (b) Si-CNTs (3-APTES type), and (c) Si-CNTs (3-APTMS type)

### 3.2 XRD Analysis of Pt/Si-CNTs

XRD analysis was introduced to reveal the structures of Pt/Si-CNT electrocatalysts and their CNT supports. XRD pattern of the starting CNTs is displayed in Figure 2a. Its diffraction peak at  $2\theta = 26.2^\circ$  corresponds to the plane (002) of graphite. Figure 2b shows the XRD pattern of Pt/Si-CNTs (3-APTMS type) with the characteristic peak of graphite at  $2\theta = 26.2^\circ$ , indicating the presence of CNT support in the Pt electrocatalyst. Four main diffraction peaks of Pt appearing at  $2\theta = 39.3, 45.9, 67.4$ , and  $81.4^\circ$  can be assigned to (111), (200), (220), and (311) crystalline plane of Pt [9,10]. Similar to the result reported from our laboratory [8], XRD pattern of Pt/Si-CNTs (3-APTES type) has same features with Figure 2b.

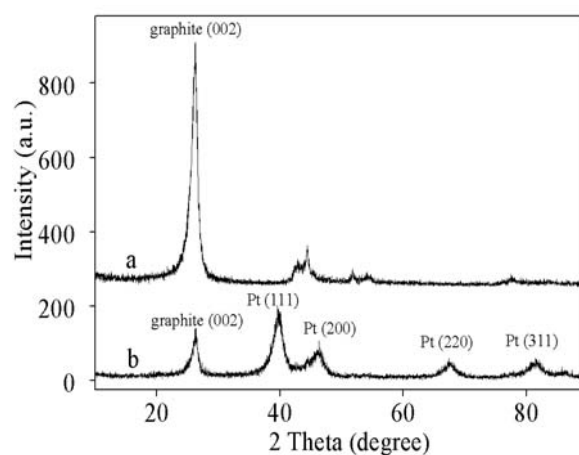


Figure 2. XRD patterns of (a) acid-treated CNTs and (b) Pt/Si-CNT (3-APTMS type) electrocatalyst

### 3.3 Electrochemical Properties of Pt/Si-CNT Electrocatalysts

Figure 3 illustrates cyclic voltammogram of the glassy carbon electrode modified with Pt/Si-CNT (3-APTMS type) electrocatalyst scanned from +1.20 V to  $-0.10$  V and  $-0.10$  V to +1.20 V in 0.5 M  $\text{H}_2\text{SO}_4$  electrolyte solution at  $50 \text{ mV}\cdot\text{s}^{-1}$ . In the negative scan, the cathodic peak for Pt oxide reduction at +0.41 V represents characteristic feature of Pt. Furthermore, the peaks at the potential region of +0.07 V to  $-0.24$  V correspond to hydrogen adsorption–desorption. These peaks can be used to determine specific electrochemical surface area (ECA) of Pt (sometimes referred to as real Pt electrocatalyst surface area) in Pt/Si-CNT electrocatalysts [11].

Electrocatalytic activity for methanol oxidation of the two Pt/Si-CNT electrocatalysts was tested and compared by means of cyclic voltammetry (Figure 4). Cyclic voltammograms of the Pt/Si-CNT modified electrode were carried out at the potential region from  $-0.10$  V to +1.20 V in 0.5 M  $\text{H}_2\text{SO}_4$  solution containing 1.0 M methanol. In the forward scan, the anodic peak appearing at approximately +0.74 V is

proven to be methanol oxidation by Pt/Si-CNT electrocatalyst. In the reverse scan, the re-oxidation peak at +0.49 V can be attributed to the removal of the incompletely oxidized carbonaceous species formed in the forward scan.

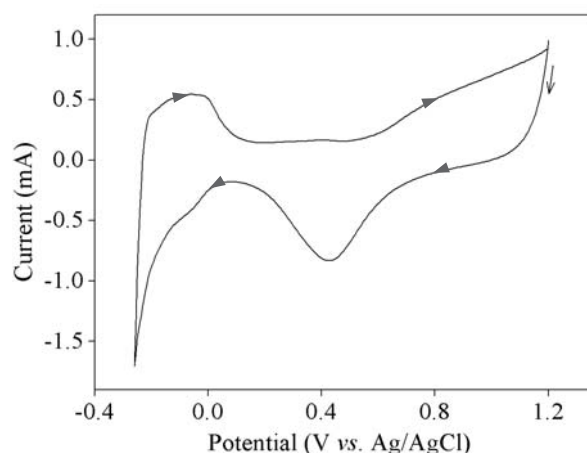


Figure 3. Cyclic voltammogram for 0.5 M H<sub>2</sub>SO<sub>4</sub> solution recorded with the Pt/Si-CNT (3-APTMS type) modified glassy carbon electrode at the scan rate of 50 mV·s<sup>-1</sup>

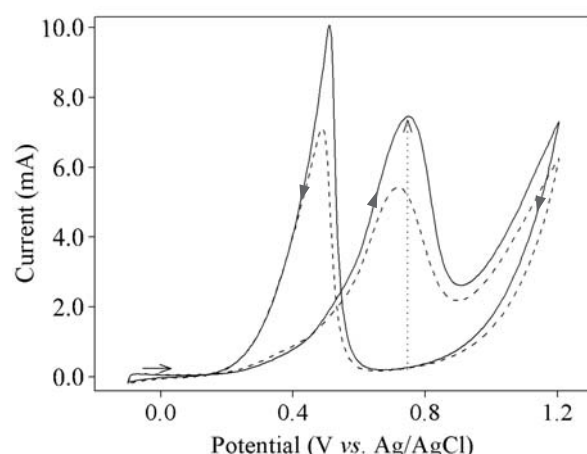


Figure 4. Cyclic voltammograms for 1.0 M methanol in 0.5 M H<sub>2</sub>SO<sub>4</sub> solution recorded with Pt/Si-CNT modified electrodes type 3-APTES (dashed line) and type 3-APTMS (solid line) at the scan rate of 50 mV·s<sup>-1</sup>

Anodic peak current at +0.74 V and specific activity (*i.e.*, anodic peak current per ECA) for methanol oxidation in the forward scan of the Pt/CNTs [12], Pt/Si-CNTs (3-APTES type), and Pt/Si-CNTs (3-APTMS type) are listed in Table 1. Both Pt/Si-CNT modified electrodes displayed better catalytic activity for methanol oxidation than the Pt/CNT electrode. These results confirm that coating CNTs with polysiloxane layer allows high distribution of Pt nanoparticles onto Si-CNTs with less aggregation. As seen in Table 1, the Pt/Si-CNT (3-APTMS type) modified electrode gave higher current and specific activity for methanol oxidation than the Pt/Si-CNT

electrode of 3-APTES type. The polysiloxane layer prepared from 3-APTMS has shorter carbon chain between two amino groups and lower distance of the Pt attached to the amino group and the CNT tube center.

Table 1. Electrocatalytic activity for methanol oxidation evaluated from cyclic voltammograms for 0.5 M H<sub>2</sub>SO<sub>4</sub> solution containing 2.0 M methanol recorded with the electrocatalyst modified electrodes at 50 mV·s<sup>-1</sup>

Electrocatalyst	Current (mA)	Specific Activity (mA·cm <sup>-2</sup> )
Pt/CNTs	2.40	0.27
Pt/Si-CNTs (3-APTES type)	8.82	1.05
Pt/Si-CNTs (3-APTMS type)	11.18	1.19

#### 3.4 Effect of pH on Electrocatalytic Activity of Pt/Si-CNT Electrocatalysts

During the preparation of Pt/Si-CNT (3-APTES type), the pH of H<sub>2</sub>PtCl<sub>6</sub>-Si-CNT mixture was varied from 1 to 11 and the electrocatalytic activity of the obtained Pt/Si-CNT was probed (Table 2). The modified electrode of Pt/Si-CNTs prepared at pH 1 gave highest specific activity. Since the pH below 7 can promote protonation at the amino group of Si-CNTs to form ammonium ion (-NH<sub>3</sub><sup>+</sup>) moiety, negatively charge PtCl<sub>6</sub><sup>2-</sup> ion is prone to attach strongly with NH<sub>3</sub><sup>+</sup> moiety to give better Pt/Si-CNT electrocatalyst. Hence, we can conclude that the optimized pH for the preparation of Pt/Si-CNTs is 1.

Table 2. Electrocatalytic activity for methanol oxidation evaluated from cyclic voltammograms for 0.5 M H<sub>2</sub>SO<sub>4</sub> solution containing 1.0 M methanol recorded at 50 mV·s<sup>-1</sup> with the electrodes modified with Pt/Si-CNTs (3-APTES type) prepared at various pH

pH	Specific Activity (mA·cm <sup>-2</sup> )
1	1.03
2	0.89
3	0.64
5	0.61
7	0.59
11	0.56

#### 4. Conclusions

We reported a successful method to synthesize Pt/Si-CNTs by coating CNT surfaces with polysiloxane layers to create the specific functional group for anchoring Pt nanoparticles. TEM and XRD results confirmed the achievement of Si-CNTs and Pt/Si-

CNTs. In electrochemical investigation, Pt/Si-CNTs made of 3-APTMS monomer exhibited better electrocatalytic performance towards methanol oxidation. Furthermore, the optimized acidic condition (pH 1) during Pt deposition on Si-CNTs provided Pt/Si-CNT electrocatalyst with highest activity for methanol oxidation.

## Acknowledgement

This work was partially supported by the 90<sup>th</sup> Anniversary of Chulalongkorn University (Ratchadaphiseksomphot Endowment Fund).

## References

- [1] T. Iwasita, *Electrochim. Acta* **47** (2002) 3663–3674.
- [2] J. Geng, X. Li, G. Sun, and B. Yi, *Sens. Actuators B* **147** (2010) 612–617.
- [3] G. Gao, G. Yang, M. Xu, C. Wang, C. Xu, and H. Li, *J. Power Source* **173** (2007) 178–182.
- [4] M. Kim, J. Hong, J. Lee, C.K. Hong, and S.E. Shim, *J. Coll. Int. Sci.* **322** (2008) 321–326.
- [5] Z.C. Wang, Z.M. Ma, and H.L. Li, *Appl. Surf. Sci.* **254** (2008) 6521–6526.
- [6] V. Selvaraj and M. Alagar, *Electrochem. Commun.* **9** (2007) 1145–1153.
- [7] T. Wang, X. Hu, X. Qu, and S. Dong, *J. Phys. Chem.* **110** (2006) 6631–6636.
- [8] S. Pratumyos, and P. Vanalabhpatana, *PACCON2011 Proc.*, Bangkok, Thailand (2011) 378–381.
- [9] G.X. Wang, J.H. Ahn, and J. Yao, *J. Power Source* **119** (2003) 16–23.
- [10] D.J. Guo and S.K. Cui, *J. Solid State Electrochem.* **12** (2008), 1393–1397.
- [11] Z.W. Zhao, “*The Liquid-phase Synthesis and Electrochemical Application of Novel Inorganic Nanoparticles*” Ph.D. Thesis, Wollongong University, (2008).
- [12] R. Cheerapradit, O. Chailapakul, and P. Vanalabhpatana, *ECS Trans* **19** (2009) 71–78.

# La<sub>1-x</sub>Sr<sub>x</sub>NiO<sub>3-δ</sub> PEROVSKITES AS ANODE ELECTROCATALYSTS FOR ALKALINE DIRECT ALCOHOL FUEL CELLS

Tiraporn Khunoad<sup>1</sup>, Soamwadee Chaianansutcharit<sup>2</sup>, Parichatr Vanalabhpattana<sup>2\*</sup>

<sup>1</sup> Program of Petrochemistry and Polymer Science, Faculty of Science, Chulalongkorn University, Bangkok, Thailand

<sup>2</sup> Department of Chemistry, Faculty of Science, Chulalongkorn University, Bangkok, Thailand

\* Author for correspondence; E-Mail: parichatr.v@chula.ac.th, Tel. 66 2218 7615

**Abstract:** Alkaline direct alcohol fuel cells (ADAFCS) have attracted public attention over the past decade due to their favorable reaction kinetics in alkaline media, high energy densities, and easy handling of the liquid fuels. Since alcohol electro-oxidation in alkaline medium is more facile than that in acidic solution, less expensive and platinum-free anode electrocatalysts can be employed in ADAFCs. In this research, La<sub>1-x</sub>Sr<sub>x</sub>NiO<sub>3-δ</sub> (0.00 ≤ x ≤ 0.50) perovskite oxides have been developed as electrocatalysts for ADAFC anode. Synthesized by the modified citrate method, the obtained perovskites were characterized by using X-ray diffraction (XRD) technique. Electrochemical activity of the La<sub>1-x</sub>Sr<sub>x</sub>NiO<sub>3-δ</sub> towards alcohol oxidation in alkaline solution was measured by means of cyclic voltammetry. La<sub>1-x</sub>Sr<sub>x</sub>NiO<sub>3-δ</sub>-modified electrodes responded extremely well to methanol by giving high anodic current for methanol oxidation. Using four-point-probe DC technique, the electrical conductivity of La<sub>1-x</sub>Sr<sub>x</sub>NiO<sub>3-δ</sub> was probed at 250-800°C. Interestingly, it was found that LaNiO<sub>3</sub> exhibited metallic feature whereas the strontium-doped LaNiO<sub>3</sub> showed semi-conducting property.

## 1. Introduction

Direct alcohol fuel cell (DAFC), one of clean energy conversion devices, has drawn great attention due to its high efficiency, high energy density, and low emission of pollutants [1–3]. Since DAFCs are compact and do not use unstable hydrogen fuel, they are particularly suitable as power sources for portable electric devices such as cellular phones and notebook computers. Compared to gaseous fuels, liquid alcohols, e.g., methanol and ethanol, provide higher volumetric energy density and better energy efficiency. Additionally, they are more easily stored and transported.

Challenging issues such as alcohol crossover, low catalytic activity of electrodes for both oxygen reduction and alcohol oxidation reaction, high cost of the currently used Pt-based electrocatalysts, and susceptibility of the catalysts to be poisoned by the CO-like intermediates formed during alcohol oxidation at anode are the main obstacles to the commercialization of DAFC technology [4–8]. Since alcohol electro-oxidation in alkaline media is more facile than that in acidic condition, less expensive and Pt-free electrocatalysts can be employed. A much wider range of materials, particularly pure or mixed oxide, is stable in alkaline solutions and can be

developed as ADAFC anode. Various attempts were made earlier to use metal oxides of V, Fe, Ni, In, Sn, La, and Pb for alcohol oxidation, but none of them showed any measurable activity except NiO [9–13].

In this research, we have tested the possibility of La<sub>1-x</sub>Sr<sub>x</sub>NiO<sub>3-δ</sub> mixed conducting perovskite-type oxides for catalyzing the electro-oxidation of methanol. Synthesized by the modified citrate method at different contents of doped metal ions, the perovskite oxide powders were characterized by using X-ray diffraction (XRD) technique. In addition, the electrochemical activity of La<sub>1-x</sub>Sr<sub>x</sub>NiO<sub>3-δ</sub> for methanol oxidation in alkaline media was measured by means of cyclic voltammetry.

## 2. Materials and Methods

**Materials:** Each of the following chemicals was used as received: lanthanum nitrate (La(NO<sub>3</sub>)<sub>3</sub>·6H<sub>2</sub>O, Ajax Chemical, 99%); strontium nitrate (Sr(NO<sub>3</sub>)<sub>2</sub>, Sigma-Aldrich, 99%); nickel nitrate (Ni(NO<sub>3</sub>)<sub>2</sub>·3H<sub>2</sub>O, Ajax Chemical, ≥ 97%); and citric acid (C<sub>6</sub>H<sub>8</sub>O<sub>7</sub>, Sigma-Aldrich, 99.5%). All solvents and other reagents were purchased from Merck and employed without purification.

**Synthesis of La<sub>1-x</sub>Sr<sub>x</sub>NiO<sub>3-δ</sub> Perovskites:** La<sub>1-x</sub>Sr<sub>x</sub>NiO<sub>3-δ</sub> (0.00 ≤ x ≤ 0.50) were prepared by the modified citrate method. Stoichiometric amounts of La(NO<sub>3</sub>)<sub>3</sub>·6H<sub>2</sub>O, Sr(NO<sub>3</sub>)<sub>2</sub>, and Ni(NO<sub>3</sub>)<sub>2</sub>·3H<sub>2</sub>O were dissolved in nitric acid solution prior to the addition of citric acid [11]. The mixed solution was stirred at room temperature and adjusted to pH of ~9. After that, the homogeneous solution was heated and stirred around 200-300°C until the dried gel was obtained. Then, the self combustion initiated and the mixture was instantaneously burned and transformed into black powder. The powder was ground and subsequently calcined in air to achieve phase purity and eliminate the residual organic species.

**Characterization and Measurements:** Phase formation of the La<sub>1-x</sub>Sr<sub>x</sub>NiO<sub>3-δ</sub> perovskites was investigated after the calcination by XRD analysis (Rigaku, DMAX 2200, Ultima USA). Electrical conductivity of the perovskites was measured by a conventional four-point-probe DC method at 250-800°C [11] using potentiostat/galvanostat (Autolab



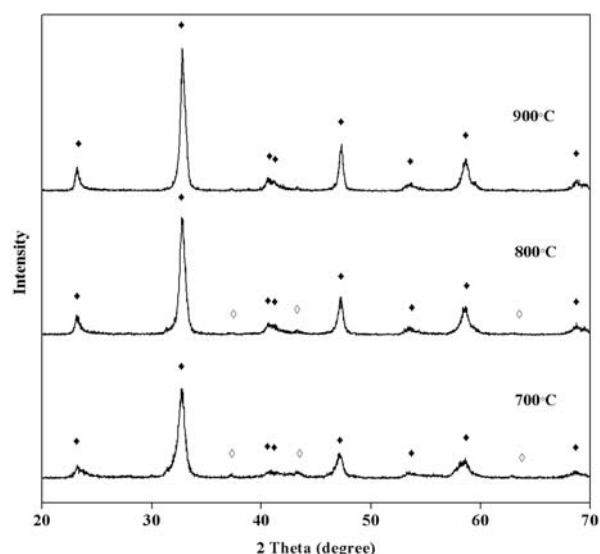
PGSTAT-302N, Eco Chemie, Methrom, The Netherlands). To obtain the sample for electrical conductivity measurement, the  $\text{La}_{1-x}\text{Sr}_x\text{NiO}_{3-\delta}$  powder was pressed into a membrane disc (20 mm in diameter and 0.7 mm in thickness) and sintered in air at 900°C for 5 h.

Electrochemical investigation of the  $\text{La}_{1-x}\text{Sr}_x\text{NiO}_{3-\delta}$  electrocatalysts was acquired by means of cyclic voltammetry using potentiostat/galvanostat (Autolab PGSTAT-101, Eco Chemie, Methrom, The Netherlands). A conventional electrochemical cell with a three-electrode configuration was used throughout this research.  $\text{La}_{1-x}\text{Sr}_x\text{NiO}_{3-\delta}$ -modified paste electrodes were employed as working electrodes. Pt wire and silver/silver chloride (Ag/AgCl, BAS, Japan) served as an auxiliary and a reference electrodes, respectively. All measurements were performed in 1.0 M NaOH solution at the scan rate of  $20 \text{ mV} \cdot \text{s}^{-1}$ .

**Preparation of  $\text{La}_{1-x}\text{Sr}_x\text{NiO}_{3-\delta}$ -modified Paste Electrodes:**  $\text{La}_{1-x}\text{Sr}_x\text{NiO}_{3-\delta}$ -modified paste electrodes were prepared by mixing weighed amounts of graphite powder,  $\text{La}_{1-x}\text{Sr}_x\text{NiO}_{3-\delta}$  and binding agent thoroughly until homogenization was attained. A portion of the prepared paste was packed firmly into an electrode holder (diameter = 2 mm) with copper wire as an electrical connector. Before use, the outer surface was smoothened against weighing paper and rinsed with milli-Q water [14].

### 3. Results and Discussion

**XRD Analysis of  $\text{La}_{1-x}\text{Sr}_x\text{NiO}_{3-\delta}$  Perovskites:** XRD patterns of  $\text{LaNiO}_3$  calcined at 700-900°C for 5 h are illustrated in Figure 1 within angles of  $2\theta$  range from Figure 1. XRD patterns of  $\text{LaNiO}_3$  calcined at 700-



900°C for 5 h ( $\text{LaNiO}_3$  (♦) and NiO (○))

20-70 degree. It was found that the calcining temperature has a determinant role on the perovskite

morphology. In combination of  $\text{LaNiO}_3$  phase (PDF No. 34-1028), NiO impurity (PDF No. 47-1049) can be observed when the calcination temperature was 700 or 800°C. XRD pattern of  $\text{LaNiO}_3$  calcined at 900°C indicates the formation of single-phase  $\text{LaNiO}_3$  powder with a perovskite-type rhombohedral structure. Thus, the calcination temperature of 900°C was selected for the preparation of all Sr-doped  $\text{LaNiO}_3$  in this work.

Figure 2 reveals XRD patterns of  $\text{La}_{1-x}\text{Sr}_x\text{NiO}_{3-\delta}$  ( $0.10 \leq x \leq 0.50$ ). XRD analysis of these oxides confirmed rhombohedral-to-tetragonal  $\text{K}_2\text{NiF}_4$ -type structure (PDF No. 11-0057) transition as well as the presence of NiO impurity phase due to partially substitution of La with Sr. For the Sr-substituted oxides ( $0.10 \leq x \leq 0.50$ ), the diffraction peaks of tetragonal and NiO phases increase with  $x$ .

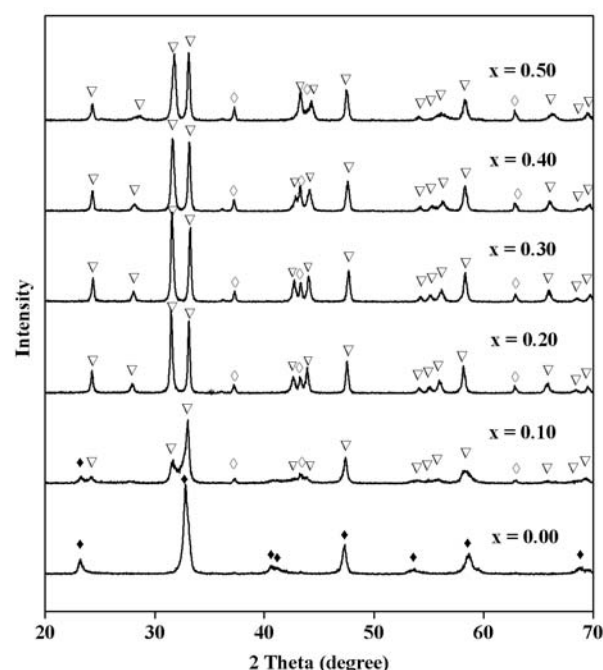


Figure 2. XRD patterns of  $\text{La}_{1-x}\text{Sr}_x\text{NiO}_{3-\delta}$  ( $x = 0.00-0.50$ ) calcined at 900°C for 5 h ( $\text{K}_2\text{NiF}_4$  (▽);  $\text{LaNiO}_3$  (♦); and NiO (○))

**Electrical Conductivity Measurement of  $\text{La}_{1-x}\text{Sr}_x\text{NiO}_{3-\delta}$  ( $0.00 \leq x \leq 0.50$ ):** Total electrical conductivity ( $\sigma$ ) of each  $\text{La}_{1-x}\text{Sr}_x\text{NiO}_{3-\delta}$  perovskite was determined by the DC four-probe method at the temperature range of 250-800°C in air (Figure 3). At all temperatures, the electrical conductivities of the sintered  $\text{LaNiO}_3$  disk have higher values than those of Sr-doped  $\text{LaNiO}_3$  disks, implying that the transition of rhombohedral  $\text{ABO}_3$ -to-tetragonal  $\text{K}_2\text{NiF}_4$ -type structure can significantly affect the conductivities of  $\text{LaNiO}_3$ -based perovskites. However, the electrical conductivity of the Sr-doped  $\text{LaNiO}_3$  ( $0.10 \leq x \leq 0.50$ ) increases with the Sr content, possibly owing to the enhancement in electron holes from the Sr addition [11].

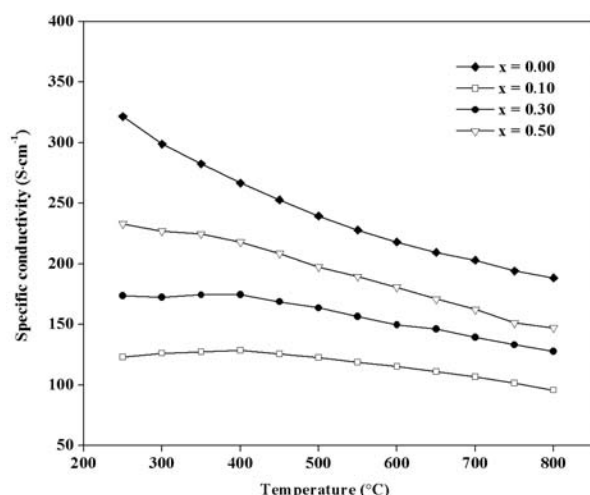


Figure 3. Temperature dependence of electrical conductivity for sintered  $\text{La}_{1-x}\text{Sr}_x\text{NiO}_{3-\delta}$  disks

**Electrochemical Studies of  $\text{La}_{1-x}\text{Sr}_x\text{NiO}_{3-\delta}$  Electro-catalysts:** Cyclic voltammograms for the electrodes modified with  $\text{La}_{1-x}\text{Sr}_x\text{NiO}_{3-\delta}$  were carried out to gain the electrocatalytic information of  $\text{La}_{1-x}\text{Sr}_x\text{NiO}_{3-\delta}$  for methanol oxidation. Figure 4 displays cyclic voltammograms of the  $\text{La}_{0.80}\text{Sr}_{0.20}\text{NiO}_3$  paste electrode in the presence and absence of 1.0 M methanol. Scanned from 0 to +0.7 V and +0.7 to 0 V in 1.0 M NaOH electrolyte solution at the scan rate of  $20 \text{ mV}\cdot\text{s}^{-1}$  at  $25^\circ\text{C}$ , the  $\text{La}_{0.80}\text{Sr}_{0.20}\text{NiO}_3$  electrode responded well to methanol, giving the anodic waves at 0.4–0.6 V for methanol oxidation in both forward and reverse scans. The appearance of the anodic wave in the reverse scan might be attributed to the slow oxidation of carbonaceous species arising from the oxidation in the forward scan.

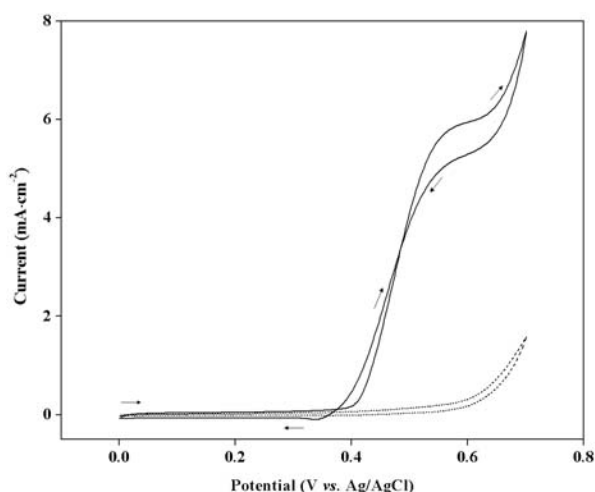


Figure 4. Cyclic voltammograms of  $\text{La}_{0.80}\text{Sr}_{0.20}\text{NiO}_3$ -modified paste electrode recorded at the scan rate of  $20 \text{ mV}\cdot\text{s}^{-1}$  in 1.0 M NaOH solution (dotted line) and 1.0 M methanol/1.0 M NaOH solution (solid line)

To find the proper condition for methanol electro-oxidation, cyclic voltammograms of the  $\text{La}_{1-x}\text{Sr}_x\text{NiO}_{3-\delta}$  modified paste electrode were collected in 0.1, 0.5, and 1.0 M NaOH electrolyte solution. Electro-

catalytic activity for methanol oxidation enhance, *i.e.*, the anodic current evaluated from cyclic voltammograms at the potential of 0.6 V in the forward scan enhanced with NaOH concentration (Table 1). Hence, 1.0 M NaOH was chosen as an electrolyte solution throughout this work.

Table 1. Electrocatalytic activity of  $\text{La}_{0.80}\text{Sr}_{0.20}\text{NiO}_3$ -modified paste electrode for methanol oxidation evaluated from cyclic voltammograms scanned in 0.1, 0.5, and 1.0 M NaOH solution

NaOH concentration (M)	Current for 0.1 M methanol ( $\text{mA}\cdot\text{cm}^{-2}$ )	Current for 2.0 M methanol ( $\text{mA}\cdot\text{cm}^{-2}$ )
0.1	0.05	0.31
0.5	0.49	5.89
1.0	1.09	11.14

Table 2 compares electrocatalytic activity of the  $\text{La}_{1-x}\text{Sr}_x\text{NiO}_{3-\delta}$  paste electrodes for 1.0 M methanol. Among all of the modified electrodes, the  $\text{La}_{0.80}\text{Sr}_{0.20}\text{NiO}_3$  paste electrode gave the highest anodic peak current for 1.0 M methanol electro-oxidation, revealing positive effect of the Sr substitution on the  $\text{La}_{1-x}\text{Sr}_x\text{NiO}_{3-\delta}$  electrocatalytic activity.

Table 2. Electrocatalytic activity of the  $\text{La}_{1-x}\text{Sr}_x\text{NiO}_{3-\delta}$  modified paste electrodes for methanol oxidation evaluated from cyclic voltammograms of 1.0 M methanol/1.0 M NaOH solution recorded at the scan rate of  $20 \text{ mV}\cdot\text{s}^{-1}$

Electrocatalysts	Current ( $\text{mA}\cdot\text{cm}^{-2}$ )
$\text{LaNiO}_3$	4.99
$\text{La}_{0.90}\text{Sr}_{0.10}\text{NiO}_3$	5.22
$\text{La}_{0.80}\text{Sr}_{0.20}\text{NiO}_3$	5.46

#### 4. Conclusions

$\text{La}_{1-x}\text{Sr}_x\text{NiO}_{3-\delta}$  ( $0.00 \leq x \leq 0.50$ ) were obtained by the modified citrate method. XRD analysis of these perovskites confirmed the rhombohedral-to-tetragonal structural transition as well as the presence of NiO minor phase due to partially substituting La with Sr. According to electrical conductivity and cyclic voltammetric results, the Sr substitution not only converted conducting property of the perovskites, but also improved the electrocatalytic performance of methanol electro-oxidation in NaOH solution. As a result, we plan to continue optimizing the Sr content in  $\text{La}_{1-x}\text{Sr}_x\text{NiO}_{3-\delta}$  and study the effect of other transition metals on the electrocatalytic performance of these La-based perovskite oxides.

#### Acknowledgements

This work has been supported by (i) Research Strategic Plan (A1B1), Faculty of Science, Chulalongkorn University and (ii) the 90<sup>th</sup> Anniversary of

## References

- [1] C.C. Yang, S.J. Chiu, and W.C. Chien, *J. Power Sources* **162** (2006), pp. 21–29.
- [2] S.T. Nguyen, H.M. Law, H.T. Nguyen, N. Kristian, S. Wang, S.H. Chan, and X. Wang, *Appl. Catalysis B: Environ.* **91** (2009), pp. 507–515.
- [3] Y.H. Qin, H.H. Yang, X.S. Zhang, P. Li, X.G. Zhou, L. Niu, and W.K. Yuan, *Carbon* **48** (2010), pp. 3323–3329.
- [4] M.E.P. Markiewicz and S.H. Bergens, *J. Power Sources* **195** (2010), pp. 7196–7201.
- [5] L. Li and Y. Xing, *J. Phys. Chem C* **111** (2007), pp. 2803–2808.
- [6] M. Li, S. Zhao, G. Han, and B. Yang, *J. Power Sources* **191** (2009), pp. 351–365.
- [7] T. Huang, R. Jiang, J. Liu, J. Zhuang, W. Cai, and A. Yu, *Electrochim. Acta* **54** (2009), pp. 4436–4440.
- [8] Z. Liu, X. Zhang, and L. Hong, *Electrochem. Commun.* **11** (2009), pp. 925–928.
- [9] V. Raghuvier, K. Ravindranathan, N. Xanthopoulos, H.J. Mathieu, and B. Viswanathan, *Solid State Ionics* **140** (2001), pp. 263–274.
- [10] V. Raghuvier, B. Viswanathan, *Fuel* **81** (2002), pp. 2191–2197.
- [11] H.C. Yu, K.Z. Fung, T.C. Guo, and W.L. Chang, *Electrochim. Acta* **50** (2004), pp. 811–816.
- [12] R.N. Singh, T. Sharma, A. Singh, M.D. Anindita, and S.K. Tiwari, *Electrochim. Acta* **53** (2008), pp. 2322–2330.
- [13] R.N. Singh, A. Singh, M.D. Anindita, and P. Chartier, *Electrochim. Acta* **185** (2008), pp. 776–783.
- [14] N. Pikroh and P. Vanalabhpattana, *ECS Trans.*, submitted.

# EFFECT OF CeO<sub>2</sub> ON GLASS PROPERTIES PRODUCED FROM RICE HUSK FLY ASH

Nattapon Srisittipokakun<sup>1,2,\*</sup>, Keerati Kridsiri<sup>1,2</sup> and J. Kaewkhao<sup>1,2,3</sup>

<sup>1</sup>Center of Excellence in Glass Technology and Materials Science (CEGM), Faculty of Science and Technology, Nakhon Pathom Rajabhat University, Nakhon Pathom, 73000, Thailand

<sup>2</sup>Science Program, Faculty of Science and Technology, Nakhon Pathom Rajabhat University, Nakhon Pathom, 73000, Thailand

<sup>3</sup>Thailand Center of Excellence in Physics, CHE, Ministry of Education, Bangkok 10400, Thailand

\* Author for correspondence; E-Mail: Nattapon2004@gmail.com, Tel. +66 847000851, Fax. +66 34261065

**Abstract:** In this research work, the glasses were prepared by melt-quenching technique and used rice husk ash (RHA sample), from Nakhon Pathom Province, Thailand as silica source with different CeO<sub>2</sub> concentration. The results show that, the density and refractive index were increased with increasing of CeO<sub>2</sub> concentration. The absorption edge of undoped glass is occurred at a wavelength of around 325 nm. It is also observed that the positions of absorption edge shift to longer wavelength as the content of CeO<sub>2</sub> increased and showed brown color, which can be confirmed by UV-Vis spectrophotometer. This research is useful in the development of glass from ash and increased utilization of industrial waste.

## 1. Introduction

Rice is grown in every region of Thailand. The by-product of the milling process is rice husk, which accounts for 20% by weight of the rice. A large amount of rice husk is dumped as waste that brings waste disposal problem and methane emissions. Moreover, rice husk can cause breathing problem due to its characteristics. To maximize advantage of the waste and also to reduce the problems, some of rice husk is used as additive in cement industries [1]. Rice husk ash (RHA) contains an active form of silica (SiO<sub>2</sub>) and is available in large quantities in Thailand. Rice Husk contains ash from 13 to 29% by weight depending on the variety, climate and geographic location [2]. However, this silica from rice husk carries too many impurities and exhibits some inferior properties. As a result, research has been carried out to convert this rice husk into high purity amorphous silica. Several methods for preparing silica from rice husk have been proposed [3]. In the glass science, color is the most obvious property of a glass object. It can also be one of the most interesting and beautiful properties. Although color rarely defines the usefulness of a glass object it almost always defines its desirability. The goal was to find substances that would produce specific colors in the glass. Colorations of different colors in glass were achieved by transition metal ions or rare earth ions [4-5].

The objective of this research is to replace the silica with RHA to fabricate the color glass. Several important physical properties, i.e. density, refractive index and UV-Visible absorption spectra were investigated. Apart from increasing the value of RHA, it is also desirable to promote the use of color glass by reducing its raw material cost.

## 2. Materials and Methods

The local RHA in Nakhon Pathom province, Thailand was sintered at 1,000 °C and was use as silica source in glass matrices. The glass samples were prepared by using high purity of chemicals as following formula (55-x)SiO<sub>2</sub> : 1Al<sub>2</sub>O<sub>3</sub> : 6.3CaO : 0.2Sb<sub>2</sub>O<sub>3</sub> : 13B<sub>2</sub>O<sub>3</sub> : 4.5BaO : 20Na<sub>2</sub>O : xCeO<sub>2</sub> (where x is in mol%, ranging from 0.0-4.0 mol%). All chemicals were weighted of about 30 g and ground for homogeneous mixture. After that, the mixture was taken in high alumina crucibles and kept for melting in electrical furnace at 1100 °C at ambient temperature. These melts were quenched at room temperature in air by pouring between stainless steel plates. The quenched glasses were annealed at 500°C for 3 hour and cool down to the room temperature for reduce thermal stress. All glass samples were cut and polished in proper shape for further studies. The undoped glass was found to be colorless, while the CeO<sub>2</sub>-doped glasses were found to be more yellowish in color with higher CeO<sub>2</sub> concentration. Figure 1 shows the obtained glass samples in this work.

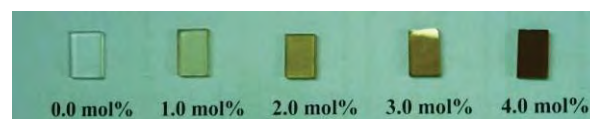


Figure 1. Undoped and CeO<sub>2</sub>-doped glasses with different CeO<sub>2</sub> concentration.

The optical absorption spectra were recorded at room temperature using a UV-Vis spectrophotometer (Cary50, Varian) in the wavelength of 300-900 nm.

The refractive index were measured by using an Abbe refractometer (ATAGO) with a sodium vapor lamp as the light source emitting wavelength,  $\lambda$ , of 589.3 nm (D line) and using mono-bromonaphthalene as the contact layer between the sample and prism of the refractometer.



### 3. Results and Discussion

The measured densities of glasses are shown in Figure 2. The result found that density increased with increasing of  $\text{CeO}_2$  concentration. This indicates that increasing the molecular weight of oxide ions used in the glass was increased due to the replacing  $\text{SiO}_2$  by  $\text{CeO}_2$ , resulting in the increase of density of these glasses.

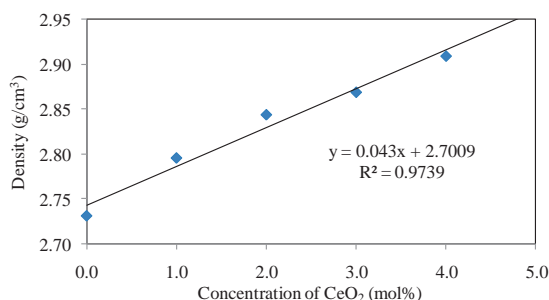


Figure 2. The density of  $\text{CeO}_2$ -doped glasses.

The refractive index (as shown in Figure 3) was measured by Abbe refractometer, which permits the measurement of refractive index up to 1.7 with an accuracy of 0.0002. The refractive index of glass samples are between  $1.5480 \pm 0.0003$  -  $1.5618 \pm 0.0000$ . It was observed that the refractive index increases with increasing concentration of  $\text{CeO}_2$ . This result shows similar trend with the density result. According to the classical dielectric theory, the refractive index depends on density and on polarizability of the atom in a given materials [6].

Optical absorption spectra of undoped and  $\text{CeO}_2$ -doped borosilicate glasses are shown in Figure 4. The absorption edge occurred at a wavelength of around 350 nm for all  $\text{CeO}_2$  concentration. It can be observed that the absorption edges were slightly shifted to the longer wavelength with increasing of  $\text{CeO}_2$  concentration.

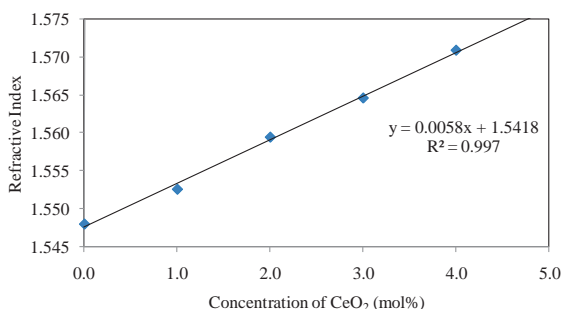


Figure 3. The refractive index of  $\text{CeO}_2$ -doped in borosilicate glasses.

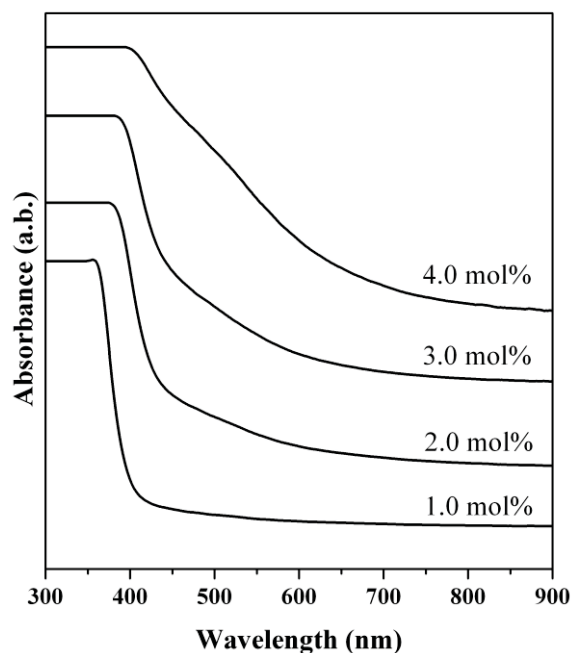


Figure 4. Optical absorption spectra of  $\text{CeO}_2$ -doped in borosilicate glasses.

Considered color of glass samples with different  $\text{CeO}_2$  concentration are illustrated in Figure 5. The undoped glass sample was colorless while the  $\text{CeO}_2$ -doped glasses were brown color due to  $\text{Ce}^{3+}$  ions in glass matrix. The brightness,  $L^*$  were decrease when the concentration of  $\text{CeO}_2$  doping increase. This is due to the higher absorption spectra in visible region (300 – 900 nm) when increasing of  $\text{CeO}_2$  concentration.

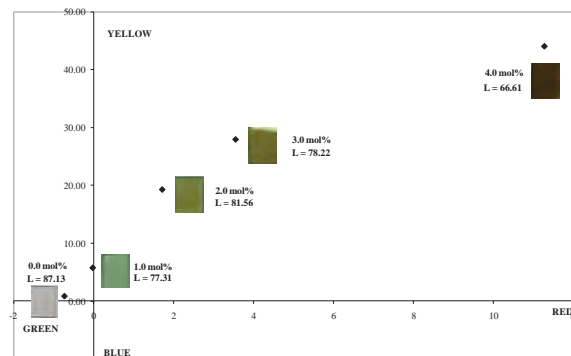


Figure 5. The CIE  $L^*a^*b^*$  color scale of  $\text{CeO}_2$ -doped in borosilicate glasses.

### 4. Conclusions

The glass samples were prepared by using high purity of  $\text{Na}_2\text{CO}_3$ ,  $\text{Al}_2\text{O}_3$ ,  $\text{B}_2\text{O}_3$ ,  $\text{CaO}$ ,  $\text{Sb}_2\text{O}_3$  and RHA (used as  $\text{SiO}_2$  source). The concentration of  $\text{CeO}_2$  is vary from 0.0 – 4.0 mol%. The undoped glass sample was colorless while the  $\text{CeO}_2$ -doped glasses were brown color due to  $\text{Ce}^{3+}$  ions in glass matrix. The density increased with the increase of  $\text{CeO}_2$  concentration. This indicates that increasing the molecular weight of oxide ions used in the glass was

due to the replacing  $\text{SiO}_2$  by  $\text{CeO}_2$ . The refractive index has been increased with increasing concentration of  $\text{CeO}_2$ . The absorption edges occurred at a wavelength of around 350 nm for all  $\text{CeO}_2$  concentration. It can be observed that the absorption edges were slightly shifted to the longer wavelength with increasing of  $\text{CeO}_2$  concentration.

### Acknowledgements

The authors wish to thank National Research Council of Thailand (NRCT) funding this research. Thanks are also due to Research and Development Institute, NPRU for facilities.

### References

- [1] T. Chungsangunsit, S.H. Gheewala and S. Patumsawad, Sustainable Energy and Environment (2004) 739-742.
- [2] C.S. Prasad, K.N. Maiti, R. Venugopal, Ceramics International **29** (2003) 907–914.
- [3] S. Chuayjuljit, S. Eiumnoh and P. Potiyaraj, The Journal of Scientific Research Chulalongkorn University, **26** (2) (2001) 227-238
- [4] J.E. vShelby, Introduction to Glass Science and Technology, Royal Society of Chemistry, London, England. (2005).
- [5] Ali A.A, Journal of Luminescence. **129**, (2009) 1314–1319.
- [6] Y. Ruangtaweep, J. Kaewkhao, K. Kirdsiri, C. Kedkaew and P. Limsuwan, Materials Science and Engineering **18** (2011) 112008

# ETHYLENE ADSORPTION ON MODIFIED BENTONITE

Saran Youngjan<sup>1\*</sup>, Kunwadee Rangsiwatananon<sup>1</sup>

<sup>1</sup> School of Chemistry, Institute of Science, Suranaree University of Technology, Nakhonratchasima 30000, Thailand

\*E-mail: [Daiwy\\_ho@hotmail.com](mailto:Daiwy_ho@hotmail.com)

**ABSTRACT:** This study focused on the ethylene adsorption on modified bentonite prepared in three different ways to produced porous materials namely organoclay, pillared clay (PILC) and porous clay heterostructure (PCH). Organoclay was prepared by modifying bentonite with various surfactants. PILC used in this work was Al-pillared clay and four samples of PCHs synthesized with different compositions were used in the adsorption. The adsorbents were characterized by XRD, FT-IR technique and surface analysis by BET method. XRD of bentonite showed a peak at  $2\theta = 6.00^\circ$ , corresponding to a basal spacing of 15.08 Å. After pillaring with Al<sub>13</sub>, the basal spacing was increased to 18.20 Å ( $2\theta = 4.80-5.00^\circ$ ). For organoclay the  $2\theta$  peak was the same as the starting bentonite. The spectra of PCHs were different from the starting bentonite indicated by the absence of peak at 1039 cm<sup>-1</sup>. PCHs have more specific surface area than PILC and organoclay. The surface area of bentonite was 32 m<sup>2</sup>/g. After modification as organoclay, PILC and PCHs the surface area was increased to 70, 235 and 897 m<sup>2</sup>/g, respectively. The ethylene adsorption isotherms indicate that the best adsorbent was PCHs able to adsorb ethylene up to 32 cm<sup>3</sup>/g, while organoclay and PILC can adsorb ethylene 12 and 13 cm<sup>3</sup>/g, respectively. The ethylene adsorption capacity depends significantly on the surface area of adsorbent.

## 1. Introduction

Ethylene is produced essentially from all part of plant, including leaves, stems, roots, flowers, fruits, tubers and seedling. During the life of plants, ethylene production is induced during certain stages of growth such as seed germination, root and shoot growth, ripening of fruits, abscission of leaves and senescence of flowers [1]. Accumulation of ethylene may result in a number of specific defects in harvest products. Therefore, removal of ethylene is of economic importance to the food and floral industry. It allows producers, handlers and sellers to spread availability over periods of strong and weak demand, maintaining supply and stabilizing cost. One of the most effective materials to remove ethylene is potassium permanganate and also other material as the adsorbent for ethylene such as zeolite [2], modified zeolite G5 [3] and clinoptilolite [4]. However, because of the chemical properties of potassium permanganate, precautions must be taken in order to prevent contamination of food products [4-5]. The search for other materials for ethylene removal capability has been focused on cheaper materials such as clay minerals.

The surface properties of clay mineral may be greatly modified with surfactant by simple ion-exchange process and the modified clay was called organoclay which has more surface area and more

hydrophobicity. Therefore, it leads to increase in adsorption capacity of organic compounds. The organoclays have attracted much interest because of their wide applications in the environmental and material sciences [6-7].

The other modification of clay mineral like montmorillonite is to make it to be pillared clay (PILC) which is porous material and has high surface area. It has been used as a catalyst for crude oil cracking processes. Various kinds of metal-PILC have been introduced such as Al-PILC, Zr-PILC, Cr-PILC, Si-PILC, Fe-PILC and Ti-PILC [8]. PILC was prepared by exchanging the charge compensating cations between the swelling clay layers with larger polymeric or oligomeric hydroxyl metal cations. Among them, Al-pillared clay, the first prepared inorganic PILC, had attracted great research interests and intensively investigated [9]. Recently, the discovery of a new class of porous materials known as porous clay heterostructure (PCH) has been proposed. The modification of porous materials offers many advantages as adsorbents, gas-separation devices, or gas-storage materials [10]. This material was prepared by the silica source has been polymerized in situ between the aluminosilicate sheets and around the micellar rods of surfactant and co-surfactant previously ion exchanged on the interlayer space of the clay. After calcinations for the removal of the organics, the mesopores are formed and the PCH obtained [10-11].

This study therefore investigated the methodology to modify the bentonite and evaluate the resulting products as adsorbents for ethylene removal.

## 2. Materials and Methods

### 2.1 Preparation of organobentonite

The clay used in this study was a bentonite obtained from the Thai Nippon Chemical Industry Co. Natural bentonite will be prepared by sieving to yield particles less than 63 µm and dried at 110 °C before using in the further steps. Organobentonite samples are prepared by modification of bentonite with phenyl trimethyl ammonium bromide (PTAB), (vinylbenzyl)trimethyl ammonium chloride (Vinyl), ethyltrimethyl ammonium iodide (C2) and methyltriphenyl phosphonium bromide (MTPB) in the concentration range from 0.2 mM to 20.0 mM. Bentonite and cationic surfactant are mixed together and stirred for 48 h. The mixture is centrifuged at 3500 rpm for 20 minutes and followed by filtration. Then

the solid will be washed with deionized water and dried at 110 °C for 3 h.

## 2.2 Synthesis of Al-pillared bentonite

The aluminum-pillared bentonite was prepared as follows: at first, to get the  $Al_{13}$  oligomer, 0.2 M NaOH was added dropwise to 0.2 M  $AlCl_3$  solution under vigorous stirring at room temperature and at 70 °C for 1 day and for 3 days. The molar (OH/Al) ratio of 2.4 was used. The pillared clay was then synthesized by adding a 2% of clay suspension with the ratio of aluminum to clay of 5 and 10 mmol/g stirring for 24 h. Intercalations of the pillar were improved by repeated washing with DI water until free of chloride. The pillared clay was then dried, ground and heated at 350 °C for 3 h. as shown in Table 1.

Table 1: The parameters for preparation of PILCs.

Sample	Time (day)	mmol $Al_{13}$	Temp.(°C)
PILC-1	1	5	R.T.
PILC-2	1	10	R.T.
PILC-3	3	5	R.T.
PILC-4	3	10	R.T.
PILC-5	1	5	70
PILC-6	1	10	70

## 2.3 Synthesis of PCHs

The method of preparing PCHs was adopted from literature [12]. A suspension of 1 g bentonite in 100 mL distilled water was mixed with 4.8 mL solution of 0.5M cetyltrimethylammonium bromide (CTAB) solution. The solution was stirred for 12 h at 50 °C and then centrifuged-washed repeatedly until pH~7 to separate the solid from the solution. Then, the solid was added with decylamine (Aldrich, 95%) and stirred for 20 minutes, after that 35.5 mL of TEOS (Aldrich, 98%) was added and stirred for 12 h. The obtained suspension was then centrifuged and air dried, after the sample was calcined at 650 °C for 5 h with a slow ramp (1°C/min). Different samples were prepared by varying the proportion volume of 0.5M CTAB, decylamine and the TEOS, as shown in Table 2.

Table 2: The ratios of the volumes for preparation of PCHs.

Sample	0.5M CTAB	decylamine
PCH1	4.8	5.3
PCH2	4.8	10
PCH3	2.4	5.3

## 2.4 Standard characterization

The adsorbent structure was determined by X-ray diffraction technique using XRD Bruker D5005 Powder X-ray diffractometer with Ni-filtered  $Cu K\alpha$  radiation source and operated at 35 kV/35 mA for recording all of the diffraction spectra. The intensity data was collected in a  $2\theta$  range from 5° to 30° with the scan rate and step size of 0.5°s<sup>-1</sup> and 0.02°step<sup>-1</sup>. Infrared spectra were obtained with a Perkin-Elmer

spectrum GX FTIR Spectrophotometer and infrared spectra were taken in the range of mid infrared (4000-400 cm<sup>-1</sup>). The samples were recorded with 13 of number scan and with 4 cm<sup>-1</sup> resolution. The samples were prepared by KBr pellet technique. Nitrogen adsorption-desorption isotherms of the prepared samples were studied at 77K on a Quantachrome Autosorb-1C instrument; (USA). The measurements of surface area, pore volume and pore size data were carried out with Autosorb-1C, Quantachrome. Prior to each measurement, the adsorbent was degassed at 300 °C for 3 hours. The total pore volume and average pore size were determined at relative pressure  $P/P_0$  equal to 1. The external surface area was determined by t-plot method at a range of relative pressure  $P/P_0$  from 0.2 to 0.5.

## 2.5 Ethylene adsorption capability

The capability of ethylene gas adsorption was studied using Nova 1200e instrument (Quantachrome) at 0 °C. The 200 mg adsorbent was degassed at 300 °C for 3 h prior to the measurement. The ethylene adsorption isotherms were determined at relative pressure  $P/P_0$  between 0 and 1.

## 3. Results and Discussion

### Standard characterization

The XRD patterns of bentonite and modified bentonite samples are displayed in Fig. 1. A typical diffraction peak of bentonite is  $2\theta = 5.92^\circ$ , responding to a basal spacing ( $d_{001}$ ) of 15.08 Å. After intercalation with the MTPB and  $Al_{13}$ - polyoxocation, this peak moves to lower angle (5.22° and 4.74° ), responding to  $d_{001}$  of 17.12 Å and 18.38 Å, respectively. It is clear that an increase in basal spacing occurs in the presence of the  $Al_{13}$ -polyoxocation and MTPB. There are small changes in the basal spacing of C2-bentonite, PTAB-bentonite and Vinyl-bentonite, but much more change on MTPB-bentonite as surfactant loading increased. These results indicated that modification of bentonite with C2, PTAB and Vinyl did not lead to significant structural changes.

FT-IR spectra of PCHs are shown in Fig. 2. It shows the peaks at 3632 cm<sup>-1</sup> is a characteristic of bentonite corresponding to the fundamental stretching vibration of hydroxyl groups of Si-OH or Al-OH [13] and the peak at 1039 cm<sup>-1</sup> is a characteristic of Si-O-Si stretching vibration of clay minerals. The peaks at around 3436 cm<sup>-1</sup> and 1630-1637 cm<sup>-1</sup> are stretching and bending vibration of water forming hydrogen bond, respectively. The spectra of PCHs were different from the starting bentonite indicated by the absence of peak at 3632 cm<sup>-1</sup> and 1039 cm<sup>-1</sup>. So it roughly infer that the structure of starting clay are changed after the modification. The sharp peak centered at about 1086-1091 cm<sup>-1</sup> can be assigned to the stretching vibration of the SiO<sub>4</sub> units of the silicate layers [14].



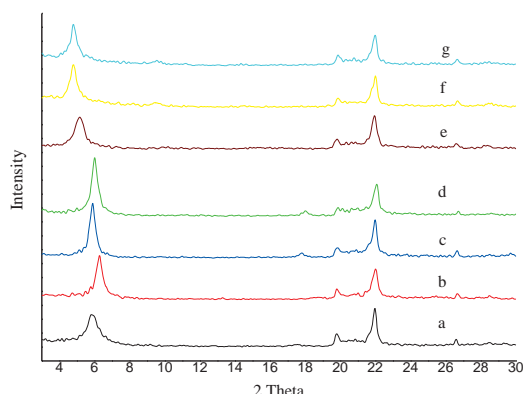


Figure 1. The XRD patterns (a) bentonite (b) C2-bentonite (c) PTAB-bentonite (d) Vinyl-bentonite (e) MTPB-bentonite (f) PILC-1 (g) PILC-2

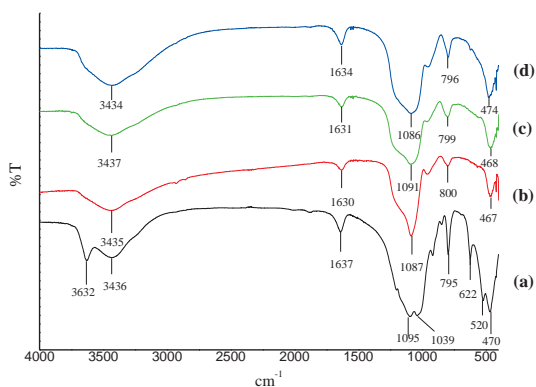


Figure 2. FT-IR patterns of (a) bentonite, (b) PCH1, (c) PCH2 and (d) PCH2.

The  $N_2$  adsorption-desorption isotherms were obtained at  $-196^\circ\text{C}$  on a Quantachrome Autosorb-1. All the samples were outgassed at  $300^\circ\text{C}$  for 3 h in a vacuum prior to analysis. The isotherm of bentonite (Fig.3) shows a characteristic of non-porous solid due to its low surface area only  $31.1\text{ m}^2/\text{g}$ . After modification, the surface areas of PILCs and PCHs increase significantly from raw clay. It is apparent that the shapes of the isotherms of all PCHs are similar and are classified as type I+II. However, the PILCs isotherms are of typical type I. The amounts adsorbed by PCHs are higher than PILCs, and the order of amount adsorbed is  $\text{PCHs} > \text{PILCs}$ . Isotherms of both PCHs show a hysteresis loop (Fig. 3), which generally reflects the presence of mesoporosity, besides the microporous structure. The presence of sufficient mesopore volumes in PCHs was again confirmed from the results in Table 3. The surface analyses of all the samples are shown in Table 3.

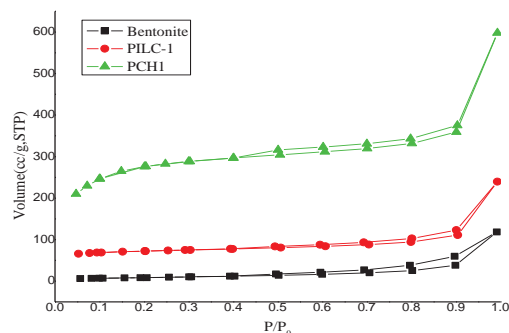


Figure 3.  $N_2$  adsorption-desorption isotherms of bentonite, PILC-1 and PCH1.

The ethylene adsorption isotherms of bentonite, organobentonite, PILCs and PCHs are shown in Figure 4. The isotherm indicated that prepared PCHs can adsorb ethylene better than PILCs and organobentonites. PCH1 is the best adsorbent which can adsorb ethylene with the maximum amount. Their adsorption capacities increased from 0 to  $32\text{ cm}^3\text{g}^{-1}$ . The large surface areas of PCHs result to the higher adsorption capacity of ethylene comparing to PILCs and organobentonites.

For the organoclay, C2-bentonite can adsorb ethylene more than the others of organobentonite due to its higher surface areas. The surface areas of PTAB-bentonite, MTPB-bentonite and vinyl-bentonite are the same as the starting bentonite. But all organoclays adsorb ethylene by additional  $\text{CH}-\pi$  interaction possibly occurring between C-H group and the C=C bond of ethylene.

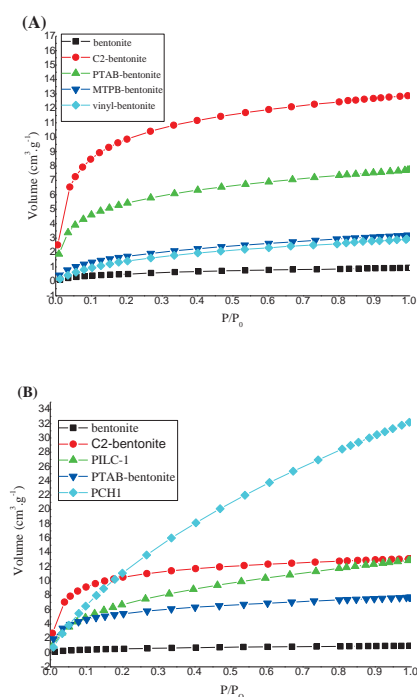


Figure 4. (A) Adsorption isotherms of ethylene on organobentonite and (B) Comparison of ethylene adsorbed on bentonite and modified bentonite samples.

Table 3: Surface analysis and ethylene adsorptions of bentonite and modified bentonites.

sample	BET m <sup>2</sup> /g	Pore volume (cc/g)	Micropore volume (cc/g)	Pore Diameter (nm)	Micropore surface (m <sup>2</sup> /g)	Ethylene adsorption (cm <sup>3</sup> /g)
Bentonite	31.1	0.1832	0	2.352	0	0
20 mM C2	70.9	0.2207	0.0113	1.244	24.42	12.87
20 mM PTAB	31.9	0.1905	0	2.387	0	7.73
20 mM MTPB	28.7	0.1682	0	2.348	0	3.20
PILC-1	184.8	0.2988	0.0653	6.466	132.9	11.56
PILC-2	138.7	0.3183	0.0438	9.178	89.06	9.85
PILC-3	150.1	0.2151	0.0501	5.730	101.5	9.16
PILC-4	178.4	0.3002	0.0617	6.733	125.7	11.33
PILC-5	224.7	0.3716	0.0854	6.616	164.0	12.89
PILC-6	199.7	0.3311	0.0691	6.632	140.6	12.79
PCH1	897.7	0.9274	0.3446	4.132	698.8	32.19
PCH2	579.2	0.7908	0.1228	5.464	252.4	25.03
PCH3	575.8	0.6551	0.2116	4.551	416.3	26.36

#### 4. Conclusions

Modification of bentonite prepared in three different ways to produced porous materials namely organoclay, PILCs and PCH, the ethylene adsorptivities of the modified products were studied. An XRD study indicated that the modification of bentonite with C2, PTAB and Vinyl does not change the  $d_{001}$  but the  $d_{001}$  of PILCs are increased. The PILCs and the PCHs showed the improvement of specific surface areas and pore volumes. The results show that the better ethylene adsorption capacity was obtained from modified bentonite which was changed to PCHs.

#### Acknowledgements

This work was supported by a research grant from the National Research Council of Thailand. Thanks are also extended to the Center for Scientific and Technology Equipment, Suranaree University of Technology.

#### References

- [1] K. Wang, H. Li and J. Ecker, *Plant Cell*. **14** (2002) 131–151.
- [2] K. Berlier, M. G. Olivier and R. Jadot, *J. Chem. Eng.* **40** (1995) 1206–1208.
- [3] N. Patdhanagul et al., *Microporous Mesoporous Mate.* **131** (2010) 97–102
- [4] B. Erdogan et al., *Appl. Surf. Sci.* **254** (2008) 2450–2457
- [5] K. Abe and A.E. Watada, *J. Food Sci.* **56** (1991) 1589–1592
- [6] C.B. Hedley, G. Yuan and B.K.G. Theng, *Appl. Clay Sci.* **35** (2007) 180–188.
- [7] S. Lee et al., *Chemosphere*. **55** (2004) 781–785.
- [8] R. Wibulswas, D. A. White and R. Rautiu, *ICChem<sup>E</sup>*. **77** (1999) 88–92.

- [9] J.Q. Jiang, C. Cooper and S. Ouki, *Chemosphere*. **47** (2002) 711–716.
- [10] R. Ishii, M. Nakatsuji, and K. Ooi, *Microporous Mesoporous Mate.* **79** (2005) 111–119.
- [11] M. Polverejan, T.R. Pauly, and T.J. Pinnavaia, *Chem. Mater.* **12** (2000) 2698–2704.
- [12] J. Pires et al., *Microporous Mesoporous Mate.* **73** (2004) 175–180
- [13] V. K. Saini, M. Pinto, and J. Pires, *Separ. Sci. Technol.* (2011) **46** 137–146.
- [14] M. Nakatsuji et al., *J. Colloid Interface Sci.* **272** (2004) 158–16

# EFFECT OF PROPYLENE OXIDE POLYOL AS CELL OPENING AGENT IN FLEXIBLE POLYURETHANE FOAM

Nitipong Chotiwiattayaporn<sup>1\*</sup> and Nuanphun Chantarasiri<sup>2</sup>

<sup>1</sup>Program in Petrochemistry and Polymer Science, Faculty of Science, Chulalongkorn University, Bangkok 10330, Thailand

<sup>2</sup>Department of Chemistry, Faculty of Science, Chulalongkorn University, Bangkok 10330, Thailand

\* Author for correspondence; E-Mail: [nitipong.chotiwiattayaporn@bayer.com](mailto:nitipong.chotiwiattayaporn@bayer.com), Tel. +66 2 3246222, Fax. +66 2 7094325

**Abstract:** Flexible polyurethane foams (FPUR foams) are versatile materials which widely used in many applications such as automotive seating, furniture or mattress. The raw materials used to produce FPUR foams are polyol, isocyanate, catalyst and blowing agent (water). Besides these raw materials, cell opening agent (COP) is also necessary in order to prevent foam shrinkage after curing in mold. Nowadays, conventional COP used in FPUR foam production is polyether polyol which contains high ethylene oxide content. However, the disadvantages of conventional cell opening agent are high cost and phase separation due to its high polarity and hydrophilic property of ethylene oxide unit which is able to form hydrogen bond with water molecules and separate from polyol system upon storage. In this work, pure propylene oxide (PO) polyol was used as a new cell opening agent in FPUR foams in automotive FPUR foam formulations using various blowing agent contents. The advantages of PO polyol as cell opening agent are low cost and good homogeneity between cell opening agent and other ingredients in FPUR foam formulation. In cup test method, this new PO polyol cell opening agent gave good foam skin with no shrinkage while in molded test method, PO polyol acted as cell opening by lowering the force-to-crush of molded foam after de-mold. Mechanical properties of FPUR foams prepared from PO polyol were studied, namely hardness, elongation, tensile and tear strength. The results showed that the new PO polyol cell opening agent gave higher foam hardness and strength while lowering the elongation due to its lower molecular weight as compared to FPUR foams prepared from conventional cell opening agent.

## 1. Introduction

Nowadays most of automotive seating is produced from FPUR foams due to its good cushioning property high comfort and durability [1]. The seating production start from pouring the mixture of polyurethane (PU) into heating aluminium molds in the conveyor line. The molds then move along conveyor from injection station, mold closing station to de-mold station to remove cured FPUR foams from the molds. Normally the curing time in molds required 4 – 6 minutes depending on FPUR foam formulation [2]. The crushing process either using crushing roller or vacuum crushing is required immediately after de-mold process in order to make cell wall rupture to prevent foam shrinkage [3]. The shrinkage comes from the close cell structure in FPUR foams which traps the hot gas generated upon PU reaction inside cell structure. After the trapped gas cooled down, the reduced internal pressure occurs and causing the foam to shrink [4, 5]. The crushing process alone cannot

completely make the cell wall rupture in FPUR foams. The FPUR foams themselves must have enough open cell content to cooperate with crushing process to prevent foam shrinkage. Cell opening agent (COP) is the necessary additive to increase open cell content in FPUR foams. Many COP studies were done since 1990 by using many types of polyether polyol [5, 6].

Nowadays, the high ethylene oxide (EO) content polyol is most commonly used as conventional COP [4]. The drawbacks of this conventional COP are high cost and phase separation. The high EO content in conventional COP forms the hydrogen bond with water in FPUR foam formulation due to its high hydrophilicity causing the phase separation of COP and water from other compositions in FPUR foam formulation upon storage.

In this study, pure PO polyol was used as COP in FPUR foam formulations. The amount of PO polyol was varied. The study was done in both cup test method and molded test method. The FPUR foams core density in molded test method was varied by varying the amount of water content (wt.%) in FPUR foam formulations. Crushability [force to crush (FTC) test], mechanical properties, namely hardness, elongation, tensile strength, tear strength and morphology were studied. The foams prepared from PO polyol were studied and compared with those prepared from conventional COP.

## 2. Materials and Methods

### 2.1 Chemicals

All materials used in this study were obtained from commercial sources. The polyether polyols, toluene diisocyanate (TDI), catalyst, crosslinker, surfactant, conventional COP and blowing agent were supported from Bayer Thai Co., Ltd. (BayerMaterialscience, Samutprakarn, Thailand). The material used in this study and its role are shown in Table 1. All chemicals were used as received.

### 2.2 Sample preparations

The FPUR foams samples prepared using conventional COP (reference formulation) and using PO polyol as COP with various blowing agent (water) content were prepared by mechanical mixing technique in two mixing steps. In the first mixing step, polyol mixture, catalyst, crosslinker, surfactant, COP and blowing agent were mixed together with mechanical stirrer at 2000 rpm for 3 minutes.

Table 1: Characteristics of the starting materials

Materials <sup>a</sup>	Molecular Weight	Role
Arcol® long chain base polyol	6,000	OH value = 28 mg KOH/g
Hyperlite® polyol	-	OH value = 20 mg KOH/g, contained 43% solid content.
Arcol® PO polyol	3,000	OH value = 56 mg KOH/g, PO polyol as COP
Conventional COP	-	OH value = 37 mg KOH/g
Glycerine	-	Crosslinker, OH value = 1830 mg KOH/g
Organo-modified polysiloxanes	-	Surfactant.
Triethylene diamine in dipropylene glycol	-	Amine catalyst
Distilled water	9	Chemical blowing agent
Toluene diisocyanate blended with Diphenylmethane diisocyanate (80:20)	-	NCO content = 44.8

<sup>a</sup> All materials were supported by Bayer Thai Co., Ltd., BayerMaterialsScience, Samutprakarn, Thailand

Then, in the second mixing step, TDI was added into the polyol mixture from the first mixing step. The mixture was immediately stirred by mechanical stirrer at 4000 rpm for 5 seconds. After that, the mixture was poured into the plastic cup with 2 liters capacity and allowed to rise up freely for reaction reactivity observation. Cream time, gel time, rise time and %settling were measured. The foams were kept at room temperature for 24 hours before free rise density analysis. While the foam sample used for force to crush measurement and mechanical property analysis were obtained from pouring the mixed reactant into the closed mold (400 x 400 x 100 mm) to produce the foams with core density of  $32-42 \pm 1.5 \text{ kg/m}^3$ .

To investigate the effect of PO polyol as COP in comparison to the conventional COP, PO polyol was used instead of conventional COP and the amount of PO polyol was varied at 2.0 – 15.0 parts per hundred parts of polyol by weight (pbw) while the amount of catalyst, crosslinker and surfactant were fixed at 0.6, 0.5 and 0.6 pbw, respectively. The amount of water was fixed at 3.5%wt per 100%wt of polyol. The amount of TDI required for the reaction with polyol mixture was calculated from the equivalent weight. The equivalent TDI was used for the sample preparation (NCO/OH = 1.00, index 100). This study was done to obtain the optimum amount of PO polyol as COP in FPUR foam formulation, in which the foam had suitable %settling and contained enough open cell content. The open cell content of FPUR foam was measured by force to crush test.

After the optimum FPUR foam formulation using PO polyol as COP was achieved, the next investigation was varying the blowing agent to 3.0%wt and 4.0%wt per 100%wt of polyol in order to vary the core density of FPUR foams in molded test method. The amount of polyol mixture, catalyst, crosslinker and surfactant were fixed at 100, 0.6, 0.5 and 0.6 pbw, respectively. The amount of TDI required for the reaction with polyol mixture was calculated from the equivalent weight. The equivalent

TDI was used for the sample preparation (NCO/OH = 1.00, NCO index 100).

### 2.3 Analytical Procedure

In cup test method, the reactivity of FPUR polymerization reaction was obtained from measuring cream time (CT), gel time (GT), rise time (RT) and %settling. The cream time was the time that FPUR mixture start rise up. The gel time was the time that FPUR foams develop enough gel strength by the reaction that form urethane and urea linkages to resist light impression and is dimensionally stable. The rise time was the time when the FPUR foams reach the maximum height before gas blow off from cell structure. %Settling was the different of foam height in percent between the maximum height and the height at 5.0 minutes after reaction. The settling is the key reactivity which represents the open cell content in FPUR foams. When the foams have more open cell content, more gas is blown off from the foam matrix, which results in higher %settling.

Free rise density (FRD) of FPUR foam samples was measured according to JIS 6400-1 by using cutting machine. The size of the free rise density specimen was 50 x 50 x 50 mm (width x length x thickness). The densities of three specimens per sample were measured and averaged.

The FTC was measured according to [4] by measured the force required to press molded FPUR foams to 25% and 50% of its original thickness after de-mold process for 1 minute. The lower FTC represents the higher open cell content in molded FPUR foams.

Mechanical properties of the FPUR foams samples were measured under ambient conditions with a Zwick/Roell universal testing machine. Hardness (25% ILD) test was performed according to ASTM D 3574-95. Tensile strength, tear strength, elongation and ball rebound were performed according to JIS 6400-1 using the specimens' thickness 10 mm. The wet and



Table 2: Composition, Reactivity, Free Rise Density and Force to crush of FPUR foams

FPUR foams Sample <sup>a</sup>	Arcol® long chain base polyol (Pbw)	Conventional COP (Pbw)	PO polyol COP (Pbw)	Water (%)	FPUR foams Reactivity				FRD (Kg./m <sup>3</sup> )	FTC <sup>b</sup> (Kg/314cm <sup>2</sup> )
					CT (sec.)	GT (sec.)	RT (sec.)	settling (%)		
A1	60.0	2.0	-	3.5	10	64	89	13.8	32.5	31.1 : 87.7
A2	↓	-	2.0	↓	10	62	104	5.3	28.2	-
A3	↓	-	4.0	↓	10	65	106	5.5	28.3	-
A4	↓	-	6.0	↓	10	65	106	5.4	28.4	-
A5	↓	-	8.0	↓	10	66	112	6.0	29.5	-
A6	↓	-	10.0	↓	10	67	114	7.5	30.4	-
A7	50.0	-	10.0	↓	10	64	96	8.1	30.3	-
A8	45.0	-	15.0	↓	10	64	87	10.7	32.6	30.1 : 84.3
B1	60.0	2.0	-	3.0	10	62	89	11.9	38.0	29.7 : 84.6
B2	45.0	-	15.0	↓	10	62	93	13.3	39.4	29.3 : 83.5
C1	60.0	2.0	-	4.0	10	66	86	15.4	33.2	-
C2	↓	1.5	-	↓	10	64	96	10.4	28.3	47.0 : 114.1
C3	45.0	-	15.0	↓	10	64	90	13.9	31.3	34.7 : 93.3
SD <sup>c</sup>	-	-	-	-	±0.5	±1.0	±1.0	±1.0	±1.0	-

<sup>a</sup> TDI blended with MDI (80:20) with Isocyanate index 100 were used in all samples. Other compositions using with the same dosage in all FPUR foam formulations are shown in table 3.

<sup>b</sup> Force to crush 25% : 50% compression.

<sup>c</sup> The reactivity and FRD testing were repeated 3 times, the SD were calculated based on three specimens.

Table 3: Formulated polyol mixture compositions. (excluding Arcol® long chain base polyol, COP, PO polyol and water)

Compositions	Pbw
Hyperlite® polyol	40.0
Glycerine	0.50
Organo-modified polysiloxanes	0.60
Amine catalyst	0.60

dry compression set were performed according to JIS 6400-1. The strengths and elongation of five specimens per sample were measured and averaged. For wet and dry compression set, three specimens per sample were measured and averaged.

Morphology of FPUR foams was studied with a Philips XL-30 scanning electron microscope. The samples were cut and gold sputtered before scanning in perpendicular to the foam rising direction. The accelerating voltage was 25 kV.

### 3. Results and Discussion

#### 3.1 Preparation of FPUR foams

FPUR foams were prepared by free rising method (cup test method) in order to study the reaction reactivity while the over-packing specimens (molded test method) were prepared for FTC measurement to measure the open cell content in FPUR foams [7,8] and for mechanical analysis. The formulations' composition, reactivity, free rise density and force to crush results are tabulated in Table 2. Table 3 showed the other compositions in FPUR foam formulation which were not shown in Table 2.

#### 3.2 Reactivity and Free rise density

FPUR foam formulations were studied by variation of PO polyol amount instead of conventional COP (A1-A6) as shown in Table 2 and 3. It was found that the higher amount of PO polyol in foam formulation gave higher foam settling and free rise density even in the absence of conventional COP (A2-A6) but still was not as high as the foam prepared from conventional COP. The reactivity of FPUR foams using high amount of PO polyol was slower than the reference formulation (A1). This is because of higher polyol content diluted the catalyst concentration in formulation. Therefore, PO polyol was used as long chain based polyol instead of Arcol® long chain based polyol at the amount of 10.0 and 15.0 pbw (A7-A8). The reactivity of A7-A8 formulations was faster than formulations A2-A6. The formulation contained 15.0 pbw PO polyol (A8) gave the same reactivity and free rise density as reference formulation (A1). Therefore, this formulation was further used in the next experiment by variation of chemical blowing agent (water).

After decreasing water content to 3.0%wt. (B1-B2), the reactivity result showed that formulation B2 that used 15.0 pbw substituted PO polyol (B2) gave the same gel time but slower rise time. This indicated that the reference formulation (B1) gave more open cell content since the gas was blown off from foam matrix was faster than the foam prepared using 15.0 pbw substituted PO polyol as COP [9]. However, from the %settling and free rise density result, formulation B2 using PO polyol gave higher %settling and free rise density which indicated that it had higher open cell content than the foam prepared using conventional COP [7].

Table 4: Mechanical properties of FPUR foams

FPUR foams Sample <sup>a</sup>	Core Density (kg/m <sup>3</sup> )	Hardness (N/314cm <sup>2</sup> )	Elongation (%)	Tensile Strength (kPa)	Tear Strength (N/cm <sup>2</sup> )	Ball Rebound (%)	Dry compression set (%)	Wet compression set (%)
A1	37.1	160	116	158	8.0	65	6.9	24.0
A8	36.4	167	110	160	7.6	62	6.2	28.6
B1	42.2	183	110	140	7.8	68	5.0	25.3
B2	42.1	191	104	170	7.3	65	6.4	31.8
C2	32.8	168	110	155	7.7	64	10.4	32.1
C3	32.4	175	106	160	7.3	61	11.4	32.7
SD <sup>b</sup>	-	-	±3.0	±1.0	±1.0	±0.5	±0.5	±0.5

<sup>a</sup> TDI blended with MDI (80:20) with Isocyanate index 100 were used in all samples. Other compositions using with the same dosage in all FPUR foam formulations are shown in table 3.

<sup>b</sup> The SD of elongation, tensile strength and tear strength were calculated based on five specimens while the SD of ball rebound, wet and dry compression set were calculated based on three specimens.

The delayed rise time may come from slower gas generation from blowing reaction since isocyanate react with PO polyol faster than Arcol<sup>®</sup> long chain base polyol. This is because PO polyol has less molecular weight than Arcol<sup>®</sup> polyol.

The increasing of water content to 4.0%wt. was done in formulations C1-C3. In formulation C1, same amount of conventional COP was used as previous experiment (2.0 pbw). Too large %settling and free rise density at NCO index 100 was observed which results in less foam stability [4]. Therefore, the amount of conventional COP in reference formulation was decreased from 2.0 pbw to 1.5 pbw (C2). The formulation C2 was used as reference formulation for the study of PO polyol effect at 4.0%wt. water content. The same amount of substituted PO polyol was used (15.0 pbw, C3) and the reactivity result showed that formulation C3 gave the same gel time as C2. Faster rise time, higher %settling and free rise were obtained in C3. This indicated that the use of substituted PO poly gave higher open cell content than conventional COP.

From the reactivity result, it is shown that use of 15.0 pbw of substituted PO polyol as COP in FPUR foam formulation gave the same performance as conventional COP. Thus, these formulations were used to prepare FPUR foams in molded method to study the crushability by force to crush test and to use for mechanical property analysis.

### 3.2 Force to crush measurement

Force to crush results in Table 2 show that the formulations using 15.0 pbw substituted PO polyol have lower force to crush at both 25% and 50% compression than the formulation using conventional COP. This results agreed with reactivity result that 15.0 pbw substituted PO polyol gave higher open cell content in FPUR foams than conventional COP [7,8].

### 3.3 Mechanical property analysis

Table 4 shows the mechanical properties of FPUR foams obtained from the molded test method at core

density of 32, 37 and 42 ± 1.5 kg/m<sup>3</sup>. It was found that no significant different in mechanical properties was observed between reference formulations (A1, B1, C2) and formulation using substituted PO polyol (A8, B2, C3). In comparison to the reference formulation, substituted PO polyol formulation had slightly higher foam hardness and tensile strength while the elongation, tear strength and ball rebound were lower. This is because of lower molecular weight of PO polyol which made FPUR foams have higher crosslink density. Therefore, the foam had higher strength but lower foam resilience and flexibility.

### 3.4 Morphology

Cell morphology of the FPUR foams from molded test method prepared using 3.5%wt. water content in comparison between reference (A1) and 15.0 pbw substituted PO polyol (A8) formulation are shown in Figure 1. SEM micrographs from both formulations show open cell structure. Formulation A8 (Figures 1c and 1d) shows similar cell structure with A1 (Figures 1a and 1b) but smaller cell size and wider cell size distribution was observed. It is clearly shown that the use of PO polyol as COP could obtained the open cell structure FPUR foams, however, the cell size and cell size distribution were slightly different from the foams prepared with conventional COP.

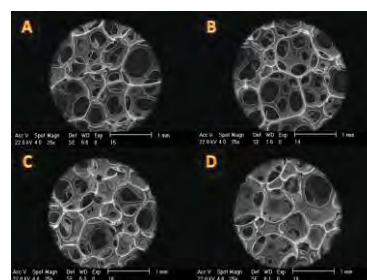


Figure 1. Cell morphology of reference and 15.0 pbw substituted PO polyol formulations with 3.5%wt water content; (a) and (b) reference formulation (A1); (c) and (d) 15.0 pbw substituted PO polyol formulation (A8)

#### 4. Conclusions

FPUR foams using PO polyol as new COP were prepared using cup test and molded test method. High open cell content FPUR foams with good mechanical properties were achieved. The results from cup test method showed that this new COP gave open cell FPUR foam without effect to foam reactivity. While in molded test method, lowering in force-to-crush (FTC) was observed which indicated that FPUR foams had higher open cell content. FPUR foams prepared from PO polyol had higher foam hardness and strength while slightly less foam flexibility and resilience were obtained.

#### Acknowledgements

Program in Petrochemistry and Polymer Science, Department of Chemistry, Faculty of Science, Chulalongkorn University and Bayer Thai Co., Ltd. are acknowledged for materials and financial supports for this research.

#### References

- [1] R. Herrington, K. Hock, *Flexible Polyurethane Foams*, The Dow Chemical Company, 1997, 11.2
- [2] Bayer Material Science, *Ullmann's Encyclopedia of Industrial Chemistry*, 7th ed., Wiley-VCH Verlag, 32-33.
- [3] R. G. Petrella et al, *Dimensional Stabilizing, Cell Opening Additives for Polyurethane Flexible Foams*, Patent U.S. 6,043,290, to Air Product and Chemicals, Inc., 2000.
- [4] K.-C. Song, S.-M. Lee and D.-H. Lee, *J. Cell. Plast*, **38** (2002), 507-522.
- [5] Tyler, Robert, *Polyurethane Foam Cell Opening Agents and Method for Making Foam Using the Same*, Patent WO 00/63269 to Inolex Investment Corporation, 2000.
- [6] J. B. Nichols et al, *Polyurethane Foam Prepared Using High Functionality Cell Openers*, Patent U.S. 4,929,646, to The DOW Chemical company, 1990.
- [7] H. H. Park, J. B. Park, *J. Cell. Plast*, **39** (2003), 291-305.
- [8] E. V. Eetvelde, C. Banner, J. Cenens and S. Chin, *J. Cell. Plast*, **38** (2002), 31-49.
- [9] P. Falke, C. Kudoke, I. Rotermund and B. Zschke, *J. Cell. Plast*, **35** (1999), 43-68.

# FABRICATION OF POLYDIACETYLENE INDICATORS FOR THERMAL AND SOLVENT SENSING

Jade-tapong Klahan<sup>1</sup>, Boonchoat Paosawatyanong<sup>2</sup> and Mongkol Sukwattanasinitt<sup>3\*</sup>

<sup>1</sup> Program of Petrochemistry and Polymer Science, Faculty of Science, Chulalongkorn University, Bangkok 10330, Thailand

<sup>2</sup> Department of physics, Faculty of Science, Chulalongkorn University, Bangkok 10330, Thailand

<sup>3</sup> Nanotec-CU Center of Excellence on Food and Agriculture, Department of Chemistry, Faculty of Science, Chulalongkorn University, Bangkok 10330, Thailand

\*E-mail: smongkol@chula.ac.th

**Abstract:** Polydiacetylenes (PDAs) are conjugated polymers which are promising active agents for colorimetric sensors and indicators. To fully utilize PDAs in sensing applications, fabricating and patterning techniques are of importance. In this work, the commercial 10, 12-pentacosadiynoic acid (PCDA) is used as a diacetylene monomeric model for fabrication on solid surface by commercial inkjet printing and airbrush painting. As the results, inkjet printing technique needed a nonionic surfactant (Brij<sup>®</sup> 58 P, Triton<sup>®</sup> X-100, Tween<sup>®</sup> 20) for high contrast and stable printing in designated area on the paper. For airbrush painting technique, it was alternatively used for the unprintable area without any surfactant needed. The color transitions of the sensors from blue to red in thermal and solvent sensing test are recorded by commercial webcam and the images are converted to RGB system by an image-processing software. The plots of %B and %R against temperature giving two curves with an intersection assigned as a color transition point.

## 1. Introduction

Thermochromic materials change reversibly colour with changes in temperature, PCDA and leuco dye are interesting thermochromic material for studies

A class of conjugated polymers known as polydiacetylenes (PDAs) has attracted enormous attention in the fields of sensors. Their color can change from blue to red by various external stimuli such as heat [1], solvent [2], mechanical stress [3], and UV irradiation leading to application such as thermal sensors, biosensors, UV sensor and chemosensors. Recently, printing and deposition of functional materials on paper substrates have been topics of great interest owing to several advantageous attributes of paper substrate that enable its use in flexible, light-weight and disposable devices. Consequently, various organic and inorganic, as well as stimulus-responsive functional materials, have been immobilized on paper substrate for applications in displays, sensors and memory devices [4-8].

Leuco dyes are composed of microcapsules that change color reversibly. When the temperature is raised to a specified temperature the pigment goes from colored to colorless. The color returns to the original color as the pigment is cooled down. The leuco dye are used in various applications like novelty items and warning signs[9].

Among the patterning methods employed for deposition of functional materials on paper substrates, the inkjet technique [10] is of great interest owing to its superior features, including the ability to generate patterns with noncontact operation on large areas, obtain end-user control of structural design of patterns utilizing software on a PC, and allow low production costs. The Airbrush technique [11] is alternatively used for the unprintable area with reduced chance of clogging and easy to use for variety of ink solutions.

The current research aims to investigate the potential fabrication of PDA by ink-jet printing and airbrush painting techniques. For inkjet printing, the commercially available nonionic surfactant (Brij<sup>®</sup> 58 P, Triton<sup>®</sup> X-100 or Tween<sup>®</sup> 20) was mixed with a diacetylene monomer (PCDA structure shown in Figure 1) in DI water by sonication to produce homogenously dispersed vesicle sols. The blue-to-red color transition temperature of the PDA coated paper sheet was determined from the RGB values. In airbrush painting method, commercial leuco thermochromic pigments were also studied in comparison with PCDA.

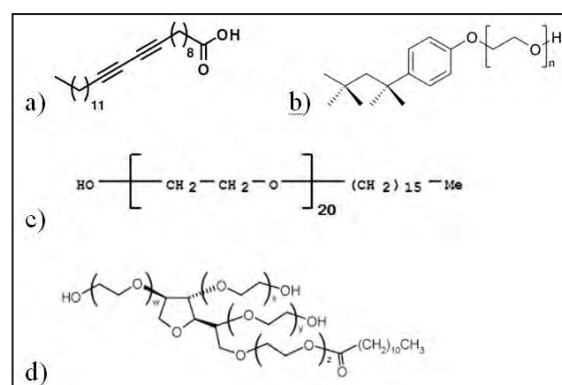


Figure 1. Structures of (a) diacetylene monomer (PCDA), (b) Triton<sup>®</sup> X-100, (c) Brij<sup>®</sup> 58 P and (d) Tween<sup>®</sup> 20.

## 2. Materials and Methods

### 2.1 Materials

10,12-Pentacosadiynoic acid (PCDA), a diacetylene monomer, was purchased from GFS Chemicals, USA. Brij<sup>®</sup> 58 P and Triton<sup>®</sup> X-100 was purchased from Fluka. Tween<sup>®</sup> 20 was purchased from Sigma-Aldrich.



Dimethyl sulfoxide was purchased from RCI Labscan. Leuco dye (Chameleon-T Powder) was purchased from Polychrom.co.ltd, Korea. Lacquer (TOA T-5000) was purchased from TOA PAINT (THAILAND) CO.,LTD, Thailand. Thinner was purchased from Ocean Rota Co., Ltd, Thailand

## 2.2 Preparation of ink solution

### 2.2.1 Ink-jet printing

A typical method for the preparation of diacetylene ink suspension is as follows. PCDA (30 mg) and a nonionic surfactant (Brij® 58 P or Triton® X-100 or Tween® 20) (30 mg) were dissolved in 0.30 mL of dimethyl sulfoxide (DMSO), and the organic solution was slowly dropped into 3.7 mL of DI water at 80 °C. The resulting suspension was sonicated (Elma S40H Elmasonic) at 80 °C for 30 min. Following the sonication, the suspension was kept at 4 °C overnight and filtered to remove lipid aggregates using sintering glass (Mesh ~ 4-5 µm) and syringe filter (0.8 µm) before usage. Ink solution (black) from a conventional inkjet office printer (HP Deskjet Ink Advantage K109a-z) cartridge was removed, and the cartridge (HP703 black) was thoroughly washed with methanol, water and dried at 100 °C for 2 hours. Then, the diacetylene ink (4 mL) was loaded into the clean cartridge.

### 2.2.2 Airbrush painting

A thermochromic dye i.e. PCDA and Leuco dye (30 mg) was dissolved in 4 mL of binder solution made of a 1:2 ratio of lacquer:thinner. The ink solution loaded into a tank of airbrush (HKX HB-3G).

## 2.3 Substrate for airbrush painting

The surfaces used during this study included clean aluminum lid, Thai coppernickel coins, PET bottle, PE thin film, PE plate, 80GSM paper (A4, Double A), wood board, white cotton textile and glass slide.

## 2.4 Photographic imaging

All images of the developed marks were obtained by a Digital SLR camera (Nikon D40X with a Nikon Nikkor lens 18–55 mm) fixed to a camera stand. Some images were obtained with use of a scanner (Epson Perfection V33) and commercial webcam.

## 2.5 Colorimetric measurements

The percentages of the red (%R), green (%G) and blue (%B) colors were calculated. The %B and %R were plotted as a function of temperature. The temperature at the crossing point between %B and %R curves was assigned as the color transition temperature [13].

## 3. Results and Discussion

The diacetylene ink was printed on conventional white A4 paper by an ink-jet printer. The printed paper was allowed for air dry for 2 hours and stored in the dark. The dry printed paper was irradiated at 254 nm

UV light (1400 µW/cm<sup>2</sup>) for 2 minutes. As shown in Figure 2, among three nonionic surfactants used, Brij® 58 P provided the highest contrast blue image of poly(PCDA) after the irradiation. The image turned to red color upon heating at 90 °C for 15 seconds.

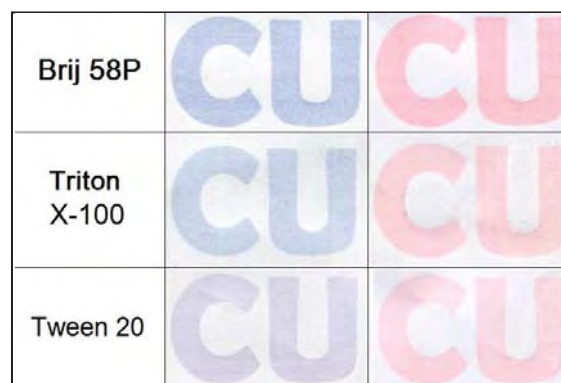


Figure 2. Photographs of printed images on paper using an ink solution mixture of PCDA and Brij® 58 P, Triton® X-100 and Tween® 20 after UV irradiation (left) and followed by heating (right).

The images of poly(PCDA) printed on A4 paper were converted to R, G and B values in the RGB system by an image processing software. The plots of %B and %R against temperature gave two curves with the intersection assigned as the color transition point (Figure 3) [13]. From this assignment, the color transition of poly(PCDA) incorporated with Brij 58 P, Triton X-100 and Tween 20 were determined as 68 °C, 63 °C and 60 °C, respectively. Thus, the transition temperature can be varied by the incorporation of different types of surfactants.

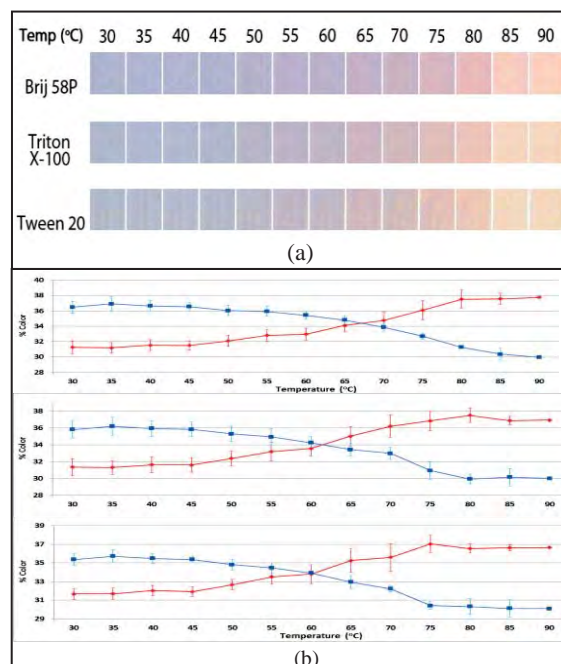


Figure 3. (a) Photographic images of UV-irradiated paper printed with PCDA ink incorporated with Brij® 58 P, Triton® X-100 and Tween® 20 upon heating

from 30 to 90 and (b) plots of %R and %B against temperature corresponding to the photographic images.

Furthermore, poly(PCDA) has been showed blue-to-red colorimetric responses upon contact with various solvents [12]. The blue UV-developed poly(PCDA) printed paper also showed similar blue-to-red solvatochromism (Figure 4). Again, the types of surfactants affected the sensitivity of poly(PCDA) toward the solvents. Among the three surfactants used in this work, Brij® 58 P demonstrated the highest solvatochromic stability comparing with Triton® X-100 and Tween® 20.

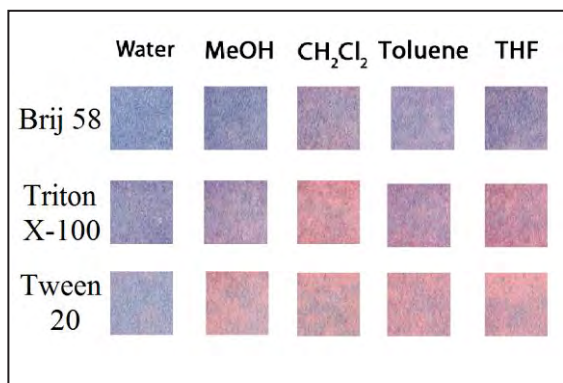


Figure 4. Photographic images of UV-irradiated paper printed with PCDA ink incorporated with Brij® 58 P, Triton® X-100 and Tween® 20 upon exposure to water (control) and various organic solvents.

Airbrush painting is a useful alternative method for dye or ink deposition on unprintable area such as stationary, large or 3-D objects and rough surface [10]. In this work, we tested the airbrush painting for deposition of PCDA on surfaces of various types of objects including clean aluminum lid, Thai coppernickel coins, PET bottle, PE thin film, PE plate, 80GSM paper, wood board, white cotton textile and glass slide. A commercial leuco thermochromic pigment (orange color, transition temperature 31 °C) was also studied for comparison. Use of the PCDA or leuco dye with binder for airbrush painting was found to be viable for surface of all types of materials as both PCDA and leuco dye attached well with the surfaces. PCDA ink produced deep to light blue color after UV irradiation (Figure 5) while the orange leuco dye gave orange to pink color (Figure 6). Upon heating both blue poly(PCDA) and orange leuco thermochromic dye changed their color to red and colorless, respectively indicating their retained thermochromic properties. It is also interesting to note that the colors of the materials affect the apparent color of the dyes on the surfaces. Darker materials led to darker shade of the final appearance of the dyes. White substrate such as paper (Figure 6d) is thus the most suitable for indicator preparation and colorimetric analyses.

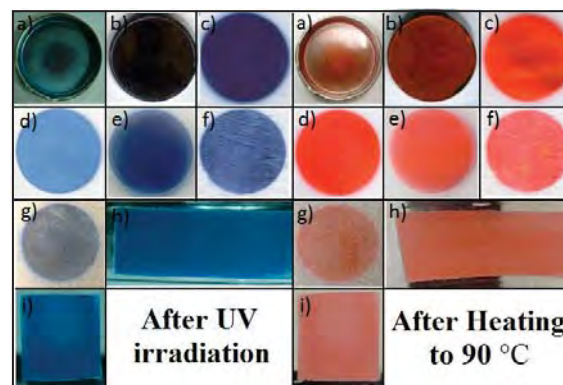


Figure 5. Airbrush painted images of PCDA/binder solution on various types of surfaces: (a) aluminum lid, (b) Thai coppernickel coins, (c) PE thin film, (d) 80GSM paper, (e) PE plate, (f) white cotton textile, (g) wood board, (h) PET bottle, (i) glass slide. The samples after UV irradiation appear as blue color (left) and the samples after heating appear as red color (right).

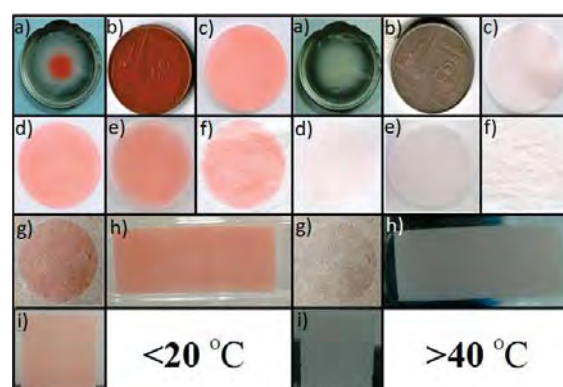


Figure 6. Airbrush painted images of orange leuco dye solution on various surfaces: (a) aluminum lid, (b) Thai coppernickel coins, (c) PE thin film, (d) 80GSM paper, (e) PE plate, (f) white cotton textile, (g) wood board, (h) PET bottle, (i) glass slide. The samples appear as pink color (left) below 20 °C and the samples appear as the substrate color above 40 °C (right).

#### 4. Conclusion

Ink-jet printing of PCDA is achievable by incorporating a nonionic surfactant i.e Brij® 58 P, Triton® X-100 or Tween® 20 into the aqueous suspension of PCDA lipid. Brij® 58 P gave most uniform printing with highest color contrast and solvent stability. It also gave the highest color transition temperature of the blue UV-developed poly(PCDA). Airbrush painting is also a convenient method for deposition of the thermochromic dyes on a wide variety of unprintable materials. The formulation of an airbrush ink is also rather simple requiring only the dye, commercial lacquer binder and thinner solvent.

## Acknowledgements

The authors thank financial supports from the Thailand Nanotechnology Center (NANOTEC, NSTDA), the IIAC Chulalongkorn University Centenary Academic Development Project, the National Research University Project of Thailand, Office of the Higher Education Commission (AM1006A), the 90th Anniversary Fund of CU and the Thai Government Stimulus Package 2 (TKK2555, SP2).

## References

- [1] D. J. Ahn, E. H. Chae, G. S. Lee, H. Y. Shim, T. E. Chang, K. D. Ahn and J. M. Kim, *J. Am. Chem. Soc.* **125** (2003) 8976–8977.
- [2] D. J. Ahn and J. M. Kim, *Acc. Chem. Res.* **41** (2008) 805–816.
- [3] R.A. Nallicheri and M. F. Rubner, *Macromolecules* **24** (1991) 517–525.
- [4] U. Zschieschang, T. Yamamoto, K. Takimiya, H. Kuwabara, M. Ikeda, T. Sekitani, T. Someya and H. Klauk, *Adv. Mater.* **23** (2011) 654.
- [5] A. Russo, B. Y. Ahn, J. J. Adams, E. B. Duoss, J. T. Bernhard and J. A. Lewis, *Adv. Mater.* **23** (2011) 3426.
- [6] M.C. Barr, J. A. Rowehl, R. R. Lunt, J. Xu, A. Wang, C. M. Boyce, S. G. Im, V. Bulovic and K. K. Gleason, *Adv. Mater.* **23** (2011) 3500.
- [7] J. Jang, J. Ha and J. Cho, *Adv. Mater.* **19** (2007) 1772.
- [8] J.-H. Kang, Z. Xu, S.-M. Paek, F. Wang, S.-J. Hwang, J. Yoon and J.-H. Choy, *Chem. Asian J.* **6** (2011) 2123.
- [9] G. Nelson, *Int. J. Pharmaceut.*, **242** (2002) 55-62
- [10] B. Yoon, D.-Y. Ham, O. Yarimaga, H. An, C. W. Lee, and J. M. Kim, *Adv. Mater.* **23** (2011) 5492-5497
- [11] A. D. Grazia, M. Mikhael, N. Stojanovska, B. Reedy, R. Shimmon and M. Tahtouh, *Forensic Sci. Int.* **216** (2012) 189–197
- [12] H. Jiang, Y. Wang and Q. Ye, *Sens. Actuators, B* **143** (2010) 789.
- [13] The method is under patenting application process.



# TRANSDERMAL DELIVERY OF NAPROXEN USING CHITIN EMULSION VIA PIG SKIN MODEL

Sukanya Raksin<sup>1</sup>, Amornpun Sereemaspun<sup>2</sup>, Wanpen Tachaboonyakiat<sup>1\*</sup>

<sup>1</sup> Department of Materials Science, Faculty of Science, Chulalongkorn University, Phayathai, Pathumwan, Bangkok, 10330 Thailand

<sup>2</sup> Department of Anatomy, Faculty of Medicine, Chulalongkorn University, Pathumwan, Bangkok, 10330 Thailand

\* Corresponding author ; E-Mail: Wanpen.Ta@chula.ac.th, Tel: +662 218-5065, FAX: +662 218-5561

**Abstract:** Encapsulation techniques were used in pharmaceuticals in order to control the delivery of encapsulated agents and protected the active agents from environmental degradation. Emulsion technique has been widely used for encapsulation. In this study, the capability of naproxen encapsulation in emulsion based chitin microcapsules was investigated. Skin permeation of naproxen from emulsion based chitin microcapsules was studied through dermatomed pig skin model. The influence of oil types (Isopropyl myristate (IPM) and soybean oil) and percentage of chitin particles to the permeation of naproxen through pig skin was investigated. Naproxen was incorporated into an oil phase before emulsification. The droplet size of drug incorporated emulsion was similar to that of no drug incorporated one, which was approximately 350-500 nm when the amount of incorporated naproxen was about 6 mg/ml. The highest naproxen permeability was afforded by using IPM as oil phase with 1%w/v of chitin particles as encapsulator. Using soybean oil as oil phase exhibited lower naproxen permeability than IPM. This was indicated that IPM enhanced permeation of drug through pig skin. Therefore, chitin microcapsule prepared via oil-in-water emulsion was suitable for lipophilic drug encapsulation which an approach for medical and pharmaceutical applications.

## 1. Introduction

Encapsulation techniques are used in pharmaceuticals, food, agriculture, laundry products, pigments, etc. Emulsion technique have been widely used for encapsulation especially used as drug carrier in pharmacy as well as templates in the production of micro/ nanocapsules and particles for controlled release [1, 2]. The emulsions stabilized by particles are usually called Pickering emulsion. This can be viewed as capsules that could be used for controlled delivery purpose [3]. Pickering emulsions are stabilized by solid particle such as titanium dioxide, carbon nanotube, chitin nanocrystal, silica, clay and many others [4-8]. Several researchers investigated as carriers for lipophilic drugs. It is well documented [9-11] that solid particles can act as excellent emulsion stabilizers. Emulsion stabilization by solid particles depends on sufficient particle adsorption and the formation of a densely packed layer at the oil-water interface, which prevents droplet flocculation and coalescence. Particles have ability to form rigid structure that can inhibit droplet coalescence. Ionic

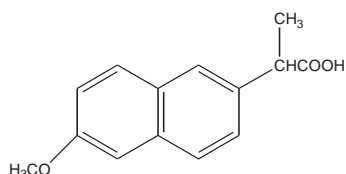
particles give rise to electrostatic repulsion, which facilitate emulsion stability against flocculation [12].

Naproxen (Np) (s)-6-methoxy- $\alpha$ -methyl-2-naphthalenenacetic acid (Scheme. 1), is a non-steroidal anti-inflammatory drug (NSAID) with analgesic effects that is used for the treatment of osteoarthritis and rheumatoid arthritis. NSAIDs are the most commonly used drugs to reduce pain and inflammation [13, 14]. Oral administration of NSAIDs is very effective but clinical use has a limit because of adverse side effects, such as irritation of the gastro-intestinal mucosa. Transdermal delivery of naproxen can prevent this side effect with oral administration and help to maintain plasma levels for long-term therapy from a single dose [15, 16].

In principle, emulsion can be used to delivery drug to patients by several routes, such as injection, oral administration. Transdermal administration of emulsions has increasing an interest [17]. Three main mechanisms have been offered to explain advantages of emulsion for transdermal drug delivery. First, the high solubility capable for both hydrophilic and lipophilic drugs in emulsion system may increase thermodynamic activity to skin. Second, composition in emulsion that acts as permeation enhancers can disrupt the structure of stratum corneum and increase drug permeation through skin. Third, permeation rate of drug from emulsion may be increased because the affinity of a drug to internal phase in emulsion can be easily modified to favor partitioning into stratum corneum by changing its part in emulsion [18-20].

Because of the primary barrier to transdermal permeation of drugs is the stratum corneum, the outermost layer of the skin, which comprises keratin-rich cells embedded in multiple lipid bilayers [21, 22]. There is not variable of drugs that permeate through the skin in therapeutic quantities. To overcome the main limitation of transdermal delivery (low permeability), penetration enhancers have been used to increase transdermal drug delivery [23, 24]. Isopropyl myristate (IPM) has been widely used as a vehicle in many cosmetic and pharmaceutical preparations because of its emollient properties, its safety and its compatibility with a wide range of compounds [25].





Scheme 1. Chemical structure of naproxen

This study was conducted with multiple aims which were (1) to study the capability of naproxen encapsulation in chitin emulsion; (2) to investigate transdermal drug delivery via pig skin; (3) to investigate the effect of oil types (soybean oil, isopropyl myristate; IPM) to enhance permeability through skin.

## 2. Materials and Methods

### 2.1 Materials

Chitin with degree of acetylation percent (%DA) of 71 was purchased from A.N. Lab, Thailand. Naproxen, methanesulfonic acid and phosphate buffer saline (PBS) were obtained from sigma Aldrich, USA. Isopropyl myristate (IPM) was purchased from Merck, Germany. Soybean oil was supplied from Thanakorn Vegetable Oil Products, Co., Ltd., Thailand. All chemicals were used without further purification. Pig skin was purchased from local slaughter house

### 2.2 Preparation of chitin particle

Chitin (40-240 mg) was dissolved in methanesulfonic acid. A 4 mL of distilled water was then added drop-wise into chitin solution under sonication. The obtained colloidal chitin nanoparticle solution was dialyzed against distilled water for 2 days. After dialysis, colloidal chitin nanoparticle solution was diluted to final concentration of 1-3 % w/v.

### 2.3 Preparation of emulsion

Chitin nanoparticles dispersed in distilled water was used as solid particles emulsifier in aqueous phase, while soybean oil or IPM was used as oil phase. The water to oil ratio was fixed at 8:2. Naproxen (1-6 mg/ml) was used as model hydrophobic drug and dissolved in oil phase before encapsulation. Drug encapsulation was obtained by emulsification of both phases under probe sonicator for 30 min.

### 2.4 Determination of chitin particle and droplet size of emulsion

Chitin particle size and droplet size of emulsion were determined by a dynamic light scattering (Zetasizer, Nanoseries model). The colloidal of chitin particle and emulsion using chitin particle as emulsifier were diluted in distilled water in order to avoid scattering.

### 2.5 Determination of encapsulated drug within emulsion

The emulsion formulations were centrifuged at 6000 rpm, 4°C for 20 min to separate the incorporated drug from non-incorporated drug. The supernatant was

analyzed by UV spectrophotometry at 229 nm for non-incorporated drug concentration. The percentage of drug encapsulation was calculated by subtracting from non-incorporated drug concentration over feeding drug concentration.

### 2.6 Transdermal drug delivery

Pig skin was used as a model for transdermal drug delivery. It was cut to a thickness of  $1.50 \pm 0.10$  mm using cryostat microtome. The thickness of each skin was measured with micrometer. The skin was shortly washed with PBS. The skin was placed at the center between the donor and the receptor compartments of Franz diffusion cells. The Franz diffusion cells have penetration area of  $1.77 \text{ cm}^2$  with receptor compartment volume of 12 ml. A 1 ml of emulsion formulation was filled on the skin surface at the donor compartment. The medium in the receptor fluid was 0.1 M PBS (pH 7.4). The experiment was carried out under controlled temperature at 37 °C for 24 h. At the specified interval time, the samples (800 µl) were withdrawn from receptor compartment and replaced with fresh PBS.

## 3. Results and Discussion

### 3.1 Determination of chitin particle and droplet size in emulsion

Chitin particles were prepared in the range of 120 -200 nm. Emulsions were prepared with the oil to water ratio 2:8. The droplet sizes assessed by DLS instrument as shown in Fig. 1. It was found that the droplet sizes of emulsion with drug was around 350-500 nm which was not much different from that of emulsion without drug.

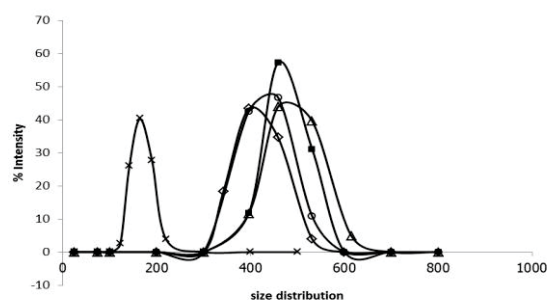


Fig.1 Particles size for chitin particles and emulsion: × chitin particle; □ soybean oil emulsion without drug; ◇ soybean oil emulsion with drug; ○ IPM emulsion without drug ; △ IPM emulsion with drug

### 3.2 Determination of drug encapsulation in emulsion

Fig.2 demonstrated the percentage of drug encapsulation efficiency in the emulsion using chitin solid particle as emulsifier, soybean oil and IPM as oil phase. The results showed that when the concentration of drug increased, drug encapsulation efficiency was increased in those emulsions when using both soybean oil and IPM as an oil phase. The percentage of naproxen encapsulation in emulsion at feeding of 1 mg/mL was around 55-60 %, whilst that in emulsions

at feeding of 2-6 mg/ml was around 80-99%. Comparing with the same drug concentration, percentage of drug encapsulation of the emulsion using IPM as oil phase was higher than that of using soybean oil. Due to the solubility of Naproxen in IPM was higher than that of solubility in soybean oil.

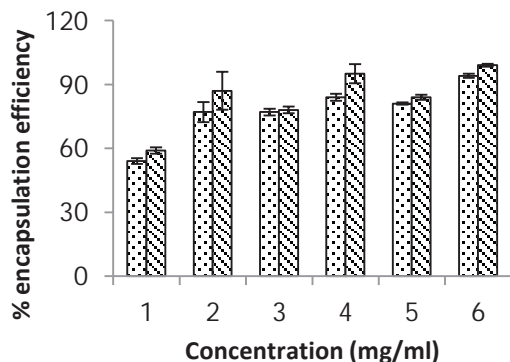


Fig.2 Percentage of naproxen encapsulation 3% w/v; ▨ IPM; ▨ soybean oil. Each value represents the mean  $\pm$  S.D. (n=3).

### 3.3 In vitro skin permeation study

To study the effect of oil type on permeability of naproxen through stratum corneum, epidermis and dermis, pig skin was used as model in this experiment. Fig.3 showed naproxen permeation through pig skin from emulsion formulations. It was found that in the same percentage of chitin (1 wt. %), the skin permeation of naproxen in IPM is highly than skin permeation in soybean oil. Due to IPM acts as an enhancer and highly disrupted the lipid barrier of the pig skin. IPM was reported as permeation enhancer for naproxen through shed snake skin [25]. It was reported that IPM have amphiphilic characteristic which contained both polar and non-polar sides similar to proteins, this polar side might interact with the intracellular proteins of stratum corneum [25]. One more mechanism was studied by comparing the permeability of naproxen from pluronic gel through the shed snake skin with delipidized one by pretreat the both shed snake skins with IPM before placing the naproxen in pluronic gel, it was found that the permeability of naproxen through both skins were approximately the same ( $P=3.57-3.61 \times 10^{-3} \text{ cm h}^{-1}$ ), indicating that IPM highly disrupted the lipid barrier of the skin [25]. Considering the emulsion form by using IPM as oil phase, Naproxen skin permeation from emulsion formulations increased significantly with decreased percentage of chitin particles i.e. the emulsion using 3% w/v as emulsifier has lower permeability than that of using 1% w/v of chitin, whilst decreasing the chitin particle concentration to 0.5% w/v, the permeability was not far from that of using 1% w/v of chitin. It may because of the higher concentration of chitin particles (3% w/v) form a thicker layer of chitin particles absorption at the interface between oil and water than that of 0.5 and 1 % w/v. The thickness of the nanoparticle interfacial layers has significantly affected to the releasing rate of

drug from oil-in-water emulsion. The thicker interfacial layer exhibited, the better sustained drug release than the thinner one, owing to its barrier property [26, 27].

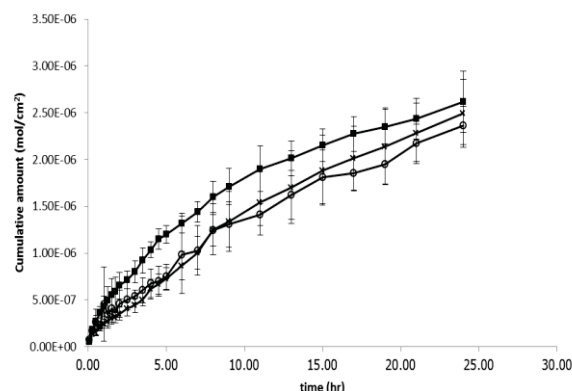


Fig.3. Cumulative amount (mol/cm<sup>2</sup>) of naproxen through pig skin in 24 hrs: ○ IPM with 3 wt% of chitin; ■ IPM with 1 wt% of chitin; □ soybean oil with 1 wt% of chitin. Each value represents the mean and S.D. (n=3).

## 4. Conclusions

Naproxen was encapsulated in O/W emulsion stabilized by chitin particles. In this study, soybean oil and IPM were used as oil phases. The emulsion prepared from fixed concentration of chitin particle (3% w/v), but different in using oil phases (IPM and soy bean oil) was found that the emulsion using IPM as an oil phase exhibited higher drug permeability through pig skin than that of using soy bean oil as an oil phase. This indicated that IPM has permeation enhancer properties. Besides, the emulsion using 1% w/v of chitin particle as emulsifier showed greater penetration of naproxen through pig skin than that of using 3% w/v of chitin particle as emulsifier. Chitin microcapsules exhibited good function for drug delivery, so it suitable for encapsulated lipophilic drug and using in pharmaceutical applications.

## Acknowledgements

The authors greatly appreciate the Integrated Innovation Academic Center: IIAC" Chulalongkorn University Centenary Academic Development Project for financial support throughout this research. We also would like to thank Center of Excellence on Petrochemical and Materials Technology and CU. Graduate School Thesis Grant, Chulalongkorn University for partially financial support.

## References

- [1] P.B. O'Donnell and J.W. McGinity. *Adv. Drug Delivery Rev.* **28** (1997) 25-42.
- [2] W. Mehnert and K. Mader. *Adv. Drug Delivery Rev.* **47** (2001) 165-196.

- [3] S. Simovic and C. A. Prestidge. *Eur. J. Pharm. Biopharm.* **67** (2007) 39–47.
- [4] T. Chen, P.J. Colver, and S. A. F. Bon. *Adv. Mater.* **19** (2007) 2286-2289.
- [5] W. Chen, X. Liu, Y. Liu and H. Kim. *Mater. Lett.* **64** (2010) 2589-2592.
- [6] M. V. Tzoumaki, T. Moschakis, V. Kiosseoglou and C. G. Biliaderis. *Food Hydrocolloid* **25** (2011) 1521-1529.
- [7] S. Wang, Y. He and Y. Zou. *Particuology* **8** (2010) 390–393.
- [8] Y. Nonomura and N. Kobayashi. *J. Colloid Interface Sci.* **330** (2009) 463–466.
- [9] N. P. Ashby and B. P. Binks. *Phys. Chem. Chem. Phys.* **2** (2000) 5640-5646.
- [10] R. Aveyard, B. P. Binks, J. H. Clint. *Adv. Colloid Interface Sci.* **100–102** (2003) 503–546.
- [11] B. P. Binks and S. O. Lumsdon. *Langmuir* **16** (2000) 8622-8631.
- [12] D.E. Tambe and M.M. Sharma. *Adv. Colloid Interface Sci.* **52** (1994) 1-63.
- [13] S. Baboota, F. Shakeel, A. Ahuja, J. Ali and S. Shafiq. *Acta pharm* **57** (2007) 315–332.
- [14] E. Escribanoo, A. C. Calpenaa, J. Queraltb, R. Obacha and J. Dome'nech. *Eur. J. Pharm. Sci.* **19** (2003) 203–210.
- [15] R. Janttharaprapap and G. Stagni. *Int. J. Pharm.* **343** (2007) 26–33.
- [16] E. Beetge, J.D. Plessis, D. G. Muller, C. Goosen and F. J. Rensburg. *Int. J. Pharm.* **193** (2000) 261–264.
- [17] S. Peltola, P. Saarinen-Savolainen, J. Kiesvaara, T.M. Suhonen and A. Urtti. *Int. J. Pharm.* **254** (2003) 99–107.
- [18] YS. Rhee, JG. Choi, ES. Park and SC. Chi. *Int. J. Pharm.* **228** (2001) 161–170.
- [19] X. Zhao, J.P. Liu, X. Zhang and Y. Li. *Int. J. Pharm.* **327** (2006) 58–64.
- [20] N. U. Okura, S. Apaydinb, N. U. K. Yavasoglu, A. Yavasoglu and H. Y. Karasulu. *Int. J. Pharm.* **416** (2011) 136–144.
- [21] I. Lavon and J. Kost. *Research focus* **9** (2004) 670-676.
- [22] J. Hadgraft and M. E. Lane. *Int. J. Pharm.* **305** (2005) 2–12.
- [23] K. Takahashi and J. H. Rytting. *J. Pharm. Pharmacol.* **53** (2001) 789-794.
- [24] M. R. Prausnitz and R. Langer. *Nat. Biotechnol.* **26** (2008) 1261-1268.
- [25] H. Suh and H. W. Iun. *J. Pharm. Pharmacol.* **48** (1996) 812-816.
- [26] C.A. Prestidge, S. Simovic. *Int. J. Pharm.* **324** (2006) 92–100.
- [27] S. Simovic, C. A. Prestidge. *Eur. J. Pharm. Biopharm.* **67** (2007) 39–47.

# EFFECT OF MULTI-COATED LEVEL OF HYDROXYPROPYL METHYLCELLULOSE ON TABLET MICROCAPSULES

Boonyong Punantapong\*

Department of Industrial Physics and Medical Instrumentation, Faculty of Applied Science,  
King Mongkut's University of Technology North Bangkok, Bangkok 10800, Thailand

\* Author for correspondence; E-Mail: bpp@kmutnb.ac.th, Tel. +66 25552000, Fax. +66 5878253

**Abstract:** The purpose of this research was to develop and characterize an oral controlled release drug delivery system. In this study, we used a new drug release model to study the effect of formulation parameters on drug release from film-coated chlorpheniramine (CPM) nonpareil system as tablet microcapsules. The film-coated CPM was prepared by using a fluid bed apparatus. A hydroxypropyl methylcellulose (HPMC) solution was blended with an aqueous ethylcellulose dispersion to adjust the permeability of the film. The apparent permeability of samples was obtained from dissolution data using a previously reported drug release equation. It was plotted versus the film coating level or the HPMC concentration in the film. The apparent permeability was found to increase with the HPMC concentration. After a critical concentration was reached, the HPMC into the film caused a rapid increase in apparent permeability. However, the decrease of apparent permeability versus coating level was related to the reduction of the total holes area. Thus the drug release can be enhanced by the dissolution of the core. It was suggested that a mechanical formed porous film could change to a nonporous film after the bead was completely coated. At the same time, the concentration of the HPMC was required to modify permeability of the film. Therefore, the drug release was found to decrease with increasing the HPMC concentration to the films. Furthermore, the soluble core can be enhanced the drug release from the coating system.

## 1. Introduction

Drug delivery was highly innovative in terms of materials to assist delivery, excipients, and technology which allow fast or slow release of drugs. These dosage forms were the advantages of reducing the frequency of dosing, lowering adverse effects and improving patient compliance [1,2]. However, the formulation was to controlled drug release for the required duration of time with optimum release pattern depends on various factors such as the physicochemical properties of the drug, nature of drug-carrier, ratio of polymer to drug, type of the dose form and route of administration [3,4,5].

In addition, one of the most commonly used methods of modulating tablet drug release was to include it in a matrix system. It is based on matrix structure, release kinetics, controlled release properties such as diffusion, erosion, swelling [6,7]. Thus it is believed that several different mechanisms are involved in the drug [8,9]. Then matrix systems are usually classified in three main groups; hydrophilic, inert, and

lipidic [10]. At the same time, hydroxypropyl methylcellulose has been one of the important polymeric materials used in microspheres and microencapsulation formulations. So it was the most commonly and successfully used hydrophilic retarding agent for the preparation of oral controlled drug delivery systems. The transport phenomena involved in the drug release from hydrophilic matrices were complex because the microstructure and macro-structure of HPMC exposed to water was strongly time dependent [11,12,13].

## 2. Materials and Methods

### 2.1 Matrix Tablets

Matrix tablets were prepared by wet granulation method. Granulation was done using a solution of polyvinylpyrrolidone (PVP K90) in sufficient isopropyl alcohol. The wet mass was passed through mesh No.8. The wet granules were air dried for 2 hours. The granules were sized by mesh No.16 and mixed with aerosol and talc. Tablets were compressed at 1000 mg weight with 18 mm oval-shaped punches. For the coating, various concentrations of HPMC K100 (10%, 20%, 30%, 40%, 50%) were developed to evaluate the drug release and to study the effect of polymer concentration on drug release. At the same time, the prepared tablets were tested as per standard procedure for weight variation (n=20), hardness (n=6), drug content, thickness (n=20), friability, water uptake, and erosion characteristics.

### 2.2 The Release Studies

The release measurements were performed using USP dissolution apparatus Type II at 50 rpm using a continuous automated monitoring system which consists of the microcomputer and dissolution test software. To analyze the mechanism of drug release from the matrix tablets, data obtained from the drug release studies were analyzed according to the equation of the zero-order model, Higuchi model, and the Korsmeyer-Peppas model as equation (1), (2), and (3) respectively [14,15,16].

$$M_t = M_o + K_o t \quad (1)$$



$$M_t = M_o + K_H t^{0.5} \quad (2)$$

$$M_t = M_o + K_k t^n \quad (3)$$

where  $M_t$  is the amount of the drug dissolved in time  $t$ ,  $M_o$  is the initial amount of drug in the solution,  $K_o$  is the zero-order release constant;  $K_H$  is the Higuchi rate constant;  $K_k$  is the release constant; and  $n$  is the release exponent, which characterizes the mechanism of drug release.

From these equations, the magnitude of the release exponent “ $n$ ” indicated the release mechanism (i.e., Fickian diffusion or anomalous transport). In this study, we limited values of  $n$  between 0.38 and 0.85 for indicated Fickian diffusion-controlled drug release and relaxational release transport; non-Fickian, zero-order release, respectively. Furthermore, the release was run in triplicate and absorbance was recorded automatically at 12 hr. Then the percentage of drug release was determined as a function of time. Thus the significance of difference between the dissolution of different studied patches with various variables was evaluated using the analysis of variance (ANOVA). The differences were considered significant at  $p \leq 0.05$ .

Table 1: Physical Properties of Formulations Prepared

Quantity	Results				
	F1	F2	F3	F4	F5
Weight (mg) mean $\pm$ SD	635 $\pm$ 1.2	672 $\pm$ 1.8	798 $\pm$ 2.1	856 $\pm$ 1.9	935 $\pm$ 1.2
Hardness (kp)	17-18	17-19	17-21	16-18	17-22
Drug content (%)	99.5	97.8	99.5	99.8	99.8
Thickness (mm)	4.9 $\pm$ 0.03	4.9 $\pm$ 0.04	5.4 $\pm$ 0.05	5.8 $\pm$ 0.06	6.2 $\pm$ 0.02
Friability (%)	0.17	0.23	0.35	0.37	0.25

\* HPMC indicates hydroxypropyl methylcellulose.

\*\* Formulations: F1, 10% HPMC; F2, 20% HPMC; F3, 30% HPMC; F4, 40% HPMC; F5, 50% HPMC.

### 3. Results and Discussion

The results of the uniformity of weight, hardness, drug content, thickness, and friability of the tablets are given in Table 1. All the samples of the test product complied with the official requirements of uniformity of weight. The drug content was found to be close to 100% of the label claim for Voveran S.R. tablet [10] in all formulations. The low friability indicates that the matrix tablets are compact and hard.

Figure 1 illustrates five different concentrations of hydroxypropyl methylcellulose (HPMC) at 10%, 20%, 30%, 40%, and 50%. We were developed to evaluate the drug release and to study the effect of

polymer concentration on drug release. In the figure, we were found that if the concentration of HPMC was increased, the percentage average release of HPMC will be decreased within 0-6 hours. After that, it will be increased slowly and saturated between 10-12 hours.

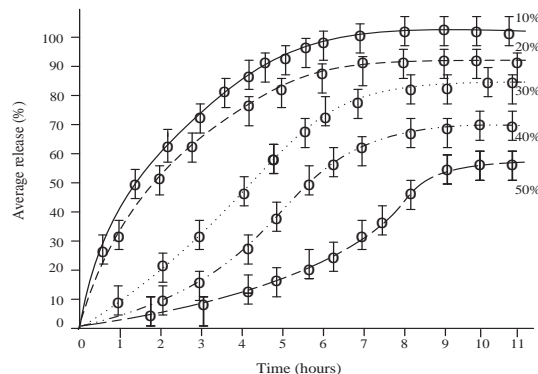


Figure 1. Percentage of the average release of HPMC K100 from matrices was containing different concentrations of hydroxypropyl methylcellulose

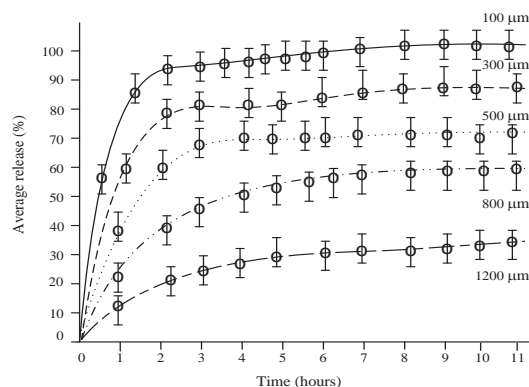


Figure 2. Percentage of HPMC release from different particle size range

Figure 2 shows the percent HPMC released from microspheres of different particle size ranges 100  $\mu$ m, 300  $\mu$ m, 500  $\mu$ m, 800  $\mu$ m, and 1200  $\mu$ m. The results showed that the release from microspheres of the size range below 300  $\mu$ m was significantly ( $p < 0.05$ ) higher than that from all other studied ranges (300-500  $\mu$ m). This presumably is due to the much larger surface area available for release and shorter path length necessary for drug to diffuse through [4,16]. There was no significant difference ( $p > 0.05$ ) in the release between the sizes of 300-500  $\mu$ m and those sizes ranged 500-800  $\mu$ m and 800-1200  $\mu$ m. The slowest release was from the largest particle size range 800-1200  $\mu$ m.